Impurity transport in tokamak plasmas: gyrokinetic study of neoclassical and turbulent transport

Peter Donnel

To cite this version:

Peter Donnel. Impurity transport in tokamak plasmas: gyrokinetic study of neoclassical and turbulent transport. Plasma Physics [physics.plasm-ph]. Aix Marseille Université, 2018. English. NNT : . tel-01961598v1

HAL Id: tel-01961598
https://hal.science/tel-01961598v1

Submitted on 20 Dec 2018 (v1), last revised 14 Oct 2019 (v2)

AIX-MARSEILLE UNIVERSITÉ
Institut de Recherche sur la Fusion par confinement Magnétique
Ecole Normale Supérieure
ECOLE DOCTORALE 352

Thèse présentée pour obtenir le grade universitaire de docteur

Discipline: Physique et sciences de la matière
Spécialité: Energie, Rayonnement et Plasma

Peter Donnel

Transport d'impuretés dans les plasmas de tokamak: étude gyrocinétique du transport néoclassique et turbulent

Impurity transport in tokamak plasmas: gyrokinetic study of neoclassical and turbulent transport

Soutenue le 10/12/2018 devant le jury composé de:

Clemente Angioni	IPP	Rapporteur
Laurent Villard	SPC	Rapporteur
Peter Beyer	PIIM	Examinateur
Pascale Hennequin	LPP	Examinateur
Alain Bécoulet	IRFM	Invité
Xavier Garbet	IRFM	Directeur de thèse
Yanick Sarazin	IRFM	co-Directeur de thèse

Abstract

Impurity transport is an issue of utmost importance for tokamaks. One reason is the choice of tungsten for ITER divertor. Indeed high-Z materials are only partially ionized in the plasma core, so that they can lead to prohibitive radiative losses even at low concentrations, and impact dramatically plasma performance and stability. On-axis accumulation of tungsten has been widely observed in tokamaks. While the very core impurity peaking is generally attributed to neoclassical effects, turbulent transport could well dominate in the gradient region at ITER relevant collisionality. The transport of low and medium-Z impurities also results from both neoclassical and turbulent transport. Up to recently, first principles simulations of corresponding fluxes were performed with different dedicated codes, implicitly assuming that both transport channels are separable and therefore additive. The validity of this assumption can be questionned.

Preliminary simulations obtained with the gyrokinetic code GYSELA have shown clear evidences of a neoclassical-turbulence synergy for impurity transport. However no clear theoretical explanation was given. New simulations have been done using a new and more accurate collision operator, improved boundary conditions and more flexible sources. The new simulations confirm the neoclassical-turbulence synergy and allow identification of a mechanism that underly this synergy.

Turbulence can induce poloidal asymmetries. An analytical work performed during this thesis allows to compute the level and the structure of the axisymmetric part of the electric potential knowing the turbulence intensity. Two mechanisms are found for the generation of poloidal asymmetries of the electric potential: at large frequencies, flow compressibility is a key player for the generation of poloidal asymmetries. In this case a $\sin\theta$ structure is predicted as in the case of GAMs. For lower frequencies, the ballooning of the turbulence is instrumental in the generation of the poloidal asymmetries. In this case, a $\cos\theta$ structure is predicted.

A new prediction for the neoclassical impurity flux in presence of large poloidal asymmetries and pressure anisotropies has been derived during this thesis. It turns out that both banana/plateau and Pfirsch-Schlüter contributions are significantly impacted by the presence of large poloidal asymmetries and pressure anisotropies. A fair agreement has been found between the new theoretical prediction for neoclassical impurity flux and the results of a GYSELA simulation displaying large poloidal asymmetries and pressure anisotropies induced by the presence of turbulence.

Résumé court

La compréhension du transport d'impuretés dans les tokamaks est cruciale. Une des raisons vient du choix d'utiliser du tungstène pour le divertor d'ITER. En effet, les noyaux lourds ne sont que partiellement ionisés dans le cœur du plasma, ils peuvent alors fortement rayonner et entrainer une diminution importante de la qualité du plasma. Une accumulation des impuretés au cœur du plasma est souvent observée au sein des tokamaks. Cette accumulation est souvent attribuée à la physique néoclassique mais le transport turbulent pourrait bien dominer dans la zone de gradient dans ITER. Dans le cas des impuretés légères, les transports néoclassique et turbulent sont du même ordre de grandeur dans les machines actuelles. Jusqu'à récemment, le calcul des flux néoclassique et turbulent étaient réalisés de façon distincte, supposant implicitement que les deux canaux de transport sont indépendants. On peut se demander si cette hypothèse est valide.

En effet, des simulations préliminaires obtenues avec le code gyrocinétique GYSELA ont montré l'existence d'une synergie entre transports néoclassique et turbulent dans le cas des impuretés. Mais la compréhension théorique de cette synergie était manquante. Des simulations utilisant un nouvel opérateur de collision, des conditions aux limites plus réalistes et des sources plus flexibles ont été réalisées. Ces simulations ont permis de confirmer l'existence d'une synergie et un mécanisme permettant sa compréhension a été trouvé.

La turbulence peut générer des asymétries poloidales. Un travail analytique réalisé pendant cette thèse permet de prédire le niveau et la structure de la partie axisymétrique du potentiel électrique. Deux mécanismes sont à l'origine des asymétries poloidales du potentiel électrique: à haute fréquence, la compressibilité du flot est à l'origine de l'asymétrie et la théorie prédit une structure en $\sin\theta$ comme dans le cas des GAMs. Pour les fréquences plus basses, le ballonnement de la turbulence engendre l'asymétrie poloidale. Dans ce cas une structure en $\cos\theta$ est prédite par le modèle analytique.

Une nouvelle prédiction du flux d'impureté néoclassique en présence d'asymétries poloidales et d'anisotropie de la pression a été réalisée. Il s'avère que les contributions banane/plateau et Pfirsch-Schlüter sont fortement impactées par la présence d'asymétries poloidales et d'anisotropie de la pression. Un bon accord a été trouvé entre la nouvelle prédiction et une simulation réalisée avec GYSELA pour laquelle la turbulence est à l'origine des asymétries poloidales et de l'anisotropie de la pression.

Résumé long

Les étoiles sont alimentées par l'énergie dégagée par les réactions de fusion. La fusion est la réaction de deux noyaux légers pour produire un noyau plus lourd. Les réactions de fusion libèrent énormément d'énergie en comparaison des réactions chimiques. La réaction la plus facile à obtenir sur Terre est la fusion du deutérium avec le tritium.

$$^2_1D +^3_1 T \rightarrow^4_2 He +^1_0 n$$

Cette réaction produit un noyau d'hélium, un neutron et libère 17.6 MeV par réaction ce qui est considérable. Le deutérium est présent en quantités quasi illimitées sur Terre. Les réserves en tritium sont en revanche faibles (quelques dizaines de kilogrammes) dû à la radioactivité de cet isotope de l'hydrogène. Heureusement il est possible de générer du tritium en bombardant du lithium avec des neutrons énergétiques comme ceux produits par les réactions de fusion. La fusion du deutérium avec le tritium nécessite des températures de l'ordre de 100 millions de degrés.

Dans ces conditions extrêmes l'état de la matière est un plasma: les électrons sont totalement découplés des noyaux (au moins pour les plus légers). Un plasma peut être considéré en première approximation comme un gaz sensible au champ électromagnétique. Cette sensibilité vient du découplage des électrons et des noyaux rendant le plasma conducteur. La sensibilité du plasma au champ électromagnétique peut être utilisée pour le confiner. Plusieurs types de pièges électromagnétiques ont été testés. En l'état actuel des connaissances le tokamak est le dispositif le plus prometteur pour générer les conditions nécessaires pour produire des réactions de fusion contrôlée sur Terre. Le tokamak ITER, qui sera de loin le plus grand tokamak au monde, est actuellement en construction sur le site de Cadarache.

Le tokamak est un piège magnétique qui repose sur le fait que des particules chargées en présence d'un champ magnétique effectuent un mouvement de giration autour des lignes de champ magnétique (en première approximation). Si les lignes de champ se referment sur elle-mêmes, on a alors créé un piège magnétique. Le champ magnétique principal du tokamak est donc un champ toroidal imposé par des bobines extérieures. Cependant, il existe une vitesse de dérive magnétique lorsque le champ magnétique n'est pas homogène. Dans le cas d'un piège magnétique purement toroidal, cette dérive est verticale et dépend du signe de la charge de la particule. Cette dérive verticale détériore fortement le confinement en créant une séparation de charge qui conduit finalement à une expulsion du plasma vers l'extérieur du tokamak via une dérive électrique. Pour compenser la séparation de charge engendrée par la dérive magnétique, un champ magnétique secondaire dans la direction poloïdale est ajouté au champ principal. Ce champ poloïdal, généré par le courantcirculant dans le plasma, permet de connecter magnétiquement le haut et le bas de la machine et limite fortement le déconfinement lié à la dérive verticale. Ce piège magnétique permet de confiner les particules chargées dans une zone délimitée de l'espace (l'intérieur du tokamak). Une fois le confinement assuré, il est possible de chauffer le plasma en injectant de l'énergie au sein de la machine notamment avec l'utilisation d'ondes. On atteint ainsi des températures suffisantes pour que les réactions de fusion puissent avoir lieu.

Un plasma de fusion parfait est composé uniquement de deutérium, de tritium et d'électrons. Toute autre espèce est considérée comme une impureté. Les impuretés peuvent provenir des réactions de fusion (hélium), être injectées pour l'opération de la machine (par exemple de l'argon) ou encore venir des parois du tokamak (cas typique du tungstène W). Les impuretés ont deux effets néfastes sur les performances d'un tokamak. Tout d'abord elles diluent les réactifs et diminuent ainsi le nombre potentiel de réactions de fusion. Ensuite les impuretés lourdes (comme le W) ne sont pas totalement ionisées même à des températures de l'ordre de 100 millions de degrés. Pour cette raison ces impuretés rayonnent énormément d'énergie même à des concentrations très faibles et refroidissent ainsi le plasma. De plus, les impuretés lourdes ont tendance à s'accumuler au centre du tokamak. Pour ces deux raisons il est crucial de comprendre comment se transportent les impuretés au sein d'un tokamak afin de tenter de les évacuer du centre du tokamak. C'est la problématique principale de cette thèse.

Il existe plusieurs approches distinctes pour décrire un plasma: l'approche particulaire qui suit chaque particule individuellement, l'approche cinétique qui est une méthode statistique reposant sur le très grand nombre de particules présentes dans le tokamak et enfin l'approche fluide qui peut être vue comme une réduction en moments de l'approche cinétique. Chacune de ces méthodes possède des avantages et des inconvénients. Dans l'étude présentée dans cette thèse, c'est l'approche cinétique qui est choisie afin de décrire correctement un maximum d'effets avec un minimum d'approximations. L'approche cinétique fait évoluer temporellement une fonction de distribution dans un espace à 6 dimensions (3 d'espace et 3 de vitesse) appelé espace des phases. La fonction de distribution représente une densité de probabilité de trouver une particule à un certain endroit de l'espace des phases à un instant donné. Cette fonction de distribution évolue temporellement à cause de la présence du champ électromagnétique. Du fait de l'évolution temporelle de la fonction de distribution, la densité et le courant qui en sont des moments, évoluent également. Finalement, dû aux équations de Maxwell le champ électromagnétique est modifié. A ce stade, très peu d'approximations ont été faites mais le système est très complexe à résoudre.

Il s'avère qu'à cause du fort champ magnétique présent dans les tokamaks (de 2 à 5T), la fréquence de giration des particules autour des lignes de champ magnétique est beaucoup plus grande que la plupart des autres fréquences typiques du plasma. Grâce à cette séparation d'échelle, il est possible de réduire l'espace des phases accessible aux particules en moyennant sur leur mouvement de giration. On passe alors d'un espace des phases à 6 dimensions à un espace des phases à 4 dimensions plus un paramètre (l'invariant adiabatique μ). Cette réduction du problème s'appelle la théorie gyrocinétique. Cette théorie possède un domaine de validité assez large. Elle est à l'heure actuelle la théorie avec le moins d'approximations qui reste numériquement abordable.

Il existe plusieurs codes gyrocinétiques dans le monde. Chacun possède des points forts et des points faibles dépendant des choix réalisés par ses développeurs. GYSELA (Fig.0.1) est un code gyrocinétique développé par une collaboration de laboratoires français et suisses et allemands, depuis le début des années 2000. Les points forts de ce code sont qu'il permet de simuler l'ensemble de la partie confinée du plasma (global) sans séparation d'échelles entre l'équilibre et les fluctuations (F total). L'état quasi-stationnaire peut être atteint en ajoutant des sources (forcé par le flux) et il autorise plusieurs espèces ioniques ce qui est crucial pour l'étude du transport des impuretés. GYSELA possède plusieurs limitations. En effet un champ magnétique simplifié est utilisé empêchant l'étude d'une géométrie plus réaliste. De plus l'hypothèse électrostatique est utilisée. Cette hypothèse limite le nombre d'instabilités pouvant se développer et empêche de prendre en compte les corrections électromagnétiques sur les instabilités électrostatiques. Remarquons tout de même que l'hypothèse électrostatique est plutôt bien vérifiée dans les plasmas de tokamak. En particulier, les deux instabilités principales se développant à l'échelle ionique on Temperature Gradient ou ITG, et Trapped Electron Modes ou TEM, sont bien décrites dans cette approximation. Enfin les électrons sont supposés avoir une réponse adiabatique dans cette thèse même si GYSELA autorise à présent de traiter les électrons cinétiquement.

Figure 0.1.: Potentiel electrique en sortie du code GYSELA

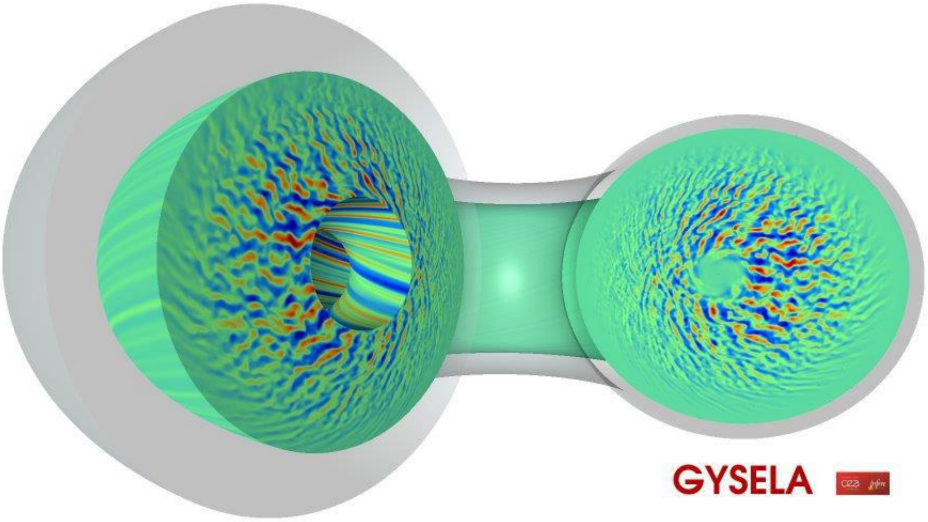

Un des canaux majeurs de transport des impuretés est associé à la présence de collisions entre les particules du plasma. On peut distinguer deux types de collisions dans les plasmas (cf Fig.0.2). Les collisions dites fortes résultent d'une interaction importante entre deux particules $(\alpha \sim 1)$ où α est l'angle de déflection défini sur la figure 0.2 . Les trajectoires des particules sont alors fortement modifiées en seulement quelques interactions. L'autre type de collision est communément appelé collision faible $(\alpha \ll 1)$. Dans ce cas, chaque interaction entre deux particules est faible d'où leur nom. Il faut alors un très grand nombre d'interactions pour modifier significativement la trajectoire d'une particule. Les collisions faibles, majoritaires, sont celles qui jouent un rôle prépondérant dans les questions de transport des particules. Ce sont les seules décrites dans cette thèse.

La fréquence de collision entre particules décroît avec la température. Au vu des températures régnant au cœur des tokamaks, les plasmas de cœur sont peu collisionnels. Il est toutefois nécessaire de prendre en compte les collisions entre particules pour une prédiction réaliste du transport de particules au sein d'un tokamak. En effet, elles sont à l'origine d'un transport dit néoclassique qui est important pour les impuretés. De plus, les collisions amortissent les écoulements macroscopiques et influencent ainsi le niveau de saturation de la turbulence. Enfin, les collisions dissipent les fluctuations à petites échelles et stabilisent ainsi les simulations numériques en limitant le développement de structures sous résolues.

Pour ces raisons un opérateur de collision linéarisé adapté au code GYSELA a été développé au cours de cette thèse. Il est valide quelle que soit la nature des espèces considérées (masse, charge, concentration). Une de ses particularités est qu'il prend en compte les dérivées par rapport à l'invariant adiabatique μ. Cela permet à cet opérateur de collision d'avoir une propriété essentielle: la relaxation collisionnelle des fonctions de distribution vers une Maxwellienne isotrope. Les dérivées par rapport à μ ont été prises en compte en utilisant une méthode de projection de la fonction de distribution sur une base de polynômes orthogonaux dans la direction μ. Cette technique permet un traitement analytique d'une grande partie de l'opérateur de collision, réduisant d'autant le coût de son traitement numérique. Les dérivées par rapport à la vitesse parallèle $v_\parallel$ sont traitées en différences finies.

Il a été vérifié numériquement que l'opérateur de collision possédait les propriétés attendues: conservations (particules, impulsion, énergie), taux de relaxation (isotropisation, échanges d'impulsion et d'énergie entre espèces). Cette étude numérique a également permis de connaître la résolution minimale nécessaire à l'opérateur de collision. En l'occurrence une discrétisation $\left(N_{v\parallel}, N_\mu\right) = (128, 64)$ est suffisante pour l'opérateur de collision.

Figure 0.2.: Gauche: Déviation d'une particule chargée par intéraction Coulombienne avec une autre particule chargée. Droite: Nombre de particules avec un paramètre d'impacte compris entre b et $b + \delta b$

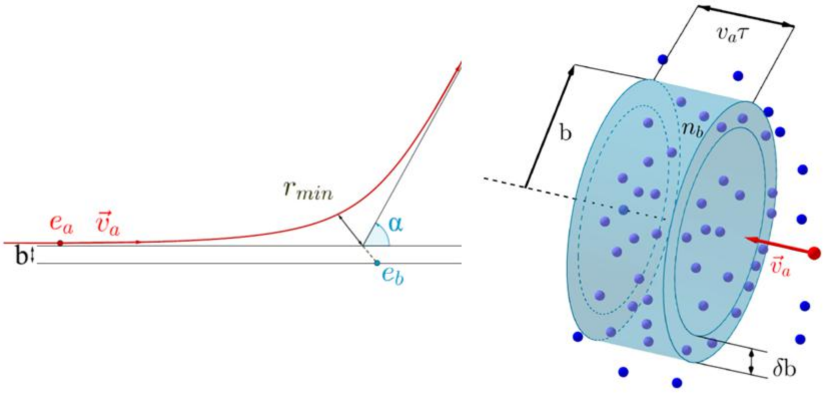

Il existe deux sortes de particules dans les tokamaks: les particules dites passantes qui suivent les lignes de champ magnétique avec une vitesse parallèle $v_\parallel$ à peu près constante et les particules dites piégées. Le piégeage vient de la dépendance du champ magnétique avec le grand rayon $B \propto R^{-1}$. Les particules n'ayant pas assez d'énergie dans la direction parallèle au champ restent alors piégées du côté bas champ (extérieur). Les collisions peuvent modifier les trajectoires des particules en modifiant leur contenu énergétique (valeur totale et répartition entre direction parallèle et perpendiculaire au champ). La théorie néoclassique permet de quantifier l'effet des collisions sur les trajectoires des particules et de calculer le transport associé.

Il existe trois régimes de collisionalité (cf Fig.0.3). Le régime “banane” correspond au cas le moins collisionnel. Dans ce cas, les trajectoires des particules sont peu affectées par les collisions. Le régime de collisionalité intermédiaire est appelé “plateau”. Pour ce régime de collisionalité, les trajectoires des particules piégées sont fortement impactées par les collisions alors que les particules passantes le sont marginalement. Enfin dans le régime de forte collisionalité appelé “Pfirsch-Schlüter” toutes les trajectoires de particules sont fortement impactées par les collisions. Les prédictions de la théorie néoclassique dépendent fortement de la collisionalité. Chaque espèce a sa propre collisionalité qui dépend essentiellement de sa densité, sa température mais aussi de sa masse, sa charge et la présence des autres espèces. L'ion majoritaire est typiquement dans le régime “banane” dans tout le coeur du tokamak alors que les impuretés sont plutôt en régime “plateau” ou “Pfirsch-Schlüter” selon les cas.

Pour un plasma sans impuretés, trois résultats néoclassiques sont importants. Tout d'abord la théorie néoclassique prévoit un transport diffusif de chaleur proportionnel au gradient de température. Même si ce transport est souvent sous dominant devant le transport turbulent, il peut se révéler compétitif lorsque la turbulence est localement réduite comme par exemple dans le piedéstal d'un plasma en mode H. La théorie néoclassique prévoit également une rotation poloïdale du plasma proportionnelle au gradient de température. Cette rotation est souvent en bon accord avec les mesures expérimentales. Enfin la théorie néoclassique prévoit un amortissement collisionel des structures aux grandes échelles comme les écoulements zonaux. Ces écoulements étant connus pour réguler la turbulence, la prise en compte des collisions est importante pour une prédiction quantitative du niveau de turbulence.

La théorie néoclassique est également très importante pour la compréhension du transport d'impuretés. En effet, le transport néoclassique est souvent dominant devant le transport turbulent dans le cas des impuretés lourdes. Ceci est dû au fait que la collisionalité d'une impureté est proportionnelle au carré de sa charge. Elle peut donc être un ou deux ordres de grandeur plus grande que pour l'ion majoritaire. La théorie néoclassique standard (sans asymétrie poloïdale autre que celle du champ magnétique) prévoit que le transport d'impureté, hormis le terme de diffusion, est dominé par deux termes convectifs en opposition: le gradient de densité de l'ion majoritaire engendre une vitesse de pincement conduisant à une accumulation des impuretés au centre. Au contraire, un gradient de température conduit en général à un flux sortant pour l'impureté.

Ceci se retrouve sur l'équation (0.0.1). Pour cette equation, $\Gamma_{z,neo}$ est le flux d'impureté prédit par la théorie néoclassique, N_z la densité d'impureté, N_i la densité d'ions majoritaires, T la température (supposée égale pour toutes les espèces). D est un coefficient de diffusion proportionnel à la fréquence de collision des impuretés sur les ions.

$$\Gamma_{z,neo} = -N_z D \left[\frac{\partial_r N_z}{N_z} - \frac{Z_z}{Z_i} \frac{\partial_r N_i}{N_i} - H_{theo} \frac{Z_z}{Z_i} \frac{\partial_r T}{T} \right] \tag{0.0.1}$$

Tous les phénomènes décrits ci-dessus ont été testés avec succès en utilisant le nouvel opérateur de collision dans GYSELA. Ces tests ont permis de vérifier l'ensemble des propriétés de l'opérateur de collision.

Figure 0.3.: Gauche: Coupe poloidale d'une trajectoire de particule passante. Droite: Coupe poloidale d'une trajectoire de particule piégée. (Extrait de la soutenance de D. Estève)

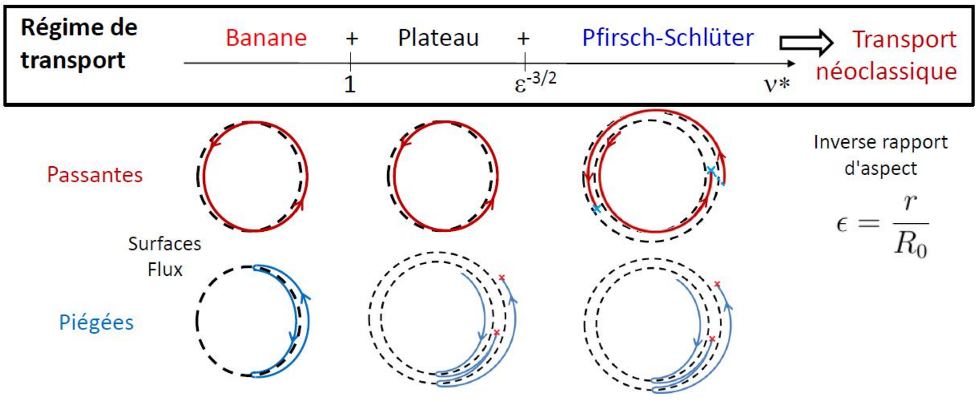

La turbulence est souvent associée à une ou plusieurs instabilités sous-jacentes. Une instabilité provient toujours d'un écart à l'équilibre thermodynamique. Cet écart correspond à un réservoir d'énergie libre qui peut être utilisé pour faire grandir une instabilité. Une fois l'instabilité développée, elle génère des fluctuations (typiquement du potentiel électrique) que l'on appelle turbulence. Dans le cas de la turbulence se développant à l'échelle ionique, une des principales instabilités sous-jacentes est due au gradient de température de l'ion majoritaire. Cette instabilité, dite ITG (Ion Temperature Gradient), est de type interchange. Cela signifie qu'elle nécessite un gradient de l'intensité du champ magnétique colinéaire au gradient de température (dans le cas où $\beta = \frac{2\mu_0 P}{B^2} \ll 1$. Cette situation arrive typiquement du côté bas champ du tokamak (vers l'extérieur). On obtient donc souvent une turbulence dite ballonnée. Cela signifie que l'intensité de la turbulence est plus grande du côté bas champ que du côté fort champ. Cette caractéristique est visible sur la figure 0.1.

Il existe plusieurs mécanismes de saturation de la turbulence. Un premier mécanisme de saturation est associé au transfert non-linéaire de l'énergie turbulente vers des grandes structures comme les écoulements zonaux (structure axisymétrique sans dépendance poloïdale). Ces écoulements zonaux sont ensuite saturés à cause des collisions et des effets non linéaires. D'autres mécanismes de saturation de la turbulence existent. Par exemple, le transport engendré par la turbulence peut réduire les gradients et donc la source d'énergie libre à l'origine de la turbulence. Les non linéarités dues à la turbulence peuvent également générer des petites échelles qui peuvent être efficacement dissipées par les collisions.

La turbulence est le principal mécanisme de transport pour l'ion majoritaire. Dans le cas des impuretés, elle peut également jouer un rôle important en particulier dans le cas où la collisionalité est suffisamment faible. C'est typiquement le cas pour les impuretés légères. La prédiction turbulente du flux d'impuretés est composée de quatre termes. Trois sont de type diffusif et associés respectivement aux gradients de densité, température et de vitesse parallèle de l'impureté. Le dernier terme est purement convectif. Le flux d'impureté prévu par la turbulence est proportionnel à l'intensité turbulente au carré.

Il est souvent observé expérimentalement que la densité des impuretés possède une asymétrie poloïdale importante (cf Fig.0.4). Dans les tokamaks actuels, cette asymétrie est souvent associée à l'utilisation de sources de chauffage extérieur. La présence d'une asymétrie poloïdale de la densité d'impureté modifie le flux néoclassique d'impureté dit "Pfirsch-Schlüter" jusqu'à un ordre de grandeur. La prise en compte de cette modification du flux néoclassique par l'asymétrie poloïdale de la densité d'impureté permet de trouver un bon accord avec les résultats expérimentaux dans les tokamaks actuels.

On peut toutefois se demander si le cadre théorique actuel est suffisant pour la prédiction du transport d'impuretés dans des machines plus grandes telles qu'ITER. En effet, pour ces machines la collisionalité des impuretés sera plus faible à cause notamment d'une température plus élevée. Les impuretés lourdes devraient typiquement être dans le régime de collisionalité intermédiaire dit "plateau". Dans ce régime, l'anisotropie de pression joue un rôle crucial. Cette anisotropie peut être générée par des sources externes mais aussi par la turbulence. Les prédictions actuelles du transport d'impuretés néoclassique ne prennent pas en compte la présence d'une éventuelle anisotropie en pression importante et doivent donc être révisée pour des machines de la taille d'ITER.

De plus, le poids relatif des sources extérieures par rapport à l'auto-organisation du plasma devrait décroitre avec la taille de la machine. Dans ce cadre, deux questions sont posées. Tout d'abord comment le flux banane/plateau d'impureté est-il modifié en prenant en compte une anisotropie de pression importante. Ensuite est-ce que la turbulence peut générer une anisotropie en pression et des asymétries poloïdales suffisantes pour impacter significativement la prédiction néoclassique du transport d'impureté. Si c'est le cas, on parlera de synergie entre les transports turbulent et néoclassique pour le transport de l'impureté. On entend par synergie la non additivité des deux mécanismes de transport. De telles synergies ont déjà été observées dans d'autres contextes comme par exemple le flux de chaleur porté par l'ion majoritaire.

Figure 0.4.: Asymétrie poloidale du rayonement associé à la présence d'impuretés

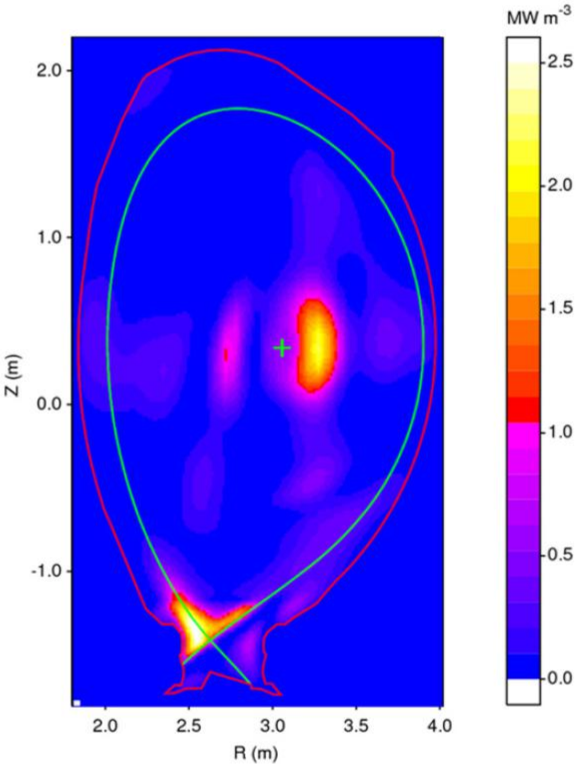

Le calcul du flux d'impuretés néoclassique en présence d'une part d'asymétrie poloïdale de densité et de pression, et d'autre part d'anisotropie en pression a été effectué. Plusieurs conclusions résultent de ce calcul. Tout d'abord le flux "banane/plateau" peut être largement amplifié par la présence d'une anisotropie en pression présentant une asymétrie poloïdale. De plus, le flux “Pfirsch-Schlüter” est lui aussi modifié par la présence d’une anisotropie en pression.

Cette prédiction du flux d’impureté a été comparée aux résultats d’une simulation à haute résolution effectuée avec le code GYSELA. Cette simulation a été effectuée en considérant l’ion majoritaire comme étant du deutérium et l’impureté comme étant du tungstène avec une charge effective de Z=40 et présente à l’état de trace. Le choix d’une impureté trace a été fait pour simplifier l’analyse. Ce choix est pertinent dans le cas du tungstène. L’ion majoritaire est en régime banane sur tout le domaine de simulation. L’impureté est en régime Pfirsch-Schlüter partout mais est très proche du régime plateau dans une certaine zone spatiale. La simulation est turbulente et aucune source susceptible de générer une asymétrie poloïdale n’a été employée.

Dans cette simulation, des asymétries poloïdales importantes ($\sim 30\%$ dans le cas de la densité) ont été observées. De plus, une anisotropie importante s’est également développée dans la zone spatiale où le tungstène est proche du régime plateau. Le niveau d’asymétrie poloïdale et d’anisotropie est suffisant pour impacter le flux néoclassique ce qui montre que la turbulence est capable de modifier la prédiction néoclassique du flux d’impuretés. Une comparaison entre le flux prédit par le modèle théorique et le flux obtenu directement en sortie du code GYSELA a été réalisée. Un bon accord a été obtenu sur l’ensemble du domaine de simulation. Sans la prise en compte de l’anisotropie en pression, il n’y aurait pas d’accord dans la zone où l’impureté est proche de régime plateau.

La charge importante des impuretés lourdes, les rend sensibles aux asymétries du potentiel électrique. En effet, une réponse de type Boltzmann stipule que $\frac{\delta N_z}{N_Z} \sim Z\frac{e\delta\phi}{T}$ où les quantités avec les deltas sont à comprendre comme un écart à la valeur moyenne sur la surface de flux. Par conséquent, une asymétrie poloïdale même modérée du potentiel électrique engendrera une asymétrie importante sur l’impureté. La dernière partie de cette thèse permet la compréhension du mécanisme de génération d’asymétrie poloïdale du potentiel électrique par la turbulence.

Le modèle analytique développé permet de comprendre la génération turbulente des écoulements zonaux, des GAMs (Geodesic Acoustic Modes) et des cellules de convection avec un seul formalisme. Les cellules de convection sont des modes de potentiel présentant une asymétrie poloïdale et évoluant à une fréquence faible devant celle des GAMs. Deux mécanismes de génération de cellule de convection ont été identifiés. Le premier est dû à la compressibilité du flot (comme dans le cas des GAMs) et domine aux fréquences intermédiaires. Ce mécanisme conduit à une asymétrie de type $\sin\theta$, où θ est l’angle poloïdal ($\theta = 0$ sur le plan équatorial, côté faible champ). Le second mécanisme est dû au ballonnement de la turbulence. Il domine à basse fréquence et conduit à une asymétrie de type $\cos\theta$.

En résumé, cette thèse a permis d'identifier un mécanisme de synergie entre physique néoclassique et turbulence dans le cadre du transport d'impuretés. Cette synergie passe par la génération d'asymétries poloïdales par la turbulence. Ce mécanisme est d'autant plus important que le tokamak est grand. En effet, le rapport de l'asymétrie poloïdale générée par la turbulence sur celle provenant des sources extérieures devrait augmenter avec la taille de la machine. Ce mécanisme doit donc être pris en compte pour une prédiction quantitative du transport d'impuretés sur ITER et les futures machines de taille comparable.

Remerciements

J'aimerais remercier l'ensemble des personnes que j'ai rencontré durant mes trois années de thèse au CEA de Cadarache, à commencer par celui sans qui cette thèse ne se serait sans doute pas aussi bien passée, j'ai nommé le grand Xavier Garbet. Un très grand merci à toi Xavier d'avoir été mon mentor durant ma thèse. Tu m'as appris énormément de choses et même s'il me reste beaucoup à apprendre, je pars avec de solides bases grâce à toi. Merci également pour ton extrême gentillesse et ta bonne humeur tout au long de ma thèse. Comme je te l'ai déjà dit, tu es un modèle pour moi et ça a été un honneur de travailler avec toi. J'aimerais également remercier Yanick Sarazin. Merci de m'avoir proposé de travailler avec Xavier et toi quand j'étais encore en master. Merci également pour l'ensemble de ton aide durant ces trois années et notamment tes nombreuses remarques pertinentes sur le fond comme la forme qui ont permis d'améliorer grandement la qualité de mes publications et présentations orales. J'ai également particulièrement apprécié d'encadrer les TP de master avec toi. Merci aussi à Virginie Grandgirard. Merci d'avoir pris le temps de m'apprendre à coder en Fortran et à utiliser GYSELA. Merci également d'avoir répondu à toutes mes « petites questions » tout au long de ma thèse et toujours dans la bonne humeur. Merci pour les soirées « Villelaurienne » très sympathiques. J'aimerais également remercier Guilhem Dif-Pradalier, Philippe Ghendrih, Guillaume Latu et Chantal Passeron. Merci à vous pour votre gentillesse et votre disponibilité lorsque je venais vous demander un conseil ou vous poser une question. Ça a été un très grand plaisir de travailler au sein de l'équipe GYSELA, non seulement grâce à chacun d'entre vous mais aussi grâce à la très bonne ambiance de travail que vous avez mis en place et que vous entretenez tous les jours. J'espère sincèrement que j'aurais de nouveau l'occasion de travailler avec vous tous.

Merci à l'ensemble des stagiaires, thésards et post-docs de l'IRFM que j'ai rencontré durant ces trois dernières années. Grâce à vous j'ai passé trois années très agréables à l'IRFM mais aussi en dehors avec nos soirées. J'aimerais remercier en particulier Laurent Valade qui a été mon co-bureau pendant la première moitié de ma thèse. Merci d'avoir partagé avec moi tes nombreuses questions de physique, que j'ai pris beaucoup de plaisir à résoudre avec toi. Merci aussi pour ton aide sur l'utilisation du Python. Malgré ton insistance, je ne suis toujours pas passé au bépo mais j'ai beaucoup ri en t'entendant tenter de convaincre tout le monde que c'était « le meilleur clavier pour écrire en français ». Merci aussi pour nos quelques ascensions de la montagne Sainte-Victoire. En bref, ça a été un très grand plaisir de partager mon bureau avec toi. Merci également à Elisabetta Caschera. Ta bonne humeur quotidienne a été vraiment très agréable pour moi. Merci également pour tes « soirées pizza » toujours très plaisantes. Je suis heureux d'avoir partagé ma fin de thèse avec toi et Anastasia Dvornova. Merci à vous deux de vous être occupé de mes cadeaux de thèse qui sont vraiment super ! Merci également à tous les « jeunes » du 513 pour la bonne ambiance générale : Jae Heon Ahn, Camille Beaudoin, Nicolas Bouzat, Guillaume Brochard, Charles Ehrlacher, Olivier Février, Camille Gillot, Nicolas Nace, Jérôme Richard et Fabien Widmer. Merci également à mes amis de l'IRSN Caroline Arcanjo, Hamza Chaif, Cécile Dubois, Alexandre Flouret, Rémi Guédon, Marine Roullier, Audrey Souloumiac et Marie Trijau. Merci à tous pour votre gentillesse et les très nombreuses soirées passées ensemble. Je suis content de vous connaitre et j'espère que nous resterons en contact.

J'en viens maintenant aux personnes qui comptent le plus pour moi. Tout d'abord ma famille : mon frère James Donnel, mon père Jonathan Donnel, mon oncle François Donnel et ma tante Brigitte Calippe. Merci à vous de m'avoir soutenu tout au long de ma vie et d'avoir toujours cru en moi. Sans vous je ne serai certainement pas arriver où j'en suis maintenant. Merci d'être toujours présent pour moi quand j'en ai besoin. J'aimerais également remercier du fond du cœur Sophia Murat. Merci pour tout ce que tu as fait pour moi depuis que je te connais et de partager ta vie avec moi.

Je dédie cette thèse à ma mère qui nous a quitté beaucoup trop tôt.

Contents

Abstract **2**

Résumé court **3**

Résumé **14**

Remerciements **16**

List of Tables **20**

List of Figures **20**

1. Introduction **24**
- 1.1. Fusion . . . 25
- 1.2. Plasmas . . . 28
  - 1.2.1. Basic description . . . 28
  - 1.2.2. Characteristic scales in hot magnetized plasmas . . . 29
- 1.3. Tokamak . . . 30
  - 1.3.1. Lawson criteria . . . 30
  - 1.3.2. Magnetic configuration . . . 31
  - 1.3.3. Particle trajectories . . . 34
  - 1.3.4. Transport accross the magnetic field: underlying mechanisms . . . 36
  - 1.3.5. Typical values . . . 37
- 1.4. Impurities . . . 37

2. The gyrokinetic code GYSELA **40**
- 2.1. Gyrokinetic theory . . . 41
  - 2.1.1. Kinetic description . . . 42
  - 2.1.2. From kinetic to gyrokinetic . . . 43
  - 2.1.3. Quasi-neutrality equation : limit of adiabatic electrons . . . 45
- 2.2. The GYSELA code . . . 48
  - 2.2.1. Main features . . . 48
  - 2.2.2. Numerical aspects . . . 50

3. A multi-species collision operator for GYSELA **54**
- 3.1. Introduction . . . 55

3.2. Presentation of the model . . . 56
3.3. Analytical approximations for an optimized numerical treatment of the collision operator . . . 59
  3.3.1. Separation of the different collision terms . . . 60
  3.3.2. Evolution of thermal energy . . . 60
  3.3.3. Approximation of the distribution function . . . 61
  3.3.4. Treatment of the μ derivatives . . . 64
  3.3.5. Evolution equation of the distribution function components 65
3.4. Numerical implementation . . . 70
  3.4.1. Numerical schemes . . . 70
  3.4.2. Numerical implementation of conservation properties . . . 71
  3.4.3. Choice of numerical parameters . . . 72
3.5. Verification of the collision operator . . . 73
  3.5.1. Single species tests . . . 73
  3.5.2. Test with two species . . . 76

4. Standard neoclassical physics **79**
4.1. Introduction . . . 80
4.2. Physical description of neoclassical theory . . . 80
4.3. Neoclassical test of the collision operator : single species case . . 84
  4.3.1. Neoclassical diffusion and poloidal rotation . . . 84
  4.3.2. Zonal flow damping . . . 87
4.4. Neoclassical test of the collision operator : trace impurity . . . 88
  4.4.1. Neoclassical prediction . . . 89
  4.4.2. Comparison with GYSELA results . . . 95

5. Turbulent prediction of impurity flux **99**
5.1. ITG turbulence . . . 100
  5.1.1. Underlying instability . . . 100
  5.1.2. Linear stability . . . 101
  5.1.3. Turbulence saturation processes . . . 106
5.2. Theoretical prediction of impurity transport related with turbulence 107

6. Neoclassical impurity flux in presence of poloidal asymmetries **110**
6.1. Experimental evidence of poloidal asymmetries of impurity . . . 111
6.2. Neoclassical impurity flux in presence of large poloidal asymmetries and pressure anisotropy . . . 112
  6.2.1. Structure of the impurity flow in presence of poloidal asymmetries . . . 113
  6.2.2. Determination of the poloidal variation of K_z . . . 114
  6.2.3. Neoclassical flux . . . 115
6.3. Comparison with results from gyrokinetic simulations . . . 117
  6.3.1. Choice of the simulation parameters . . . 117

- 6.3.2. Definitions of fluxes . . . 120
- 6.3.3. Poloidal asymmetries and anisotropy . . . 122
- 6.3.4. Comparison between GYSELA results and theoretical predictions . . . 124
- 6.4. Discussion on the theoretical model . . . 127

7. A mechanism of turbulent generation of poloidal asymmetries 130

- 7.1. Evidence of impurity poloidal asymmetries generated by poloidal asymmetries of the electric potential . . . 131
- 7.2. Context for the generation of axisymmetric modes of the electric potential . . . 133
- 7.3. Evolution of a toroidally symmetric mode . . . 136
  - 7.3.1. GAMs . . . 138
  - 7.3.2. Poloidal convective cells . . . 140
- 7.4. Link between source terms and turbulent Reynolds stress tensor 142
- 7.5. Discussion . . . 144
  - 7.5.1. Phase and amplitude of poloidal convective cells . . . 144
  - 7.5.2. Numerical solution . . . 145
  - 7.5.3. Limits of the model . . . 146
  - 7.5.4. Poloidal asymmetry of the distribution function . . . 148

Conclusion 150

Appendix 153

- A. Derivation of the Vlasov with $\bar{g}$ . . . 153
- B. Vlasov equation of the resonant part of the distribution in ballooning representation . . . 154
- C. Linear response of the distribution function . . . 155
- D. Derivation of the collisional parallel momentum exchange for trace and heavy impurities . . . 155
- E. Flux of vorticity . . . 157
- F. Treatment of the resonant functions $L_j\left(\Omega\right)$ and numerical solution 158

Bibliography 171

List of Tables

1.1. Typical values in a Tokamak 37

6.1. Parameters scanned 119

List of Figures

0.1. Potentiel electrique en sortie du code GYSELA 7
0.2. Gauche: Déviation d'une particule chargée par intéraction Coulombienne avec une autre particule chargée. Droite: Nombre de particules avec un paramètre d'impacte compris entre b et $b + \delta b$ . . . 8
0.3. Gauche: Coupe poloidale d'une trajectoire de particule passante. Droite: Coupe poloidale d'une trajectoire de particule piégée. (Extrait de la soutenance de D. Estève) 10
0.4. Asymétrie poloidale du rayonement associé à la présence d'impuretés 12

1.1. The Aston curve represents the average binding energy per nucleon as a function of the number of nucleons. Large values corresponds to stable nucleus. The maximum is reached for Fe^{56}, which is therefore the most stable nucleus. 26
1.2. Reaction rate of various fusion reactions. The curve in red corresponds to the reaction of deuterium with tritium Eq.$(1.1.1)$ which is the one envisaged for fusion reactors. 28
1.3. Left : Coulomb collision between two particles in the frame of the particle b. The deflection angle α depends on the impact parameter b. Right : number of particle colliding with a particle a with an impact parameter between b and $b + \delta b$. It increases with b. 30
1.4. Drift instability of a plasma in a pure toroidal magnetic field. The drift velocity depends on the sign of the charge. It leads to a separation of charge and so a vertical electric field. The $E \times B$ drift then leads to an outward movement of the plasma. 32
1.5. A general magnetic surface. 33

1.6. Magnetic field lines (blue) define magnetic surfaces (yellow) which are toruses. The toroidal component of the magnetic field is created by the coils depicted in red. 34
1.7. Poloidal projection of an unperturbed particle trajectories. On the left for a passing particle and on the right for a trapped particle . . 36
1.8. Radiative collapse due to tungsten accumulation in the core. The top left graph shows the increase of radiative power as a function of time. The right hand side figure shows a radiative spot in the core due to tungsten accumulation. 38

2.1. Potential fluctuations obtained with the gyrokinetic code GYSELA 48
2.2. In Lagrangian-PIC methods, markers initial positions are loaded pseudo- (or quasi-) randomly in phase space (A). Markers are evolved along their orbits (B). Charge and current perturbations are assigned (projected) to real space (C). Field equations are solved (D), e.g. on a fixed grid in real space. Figure coming from [35]. 51
2.3. In Eulerian methods, a fixed grid is defined in phase space (A). Finite difference expressions are used (B) in order to obtain value of f at grid point at the next time step (C). Field equations are then solved (D) after integration over velocity space. Figure coming from [35]. 52
2.4. In semi-Lagrangian methods, a fixed grid is defined in phase space (A). The orbits are integrated back in time from each grid point (B). The value of f at grid points is obtained by interpolation at the foot of the orbit (C) and using the property f = const along orbits. Field equations are then solved (D) after integration over velocity space. Figure coming from [35]. 53

3.1. Velocity dependence of the velocity modulus diffusion rate $\nu_{v,ab}$ (blue), the deflection frequency $\nu_{d,ab}$ (red), the slowing-down frequency $\nu_{s,ab}$ (black) and the absolute value of the energy-loss rate $|\nu_{E,ab}|$ (green). All quantities are normalized to ν_{ab}^{HS} 59
3.2. Velocity dependence of $D_{d,ab}$ (solid line) and of its fit (dashed line) defined by Eq.$(3.3.11)$ 68
3.3. Velocity dependence of $\nu_{v,ab}-\nu_{d,ab}$ (solid line) and of its fit (dashed line) defined by Eq.$(3.3.12)$ 69
3.4. Initial (top) and final (bottom) slices of the distribution function in velocity space are given. The initial distribution function is far from a Maxwellian in the $v_\perp$ direction on the left and in the $v_\parallel$ direction on the right. In both cases, the converged state is an isotropic Maxwellian. 74

3.5. Top : Time evolution of the perpendicular $T_\perp$ (red), the parallel temperature $T_\parallel$ (green), and the total temperature $T_{tot} = \frac{2T_\perp + T_\parallel}{3}$ (blue). Bottom : Time evolution of the logarithmic difference of temperatures. The slope of the curve gives the relaxation rate. . . 76
3.6. Left : Time evolution of the parallel velocity of the main species $V_{\parallel,0}$ (red), and of a trace impurity $V_{\parallel,1}$ (blue). Right : Time evolution of the logarithmic difference of parallel velocities. The slope of the curve gives the momentum exchange rate. 77
3.7. Left : Time evolution of the temperature of the main species T_0 (red), and of a trace impurity T_1 (blue). Right : Time evolution of the logarithmic difference of temperatures. The slope of the curve gives the thermal energy exchange rate. 78

4.1. Trajectory of a particle (red) in the phase space $\left(\theta, v_\parallel\right)$ in presence of collisions. The jumps in the $v_\parallel$ direction represent the effect of the diffusion in the velocity due to collisions. Due to this diffusion, a particle can cross the frontier between the trapping and passing domains (green) and change its nature. 81
4.2. Pfisrch-Schlüter diffusion. On the top, collisions lead to an outward flux. On the bottom collisions lead to an inward flux. 83
4.3. Comparison between the classical prediction (blue), the banana-pateau contribution (red) and the Pfirsch-Schlüter contribution (green) 84
4.4. $k_{neo} = eB\frac{v_\theta}{\nabla T}$ versus $\nu_\star$ predicted by theory (dashed line) compared with GYSELA results (red dots) 86
4.5. $\chi_{neo} = -\frac{Q}{N\nabla T}$ versus $\nu_\star$ predicted by theory (dashed line) compared with GYSELA results (red dots) 86
4.6. Time evolution of the normalized ϕ_{00} coming from the code GYSELA (red) compared with the theoretical prediction (blue). 88
4.7. Normalized particle flux of impurities versus density gradients. The solid line corresponds to GYSELA results and the dotted line to its linear fit. 97
4.8. Normalized particle flux of impurities versus temperature gradient. The solid line corresponds to GYSELA results and the dotted line to its linear fit. 98

5.1. Qualitative explanation of an interchange instability. The initial potential fluctuations (blue and red circles) are growing due to an umbalanced v_E advection. Indeed due to the pressure gradient, there are more particles going to the right than in the opposite direction. Combined with the vertical drift due to magnetic curvature, this leads to an instability. 101
5.2. Linear threshold for the ITG instability in the case $s = q$ 106

5.3. Mechanism for turbulence generation and saturation by zonal flows . . . 107

6.1. Poloidal reconstruction of radiative power loss in a JET discharge [58]. This radiative power is attributed to impurity. . . . 112
6.2. Radial variation of collisionality of the impurity (blue). The limit between plateau and Pfirsch-Schlüter regime is represented by the black line . . . 120
6.3. Radial variation of the impurity fluxes. These fluxes are time averaged on approximately $3000\omega_{ci}$. . . . 121
6.4. Left: poloidal asymmetry of the impurity density. Right: reconstruction of the poloidal asymmetry with $\delta(\psi)$ and $\Delta(\psi)$ . . . 123
6.5. Radial shape of Eq.$(6.3.5)$ in red and Eq.$(6.3.6)$ in green. The blue curve represents the radial shape of Eq.$(6.3.5)$ in the absence of poloidal asymmetry of the impurity density, i.e. for $\delta = \Delta = 0$. . . . 124
6.6. Left: parallel pressure. Middle: perpendicular pressure. Right: CGL tensor divided by the magnetic field. . . . 124
6.7. Components of the neoclassical flux. The banana/plateau contribution Eq.$(6.2.12)$ is represented in green. The Pfirsch-Schlüter contribution Eq.$(6.2.13)$ with $H = -\frac{1}{2}$ and $H = 0$ are depicted respectively by the red and the blue curves. The various profiles, including their possible asymmetries, are taken from the GYSELA simulation. . . . 126
6.8. Radial comparison of the theoretical predictions of the neoclassical radial impurity flux ($H = -\frac{1}{2}$ in red, $H = 0$ in blue) with the neoclassical flux coming from the GYSELA code (black). . . . 127
6.9. Mach number of the impurity . . . 128

7.1. Amplitude of the non zonal electric potentital in the GYSELA simulation . . . 132
7.2. Comparison of density poloidal asymmetry with (solid line) or without (dotted line) poloidal asymmetry of electric potential. A time average on several turbulence correlation time has been performed. 133
7.3. *Absolute value of* $\Omega h_{0,\Omega}$ *and* $\Omega h_{1,\Omega}$ . . . 146
7.4. *Real and imaginary parts of the ratio* $\frac{h_{1,\Omega}}{h_{-1,\Omega}}$ *vs* Ω . . . 146
7.5. *Phase of* $\frac{h_{1,\Omega}}{h_{0,\Omega}}$ . . . 147
7.6. *Real and imaginary parts of the ratio* $\frac{h_{1,\Omega}}{h_{-1,\Omega}}$ *vs* Ω *for* $K_r\rho_i = 0.25$ . . . 148

1. Introduction

1.1. Fusion

Stars are hot and dense astronomic objects. They release a considerable amount of energy by radiation over billions of years. One could consider that the totality of this energy comes from the gravitational energy lost by the star while contracting. The Kelvin-Helmholtz time scale τ_{KH} is the approximate time it takes for a star to radiate away its gravitational energy content at its current luminosity rate. In the case of the sun, $\tau_{KH} \sim 3 \cdot 10^7$years which is small compared to the sun lifetime $\tau_s \sim 1.5 \cdot 10^{10}$years. Hence the sun, and all stars in general, needs to produce their own energy.

There are two kinds of reactions that can produce energy : chemical and nuclear. Chemical reactions consist in an exchange of electrons between atoms, that can either produce or require energy. In any case, chemical reactions leave atomic nucleii untouched. On the contrary, nuclear reactions are by definition associated with an evolution of the nucleus composition. Chemical reactions are long range interactions ($\sim 10^{-9}$m) compared with nuclear reactions ($\sim 10^{-15}$m). For this reason, the energetic density of nuclear reactions is approximately 10^6 larger than the one of chemical reactions. Considering the sun composition (~ 74% of hydrogen, ~ 24% of helium) and the relatively small energetic density of chemical reactions, one can safely discard chemical reactions to explain the enormous amount of energy contained in stars.

Nuclear reactions consist in a evolution of nucleus, which are composed of nucleons (neutrons and protons). The coherence of a nucleus is due to a binding energy between nucleons. The average binding energy per nucleon represents the stability of a nucleus. This quantity depends on the nucleus which is considered. The Aston curve, shown in the figure 1.1, represents the average binding energy per nucleon as a function of the number of nucleons in the nucleus. For small nucleii, the average binding energy per nucleon increase with the size of the nucleus. That means that small nucleii can react together to create heavier elements while releasing energy. This kind of reaction is called a fusion reaction. For elements heavier than Fe^{56}, the Aston curve is decreasing. That means that heavy elements can release energy if they become lighter. This kind of reaction is called fission.

Fission reactions are already exploited in conventional nuclear reactors to produce energy. Indeed these reactions are relatively easy to trigger on earth. Eventhough fission reactions allow producing large amount of energy for a relatively low cost, the drawbacks of this energy are well known. The main drawback of fission is the treatment of its nuclear wastes. Indeed, no sustainable solution has been found yet and the storage of nuclear wastes in a safe place for tens of thousands of years is a challenging issue. Another issue with current fission reactors is related to safety. Indeed, eventhough nuclar accidents are rare, they have led to major catastrophes for both humans and nature like Tchernobyl and Fukushima accidents.

Figure 1.1.: The Aston curve represents the average binding energy per nucleon as a function of the number of nucleons. Large values corresponds to stable nucleus. The maximum is reached for Fe^{56}, which is therefore the most stable nucleus.

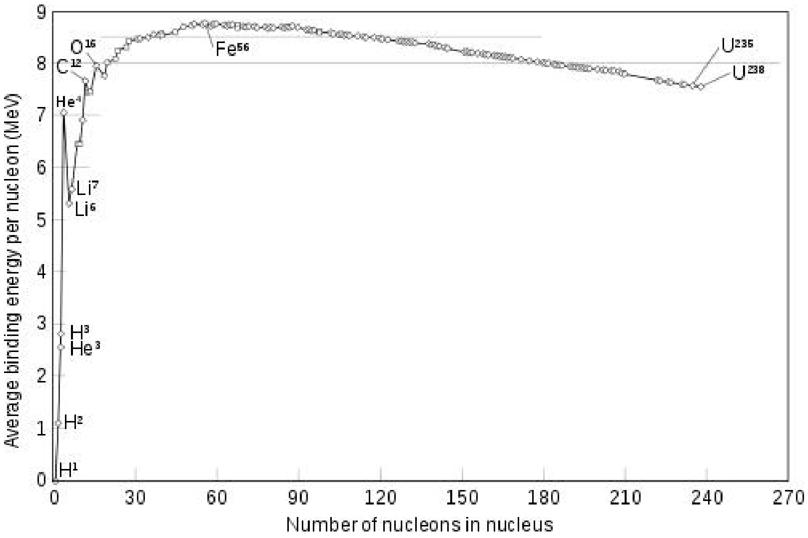

Stars are fuelled by fusion reactions. Indeed, stars are mainly composed of hydrogen, which is the lighter element. The fusion of hydrogen in helium is the nuclear reaction that produces the largest energy per mass. Indeed, the slope of the Aston curve (fig.1.1) is maximal in absolute value for light elements. The chain reactions of fusion in stars are complex and would be really difficult to be reproduced on earth. Nethertheless, this proves the enormous potential of fusion energy production. Furthermore, light elements are abundant on earth. Hence fusion reactions are good candidates to obtain a new source of sustainable energy on earth.

Different fusion reactions can be envisaged on earth. The figure 1.2 shows the reaction rate $\langle \sigma v \rangle$ which measures the probability of reaction for two species at equilibria (Boltzmann distribution function) as a function of temperature for different reactions. This curve shows that the best candidate for a fusion reaction on earth is the fusion of deuterium (D) with tritium (T), both isotopes of hydrogen. This reaction produces an helium nucleus, a neutron and releases 17.6 MeV by reaction.

$$^2_1D +^3_1 T \rightarrow^4_2 He +^1_0 n \tag{1.1.1}$$

Deuterium is abundant on earth. Indeed the massic concentration of deuterium in water is $\sim 33g \cdot m^{-3}$. On the other hand tritium is rare as it is a radioactive element with a half time life of approximately 12 years. Tritium can be produced either naturally in the atmosphere by cosmic rays or industrially in fission plants and laboratories. The current stock is approximately 20 kg. This stock will not be enough for a fusion plant. Indeed a 800 MW fusion plant will require ~ 300 g of tritium per day [55]. Fortunately, it is possible to produce tritium by bombarding lithium with energetic neutrons like those created by fusion reactions. It is envisaged to use this method to generate tritium in fusion plants. The lithium stock is by far enough for fusion plants operation using this method of tritium generation.

The required conditions to achieve fusion reactions are unusual on earth. Indeed one can make a rapid estimation of the energy required to overcome the Coulomb repulsion between nucleus by assuming that fusion reactions require that both nucleus are at a distance of the same order as the typical size of a nucleus ($\simeq 10^{-15}$m). Because nucleus are much smaller than atoms ($\simeq 10^{-10}$m) one can neglect electron screening. As both nucleus are positively charged, they repel. The typical energy of Coulomb interaction between a deuterium and a tritium nucleus at a distance $r \simeq 10^{-15}$m is given by $E_{Coulomb} = \frac{e^2}{4\pi\epsilon_0 r} \simeq 10^6 eV$. This is an enormous energy. In fact due to a tunnel effect, the probability of fusion between nuclei at a distance larger than $r \simeq 10^{-15}$m is increased, therefore the required conditions to produce fusion reactions are less stringent. The figure 1.2 accounts for the tunnel effect and shows a maximum for $\sim 10^5 eV$ for the reaction of deuterium with tritium (1.1.1). This is two orders of magnitude higher than the temperature at the center of the sun. We mention here that star core temperature ($\sim 10^3 eV$) is typically two order of magnitude lower that the temperature of the maximum efficiency of fusion reactions. Nethertheless, fusion reactions are efficient in stars thanks to the enormous densities and excellent confinement resulting from gravity. These criteria are of great importance to assess the performance of a laboratory device. They will be detailed in the section 1.3. In anycase, the extreme temperature required for fusion reactions is one of the reason why it is so hard to produce fusion reactions on earth. But this difficulty is also a good news concerning safety issues : if fusion conditions were met in a reactor and an incident was to occur, the pressure would decay rapidly and the energy production would drop extremely fast. For such high temperatures, matter is in the form of a plasma. In the next section we present briefly what is a plasma.

Figure 1.2.: Reaction rate of various fusion reactions. The curve in red corresponds to the reaction of deuterium with tritium Eq.(1.1.1) which is the one envisaged for fusion reactors.

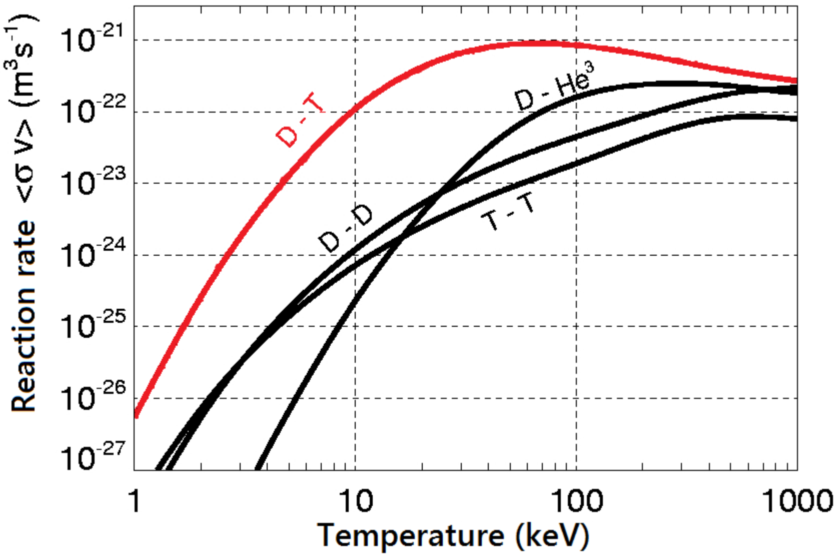

1.2. Plasmas

1.2.1. Basic description

A plasma is composed of nuclei and electrons. In a plasma some or all electrons are unbounded to nuclei, thus plasma are conductors. On the other hand, nuclei are also in an unorganized state, as in gases. The easiest way to understand a plasma is then to consider it as a conductor gas, and as such, it is sensitive to electromagnetic fields and can also generate them.

A plasma can be either partially or fully ionized. The ionisation rate depends on the density, the temperature and the different elements which compose the plasma. If the plasma is partially ionized, some nuclei conserve bounded electrons. Atomic physics then plays a role as these ions may absorb or produce photons and may also change their ionization state. In this thesis we will study hot plasmas. In this case, only heavy impurities are not fully ionized. In the following of this thesis, no atomic physics effects will be taken into account.

Another important parameter to characterize a plasma is the plasma coupling parameter defined as $\Gamma \simeq \frac{\langle E_p \rangle}{\langle E_c \rangle} \simeq \frac{e^2 N^{1/3}}{\epsilon_0 k_B T}$ where N is the density of the plasma, e the charge of a proton, ϵ_0 the vaccum permitivity and $k_B T$ is the thermal energy. Note that in the rest of this manuscript, we will omit k_B, therefore the notation T will corresponds to a energy. If $\Gamma \gg 1$, the plasma is strongly coupled meaning that a particle experiences some large interactions with other particles. On the other hand, if $\Gamma \ll 1$ the plasma is weakly coupled meaning that collective effects play a key role. In the following, we will study diluted and hot plasmas and so $\Gamma \ll 1$.

1.2.2. Characteristic scales in hot magnetized plasmas

In hot magnetized plasmas many characteristic lengths, frequencies and velocities need to be introduce to study the physics of plasmas. In this section we give a brief overview of the most frequent ones. Other quantities will be introduced when needed.

Characteristic frequencies: In presence of a constant and homogenous magnetic field, charged particles exhibit a cyclotron motion. In a plane orthogonal to the magnetic field, trajectories are circular. The characteristic pulsation associated with this motion is known as the cyclotron pulsation $\omega_{c,s} = \frac{e_s B}{m_s}$, where e_s is the charge of the particle considered and m_s its mass. The magnetic field is noted B and the index s design the species considered ($s = e$ for electrons, $s = i$ for the main ion and $s = z$ for an impurity). Another important quantity is the plasma pulsation $\omega_{p,s} = e_s \sqrt{\frac{N_s}{\epsilon_0 m_s}}$, which is the typical frequency of response of charges to an electrostatic field. Finally, the collision frequency associated with a species a colliding on a species b, $\nu_{ab} = \frac{4\sqrt{2\pi}}{3} \frac{e_a^2 e_b^2 \ln\Lambda}{(4\pi\epsilon_0)^2} \frac{N_b}{m_a} \left(\frac{1}{m_a} + \frac{1}{m_b}\right) \frac{1}{\left(v_{Ta}^2 + v_{Tb}^2\right)^{3/2}}$ will play an important role. Here $\ln\Lambda \simeq 20$ is the Coulomb logarithm and $v_{T,s} = \sqrt{\frac{T_s}{m_s}}$ is the thermal velocity of the species s. A full chapter (chapter III) will be dedicated to collisions.

Characteristic lengths: The first characteristic length that can be defined is the typical distance between ions. It is known as the Loschmidt length and defined as $\lambda_{l,s} = N_s^{-1/3}$. The second one is the radius associated with the gyromotion. It is known as the Larmor radius (or gyroradius) and defined as $\rho_{L,s} = \frac{v_{T,s}}{\omega_{c,s}}$. The Debye length $\lambda_{D,s} = \sqrt{\frac{\epsilon_0 T_s}{e^2 N_s}}$ is the typical length above which a charge is screened by the others. The Landau distance $\lambda_{L,s} = \frac{e_s^2}{4\pi\epsilon_0 T_s}$ is the minimal distance approach when considering two particles of identical charge e_s. Note that $\Gamma = \frac{\lambda_L}{\lambda_l}$ allowing a clearer interpretation of the coupling parameter. Indeed, $\Gamma \ll 1 \Leftrightarrow \lambda_L \ll \lambda_l$. It means that strong ($\alpha \sim 1$) collisions, which are collisions with an impact parameter $b \sim \lambda_L$ and so a large deflection angle $\alpha \sim 1$, are rare events. In this case, the main contribution of the collisions comes from weak collisions, which means that a particle experiences a huge number of small interactions ($\alpha \ll 1$) with other particles instead of few strong interaction with other particles. The left hand side of the Fig.1.3 depicts a Coulomb collisions between two particles and clarify the notions of impact parameter b and deflection angle α. The right hand side of Fig.1.3 shows all the particles interacting with the particle of reference. In practice, all particles with an impact parameter in the range $\lambda_L \ll b \ll \lambda_D$ participate to weak collisional processes. The upper limit is the Debye length. Indeed, λ_D corresponds to the maximal distance of interaction between two charged particles. We introduce also the parameter Λ which is in the Coulomb logarithm is simply given by $\Lambda \simeq \frac{\lambda_D}{\lambda_L}$.

Figure 1.3.: Left : Coulomb collision between two particles in the frame of the particle b. The deflection angle α depends on the impact parameter b. Right : number of particle colliding with a particle a with an impact parameter between b and $b + \delta b$. It increases with b.

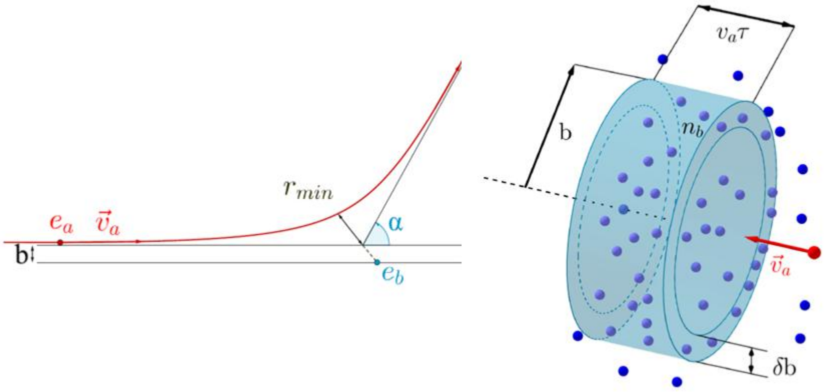

1.3. Tokamak

1.3.1. Lawson criteria

We have seen in the part 1.1 that fusion reactions can produce a large amount of energy. But the condition on the temperature to get efficient fusion reactions is extreme. Two other parameters are critical for a fusion reactor : the density and the confinement time of energy defined as $\tau_E = \frac{W}{P_{loss}}$ where W is the internal energy and P_{loss} the power loss. The number of fusion reactions is indeed proportionnal to the square of the density (if deuterium and tritium are present in the same proportion). On the other hand the confinement of energy is naturally an important parameter to maintain a hot plasma.

In principle, the energy needed to sustain the temperature of a burning plasma can be entirely produced by fusion reactions. Indeed α particles (=helium) created by the DT fusion reaction have a large energy ($E_\alpha \simeq 3.5 MeV$). If the number of fusion reactions is large enough and α particles are confined long enough to transfer their energy to the deuterium/tritium mixture, then no external heating system is required. This is called ignition. A 0D model allows to compute a criterion to obtain ignition. In this model, the only ion species are deuterium and tritium in equal proportions. They have the same density $\frac{N}{2}$ and temperature T (no temporal or spatial dependences is taken into account). The internal energy is given by $W = 3NT$ whereas the fusion power is given by $P_{fus} = E_\alpha \frac{N^2}{4} \left\langle \sigma v \right\rangle$. For ignition, this power has to be greater than the power loss $P_{fus} \geq P_{loss}$. This inequality can be writen as

$$NT\tau_E \geq \frac{12T^2}{E_\alpha \left\langle \sigma v \right\rangle}$$

This is the Lawson criteria. The minimum of $\frac{T^2}{\left\langle \sigma v \right\rangle}$ is obtained for a temperature of $T_{opt.} \simeq 14keV$. For this temperature, one get $NT\tau_E \geq 3 \cdot 10^{21} m^{-3} \cdot keV \cdot s$.

With the help of this criterion, we see that two kinds of approaches can been envisaged to obtain fusion on earth. Indeed, the temperature is more or less fixed around $T_{opt.}$. Then one can try either to increase the density or the confinement time.

The first approach consists in maximizing the density. This is called inertial fusion. It consists in compressing and heating a target via lasers. This solution relies on the use of powerful, carefully shaped and well synchronized lasers. Inertial fusion energy production at large scales seems currently unrealistic. Indeed it suffers major drawbacks : low frequency rate, lack of energy efficiency for laser production, high cost of target production. For these reasons, inertial fusion research is mainly dedicated to military purposes. The two largest installations are the NIF in the USA and the Laser Mégajoule in France.

The second category of device that can be used to obtain fusion relies on the sensitivity of plasmas to electromagnetic fields. The idea is to create a static electromagnetic trap for charged particles. Different kinds of devices have been studied like Z-pinches, θ-pinches, stellarators and tokamaks. Tokamaks have demonstrated the most promising performances in the past. The present record of fusion energy production has indeed been obtained in 1997 in the tokamak JET, the current biggest tokamak in the world, located in UK. In the rest of this thesis, only tokamaks are considered.

1.3.2. Magnetic configuration

Tokamaks use a magnetic field to confine a plasma. The main magnetic field is toroidal and is created by magnetic coils. If charged particles were only following magnetic field lines, this toroidal magnetic field would be enough to confine perfectly a plasma. Indeed, it produces closed field lines. Unfortunately, if the magnetic field is not uniform, particles experience a magnetic drift. It is possible to show that this velocity takes the form $\boldsymbol{v}_D = \frac{1}{2\omega_c} \left(v_\perp^2 + 2v_\parallel^2 \right) \frac{\boldsymbol{B} \times \nabla B}{B^2}$ in the low β limit. Where the parameter $\beta = \frac{NT}{\frac{B^2}{2\mu_0}}$ is the ratio between the thermal pressure and the magnetic pressure. For tokamaks, the limit $\beta \ll 1$ is relevant. Here $v_{\parallel}$ represents the velocity of the particle projected on the direction of the magnetic field $v_{\parallel} = \boldsymbol{v} \cdot \boldsymbol{b}$ with $\boldsymbol{b} = \frac{\boldsymbol{B}}{B}$ and $v_{\perp}$ is the norm of the velocity component perpendicular to the magnetic field line (we assume isotropy in the plan perpendicular to the magnetic field) $v_{\perp} = \sqrt{\frac{v^2 - v_{\parallel}^2}{2}}$.

In a pure toroidal magnetic field $\boldsymbol{B} = \frac{B_0 R_0}{R} \boldsymbol{e}_{\varphi}$, this velocity is vertical and depends on the sign of the charge $\boldsymbol{v}_D = \frac{1}{2\omega_c R}\left(v_{\perp}^2 + 2v_{\parallel}^2\right)\boldsymbol{e}_z$. Notice that the major radius dependence of the toroidal magnetic field comes from the Maxwell equation div$\boldsymbol{B}$=0. Since ions and electrons have opposite charges, the magnetic drift creates a separation of charge and thus a vertical electric field. A charge in the presence of both a magnetic and an electric field experiences an electric drift velocity $\boldsymbol{v}_E = \frac{\boldsymbol{E} \times \boldsymbol{B}}{B^2}$. This velocity does not depend on mass or charge. Therefore it corresponds to a velocity of the whole plasma. The electric field created by the charge separation then causes a net movement of the plasma in the outward direction leading to a rapid loss of confinement. This simple mechanism of deconfinement is illustrated in Fig.1.4.

Figure 1.4.: Drift instability of a plasma in a pure toroidal magnetic field. The drift velocity depends on the sign of the charge. It leads to a separation of charge and so a vertical electric field. The $E \times B$ drift then leads to an outward movement of the plasma.

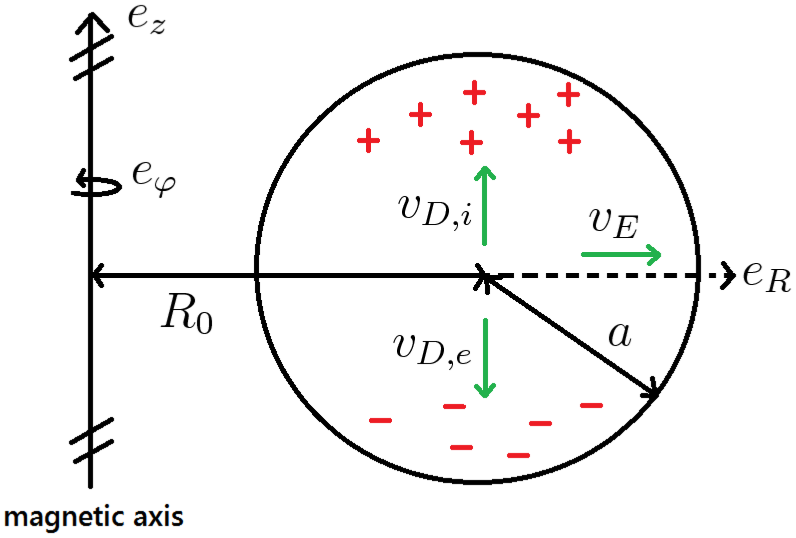

To solve this problem, a secondary magnetic field is added. It is a poloidal magnetic field created by the plasma current flowing in the toroidal direction. This secondary magnetic field reduces drastically the electric field by averaging poloidaly the distribution of charge. A tertiary vertical magnetic field is added for stability reasons.

It can be shown that for an axisymmetric magnetic field ($\frac{\partial \boldsymbol{B}}{\partial \varphi} = \boldsymbol{0}$), the existence of magnetic surfaces is ensured. In this case, the magnetic field has to take the form

$$\boldsymbol{B} = I\left(\psi\right)\boldsymbol{\nabla}\varphi + \boldsymbol{\nabla}\varphi \times \boldsymbol{\nabla}\psi$$

where $I = \frac{\mu_0 I_p(\Psi)}{2\pi}$ and $\psi = -\frac{\psi_p}{2\pi}$ with $I_p = \int_S \boldsymbol{J} \cdot d\boldsymbol{S}$ the current and $\psi_p = \int_S \boldsymbol{B} \cdot d\boldsymbol{S}$ the flux of the magnetic field accross the surface S defined as the intersection of the magnetic surface considered and a poloidal plane. The notations are illustrated on Fig.1.5. We can define an intrinsic poloidal angle $\theta^\star$ such that the safety factor q is a flux function $\frac{\boldsymbol{B}\cdot\nabla\varphi}{\boldsymbol{B}\cdot\nabla\theta^\star} = q^\star(\psi)$.

Figure 1.5.: A general magnetic surface.

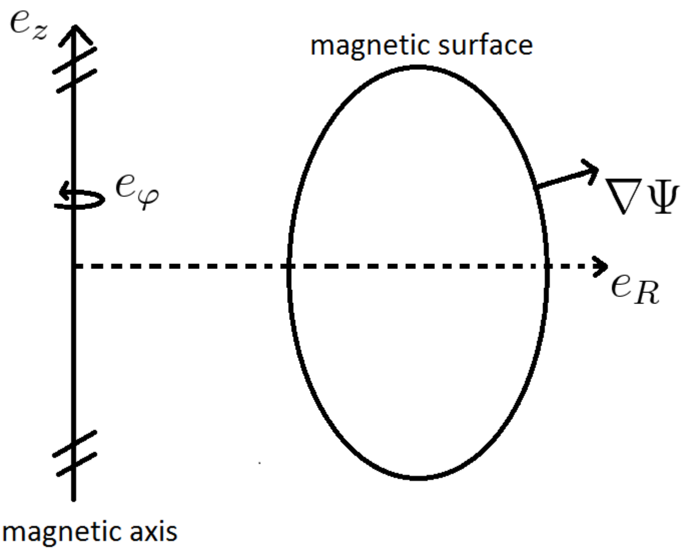

In the rest of this thesis we consider the limit case of circular magnetic surfaces for which the magnetic field lines lay down on circular concentric toruses as illustrated on Fig.1.6. In this case, it possible to show that $I\left(\psi\right) = B_0 R_0 = cst$ where R_0 is the major radius of the plasma and B_0 the norm of the magnetic field on the magnetic axis. The magnetic field then takes the form

$$\boldsymbol{B} = B_0 R_0 \boldsymbol{\nabla}\varphi + \boldsymbol{\nabla}\varphi \times \boldsymbol{\nabla}\psi$$

An alternative form of the magnetic field is given by

$$\boldsymbol{B} = B_\theta \boldsymbol{e}_\theta + B_\varphi \boldsymbol{e}_\varphi$$

with $B_\varphi = \frac{B_0 R_0}{R}$ where R is the local major radius. It is stressed here that the angle θ is the geometric angle and not the intrinsic poloidal angle $\theta^\star$. Indeed, it can be shown that

$$\theta^{\star}=2\arctan\left(\sqrt{\frac{1-\epsilon}{1+\epsilon}}\tan\left(\frac{\theta}{2}\right)\right)$$

where we have use the local inverse aspect ratio $\epsilon=\frac{r}{R_0}$, r being the local minor radius. The large aspect ratio limit $\epsilon \ll 1$ is often considered for which the difference between the two angles is small. Anyway, the use of the geometrical angle implies the introduction of a new the safety factor $q\left(r,\theta\right)=\frac{\boldsymbol{B}\cdot\nabla\varphi}{\boldsymbol{B}\cdot\nabla\theta}=\frac{rB_{\varphi}}{RB_{\theta}}$, B_{φ} is the local toroidal field and B_{θ} the local poloidal field. One can introduce the cylindrical safety factor which is the limit of the previous safety factor for infinite aspect ratio $q_{cyl}\left(r\right)=\frac{rB_{\varphi}}{R_0B_{\theta}}$ and allows to rewrite the safety factor $q\left(r,\theta\right)=q_{cyl}\left(r\right)\frac{R_0}{R}$. The advantage of q_{cyl} is that it is a function of the radius only. Finally, one can also define the aspect ratio of the machine $\frac{R_0}{a}$ where a is the minor radius of the plasma. Most tokamaks have an aspect ratio in the range $\frac{3}{2}\leq\frac{R_0}{a}\leq 6$.

Figure 1.6.: Magnetic field lines (blue) define magnetic surfaces (yellow) which are toruses. The toroidal component of the magnetic field is created by the coils depicted in red.

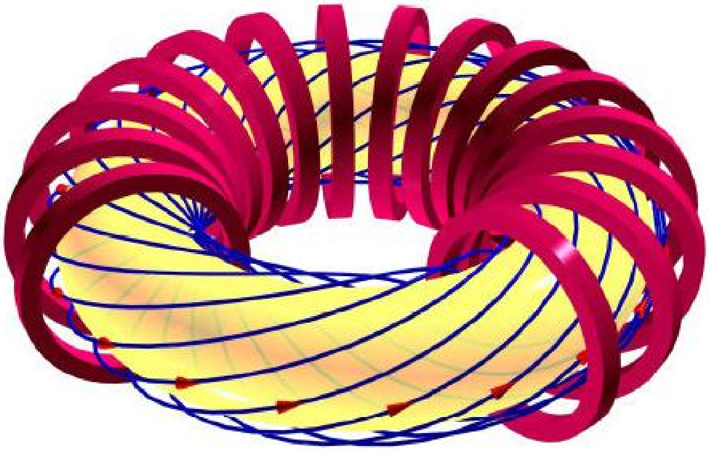

1.3.3. Particle trajectories

The unperturbed equation of motion of a particle in a tokamak is integrable, since there exists three motion invariants, namely

- the unperturbed Hamiltionian $H_{eq}=\frac{1}{2}mv^2+e\Phi_{eq}$. It comes from the stationarity of the electromagnetic field.
- the magnetic moment $\mu=\frac{mv_{\perp}^2}{2B}$ which is an adiabatic invariant coming from the fast cyclotron motion.

- the kinetic toroidal momentum $P_\varphi = -e\psi + mR\frac{B_\varphi}{B}v_\parallel$. Its invariance comes from the invariance of the problem by rotation in the φ direction.

The parallel velocity can be written as a function of the Hamiltonian and the magnetic moment $\left|v_\parallel\right| = \sqrt{\frac{2}{m}\left(H_{eq} - \mu B\right)}$. This formula implies that the parallel velocity changes along a magnetic field line due to the variation of B. If $H_{eq} > \mu B_{max}$ then the sign of the parallel velocity has to be constant. This particle is called passing or circulating. On the other hand if $H_{eq} < \mu B_{max}$, there is a point on the trajectory of the particle where $v_\parallel = 0$ and the particle bounces back. The particle is trapped on the low field side of the tokamak. Making a development at leading order with respect to ϵ, the trapping condition can be recast as $\left.\frac{v_\parallel}{v_\perp}\right|_{\theta=0} \leq \sqrt{2\epsilon}$

If $\mu B_{max} \ll H_{eq}$, then the variation of $v_\parallel$ along the particle trajectory can be neglected. The particle trajectory projected on the poloidal plan is a circle. The pulsation of the motion in the toroidal direction is given by $\omega_\varphi = \frac{v_\parallel}{R_0}$ whereas the one associated with the poloidal direction is given by $\omega_\theta = \frac{v_\parallel}{qR_0}$. Due to the term $B_\varphi v_\parallel$ in the definiton of P_φ, there is a shift of particle trajectories compared to the reference magnetic surface which depends on the sign of $eB_\varphi v_\parallel$. If $eB_\varphi v_\parallel > 0$ then the shift is in the low field side direction whereas for $eB_\varphi v_\parallel < 0$ the shift is in the opposite direction. The shift is given by $\delta_c = \frac{qv_D R_0}{v_\parallel} \simeq \frac{qv_\parallel}{\omega_c}$.

If $\mu B_{max} \gg H_{eq}$, the particle is deeply trapped on the low field side of the tokamak. The bounce frequency is given by $\omega_b = \sqrt{\frac{\mu B_0 r}{mq^2 R_0^3}}$. Again, due to the term $B_\varphi v_\parallel$ in the definition of P_φ, there is a shift of particle trajectories compared to the reference magnetic surface which depends on the sign of $eB_\varphi v_\parallel$ This gives a banana width $\delta_b = \frac{2q}{\epsilon}\frac{v_{\parallel,\theta=0}}{\omega_c}$.

The two kinds of trajectories are represented on Fig.1.7. In absence of collisions and electromagnetic field evolution, the type of trajectory cannot change. The particle is thus perfectly confined. It is shown in the next section that collisions or the evolution of the electromagnetic field can lead to transport.

Figure 1.7.: Poloidal projection of an unperturbed particle trajectories. On the left for a passing particle and on the right for a trapped particle

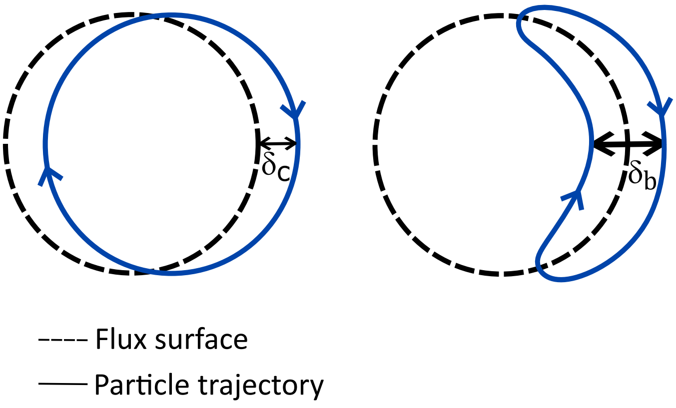

1.3.4. Transport accross the magnetic field: underlying mechanisms

The description of the particle trajectories is an opportunity to introduce particle transport. Indeed, one can imagine different ways to perturb particle trajectories, leading to transport. The easiest way to impact particle trajectories is to change the magnetic field. Indeed, particles are following closely magnetic field lines. The large parallel motion of particles lead to an efficient homogeneization of all quantities (density, temperature...) along a magnetic field line. Therefore, if a magnetic field line connects two areas with different densities and/or temperature, it creates a huge transport leading to a rapid loss of confinement. Depending on the areas which are connected, this loss of confinement can be either localized radially (i.e. magnetic island) or global (i.e. disruption). The magnetic stability of a plasma is described within the MagnetoHydroDynamics (MHD) theory.

Another way to perturb particle trajectories is to include collisions. Indeed, collisions are responsible for a diffusion in the velocity space. Therefore, a particle trajectory can change in nature (trapped/passing) as time goes by. As $\delta_c < \delta_b$, a change of nature for the particle leads to a net radial transport. Note that the detrapping frequency of the main ion species is $\nu_{detrap} = \frac{\nu_{ii}}{2\epsilon}$. One can therefore create a diffusion coefficient $D = \nu_{detrap}\delta_b^2$. This simple reasoning gives the right order of magnitude for the diffusion coefficient in the low collision frequency limit. The neoclassical theory describes the effects of collisions on particle trajectories and the resulting transport. The chapter 4 is dedicated to the neoclassical theory.

Finally, turbulence that corresponds to small scales and rapid fluctuations of the electromagnetic field around its equilibrium state can be responsible for a large transport. These fluctuations are the signature of the non linear response

Table 1.1.: Typical values in a Tokamak

distance	values (m)
ρ_L	$3 \cdot 10^{-3}$
δ_c	$6 \cdot 10^{-3}$
δ_b	$4 \cdot 10^{-2}$
λ_L	10^{-13}
λ_D	$6 \cdot 10^{-4}$
λ_l	$2 \cdot 10^{-7}$

frequency	value (Hz)
ω_c	$2 \cdot 10^{8}$
ω_θ	10^{5}
ω_b	$4 \cdot 10^{4}$
ν_{ii}	$2 \cdot 10^{3}$
ω_p	10^{10}

velocity	value (m/s)
v_T	$7 \cdot 10^{5}$
v_E	$2 \cdot 10^{3}$
v_D	$3 \cdot 10^{2}$

of the plasma to different instabilities. Different instabilities are possible in a tokamak and they can co-exist. In this thesis, we will focus on only one instability : the Ion Temperature Gradient (ITG) driven instability. It is one of the main instability in the core region (along with trapped electron modes). More details about this instability and the turbulence associated are given in the chapter 5.

In principle, these three channels of transport should be treated on equal footing. However in this thesis, only neoclassical and turbulent transport are considered.

1.3.5. Typical values

In this section some typical values of the different quantities introduced previously are given. These quantities are just indicative and can of course vary depending on the machine considered. We consider a tokamak with a central ion density of $N \sim 10^{20} m^{-3}$, a central temperature of $T \sim 10^4 eV$, and a toroidal magnetic field of $B_\varphi \sim 5T$. The minor radius is $a \sim 1m$ and the major radius $R_0 \sim 3m$. For the values given we place ourselves at $r = \frac{a}{2}$ so $\epsilon \sim \frac{1}{6}$. We consider a safety factor of $q \sim 2$ and a typical radial electric field of $10^4 V/m$. The considered species is deuterium. The typical values are given in Tab.1.1. One can also introduce four dimensionless parameters: the normalized Debye length $\frac{\rho_{L,i}}{\lambda_D} \sim 5$, the normalized gyro-radius $\rho_\star = \frac{\rho_i}{a} \sim 3 \cdot 10^{-3}$, the collisionality $\nu_\star = \frac{\nu_{detrap.}}{\omega_b} = \frac{\nu_{ii}}{2\epsilon^{3/2}\frac{v_T}{qR}} \sim 4 \cdot 10^{-1}$ and the bêta parameter $\beta = \frac{nT}{\frac{B^2}{2\mu_0}} \sim 10^{-2}$. These four dimensionlees parameters will serve to establish the model that will be used to described the plasma. The model will be detailed in the chapter 2.

1.4. Impurities

An ideal fusion plasma is composed of deuterium, tritium and electrons. Any other species is considered as an impurity. Impurities may come from fusion reactions (helium), the wall (tungsten, berillium) or be injected on purpose to radiate energy and reduce the heat flux on plasma facing component (e.g. argon).

Impurities have a deleterious effect on plasma performance. Indeed impurities that accumulate in the core of the plasma can dilute the fuel ($N \searrow$), thus leading to a decrease of the fusion reactions rate and/or radiate intensely ($\tau_E \searrow$) if they are not fully ionized. This is typically the case for heavy impurities like tungsten. The radiation of energy is critical even for tokamaks without fusion reactions. Indeed, even at low concentration, heavy impurities can cool down efficiently a plasma and lead eventually to a radiative collapse. An exemple is given in Fig.1.8 [58] where a radiative collapse due to accumulation of tungsten in the core of JET is shown.

Figure 1.8.: Radiative collapse due to tungsten accumulation in the core. The top left graph shows the increase of radiative power as a function of time. The right hand side figure shows a radiative spot in the core due to tungsten accumulation.

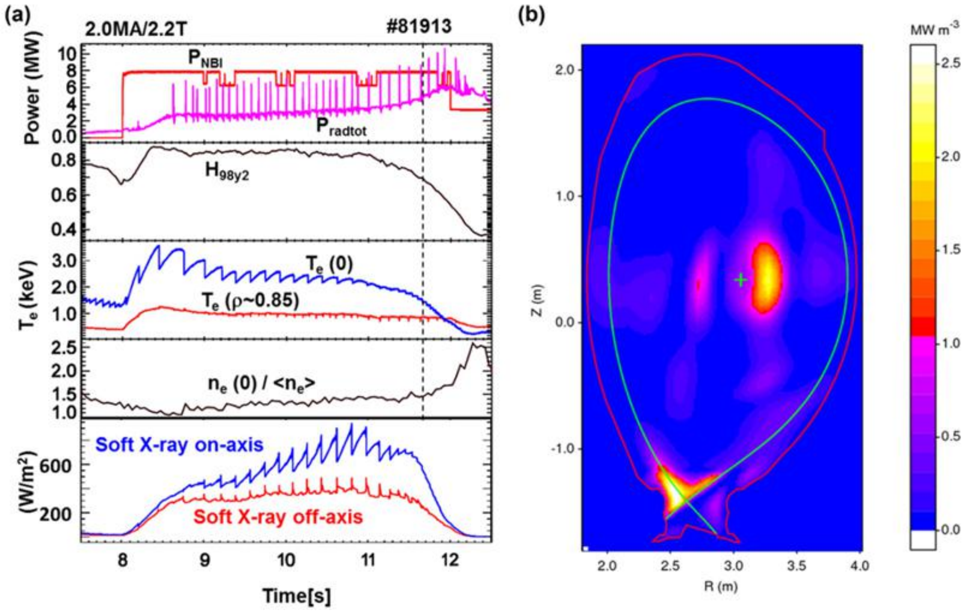

The understanding of impurity transport is therefore of utmost importance for core plasma performance. Like any particles, impurities are transported via three channels : neoclassical, turbulent and MHD. MHD activity is known to be able to impact significantly impurity transport [3]. But in this thesis we will focus on the two other channels.

For heavy impurities, neoclassical transport is expected to be dominant due to their high collisionalities. In absence of strong poloidal asymmetries, neoclassical theory predict an inward flux due to the gradient of density of the main species and an outward flux due to the temperature gradient [47]. But it has been recently shown that neoclassical prediction is significantly affected by poloidal asymmetries [4]. These poloidal asymmetries may originate from turbulence

[26] or sources [7, 5]. For light impurities, turbulent transport is expected to compete with neoclassical transport [11] due to lower collisionalities compared with heavy impurities.

In this context, one can ask many questions on impurity transport:

- What is the dominant channel of transport depending on the nature of the impurity (light versus heavy), plasma parameters (density and temperature profiles, geometry...) and the nature of the sources?
- Can transport processes interact?
- Can we predict the impurity flux with a simple model?

The aim of the present work is to tackle these questions on both theoretical and numerical grounds. In chapter 2, the numerical tool used to described the plasma is detailed. Chapter 3 is dedicated to collisions. Chapter 4 is dedicated to the standard neoclassical physics. Chapter 5 deals with turbulent prediction for impurity transport. Chapter 6 gives numerical results for the impurity transport in the case of turbulent generated poloidal asymmetries. Chapter 7 clarifies the turbulent generation of poloidal asymmetries. Finally a conclusion is drawn.

2. The gyrokinetic code GYSELA

Contents

1.1. Fusion **25**

1.2. Plasmas **28**

  1.2.1. Basic description 28

  1.2.2. Characteristic scales in hot magnetized plasmas 29

1.3. Tokamak **30**

  1.3.1. Lawson criteria 30

  1.3.2. Magnetic configuration 31

  1.3.3. Particle trajectories 34

  1.3.4. Transport accross the magnetic field: underlying mechanisms 36

  1.3.5. Typical values 37

1.4. Impurities **37**

2.1. Gyrokinetic theory

As mentionned in the introduction, plasmas are composed of charged nuclei in presence of electrons. One can envisage three kinds of description to calculate the plasma response.

- Particle description: the evolution of each particle is described in a 6D phase space (3 dimensions of space and 3 of velocity). The particles are interacting via Maxwell equations. In this approach all informations are retained. This approach is by far too costly to be envisaged as the density of a fusion plasma is $N_e \simeq 10^{20}$particles $/m^3$. Even if this kind of approach was possible, it would contain a lot of useless information: there is no need to follow each particle individually to understand phenomena happening in the plasma.
- Kinetic description: given the huge number of particles, a clever way to describe a plasma is to use a statistical approach. An assembly of particles of a same type (for instance electrons) is statistically described by a distribution function living in a bounded 6D phase space : three dimensions of space bounded by the physical space in which the plasma is evolving (for instance the tokamak chamber) and three dimensions of speed bounded for instance by the speed of light. In this approach the elementary volume of phase space $f\left(\boldsymbol{x},\boldsymbol{v}\right) d\boldsymbol{x}d\boldsymbol{v}$ represents the probability for a particle to be in the elementary volume $d\boldsymbol{x}d\boldsymbol{v}$ centered on the point $(\boldsymbol{x},\boldsymbol{v})$ times the total number of particles. The distribution function is evolved via the Fokker-Planck equation which needs to be coupled to Maxwell equations for a complete description. This approach allows a description of all phenomena of interest but stays at the moment challenging from the numerical point of view.
- Fluid description: this approach is obtained by considering a limited number of moments of the distribution function. These moments evolve in a 3D space. The major advantage of this approach is the reduction of the space allowing a huge reduction of computational cost. On the other hand a part of the physics is overlooked in this approach. For instance wave-particles interactions that often involve resonances in the velocity space cannot been studied. Moreover certain classes of particles (e.g. trapped, fast) require a specific treatment. The limited number of moments which is retained implies a closure procedure that remains a delicate problem.
  The fluid approach is valid in different cases. For instance, if collisions are strong enough, they will push the distribution function to evolve in the direction of Maxwellian which is fully described by three moments. But core fusion plasmas are almost collisionless and deviations from Maxwellians are possible especially in presence of external drives like those used to heat

the plasma. The fluid approach is also valid, if wave-particles interactions and the effect of trapped particles is negligible. This is typically the case if the two following conditions are fulfilled $kv \ll \omega$ and $k\delta \ll 1$ with k the wave number of the wave, ω its puslsation and δ the trajectory width.

2.1.1. Kinetic description

In this part we show how to obtain the Fokker-Plack equation starting from the equation of motion of a particle. Two approaches are possible for this demonstration: one based on the Klimontovich approach and another one starting from the Liouville equation and using the so-called BBGKY (Bogoliubov Born Green Kirkwood Yvon) hierarchy [68]. A brief presentation the Klimontovich approach is given. More details on the two derivations can be found in [73].

The phase space density N_s corresponding to N_0 particles of the species s is given by

$$N_s\left(\boldsymbol{x}, \boldsymbol{v}, t\right) = \sum_{i=1}^{N_0} \delta\left(\boldsymbol{x} - \boldsymbol{X}_i\left(t\right)\right) \delta\left(\boldsymbol{v} - \boldsymbol{V}_i\left(t\right)\right)$$

where $\boldsymbol{X}_i\left(t\right)$ and $\boldsymbol{V}_i\left(t\right)$ are respectively the position and the velocity of the particle i at time t. Taking the time derivative, one obtains

$$\begin{aligned}\frac{\partial}{\partial t} N_s\left(\boldsymbol{x}, \boldsymbol{v}, t\right) = &-\sum_{i=1}^{N_0} \frac{d\boldsymbol{X}_i}{dt} \cdot \nabla_x \left[\delta\left(\boldsymbol{x} - \boldsymbol{X}_i\left(t\right)\right) \delta\left(\boldsymbol{v} - \boldsymbol{V}_i\left(t\right)\right)\right] \\ &-\sum_{i=1}^{N_0} \frac{d\boldsymbol{V}_i}{dt} \cdot \nabla_v \left[\delta\left(\boldsymbol{x} - \boldsymbol{X}_i\left(t\right)\right) \delta\left(\boldsymbol{v} - \boldsymbol{V}_i\left(t\right)\right)\right]\end{aligned}$$

Using the equations of motions and the fact that $a\delta\left(a-b\right) = b\delta\left(a-b\right)$, one get

$$\begin{aligned}\frac{\partial}{\partial t} N_s\left(\boldsymbol{x}, \boldsymbol{v}, t\right) = &-\sum_{i=1}^{N_0} \boldsymbol{v} \cdot \nabla_x \left[\delta\left(\boldsymbol{x} - \boldsymbol{X}_i\left(t\right)\right) \delta\left(\boldsymbol{v} - \boldsymbol{V}_i\left(t\right)\right)\right] \\ &- \frac{e_s}{m_s} \sum_{i=1}^{N_0} \left(\boldsymbol{E}^m + \boldsymbol{v} \times \boldsymbol{B}^m\right) \cdot \nabla_v \left[\delta\left(\boldsymbol{x} - \boldsymbol{X}_i\left(t\right)\right) \delta\left(\boldsymbol{v} - \boldsymbol{V}_i\left(t\right)\right)\right]\end{aligned}$$

$$\Leftrightarrow \frac{\partial N_s}{\partial t} + \boldsymbol{v} \cdot \nabla_x N_s + \frac{e_s}{m_s} \left(\boldsymbol{E}^m + \boldsymbol{v} \times \boldsymbol{B}^m\right) \cdot \nabla_v N_s = 0 \tag{2.1.1}$$

Where e_s is the charge of the species s and m_s its mass. This equation is known as the Klimontovich equation. It is exact but still contains all the information on the position in phase space of all particles. To remove useless information, a statistical average of the Klimontovich equation is considered. We define

$$\begin{aligned} N_s &= F_s + \delta F_s \\ \boldsymbol{E}^m &= \boldsymbol{E} + \delta \boldsymbol{E} \\ \boldsymbol{B}^m &= \boldsymbol{B} + \delta \boldsymbol{B} \end{aligned}$$

where $F_s = \langle N_s \rangle$, $\boldsymbol{E} = \langle \boldsymbol{E}^m \rangle$ and $\boldsymbol{B} = \langle \boldsymbol{B}^m \rangle$ are statistical mean values of respectively N_s, $\boldsymbol{E}^m$ and $\boldsymbol{B}^m$. Taking the statistical average denoted $\langle \cdot \rangle$ of Eq.(2.1.1). one find

$$\frac{\partial F_s}{\partial t} + \boldsymbol{v} \cdot \nabla_x F_s + \frac{e_s}{m_s} \left(\boldsymbol{E} + \boldsymbol{v} \times \boldsymbol{B} \right) \cdot \nabla_v F_s = \sum_{s'} C \left(F_s, F_{s'} \right)$$

where $C \left(f_s \right) = -\frac{e_s}{m_s} \left\langle \left(\delta \boldsymbol{E} + \boldsymbol{v} \times \delta \boldsymbol{B} \right) \cdot \nabla_v \delta f_s \right\rangle$ is the collision operator which will be discuss in detail in the third chapter. This equation is the Fokker-Planck equation. Note that using the ergodic hypothesis, the statistical average can be replaced by a temporal average. This statistical approach holds if the number of particles in an elementary volume of phase space $\Delta x \Delta v$ is large enough. Indeed, if one consider fluctuations $\delta N_{\Delta x \Delta v}$ of the order of $\sqrt{N_{\Delta x \Delta v}}$, where $N_{\Delta x \Delta v}$ is the number of particles in the elementary volume $\Delta x \Delta v$ then the statistical approach can be consired as valid if the fluctuations are much smaller than the mean value. For instance, $\frac{\delta N_{\Delta x \Delta v}}{N_{\Delta x \Delta v}} \leq 10\% \Leftrightarrow N_{\Delta x \Delta v} \geq 100$.

In practice, this thesis considers the following assumption $\Delta x \geq \lambda_D$. In the Debye sphere there are $N \lambda_D^3 \simeq 10^{10}$ particles. These particles need to be distributed in a 3D velocity space. The constraint $N_{\Delta x \Delta v} \geq 100$ left more than 100 values in each direction if one consider a cartesian description. It will be considered as sufficient and we will consider in the following that the statistical approach is valid. The Fokker Planck equation needs to be coupled with Maxwell's equations to have a self consistent description of the evolution of the distribution function together with the electromagnetic field.

2.1.2. From kinetic to gyrokinetic

We have mentionned in the section I.3.2 that the motion of particles in a tokamak is integrable if the electromagnetic field is static and the system considered as toroidally symmetric. If the perturbations are weak enough, the KAM (Kolmogorov Arnold Moser) theorem states that some of the quasi-periodic motion persists. In core fusion plasmas, electromagnetic fluctuations are small and slow compared to the ion cyclotron frequency. Indeed, experimental results suggest the following ordering for small scale turbulence [35]

$$\frac{\delta B}{B} \sim \frac{e \delta \phi}{T_i} \sim \frac{\omega}{\omega_{c,i}} \sim O \left(\rho_{\star,i} \right) \ll 1$$

where the subscript i stands for the main ion species. Due to this ordering, the gyromotion which is the fastest of the three quasi periodic motions, is only slightly affected by the electromagnetic perturbations and the adiabatic invariant μ which is proportional to the action associated with this moment ($J_{\parallel} = \frac{m}{e}\mu$) can be redefined to give another invariant. The gyrokinetic approach is basically a change of variable ensuring that the new adiabatic invariant $\bar{\mu} = \mu + o\left(\mu\right)$ is a time invariant (in absence of collisions). With this change of variable, the phase space associated with the gyromotion is orthogonal to the rest of the phase space. Therefore, the dimensionality of the problem is reduced: one passes from a 6D phase space to a 4D phase space plus a parameter $\bar{\mu}$.

A rigorous derivation of the gyrokinetic equation that will be used can be found in the review paper of A.Brizard [13]. Details on the derivation of the model are not given in this thesis. We just mention that the derivation of the gyrokinetic equation from the Fokker-Planck equation is done in two steps: the first step, called guiding-center transform, allows one to obtain the evolution equation of the guiding-center by eliminating the gyroangle coordinate from the Fokker-Planck equation. At this stage, the guiding-center magnetic moment μ is a dynamical invariant. The introduction of low-frequency electromagnetic fluctuations reintroduces the gyroangle dependence in the perturbed guiding-center problem. A second transformation, called gyro-centre transform, allows one to remove the fast gyroangle dependence of the problem and leads to the gyrokinetic equation:

$$\frac{\partial \bar{F}_s}{\partial t} + \frac{d\boldsymbol{X}_{G,s}}{dt} \cdot \boldsymbol{\nabla}_G \bar{F}_s + \frac{dv_{G,\parallel}}{dt} \frac{\partial \bar{F}_s}{\partial v_{G,\parallel}} = \sum_{s'} \bar{C}\left(\bar{F}_s, \bar{F}_{s'}\right) \tag{2.1.2}$$

where the index G stands for the gyrocenter coordinates. The equation of motion of the gyrocenters is given by

$$\frac{d\boldsymbol{X}_{G,s}}{dt} = v_{G,\parallel} \boldsymbol{b}_s^{\star} + \boldsymbol{v}_{E\times B,s} + \boldsymbol{v}_{D,s}$$

where $\boldsymbol{v}_{E\times B,s}$ and $\boldsymbol{v}_{D,s}$ are respectively the electric and magnetic drift velocities that have been introduced in the section 1.3.2 but expressed in the gyrocenter framework. We also define $\boldsymbol{b}_s^{\star} = \frac{\boldsymbol{B}}{B_{\parallel s}^{\star}} + \frac{m_s v_{G,\parallel}}{q_s B_{\parallel s}^{\star} B} \boldsymbol{\nabla} \times \boldsymbol{B}$ with $B_{\parallel s}^{\star} = B + \frac{m_s}{q_s} v_{G,\parallel} \boldsymbol{b} \cdot (\boldsymbol{\nabla} \times \boldsymbol{b})$ which corresponds to the Jacobian of the gyrocenter system of coordinates.The gyrocenter parallel velocity evolution equation is given by

$$m_s \frac{dv_{G,\parallel}}{dt} = -\bar{\mu}_s \boldsymbol{b}_s^{\star} \cdot \boldsymbol{\nabla} B - q_s \boldsymbol{b}_s^{\star} \cdot \nabla \bar{\phi} + \frac{m_s v_{G,\parallel}}{B} \boldsymbol{v}_{E\times B,s} \cdot \boldsymbol{\nabla} B$$

where $\bar{\phi} = \mathcal{J} \cdot \phi$ is the gyro-average potential with $\mathcal{J}$ the gyroaverage operator.

One should note that the new adiabatic invariant $\bar{\mu}$ is a real invariant only without collisions. In this thesis, we will also consider the slow evolution of this quantity due to collisions. One could question the validity of the gyrokinetic approach when collisions are accounted for because of the evolution of the magnetic moment. Fortunately, core fusion plasmas have collision frequencies much smaller than gyration frequencies $\nu_{s,s'} \ll \omega_c$ and the gyrokinetic approach is relevant to study core fusion plasmas even when collisions are accounted for.

2.1.3. Quasi-neutrality equation : limit of adiabatic electrons

The gyrokinetic equation has to be coupled with the evolution equation of the electromagnetic field. In the following, the electrostatic limit is considered. It consists in neglecting the time derivative of the potential vector $\partial_t \boldsymbol{A} = \boldsymbol{0}$. With this assumption, the evolution of the electric field is linked to the one of the potential $\boldsymbol{E} = -\boldsymbol{\nabla}\phi$. The evolution of the potential is governed by the Poisson equation

$$\nabla^2\phi = -\frac{1}{\epsilon_0}\sum_s N_s Z_s e$$

where $N_s = \int F_s d^3v$ is the density of the particles and the sum is on all the species considered. Defining the dimentionless parameters $\hat{\phi} = \frac{e\phi}{T_{e0}}$, $\hat{N}_s = \frac{N_s}{N_{e0}}$ and L the typical dimension of the problem considered, the Poisson equation can be recast

$$\frac{\lambda_{D,e}^2}{L^2}\hat{\nabla}^2\hat{\phi} = -\sum_s \hat{N}_s Z_s$$

where $\lambda_{D,e}$ is the Debye length of electrons. As seen previously, if one consider scales larger than the Debye length $\lambda_{D,e} \ll L$, then the plasma can be treated as quasi-neutral. This result is retrieved here and the quasi-neutrality is simply given by

$$\sum_s N_s Z_s = 0$$

ITG (Ion Temperature Gradient) turbulence, which is the one considered in this thesis, develops at scales of the order of a few Larmor radii of the main ions (with $\rho_i \sim 10^{-3}m$) whereas the Debye length is typically $\lambda_D \sim 10^{-4}m$. The scale separation justifies the quasi-neutrality approach. One should note that $\lambda_{D,e} \sim \rho_e$, which means that for a turbulence developing at the electron scale like ETG (Electron Temperature Gradient), one should not use the quasi neutrality equation.

At this stage, the gyro-average potential dependence is not obvious. Moreover, one should note that the quasi-neutrality equation uses the density of particles and not the the density of gyrocenters. We can rewrite the quasi-neutrality condition to make the dependence on the potential and the density of gyrocenters explicit. To do so, one can use the link between the distribution function of gyrocenter $\bar{F}_s$ and the one of particles F_s:

$$F_s(\boldsymbol{x},\boldsymbol{v},t) = -\frac{Z_s e}{T_{eq,s}(\boldsymbol{x})} F_{eq,s}(\boldsymbol{x},\boldsymbol{v}) \left[\phi(\boldsymbol{x},t) - \bar{\phi}(\boldsymbol{x}_G,t)\right] + \bar{F}_s(\boldsymbol{x}_G,\boldsymbol{v}_G,t) \tag{2.1.3}$$

where $F_{eq,s}$ is the equilibrium distribution function of the species s, which is a Maxwellian. Integrating over the velocity space, one has

$$N_s(\boldsymbol{x},t) = \int F_s(\boldsymbol{x},\boldsymbol{v},t)\, d^3v = N_{G,s}(\boldsymbol{x},t) + N_{pol,s}(\boldsymbol{x},t)$$

where

$$N_{G,s}(\boldsymbol{x},t) = \int \left[\mathcal{J}\bar{F}_s\right](\boldsymbol{x},\boldsymbol{v}_G,t)\, d^3v_G$$

is the density of gyrocenters and

$$N_{pol,s}(\boldsymbol{x},t) = -\frac{Z_s e}{T_{eq,s}(\boldsymbol{x})} \int F_{eq,s}(\boldsymbol{x},\boldsymbol{v}) \left[\phi(\boldsymbol{x},t) - \left[\mathcal{J}^2\phi\right](\boldsymbol{x},t)\right] d^3v_G$$

is the polarisation density. Indeed, the gyroaverage operator $\mathcal{J}$ can been understood as an operator allowing to pass from particle space to the gyrocenter space. From now on we do not explicit the spatial dependence. The quasi-neutrality in the gyrokinetic framework can be written

$$\sum_s eZ_s \int \mathcal{J}\bar{F}_s d^3v = \sum_s \frac{(Z_s e)^2}{T_{eq,s}} \int F_{eq,s}\left(\phi - \mathcal{J}^2\phi\right) d^3v \tag{2.1.4}$$

In the long wavelength limit, the gyroaverage operator reads

$$\mathcal{J}\phi \simeq \phi + \frac{1}{2}\nabla\cdot\left(\frac{m_s\mu}{(Z_s e)^2 B_{eq}}\nabla_\perp\phi\right) \tag{2.1.5}$$

Using Eq.(2.1.5) in Eq.(2.1.4), the quasi-neutrality becomes

$$\sum_s Z_s \int \mathcal{J}\bar{F}_s d^3v = -\sum_s \nabla\cdot\left(\frac{N_{eq,s} m_s}{eB_{eq}^2}\nabla_\perp\phi\right) \tag{2.1.6}$$

where $N_{eq,s}$ is the unperturbed density of the species s. Notice that, due to the proportionality to the mass of the polarization density, one can restrict the sum over the ions on the RHS of Eq.2.1.6. At this stage, we assume that electrons have an adiabatic response on a flux surface, namely

$$N_e(\boldsymbol{x},t) = N_{e0}(r)\exp\left[\frac{e\left(\phi(\boldsymbol{x},t) - \langle\phi\rangle_{FS}(\boldsymbol{x},t)\right)}{T_{e0}(r)}\right] \tag{2.1.7}$$

where N_{e0} and T_{e0} are respectively the electron density and temperature and

$\langle\phi\rangle_{FS}$ the flux surface average of the potential defined as

$$\langle\phi\rangle_{FS} = \frac{\int J_x^\star \phi d\theta^\star d\varphi}{\int J_x^\star d\theta^\star d\varphi}$$

where $\theta^\star$ is the intrinsic angle introduce in the section 1.3.2 and $J_x^\star = \frac{1}{\boldsymbol{B}\cdot\boldsymbol{\nabla}\theta^\star}$ is the the Jacobian in space. Note that in the special case of a circular geometry, using the geometrical angle θ, one has

$$\langle\phi\rangle_{FS} = \frac{\int J_x \phi d\theta d\varphi}{\int J_x d\theta d\varphi}$$

$J_x = J_x^\star \frac{\boldsymbol{B}\cdot\boldsymbol{\nabla}\theta^\star}{\boldsymbol{B}\cdot\boldsymbol{\nabla}\theta} = \frac{1}{\boldsymbol{B}\cdot\boldsymbol{\nabla}\theta}$. This adiabatic response is chosen to reduce the numerical cost of the simulation. Indeed it reduces the number of species to treat. Moreover, the gyrokinetic resolution of electrons requires to refine the grid size and the time step. Indeed, if one considers the main species to be deuterium, then $\frac{\omega_{ce}}{\omega_{ci}} = \frac{m_i}{m_e} \sim 3.6\cdot 10^3$ and $\frac{\rho_e}{\rho_i} = \frac{v_{Te}\omega_{ci}}{v_{Ti}\omega_{ce}} = \sqrt{\frac{m_e}{m_i}} \sim \frac{1}{60}$. The development of a version of GYSELA retaining the gyrokinetic contribution of trapped electrons has been developed recently but has not been used during this thesis. The fact that only ions are treated on a gyrokinetic framework implies that only ITG turbulence is retained. The instability underlying this kind of turbulence will be explained in the chapter 5. We just mention here that this is the main type of turbulence observed in the core of current tokamaks. Introducing the adiabatic response Eq.(2.1.7) in the quasi-neutrality Eq.(2.1.6), one gets

$$\sum_s Z_s \int \mathcal{J}\bar{F}_s d^3v - N_{e0}(r)\exp\left[\frac{e\left(\phi(\boldsymbol{x},t) - \langle\phi\rangle_{FS}(\boldsymbol{x},t)\right)}{T_{e0}(r)}\right] = -\sum_s \nabla\cdot\left(\frac{N_{eq,s}m_s}{eB_{eq}^2}\nabla_\perp\phi\right) \tag{2.1.8}$$

where the sum is from now on understood as a sum on the ionic species only.

Eq.(2.1.8) contains a degree of freedom being the initial value of the potential. If one is not careful in this choice, a large potential appears rapidly and the numerical resolution of Eq.(2.1.8) becomes tricky. To avoid this problem, we assume that there exist a distribution of ions $\bar{F}_{eq,s}$ such that the potential is zero. This distribution function is chosen at initial state. Furthermore, the potential fluctuations are expected to be small $\frac{e\delta\phi}{T} = o(\rho_\star)$. Therefore one can develop the exponential $\exp\left[\frac{e\left(\phi(\boldsymbol{x},t)-\langle\phi\rangle_{FS}(\boldsymbol{x},t)\right)}{T_{e0}(r)}\right] \simeq 1 + \frac{e\left(\phi(\boldsymbol{x},t)-\langle\phi\rangle_{FS}(\boldsymbol{x},t)\right)}{T_{e0}(r)}$.

Dividing by $N_{e0}(r)$ Eq.(2.1.8) one gets

$$\begin{aligned}\frac{1}{N_{e0}(r)}\sum_s Z_s \int \mathcal{J}\left(\bar{F}_s - \bar{F}_{eq,s}\right)d^3v = \\ -\frac{1}{N_{e0}(r)}\sum_s \nabla\cdot\left(\frac{N_{eq,s}m_s}{eB_{eq}^2}\nabla_\perp\phi\right) + \frac{e\left(\phi(\boldsymbol{x},t) - \langle\phi\rangle_{FS}(\boldsymbol{x},t)\right)}{T_{e0}(r)}\end{aligned} \tag{2.1.9}$$

This is the version of quasi-neutrality that is used in GYSELA.

2.2. The GYSELA code

The gyrokinetic code GYSELA (Fig.2.1) is developed since the beginning of the 2000's. It evolves continuously to include more and more physics, taking advantage of the development of bigger computers and uses state-of-the-art high performance computing. Despite access to a large amount of numerical ressources (≈ 100 millions of CPU hours per year) it is currently impossible to describe all the physics happening in a tokamak with a single code. Some choices have been made to retain some part of the physics and simplify others. This choice is not unique and different codes have emerged, each with its strenghs and weaknesses. In this section, we will first make a short overview of the main characteristics of the GYSELA code and then give some numerical aspects of the code.

Figure 2.1.: Potential fluctuations obtained with the gyrokinetic code GYSELA

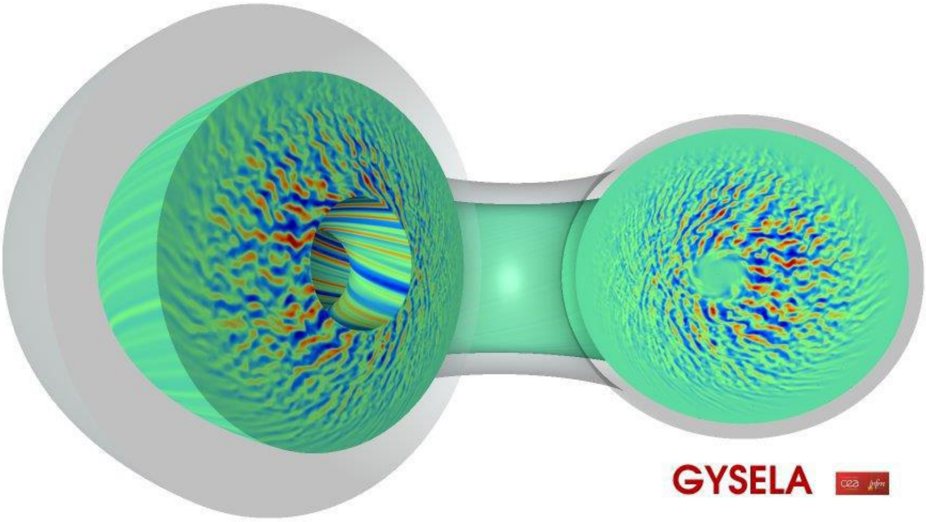

2.2.1. Main features

As mentioned previously, the GYSELA model uses the electrostatic limit. It implies that the magnetic field is static. Furthermore GYSELA uses of a simplified geometry for the magnetic field which is given by $\boldsymbol{B} = \frac{B_0 R_0}{R}\left(\frac{r}{q_{GYS}(r) R_0}\boldsymbol{e}_\theta + \boldsymbol{e}_\varphi\right)$. The definition of q_{GYS} corresponds to the cylindrical safety factor introduce in the section 1.3.2: $q_{GYS}\left(r\right) = q_{cyl}\left(r\right)$. The radial shape of the safety factor $q_{GYS}(r)$

is an input parameter of the GYSELA code. Despite its simplicity, this approximated magnetic field retains the main characteristics of the magnetic field in a tokamak as described in the introduction. Unfortunately, the electrostatic assumption implies that all MHD activity is neglected removing de facto one channel of transport. Moreover only electrostatic turbulence can be studied.

GYSELA is a full-F code, meaning that the full distribution function can evolve and in particular the background profiles are free to evolve. The code is also global, which means that the domain of simulation is not limited to the neighboring of a magnetic field line but is on the contrary extended to the totality of the core of the tokamak. The fact that GYSELA is both a full-F and global code raises the question of evolution of background profiles on long times scales. Indeed, without sources, the heat radial transport would lead to a flattening of the temperature profile, which would ultimately reach marginal stability. To avoid this phenomenon, GYSELA is flux driven. It means that a source is added in the right hand side of Eq.(2.1.2). This source term can in principle model a source or a sink of any moment of the distribution function. In GYSELA, the source term can represent a source of particles, momentum, energy or vorticity [38].

The global feature of GYSELA raises the question of boundary conditions. The use of polar coordinates to describes the poloidal plan implies an unphysical boundary condition on the magnetic axis. This boundary condition has been recently removed [63]. On the other hand, a physical boundary condition exists at the outer edge of the simulation domain. Indeed, this boundary corresponds to the passage between the core to the scrape-off-layer which is magnetically connected to the wall. The physics in the scrape-off-layer is complex and is not tackled by GYSELA. On the point of view of the core, the scrape-off-layer can be seen at leading order as a sink of energy (and a source of particles). To mimic this effect, the exhaust of energy on the outer region of the domain simulation is assured via a Krook term which makes the distribution function relax toward a target distribution function, in practice a Maxwellian with low temperature [24]. This approach allows one to limit the impact of numerical boundary conditions which are often unphysical. Another thesis is currently dedicated to the improvement of the outer boundary condition in GYSELA. The goal is to mimic the effect of a limiter. The limiter like boundary condition has not been used in this thesis.

The last main feature of GYSELA is that it allows different species to evolve simultaneously, tacking into account accurately intra and interspecies collisions. The description of the multispecies collision operator developed during this thesis is presented in the chapter 3. The multi species characteristic of the code and the use of a precise collision operator is of prime importance for this study which aims at studying the transport of impurities.

2.2.2. Numerical aspects

The GYSELA code has to solve self-consistently the evolution of the distribution function Eq.(2.1.2) and compute the electric potential at each time step thanks to the quasi-neutrality Eq.(2.1.9). Different methods of resolution are available in the GYSELA code. In this part, we present the method of resolution used for the results presented in this thesis.

The evolution of the distribution function Eq.(2.1.2) can be splitted into two parts. One part consists in an advection in phase space assuming collisions and sources to be zero. It is the Vlasov part of the equation

$$\frac{\partial \bar{F}_s}{\partial t} + \frac{d\boldsymbol{X}_{G,s}}{dt} \cdot \boldsymbol{\nabla}_G \bar{F}_s + \frac{dv_{G,\parallel}}{dt} \frac{\partial \bar{F}_s}{\partial \bar{v}_\parallel} = 0 \tag{2.2.1}$$

The second one corresponds to the evolution of the distribution due to collisions and sources only

$$\frac{\partial \bar{F}_s}{\partial t} = \sum_{s'} \bar{C}\left(\bar{F}_s, \bar{F}_{s'}\right) + \bar{S}_s \tag{2.2.2}$$

The evolution of the distribution function due to collisions and sources Eq.(2.2.2) is solved independently of the Vlasov part Eq.(2.2.1) of the gyrokinetic equation and can be done with a different time step. This separation allows a critical reduction of numerical cost of collisions (and sources) and respect the time scale separation between turbulent time scales τ_{turb} and collision time scales τ_{coll}. Indeed, except in some singular cases like the one of heavy impurities, we have $\tau_{turb} \ll \tau_{coll}$.

The resolution of the turbulent time scale described by the set of equations ((2.1.9)-(2.2.1)) is the following : at the begining of each time step, the electric field is computed $\boldsymbol{E}\left(t_n\right)$ by solving the quasi-neutrality Eq.(2.1.9) and taking its gradient. The distribution function is evolved by solving the Vlasov Eq.(2.2.1) on half a time step allowing the computation of $\bar{F}_s\left(t_{n+\frac{1}{2}}\right)$. This new distribution function is employed to compute the new electric field $\boldsymbol{E}\left(t_{n+\frac{1}{2}}\right)$ thanks to the quasi-neutrality Eq.(2.1.9). Finally, the electric field at time t is replaced by $\boldsymbol{E}\left(t_{n+\frac{1}{2}}\right)$ in Vlasov Eq.(2.2.1) to compute the evolution of the distribution function on a full time step $\bar{F}_s\left(t_{n+1}\right)$ starting from $\bar{F}_s\left(t_n\right)$. This method of resolution called predictor-corrector requires the temporary saving of two distribution functions $\bar{F}_s\left(t_n\right)$ and $\bar{F}_s\left(t_{n+\frac{1}{2}}\right)$ but increases dramaticaly the precision of the resolution.

There exists a large number of gyrokinetic codes. Each code has its strenghs and weaknesses both in terms of physics which is described and numerical aspects. One way to distinguish these codes (not unique) is to consider the choice for the numerical resolution of the Vlasov equation (2.2.1). Three categories exist for solving of the Vlasov equation.

- Lagrangian-PIC code (Fig.2.2): The Lagrangian approach, often referred to as “particle-in-cell” (PIC), relies on the invariance of the distribution function along trajectories during the solving of Eq.(2.2.1). The method consists in sampling initially the 5D phase-space with markers and then follow their orbits in the phase-space. At each time step, the density and currents are recomputed to feed the Maxwell equations (or a subset) to compute the 3D electromagnetic field which is then used to compute the particle trajectories at the next time step. The main advantage of this method is its relatively easy parallelization. The main drawback of the method is the numerical noise associated with the computing of the fields (“assignment”). Indeed, the “assignment” can be interpreted as a Monte Carlo integration having a relative error proportionnal to $\sqrt{\frac{1}{N}}$ where N is the the number of markers in the cell. A large number of particles is therefore needed to increase the signal-to-noise level. Historically, the PIC approach has been the first to be used. Several codes are based on this PIC method e.g. GTC[64], ORB5[59], XGC[40] (the list is not exhaustive).

Figure 2.2.: In Lagrangian-PIC methods, markers initial positions are loaded pseudo- (or quasi-) randomly in phase space (A). Markers are evolved along their orbits (B). Charge and current perturbations are assigned (projected) to real space (C). Field equations are solved (D), e.g. on a fixed grid in real space. Figure coming from [35].

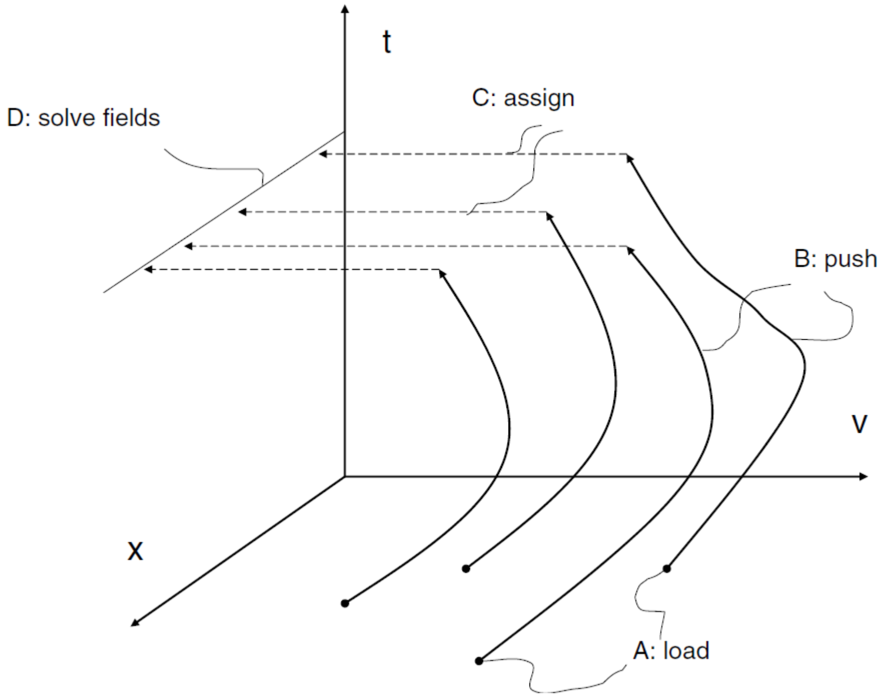

- Eulerian code (Fig.2.3): The Eulerian approach uses a fixed grid in the 5D phase space. Finite differences or spectral methods are used to obtain the value of the distribution function at time $t + \delta t$ knowing the distribution function at time t. Eulerian codes are not subject to numerical sampling noise and are able to accurately treat the $E \times B$ non linearity. On the other hand, these codes often use an explicit time step and are therefore subject to the Courant-Friedrichs-Lewy (CFL) stability condition, which reduces the time step. The Eulerian technic is used by the gyrokinetic codes GS2[28], GYRO[15], GENE[56], GKV[86], GKW[72] and GT5D[53] (the list is not exhaustive).

Figure 2.3.: In Eulerian methods, a fixed grid is defined in phase space (A). Finite difference expressions are used (B) in order to obtain value of f at grid point at the next time step (C). Field equations are then solved (D) after integration over velocity space. Figure coming from [35].

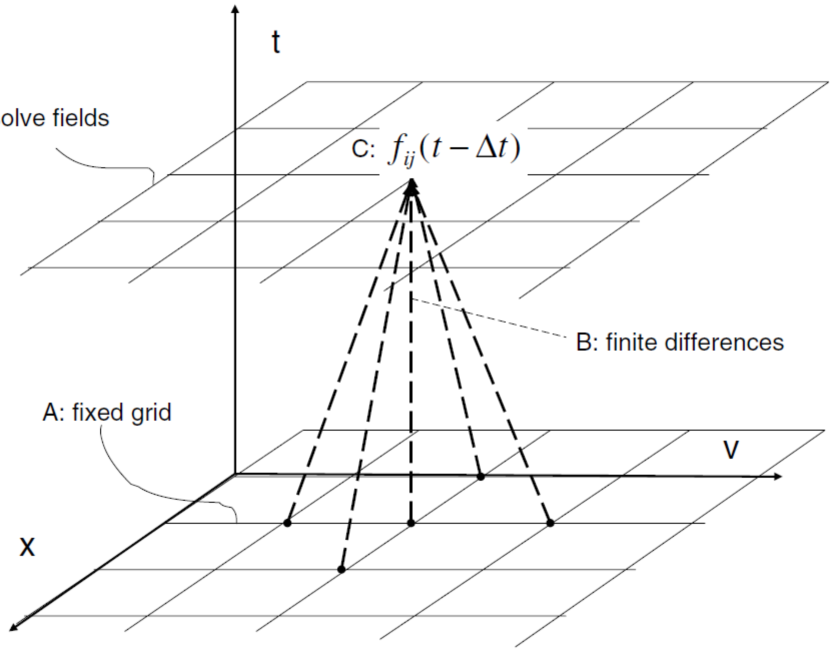

- Semi-Lagrangian code (Fig.2.4): The last method is an hybrid method between the two previous methods. It is called semi-Lagrangian. It is based on a fixed Eulerian grid but uses the invariance of the distribution function along trajectories when solving of Eq.(2.2.1) like PIC codes. GYSELA [38] (GYrokinetic SEmi LAgrangian) is the only large gyrokinetic code to use this method of resolution. The method of resolution used in GYSELA is the following : starting from a grid point of the phase space at time $t + \Delta t$, one computes the position of this point at time t by solving the trajectory equation (2.2.1) backward in time. At this stage, the value of the distribution function is the same as the one at the starting point $\bar{F}_s(t+\Delta t, \boldsymbol{z}(t+\Delta t)) = \bar{F}_s(t, \boldsymbol{z}(t))$ where $\boldsymbol{z}(t+\Delta t)$ is the coordinate of the starting point and $\boldsymbol{z}(t)$ the corresponding coordinate at time t. Unfortunately, in most cases $\boldsymbol{z}(t)$ does not correspond to a mesh point. An interpolation is thus done to compute $\bar{F}_s(t, \boldsymbol{z}(t))$ knowing the distribution function at all points of the mesh at time t.

This method is not subject to numerical sampling noise nor CFL condition, but the time step is constrained by accuracy requirements. Moreover two difficulties appear with the semi-Lagrangian method. The first one is the choice of interpolation operators. Indeed a trade-off between numerical dissipation and unphysical oscillations coming from the high order interpolation technic has to be found. Moreover the conservation of particle is not granted. Small errors made on particle conservation, lead to large unphysical electric potential.

Figure 2.4.: In semi-Lagrangian methods, a fixed grid is defined in phase space (A). The orbits are integrated back in time from each grid point (B). The value of f at grid points is obtained by interpolation at the foot of the orbit (C) and using the property $f = \text{const}$ along orbits. Field equations are then solved (D) after integration over velocity space. Figure coming from [35].

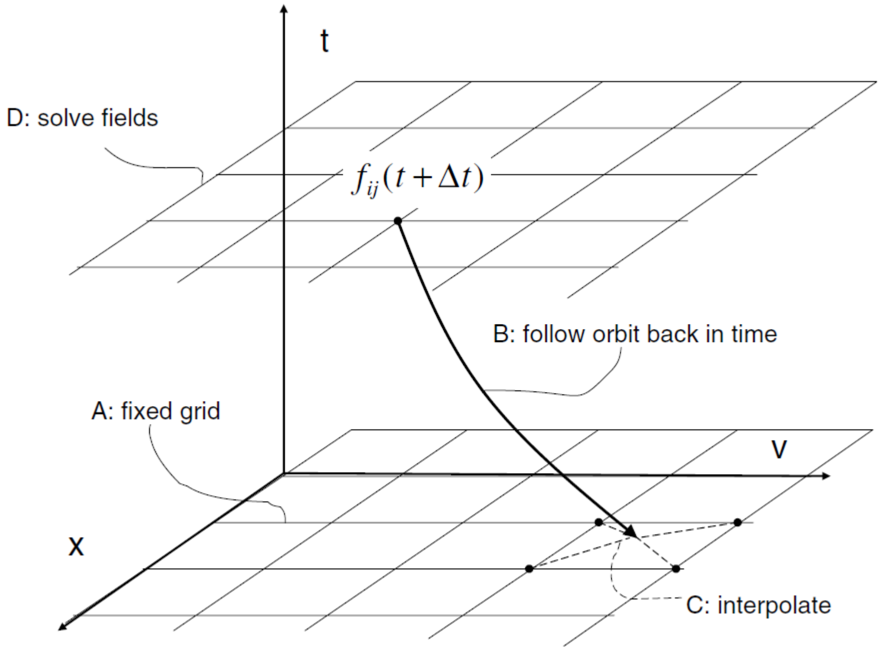

3. A multi-species collision operator for GYSELA

Contents

2.1. Gyrokinetic theory **41**
    2.1.1. Kinetic description 42
    2.1.2. From kinetic to gyrokinetic 43
    2.1.3. Quasi-neutrality equation : limit of adiabatic electrons . 45
2.2. The GYSELA code **48**
    2.2.1. Main features 48
    2.2.2. Numerical aspects 50

The containt of this chapter is coming from [27].

3.1. Introduction

The perpendicular transport in core fusion plasmas is dominated by turbulent processes. Nevertheless, accounting for collisions remains essential for several reasons. First, to a large extent, collisions govern the level of large scale flows – both the mean ion poloidal flow and turbulence-driven zonal flows – via the friction on trapped particles. Second, neoclassical transport can reveal dominant (or at least competitive) with respect to turbulent transport in certain regimes such as transport barriers, or for certain classes of particles such as heavy impurities like tungsten. Third, collisions are essential for trapped electrons which are often in a collisional regime. Finally, and more fundamentally, collisions ensure the relaxation of the distribution function towards a Maxwellian. In turn, they are critical for gyrokinetic simulations since they smooth out small scale structures in velocity space, contributing to numerical stability.

The full collision operator and its properties are well known but its non linear character makes it impossible to use numerically with present gyrokinetic codes. It is then necessary to develop a linearized model of collision operator easier to handle numerically. Different model operators have been developed in the literature [1]. Depending on its specificity, each code chooses a different model. A PIC code like ORB5[81] uses a different operator than an Eulerian code like GENE[37], GKW [65] or GS2 [9]. In the framework of the GYSELA code, one of the major difficulties is to write an operator in the variables $\left(v_{\parallel}, \mu\right)$ whereas the collision operator is separable in the set of variables $\left(v, \frac{v_{\parallel}}{v}\right)$. This difficulty has been overcome by Esteve [30]. The collision operator is linearized around unshifted Maxwellians and is gyroaveraged using the method developed by Brizard [13]. It is valid for arbitrary species and can be shown to fulfill all properties required for a model collision operator. Its derivation and analytical verification can be found in detail in [30]. A simplified version of this operator has been implemented in GYSELA and benchmarked against neoclassical theory [30]. It uses the slow limit approximation (energy and pitch-angle scattering are assumed equal) and removes all μ derivatives. A particular consequence of these approximations is that the implemented model is only valid for trace thermal impurities. This article describes the treatment of the collision operator without those two assumptions, hence alleviating the former restrictions regarding the domain of validity.

The outline of this chapter is the following. In 3.2 the important results of the model derived by Esteve et al [30] are recalled. Part 3.3 is dedicated to the description of analytical approximations for an optimized numerical treatment of the collision operator. Part 3.4 presents different aspects of the numerical implementation. Finally, the section 3.5 consists in a serie of tests which validate the collision operator.

3.2. Presentation of the model

The model described here is derived directly from [30]. The linearized collisional operator describing the collisions of species a colliding on species b takes the form

$$C_{ab}(F_a, F_b) = C^0_{ab}(F_{M0a}, F_{M0b}) + C^1_{ab}(F_a, F_b)$$

where F_{M0a} represents the local unshifted Maxwellian with density n_a and temperature T_a

$$F_{M0a}(\boldsymbol{x}, \boldsymbol{v}, t) = N_a(\boldsymbol{x}, t)\left(\frac{1}{2\pi v_{Ta}^2}\right)^{3/2} \exp\left(-x_a^2\right)$$

The normalized speed has been used $x_a = \frac{v}{\sqrt{2}v_{Ta}}$,with $v_{Ta} = \sqrt{\frac{T_a}{m_a}}$ the thermal velocity.

C^0_{ab} represents the exchange of energy between the unshifted Maxwellians

$$C^0_{ab}(F_{M0a}, F_{M0b}) = \frac{T_b - T_a}{T_b} x_a^2 \nu_{E,ab} F_{M0a} \tag{3.2.1}$$

Neglecting all finite Larmor radius effects, C^1_{ab} is composed of three terms

$$C^1_{ab}(F_a, F_b) = C_{v,ab}(F_a) + C_{d,ab}(F_a) + C_{\parallel,ab}(F_a, F_b)$$

$C_{v,ab}$ is an operator acting on the norm of the velocity. When written in the set of variables $\left(v_\parallel, v_\perp\right)$, it reads as follows ($g_{ab}$ is close to the normalized distribution function and is defined below):

$$\begin{aligned} C_{v,ab}\left(F_a\right) &= \frac{1}{2v_\perp}\frac{\partial}{\partial v_\perp}\left[F_{M0a}\nu_{v,ab}v_\perp^2\left(v_\perp\frac{\partial g_{ab}}{\partial v_\perp} + v_\parallel\frac{\partial g_{ab}}{\partial v_\parallel}\right)\right] \\ &+ \frac{1}{2}\frac{\partial}{\partial v_\parallel}\left[F_{M0a}\nu_{v,ab}v_\parallel\left(v_\perp\frac{\partial g_{ab}}{\partial v_\perp} + v_\parallel\frac{\partial g_{ab}}{\partial v_\parallel}\right)\right] \end{aligned} \tag{3.2.2}$$

Conversly $C_{d,ab}$ only modifies the direction of the velocity vector (deflection)

$$\begin{aligned} C_{d,ab}\left(F_a\right) &= \frac{1}{2v_\perp}\frac{\partial}{\partial v_\perp}\left[F_{M0a}\nu_{d,ab}v_\perp v_\parallel\left(v_\parallel\frac{\partial g_{ab}}{\partial v_\perp}-v_\perp\frac{\partial g_{ab}}{\partial v_\parallel}\right)\right] \\ &+ \frac{1}{2}\frac{\partial}{\partial v_\parallel}\left[F_{M0a}\nu_{d,ab}v_\perp\left(-v_\parallel\frac{\partial g_{ab}}{\partial v_\perp}+v_\perp\frac{\partial g_{ab}}{\partial v_\parallel}\right)\right] \end{aligned} \tag{3.2.3}$$

Finally the term $C_{\parallel,ab}$ ensures momentum exchange between species and conservation of the total parallel momentum.

$$C_{\parallel,ab}\left(F_a,F_b\right)=-\frac{\nu_{s,ab}(v)}{v_{Ta}^2}v_\parallel\left(U_{\parallel d,a}-U_{\parallel ba}\right)F_{M0a} \tag{3.2.4}$$

The normalized distribution function has to be shifted to ensure that $C_{v,ab}$ and $C_{d,ab}$ conserve momentum and energy

$$g_{ab}=f_a-\frac{v_\parallel U_{\parallel d,a}}{v_{Ta}^2}-x_a^2q_{ba} \text{ with } f_a=\frac{F_a}{F_{M0a}}$$

More specifically, $U_{\parallel d,a}$ ensures that $C_{v,ab}$ and $C_{d,ab}$ conserve momentum.

$$\frac{v}{v_{Ta}^2}U_{\parallel d,a}\left(v\right)=\frac{3}{2}\int d\xi\xi f_a \text{ with } \xi=\frac{v_\parallel}{v}$$

Then in order to take into account momentum exchange between species while keeping the total momentum constant, a second velocity $U_{\parallel ab}$ is chosen as

$$U_{\parallel ab}=\frac{\left\langle\nu_{s,ab}v^2U_{\parallel d,a}\right\rangle_v}{\left\langle\nu_{s,ab}v^2\right\rangle_v}$$

A dimensionless parameter q_{ab} accounting for energy exchange between species is defined as

$$q_{ab}=T_b\frac{\left\langle\nu_{E,ab}\frac{m_av^2}{2}f_a\right\rangle_v}{\left\langle\nu_{E,ab}\left(\frac{m_av^2}{2}\right)^2\right\rangle_v}$$

The bracket corresponds to mean values in velocity space $<\ldots>_v=\int d^3\boldsymbol{v}\frac{F_{M0a}}{N_a}\ldots$. Various frequencies appear in the previous expressions. They are defined as follows :

- the Hirshman and Sigmar's inter-species collision frequency [47] $\nu_{ab}^{HS}=\sqrt{2}\frac{N_bZ_b^2}{N_aZ_a^2}\nu_{aa}$ where $\nu_{aa}=\frac{4\sqrt{\pi}}{3}\frac{Z_a^4e^4\ln\Lambda}{(4\pi\epsilon_0)^2}\frac{N_a}{m_a^2v_{Ta}^3}$ is the intraspecies collision frequency and $\ln\Lambda\simeq 20$ is the Coulomb logarithm.
- the velocity modulus diffusion rate $\nu_{v,ab}\left(x_a\right)=\nu_{ab}^{HS}x_{ba}\frac{\Theta(x_b)}{x_a^2}$
- the deflection frequency $\nu_{d,ab}\left(x_a\right)=\nu_{ab}^{HS}x_{ba}\frac{\Psi(x_b)}{x_a^2}$

- the slowing-down frequency $\nu_{s,ab} = \nu_{ab}^{HS}\left(1+\frac{m_a}{m_b}\right)x_{ba}^3\Theta(x_b)$
- the energy-loss rate $\nu_{E,ab} = -\frac{1}{v^4 F_{M0a}}\frac{\partial}{\partial v}\left(\nu_{v,ab}F_{M0a}v^5\right)$

Where the ratio between the thermal velocities is introduced $x_{ba} = \frac{v_{Ta}}{v_{Tb}}$. The following functions are also define

$$\begin{aligned}
\Psi\left(x\right) &= \frac{3\sqrt{\pi}}{4}\frac{1}{x}\left[\Phi\left(x\right)-G\left(x\right)\right]\\
\Theta\left(x\right) &= \frac{3\sqrt{\pi}}{2}\frac{G\left(x\right)}{x}\\
G\left(x\right) &= \frac{1}{2x^2}\left[\Phi\left(x\right)-x\Phi'\left(x\right)\right]\\
\Phi\left(x\right) &= \frac{2}{\sqrt{\pi}}\int_0^x dy\exp\left(-y^2\right)
\end{aligned}$$

The function Φ is the error function and G is the Chandrasekhar function. The different frequencies normalized to ν_{ab}^{HS} are plotted in Fig.(3.1).

We mention here that a Jacobian appears in the original model, namely prefactors $B_{\parallel,a}^{\star} = B + \frac{m_a v_{\parallel}}{Z_a}\boldsymbol{b}\cdot(\nabla\times\boldsymbol{b})$ in the definitions of $C_{v,ab}$ and $C_{d,ab}$ (equations (73) and (74) of [30]). These terms have been dropped as $B_{\parallel,a}^{\star} = B + O\left(\frac{\rho_a}{a}\right)$ where $\rho_a = \frac{v_{Ta}}{\omega_{ca}}$ is the Larmor radius and a the minor radius of the tokamak considered. In all cases considered, one has $\frac{\rho_a}{a} \leq 10^{-2}$ justifying the approximation used in this article $B_{\parallel,a}^{\star} \simeq B$. With this approximation, the magnetic field dependence disappears and one gets the definitions given previously (3.2.2) and (3.2.3). To ensure rigourously the conservation of particles, the $B_{\parallel,a}^{\star}$ dependence should be taken into account. The loss of accuracy on particle conservation due to the approximation $B_{\parallel,a}^{\star} = B$ is partly compensated by the use of a numerical treatment detailed in part 3.4.2. The mismatch on particle conservation is presented in part 3.5.1.

Figure 3.1.: Velocity dependence of the velocity modulus diffusion rate $\nu_{v,ab}$ (blue), the deflection frequency $\nu_{d,ab}$ (red), the slowing-down frequency $\nu_{s,ab}$ (black) and the absolute value of the energy-loss rate $|\nu_{E,ab}|$ (green). All quantities are normalized to ν_{ab}^{HS} .

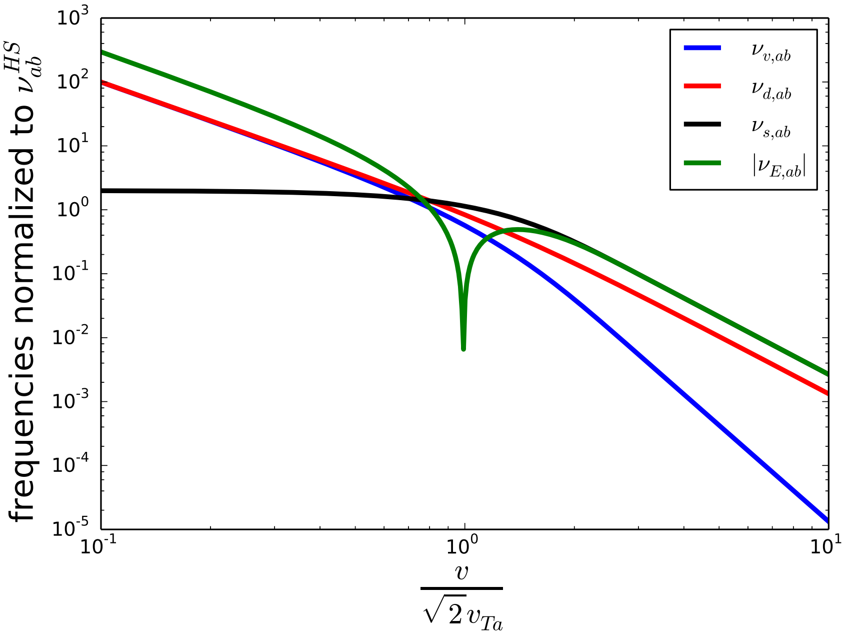

3.3. Analytical approximations for an optimized numerical treatment of the collision operator

This section is devoted to the description of various approximations required for an efficient numerical implementation of the collision operator. Section 3.3.1 describes the separation of the collision operator in three sub parts. The first one (C_0 (3.2.1)) acts on the Maxwellian distribution functions and corresponds to the exchange of energy between species. This term is detailed in section 3.3.2. A second part of the operator ($C_{\parallel}$(3.2.4)) corresponds to the evolution of the parallel momentum. Section 3.3.3 is mostly devoted to the description of this part of the operator. The last part of the operator ($C_v + C_d$ (3.2.2) and (3.2.3)) is the trickiest one as it governs the evolution of the distribution function in velocity space. Section 3.3.4 details to the treatment of μ derivatives, using a projection on a set of orthogonal polynomials. Finally section 3.3.5 describes a complete rewritting of the evolution of the distribution due to $C_v + C_d$ using the approximations presented in the parts 3.3.3 and 3.3.4.

3.3.1. Separation of the different collision terms

The collision operator is difficult to treat as a whole. It is much easier to split the different parts of the operator and treat them separately with a time splitting scheme. The first step is to discriminate the evolutions of F_{M0a} and δF_a via collisions. The equation that needs to be solved is

$$\frac{\partial F_a}{\partial t} = \sum_b C_{ab}\left(F_a, F_b\right)$$

which can be split as

$$\begin{cases} \frac{\partial F_{M0a}}{\partial t} = \sum_b C^0_{ab}\left(F_{M0a}, F_{M0b}\right) \\ \frac{\partial \delta F_a}{\partial t} = \sum_b C^1_{ab}\left(F_a, F_b\right) \end{cases}$$

The second equation of the system can be recast as the evolution of the total distribution assuming that the Maxwellian is unchanged. This alternative expression is valid provided that the evolution of the Maxwellian is treated by the first equation. This new expression is useful especially for the treatment of the μ derivatives.

$$\frac{\partial F_a}{\partial t} = \sum_b C^1_{ab}\left(F_a, F_b\right) \text{ with } F_{M0a} = cst$$

A second step is to separate the evolution of δF_a in two parts for the numerical resolution. Indeed, the evolution governed by $C_{v,ab} + C_{d,ab}$ is difficult to treat as it includes μ derivatives. It will be treated differently from $C_{\|,ab}$ which is easier to implement. In the end, the problem can be split in three parts for the numerical resolution: the evolution of the Maxwellian due to C^0_{ab}, the evolution of the distribution function due to $C_{\|,ab}$, and the evolution of the distribution function due to $C_{v,ab} + C_{d,ab}$. The last two steps are performed by keeping constant the Maxwellian F_{M0a}.

$$\begin{cases} \frac{\partial F_{M0a}}{\partial t} = \sum_b C^0_{ab}\left(F_{M0a}, F_{M0b}\right) & \\ \frac{\partial F_a}{\partial t} = \sum_b C_{\|,ab}\left(F_a, F_b\right) & \left(F_{M0a} = cst\right) \\ \frac{\partial F_a}{\partial t} = \sum_b C_{v,ab}\left(F_a, F_b\right) + C_{d,ab}\left(F_a, F_b\right) & \left(F_{M0a} = cst\right) \end{cases} \tag{3.3.1}$$

3.3.2. Evolution of thermal energy

Here we detail how the thermal energy evolves due to collisions. The effect of C^0_{ab} is to exchange thermal energy between Maxwellians. The thermal energy exchange is exactly known in the case of Maxwellians. It is made of two contributions : the first term corresponds to the thermal energy equipartition and the second one corresponds to the opposite of the work of the friction force.

$$Q_{M,ab} = -3n_a \frac{m_a}{m_a + m_b} \nu_{ab} (T_a - T_b) + n_a m_a \nu_{ab} V_{\parallel a} \left(V_{\parallel a} - V_{\parallel b} \right)$$

where $V_{\parallel a} = \frac{1}{n_a} \int F_{Ma} v_\parallel d^3v$ is the parallel velocity associated to the Maxwellian. The evolution of thermal energy is governed by $Q_{M,ab}$

$$\frac{3}{2} n_a \frac{\partial T_a}{\partial t} = \sum_b Q_{M,ab}$$

which is equivalent to

$$\frac{\partial T_a}{\partial t} = \sum_b m_a \nu_{ab} \left[\frac{2}{m_a + m_b} (T_b - T_a) + \frac{2}{3} V_{\parallel a} \left(V_{\parallel a} - V_{\parallel b} \right) \right] \tag{3.3.2}$$

This relation will be used to compute the evolution of the Maxwellian distribution in eq.(3.3.1). Note that the total (thermal + kinetic) energy remains unaffected by the latter term, as it should to preserve Galilean invariance.

3.3.3. Approximation of the distribution function

The quantities $U_{\parallel ab}$ and q_{ab} are difficult to compute numerically . Indeed both include collision frequencies ($\nu_{s,ab}$ and $\nu_{E,ab}$) that depend on the mass ratio $\frac{m_a}{m_b}$ and the integrals are then difficult to compute in the two limits $\frac{m_a}{m_b} \gg 1$ and $\frac{m_a}{m_b} \ll 1$. An analytical approach is used to overcome this difficulty.

3.3.3.1. Expansion on a set of orthogonal polynomials

Following the method developed by Hirshman and Sigmar [48], the distribution function is projected on a set of orthogonal polynomials

$$F(v, \theta, \varphi_c) = \sum_{\ell,m} F_{\ell,m}(v) Y_{\ell,m}(\theta, \varphi_c)$$

with φ_c the phase of the cyclotronic motion and $Y_{\ell,m}(\theta, \varphi_c)$ the spherical harmonics

$$Y_{\ell,m}(\theta, \varphi_c) = P_{\ell,m}(\xi) e^{im\varphi_c} \text{ and } \cos\theta = \xi = \frac{v_\parallel}{v}$$

As the method is used in a gyrokinetic approach only the $m = 0$ component is kept :

$$F(v, \theta) = \sum_\ell F_\ell(v) P_\ell(\xi)$$

where P_ℓ are Legendre polynomials.

Then each component $F_\ell(v)$ is expanded in Laguerre polynomials

$$F_\ell(v) = \sum_j \left(\frac{v}{2v_{Ta}^2}\right)^\ell \mathcal{F}_j^{(\ell)} L_j^{(\ell+\frac{1}{2})}(x_a^2) F_{M0a} \tag{3.3.3}$$

with

$$\begin{aligned}\mathcal{F}_j^{(\ell)} &= \left\langle F_\ell | L_j^{(\ell+\frac{1}{2})} \right\rangle \\ &= \frac{2\pi^{3/2} j!}{\Gamma(j+\ell+\frac{3}{2})} \int_0^\infty v^\ell L_j^{(\ell+\frac{1}{2})}(x_a^2) \frac{F_\ell(v)}{n_a} v^2 dv\end{aligned}$$

where $L_j^{(\ell+\frac{1}{2})}$ is the generalized Laguerre polynomial of order $\ell+\frac{1}{2}$. Note that the $L_j^{(\ell+\frac{1}{2})}$ are chosen as functions of v^2. The underlying rationale is that the lowest order terms of the expansion capture explicitely the dependence with respect to the two motion invariants: the kinetic energy $E = \frac{mv^2}{2} = \frac{mv_\parallel^2}{2} + \mu B$ and the kinetic toroidal momentum $P_\varphi = -e\Psi + mRv_\varphi$, where Ψ is the poloidal magnetic flux and $v_\varphi = \frac{B_\varphi}{B} v_\parallel$ is the velocity in the toroidal direction. Note that in the present study, Ψ is a parameter as the problem is spatially local due to the neglect of finite Larmor radius effect. Finally, $(l=1, j=0)$ scales like $v_\parallel$, hence capturing the P_φ dependence, while $(l=0, j=1)$ scales like v^2 which corresponds to the energy. Using these definitions it is possible to show that $\mathcal{F}_0^{(0)} = 1$, $\mathcal{F}_1^{(0)} = 0$, $\mathcal{F}_0^{(1)} = 2V_{\parallel a}$, $\mathcal{F}_2^{(0)} = \frac{2}{15} \langle x_a^4 (f_a - 1) \rangle$ and

$$\mathcal{F}_1^{(1)} = -\frac{4q_{\parallel a}}{5n_a T_a} = -\frac{4}{5} \left\langle v_\parallel \left(x_a^2 - \frac{5}{2}\right) f_a \right\rangle_v \tag{3.3.4}$$

where $q_{\parallel a}$ respresents the parallel heat flux. Then keeping only the first two polynomials in both directions, the normalized distribution function can be approximated by

$$f_a \simeq 1 + \frac{v_\parallel}{v_{Ta}^2} \left[V_{\parallel a} - \frac{q_{\parallel a}}{n_a T_a} \left(1 - \frac{2x_a^2}{5}\right)\right] \tag{3.3.5}$$

We mention here that the expansion (3.3.5) is the minimal expansion in order to recover the predictions of the standard neoclassical theory [47], in particular the thermal screening effect studied in section 4.4. The expansion is restricted to the lowest required orders since keeping higher order corrections would require a refined discretization of the velocity space, hence increasing the numerical cost of the operator. Note however that it has been recently pointed out that higher order moments could modify the screening factor (see the discussion in section 6.3.4)

3.3.3.2. Expression of $C_{\parallel,ab}$

The $C_{\parallel,ab}$ term deals with momentum exchange between different species. Indeed one can show that the rate of momentum exchange of the total operator is given by

$$R_{\parallel ab} = -n_a m_a \nu_{ab}\left(U_{\parallel ab} - U_{\parallel ba}\right)$$

To evaluate the two quantities $U_{\parallel d,a}(v)$ and $U_{\parallel ab}$ the approximate distribution function (3.3.5) is used. It gives :

$$U_{\parallel d,a} = V_{\parallel a} - \frac{q_{\parallel a}}{n_a T_a}\left(1 - \frac{2}{5}x_a^2\right) \tag{3.3.6}$$

$$U_{\parallel ba} = V_{\parallel b} - \frac{3}{5}\frac{q_{\parallel b}}{n_b T_b}\left(\frac{1}{1+x_{ba}^2}\right)$$

and so

$$C_{\parallel,ab} = \nu_{s,ab}\frac{m_a}{T_a}v_\parallel F_{M0a}\left[V_{\parallel b} - V_{\parallel a} + \frac{q_{\parallel a}}{n_a T_a}\left(1 - \frac{2}{5}x_a^2\right) - \frac{3}{5}\frac{q_{\parallel b}}{n_b T_b}\left(\frac{1}{1+x_{ba}^2}\right)\right]$$

The collisional drag force becomes

$$R_{\parallel ab} = -n_a m_a \nu_{ab}\left[V_{\parallel a} - V_{\parallel b} - \frac{3}{5}\frac{q_{\parallel a}}{n_a T_a}\left(\frac{1}{1+x_{ab}^2}\right) + \frac{3}{5}\frac{q_{\parallel b}}{n_b T_b}\left(\frac{1}{1+x_{ba}^2}\right)\right]$$

For a Maxwellian, the result is exact and reduces to the friction force :

$$R_{\parallel M,ab} = -n_a m_a \nu_{ab}\left[V_{\parallel a} - V_{\parallel b}\right]$$

To ensure this property, one needs $q_{\parallel a} = 0$ for a Maxwellian distribution function. Then the definition of $q_{\parallel a}$ is adapted accordingly :

$$q_{\parallel a} = \frac{1}{2}\int d^3\boldsymbol{v} m_a\left[\left(v_\parallel - V_{\parallel a}\right)^2 + v_\perp^2\right]\left(v_\parallel - V_{\parallel a}\right)F_a$$

This new definition is equivalent to the one used in Eq.(3.3.4) in the limit of small Mach number. It is the one used in [30].

A long but straightforward calculation allows one to show that for the simplified distribution function (3.3.5) $q_{ab} = 0$. This approximation will be used in the rest of this article. Then g_{ab} reduces to

$$g_a = f_a - \frac{m_a v_\parallel U_{\parallel d,a}}{T_a} \tag{3.3.7}$$

3.3.4. Treatment of the μ derivatives

Derivatives with respect to μ are present in the terms $C_{v,ab}$ and $C_{d,ab}$. The treatment of these derivatives by finite differences may be problematic if one wants to use a relatively low resolution in the μ direction. An alternative method based on a projection on orthogonal polynomials in μ is adopted. It allows one to solve the problem while keeping a relatively low resolution in the μ direction (typically $N_\mu = 64$). The equation solved with this method is

$$\frac{\partial F_a}{\partial t} = \sum_b C_{v,ab}\left(F_a, F_b\right) + C_{d,ab}\left(F_a, F_b\right) \Leftrightarrow \frac{\partial f_a}{\partial t} = \sum_b \bar{C}_{ab} \tag{3.3.8}$$

where we have introduced the normalized collision operator $\bar{C}_{ab}(F) = \frac{C_{v,ab}(F)+C_{d,ab}(F)}{F_{M0a}}$. This approach is possible because a Maxwellian is in the kernel of $C_{v,ab} + C_{d,ab}$. This term can be expressed differently to simplify its numerical treatment.

$$\begin{aligned}\bar{C}_{ab}(g_a) \quad = \quad & K_{1,ab}\frac{\partial g_a}{\partial v_\parallel} + K_{2,ab}\frac{\partial^2 g_a}{\partial v_\parallel^2} + K_{3,ab}u\frac{\partial^2 g_a}{\partial v_\parallel \partial u} \\ & + K_{4,ab}u\frac{\partial g_a}{\partial u} + \bar{C}_{m,ab}(g_a)\end{aligned}$$

where $u = \frac{\mu B}{T_a}$. Defining $D_{d,ab} = \frac{1}{2}\nu_{d,ab}v^2$, it is possible to show that

$$\begin{aligned}K_{1,ab} &= v_\parallel\left[\frac{1}{v}\frac{\partial D_{d,ab}}{\partial v} - \frac{D_{d,ab}}{v_{Ta}^2}\right] + \frac{v_\parallel v}{2}\frac{\partial\left(\nu_{v,ab} - \nu_{d,ab}\right)}{\partial v} \\ &\quad + v_\parallel\left(\nu_{v,ab} - \nu_{d,ab}\right)\left(2 - x_a^2\right) \\ K_{2,ab} &= D_{d,ab} + \frac{v_\parallel^2}{2}\left(\nu_{v,ab} - \nu_{d,ab}\right) \\ K_{3,ab} &= 2v_\parallel\left(\nu_{v,ab} - \nu_{d,ab}\right) \\ K_{4,ab} &= \left(1 - \frac{v_\parallel^2}{v_{Ta}^2}\right)\left(\nu_{v,ab} - \nu_{d,ab}\right) + \frac{v_\parallel^2}{v}\frac{\partial\left(\nu_{v,ab} - \nu_{d,ab}\right)}{\partial v} \\ \bar{C}_{m,ab}(g_a &= \frac{2}{v_{Ta}^2 F_{M0a}}\frac{\partial}{\partial u}\left[F_{M0a}\left(D_{d,ab} + v_{Ta}^2 u\left(\nu_{v,ab} - \nu_{d,ab}\right)\right)u\frac{\partial g_a}{\partial u}\right]\end{aligned}$$

f is projected on a set of orthogonal polynomials:

$$f_a(\boldsymbol{r}, v_\parallel, u, t) = \sum_l \alpha_{\ell,a}(\boldsymbol{r}, v_\parallel, t)P_\ell(u)$$

Projecting equation (3.3.8) on polynomial P_ℓ gives

$$\frac{\partial \alpha_{\ell,a}}{\partial t} = \sum_b \left\langle \bar{C}_{ab}\left(g_a\right)|P_\ell\right\rangle$$

In practice, Laguerre polynomials are chosen. Thus it defines the scalar product as

$$\langle f|g\rangle = \int_0^\infty dx e^{-x} f(x)\, g(x)$$

3.3.5. Evolution equation of the distribution function components

3.3.5.1. Projection of g_a on Laguerre polynomials

The first step is to compute the projection of g_a on Laguerre polynomials. Starting from the equation(3.3.7), one gets

$$g_a = f_a + P_0(u)\kappa_{0,a} + P_1(u)\kappa_{1,a}$$

with

$$\kappa_{0,a} = -\left\{\frac{m_a v_\|}{T_a}\left[V_{\|a} - \frac{q_{\|a}}{N_a T_a}\left(\frac{3}{5} - \frac{m_a v_\|^2}{5T_a}\right)\right]\right\}$$

and

$$\kappa_{1,a} = \frac{2m_a v_\| q_{\|a}}{5N_a T_a^2}$$

So g_a can be easily projected on Laguerre polynomials

$$g_a = \sum_i \alpha'_{i,a} P_i$$

with

$$\begin{cases} \alpha'_{i,a} = \alpha_{i,a} + \kappa_{i,a} & \text{if } i < 2 \\ \alpha'_{i,a} = \alpha_{i,a} & \text{otherwise} \end{cases}$$

3.3.5.2. Expression of the $C_v + C_d$ part of the operator

Using the properties of Laguerre polynomials, and summing over the species, Eq.(3.3.8) can be written

$$\frac{\partial \alpha_{\ell,a}}{\partial t} = \sum_j \left[\alpha'_{i,a} N^{jl}_{0,a} + \frac{\partial \alpha'_{i,a}}{\partial v_\|} N^{jl}_{1,a} + \frac{\partial^2 \alpha'_{i,a}}{\partial v_\|^2} N^{jl}_{2,a}\right] \tag{3.3.9}$$

with

$$
\begin{aligned}
N^{jl}_{0,a} &= \sum_b \left\langle jK_{4,ab}\left(P_j - P_{j-1}\right) + \bar{C}_{m,ab}(P_j)|P_l\right\rangle \\
N^{jl}_{1,a} &= \sum_b \left\langle K_{1,ab}P_j + jK_{3,ab}\left(P_j - P_{j-1}\right)|P_l\right\rangle \\
N^{jl}_{2,a} &= \sum_b \left\langle K_{2,ab}P_j|P_l\right\rangle
\end{aligned}
$$

At this stage, these quantities remain somewhat too intricate to be computed analytically. Using the definitions given in the previous part and defining the following quantities

$$
P_jP_\ell = \sum_{i=0}^{j+\ell} C^i_{j\ell}u^i
$$

$$
\begin{aligned}
L^{(0)}_{i,ab} &= \left\langle \frac{D_{d,ab}}{v^2_{Ta}}|u^i\right\rangle \\
L^{(1)}_{i,ab} &= \left\langle \frac{1}{v}\frac{\partial D_{d,ab}}{\partial v}|u^i\right\rangle \\
L^{(2)}_{i,ab} &= \left\langle \nu_{v,ab} - \nu_{d,ab}|u^i\right\rangle \\
L^{(3)}_{i,ab} &= \left\langle \frac{v}{2}\frac{\partial\left(\nu_{v,ab} - \nu_{d,ab}\right)}{\partial v}|u^i\right\rangle \\
L^{(4)}_{i,ab} &= \left\langle \frac{v^2_{Ta}}{v}\frac{\partial\left(\nu_{v,ab} - \nu_{d,ab}\right)}{\partial v}|u^i\right\rangle
\end{aligned}
\tag{3.3.10}
$$

It can be shown that

$$
\begin{aligned}
N^{jl}_{0,a} &= j\sum_b\sum_{i=0}^{j+\ell} C^i_{j\ell}\left[\begin{array}{c} \left(3 - \frac{v^2_\parallel}{v^2_{Ta}}\right)L^{(2)}_{i,ab} + \left(2 + \frac{v^2_\parallel}{v^2_{Ta}}\right)L^{(4)}_{i,ab} \\ -2L^{(0)}_{i,ab} + 2L^{(1)}_{i,ab} - 2L^{(2)}_{i+1,ab} \end{array}\right] \\
&- j\sum_b\sum_{i'=0}^{j+\ell-1} C^{i'}_{j-1,\ell}\left[\begin{array}{c} 2L^{(1)}_{i',ab} + \left(3 - \frac{v^2_\parallel}{v^2_{Ta}}\right)L^{(2)}_{i',ab} \\ + \left(2 + \frac{v^2_\parallel}{v^2_{Ta}}\right)L^{(4)}_{i',ab} \end{array}\right]
\end{aligned}
$$

$$
\begin{aligned}
N^{jl}_{1,a} &= v_\parallel\sum_b\sum_{i=0}^{j+\ell} C^i_{j\ell}\left[\begin{array}{c} -L^{(0)}_{i,ab} + L^{(1)}_{i,ab} - L^{(2)}_{i+1,ab} + L^{(3)}_{i,ab} \\ + \left(2 + 2j - \frac{v^2_\parallel}{2v^2_{Ta}}\right)L^{(2)}_{i,ab} \end{array}\right] \\
&- v_\parallel\sum_b\sum_{i'=0}^{j+\ell-1} C^{i'}_{j-1,\ell}2jL^{(2)}_{i',ab}
\end{aligned}
$$

$$N_{2,a}^{jl} = \sum_b \sum_{i=0}^{j+\ell} C_{j\ell}^{i} v_{Ta}^2 \left[L_{i,ab}^{(0)} + \frac{v_\parallel^2}{2v_{Ta}^2} L_{i,ab}^{(2)} \right]$$

3.3.5.3. Computation of the scalar products

Integrating by parts the expressions of the $L_{i,ab}^{(j)}$ Eq.(3.3.10), it is possible to show that

$$\begin{cases} L_{0,ab}^{(1)} = & -\frac{D_{d,ab}\left(v_\parallel, u=0\right)}{v_{Ta}^2} + L_{0,ab}^{(0)} \\ L_{i>0,ab}^{(1)} = & L_{i,ab}^{(0)} - iL_{i-1,ab}^{(0)} \end{cases}$$

$$\begin{cases} L_{0,ab}^{(3)} = & \frac{v_\parallel^2}{2v_{Ta}^2} \left[L_{0,ab}^{(2)} - \left(\nu_{v,ab} - \nu_{d,ab}\right) \left(v_\parallel, u=0\right) \right] \\ & +L_{1,ab}^{(2)} - L_{0,ab}^{(2)} \\ L_{i>0,ab}^{(3)} = & \frac{v_\parallel^2}{2v_{Ta}^2} \left[L_{i,ab}^{(2)} - iL_{i-1,ab}^{(2)} \right] + L_{i+1,ab}^{(2)} - (i+1)\, L_{i,ab}^{(2)} \end{cases}$$

$$\begin{cases} L_{0,ab}^{(4)} = & L_{0,ab}^{(2)} - \left(\nu_{v,ab} - \nu_{d,ab}\right) \left(v_\parallel, u=0\right) \\ L_{i>0,ab}^{(3)} = & L_{i,ab}^{(2)} - iL_{i-1,ab}^{(2)} \end{cases}$$

The only last difficulty is then to compute $L_{i,ab}^{(0)}$ and $L_{i,ab}^{(2)}$. Unfortunately, the v dependences of $\nu_{v,ab}$ and $\nu_{d,ab}$ prevent one from computing these scalar products analytically without approximation. On the other hand a numerical approach would be too costly. A solution consists in fitting the v dependence of $D_{d,ab}$ and $(\nu_{v,ab} - \nu_{d,ab})$ by suitable functions that enable an analytic computation of the scalar products. The following fits are made

$$\frac{D_{d,ab}}{v_{Ta}^2} = \frac{0.75\sqrt{\pi}}{\sqrt{x_a^2 + \frac{9\pi}{16}\left(\frac{v_{Ta}}{v_{Tb}}\right)^2}} \nu_{ab}^{HS} \tag{3.3.11}$$

$$\nu_{v,ab}\text{-}\nu_{d,ab} = -\frac{0.75\sqrt{\pi}}{\left(x_a^2 + 2.1\left(\frac{v_{Ta}}{v_{Tb}}\right)^2\right)^{3/2}} \nu_{ab}^{HS} \tag{3.3.12}$$

The fits are given respectively in Fig.3.2 and Fig.3.3 for the self collision case which is the most sensitive one. These fits have been obtained by building continuous functions matching the two asymptotic cases $\frac{v}{\sqrt{2}v_{Ta}} \ll 1$ and $\frac{v}{\sqrt{2}v_{Ta}} \gg 1$. The case $\frac{v}{\sqrt{2}v_{Ta}} \sim 1$ is therefore the most stringent test for the fits as one can notice in Fig.3.2 and Fig.3.3.

Figure 3.2.: Velocity dependence of $D_{d,ab}$ (solid line) and of its fit (dashed line) defined by Eq.(3.3.11)

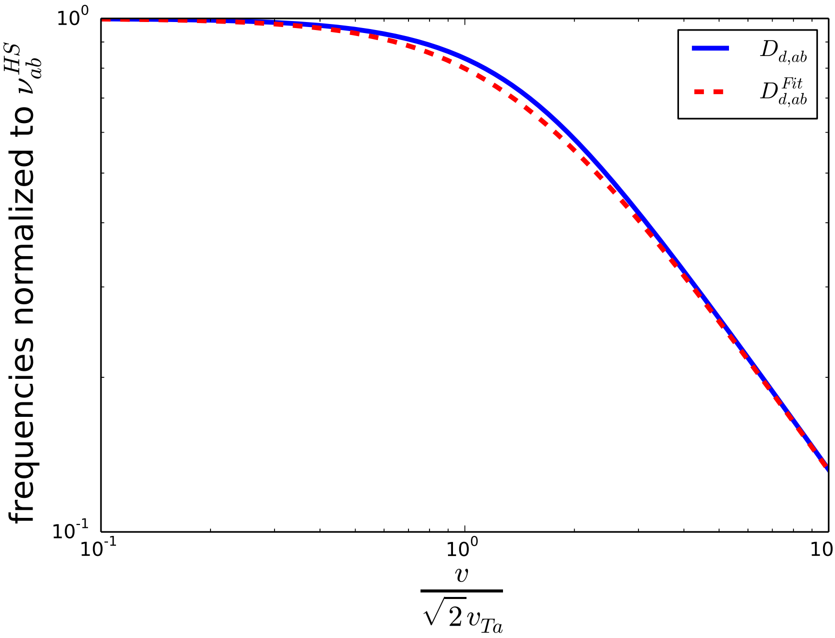

Figure 3.3.: Velocity dependence of $\nu_{v,ab} - \nu_{d,ab}$ (solid line) and of its fit (dashed line) defined by Eq.(3.3.12)

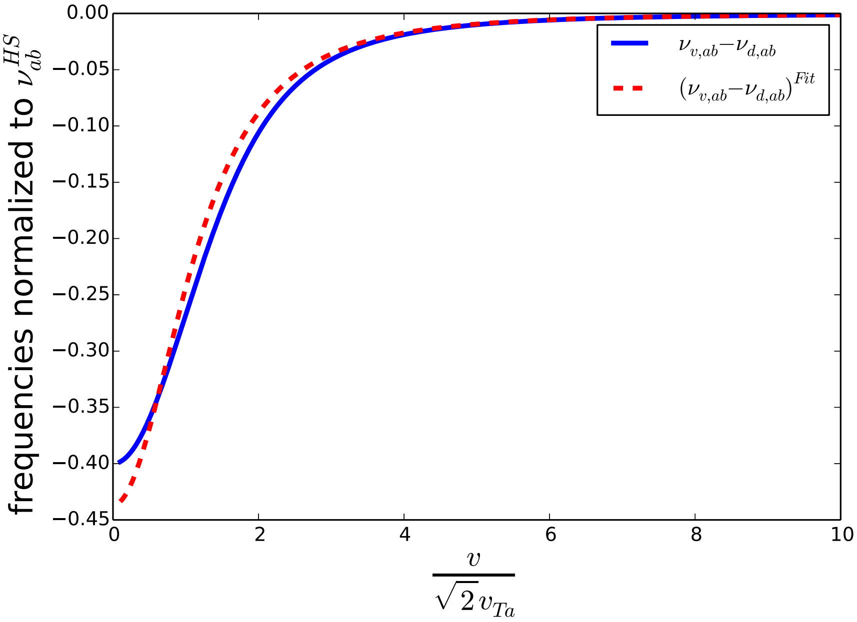

Thanks to these fits, the scalar products can be approximated by analytical expressions :

$$\begin{aligned} L_{i,ab}^{(0)} &= 0.75\sqrt{\pi}\nu_{ab}^{HS} I_i^{(0)} \left(\frac{v_\parallel^2}{2v_{Ta}^2} + \frac{9\pi}{16}\frac{v_{Tb}^2}{v_{Ta}^2} \right) \\ L_{i,ab}^{(2)} &= -0.75\sqrt{\pi}\nu_{ab}^{HS} I_i^{(1)} \left(\frac{v_\parallel^2}{2v_{Ta}^2} + 2.1\frac{v_{Tb}^2}{v_{Ta}^2} \right) \end{aligned}$$

With

$$\begin{aligned} I_i^{(n)}(x) &= \int_0^\infty du \frac{u^i e^{-u}}{(u+x)^{n+1/2}} \\ &= e^x \sum_{k=0}^{i} \begin{pmatrix} i \\ k \end{pmatrix} (-x)^{i-k} J_{k-n}(x) \end{aligned}$$

where $J_i(x) = \int_x^\infty du\, e^{-u} u^{i-1/2}$, can be easily computed by recurrence.

3.4. Numerical implementation

This section describes some numerical aspects associated with the implementation of the collision operator.

3.4.1. Numerical schemes

An explicit scheme is used to compute the evolution of the distribution function due to C^0_{ab} and $C_{\|ab}$. For stability reasons Eq.(3.3.9) is solved with a Crank-Nicholson scheme [21], detailed here: the problem can be written in a vectorized form:

$$\frac{\partial \boldsymbol{\alpha}}{\partial \hat{t}} = T\boldsymbol{\alpha} + \boldsymbol{S}$$

with

$$\boldsymbol{\alpha} = \begin{pmatrix} \vdots \\ \alpha_0^{(k)} \\ \alpha_1^{(k)} \\ \vdots \\ \alpha_{Npol-1}^{(k)} \\ \alpha_0^{(k+1)} \\ \vdots \end{pmatrix}$$

and $0 \leq k \leq k_{max}$,

$$T = \begin{pmatrix} B_0 & C_0 & 0 & 0 & 0 & 0 & 0 \\ A_1 & B_1 & C_1 & 0 & 0 & 0 & 0 \\ 0 & A_2 & B_2 & C_2 & 0 & 0 & 0 \\ 0 & 0 & . & . & . & 0 & 0 \\ 0 & 0 & 0 & . & . & . & 0 \\ 0 & 0 & 0 & 0 & . & . & C_{k_{max}-1} \\ 0 & 0 & 0 & 0 & 0 & A_{k_{max}} & B_{k_{max}} \end{pmatrix}$$

where N_{pol} is the number of Laguerre polynomials that are kept, k is the index associated with the $v_\|$ direction, and the A_k, B_k, C_k are square blocks of size N_{pol}. Their respective components are

$$\begin{cases} a_{lj}^{(k)} & = & -\frac{\hat{N}_{1,a}^{jl(k)}}{2\Delta v_\|} + \frac{\hat{N}_{2,a}^{jl(k)}}{\Delta v_\|^2} \\ b_{lj}^{(k)} & = & \hat{N}_{0,a}^{jl(k)} - 2\frac{\hat{N}_{2,a}^{jl(k)}}{\Delta v_\|^2} \\ c_{lj}^{(k)} & = & \frac{\hat{N}_{1,a}^{jl(k)}}{2\Delta v_\|} + \frac{\hat{N}_{2,a}^{jl(k)}}{\Delta v_\|^2} \end{cases}$$

and

$$\boldsymbol{S} = \begin{pmatrix} \vdots \\ S_0^{(k)} = \kappa_{0,a}^{(k)} \hat{N}_{0,a}^{jl} + \frac{\partial \kappa_{0,a}^{(k)}}{\partial \hat{v}_\parallel} \hat{N}_{1,a}^{jl} + \frac{\partial^2 \kappa_{0,a}^{(k)}}{\partial \hat{v}_\parallel^2} \hat{N}_{2,a}^{jl} \\ S_1^{(k)} = \kappa_{1,a}^{(k)} \hat{N}_{1,a}^{jl} + \frac{\partial \kappa_{1,a}^{(k)}}{\partial \hat{v}_\parallel} \hat{N}_{1,a}^{jl} + \frac{\partial^2 \kappa_{1,a}^{(k)}}{\partial \hat{v}_\parallel^2} \hat{N}_{2,a}^{jl} \\ S_2^{(k)} = 0 \\ \vdots \\ S_{Npol-1}^{(k)} = 0 \\ \vdots \end{pmatrix}$$

The Cranck Nicholson scheme is split in the following way

$$\begin{cases} \left(I - \frac{\Delta t}{4} T^n\right) \tilde{\boldsymbol{\alpha}} & = \left(I + \frac{\Delta t}{4} T^n\right) \boldsymbol{\alpha}^n \\ \tilde{\tilde{\boldsymbol{\alpha}}} & = \tilde{\boldsymbol{\alpha}} + \Delta t \boldsymbol{S}^n \\ \left(I - \frac{\Delta t}{4} T^n\right) \boldsymbol{\alpha}^{n+1} & = \left(I + \frac{\Delta t}{4} T^n\right) \tilde{\tilde{\boldsymbol{\alpha}}} \end{cases}$$

where n stands for the time index and I is the identity matrix. The scheme is split for stability reason. Indeed, the tridiagonal by blocks inversion problem can be solved thanks to a LU decomposition valid only if the left hand side matrix is diagonal dominant. This condition gives a limit on the time step for collision as the dominant off diagonal term is proportional to $\frac{\Delta t}{\Delta v_\parallel^2}$. Interestingly the splitting allows for a time step twice bigger than the one without splitting.

3.4.2. Numerical implementation of conservation properties

Due to numerical and physical ($B_\parallel^\star \simeq B$) approximations, conservation properties are not perfectly satisfied. We present here a method used to improve these conservation laws. It is used to correct only the C^1 part. Indeed the way C^0 is treated automatically satisfies conservation properties. All fluid quantities without indices correspond to the initial values. The ones noted with the prime correspond to values after the use of C^1. Finally the quantities with two primes are corrected values. The procedure is the following, in chronological order :

i)Density is corrected by simply applying an homothety on the distribution function

$$F'' = \frac{F'N}{N'}$$

ii) the parallel velocity and the temperature are then corrected simultanously by removing the Maxwellian after collisions F'_M and adding a new Maxwellian F''_M with the corrected moments defined as

$$\begin{cases} V''_{\|a} = & V_{\|a} + \Delta t \sum_b \frac{R_{\|ab}}{N_a m_a} \\ T''_a = & T_a \end{cases}$$

The corrected parallel velocity comes from the momentum evolution equation

$$N_a m_a \frac{\partial V_{\|a}}{\partial t} = \sum_b R_{\|ab}$$

where the exchange rate of momentum is given by Eq.(3.3.7). The temperature has to be kept constant $T'' = T$ to be consistent with the development made in section 3.3.2. Indeed, one can show that the exchange rate of energy due to C^1_{ab} is :

$$W^1_{ab} = W_{\|ab} + W_{v,ab} + W_{d,ab}$$

with $W_{\|ab}$ the work of the drag force

$$W_{\|ab} = V_{\|a} R_{\|ab}$$

and

$$W_{v,ab} + W_{d,ab} = \frac{3 T_a T_b n_a m_a \nu_{ab}}{m_a + m_b} \left(\frac{q_{ba}}{T_a} - \frac{q_{ab}}{T_b} \right) = 0 \text{ as } q_{ab} = 0$$

It follows that the energy evolution of species a due to the C^1 part is then given by

$$\frac{3}{2} n_a \left. \frac{\partial T_a}{\partial t} \right|_{C^1} + n_a m_a V_{\|a} \frac{\partial V_{\|a}}{\partial t} = \sum_b W^1_{ab} \Rightarrow \left. \frac{\partial T_a}{\partial t} \right|_{C^1} = 0$$

3.4.3. Choice of numerical parameters

The choice of the main numerical parameters used for the collision operator is detailed here. The first choice is the number of polynomials N_{pol} kept for the projection in the μ direction. For this choice, the most stringent test is to retrieve neoclassical prediction for the poloidal rotation presented in the section 4.3.1. The minimal number of polynomials to have the expected poloidal rotation is $N_{pol} = 3$. Once the number of polynomials is set, one has to choose the discretization in the μ direction. A necessary condition for the projection to work properly is to ensure the orthonormality of the polynomials and so to check the condition

$$\left\| \delta_{ij} - \int du e^{-u} P_i(u) P_j(u) \right\| \ll 1 \text{ for any i,j}$$

The optimal choice for the number of points in the μ direction has been found to be $N_\mu = 64$ and the optimal value for the upper limit in the μ direction is $\mu_{max} \simeq \frac{16T}{B}$. The number of points in the $v_\|$ direction is less critical in terms of numerical cost. 128 points reveal sufficient for the collision operator.

The last point is to choose the collisional time step Δt_{coll}. Indeed in order to save computational resources, the collision operator can be used on a different time scale compared with the rest of the code GYSELA. Of course, the collisional time step Δt_{coll} has to scale with $(\max\ (\nu_s^\star))^{-1}$where $\nu_s^\star$ is the collisionality of the s species . In practice, a collisional time step $\Delta t_{coll} \simeq 2 \cdot 10^{-2} {\nu_{ii}}^{-1}$ is sufficient to recover the main results of neoclassical theory. In the case of developed turbulence, the collisional time step should be reduced compared with a pure neoclassical case to properly take into account the effect of collisions on turbulence. An upper limit for the collisional time step $\Delta t_{coll} \leq 10 \Delta t_{GYS}$ is suggested. This limit already allows reducing drastically the numerical cost of collisions.

3.5. Verification of the collision operator

To validate the collision operator, a first step is to perform conservation and relaxation tests by solving collisions only, i.e. without the effects of trajectories

$$\frac{\partial f_a}{\partial t} = \sum_b C_{ab}$$

In this section critical physical properties of the collision operator are tested : conservation properties, relaxation toward the Maxwellian and its dynamics and the exchange rates of momentum and energy between species. All the results shown here are obtained with a discretization of $(N_{v_\parallel}, N_\mu) = (128, 64)$ which is the optimal discretization for this operator. For these simulations, the collisionality of the main species is $\nu_\star = 1$. For the single species cases, the time step in GYSELA is $\Delta t = 100 \omega_{ci}$. For the multispecies cases performed with deuterium as first species and tungsten as second species, the time step is reduced to take into account that the collisionality of the impurity is higher than the one of the main species. These tests are performed without gyroaverage to be consistent with the fact that FLR effects are not included in the present version of the collision operator.

3.5.1. Single species tests

Collisions should conserve particles $N = \int F d^3v$, parallel momentum $p_\parallel = \int m v_\parallel F d^3v$ and kinetic energy $E_k = \int \frac{1}{2} m v^2 F d^3v$. Conservation laws are tested by initializing a Maxwellian that belongs to the kernel of the operator and should therefore remain constant in time. After approximately one collision time, the following conservations are observed for an initial mach number $M_\parallel = 0$:

$$\frac{\Delta N}{N} \simeq 7 \cdot 10^{-7} \qquad \Delta p_\parallel \simeq 10^{-9} \qquad \frac{\Delta E_k}{E_k} \simeq 6 \cdot 10^{-6}$$

For an initial Mach number of $M_{\|} = 1$ comparable conservation properties are found. The mismatches are much smaller than the ones (of the order of few percents) obtained when running the entire code in the turbulent regime [38]. This means that the collision operator can be used for Mach numbers $M_{\|} \leq 1$ without any breakdown of its conservation properties.

Relaxation toward the Maxwellian has been tested by initializing two different distribution functions. For the parallel direction, the initial distribution function is chosen as

$$F_a = F_{M0a}\left(1 + \frac{m_a v_{\|}^2}{2T_a}\right)$$

For the perpendicular direction, the initial distribution function is

$$F_a = F_{M0a}\left(1 + \frac{m_a v_{\perp}^2}{2T_a}\right)$$

The results are shown on Fig.3.4 . As expected, a relaxation toward the Maxwellian is observed in both cases after a few collision times.

Figure 3.4.: Initial (top) and final (bottom) slices of the distribution function in velocity space are given. The initial distribution function is far from a Maxwellian in the $v_\perp$ direction on the left and in the $v_\|$ direction on the right. In both cases, the converged state is an isotropic Maxwellian.

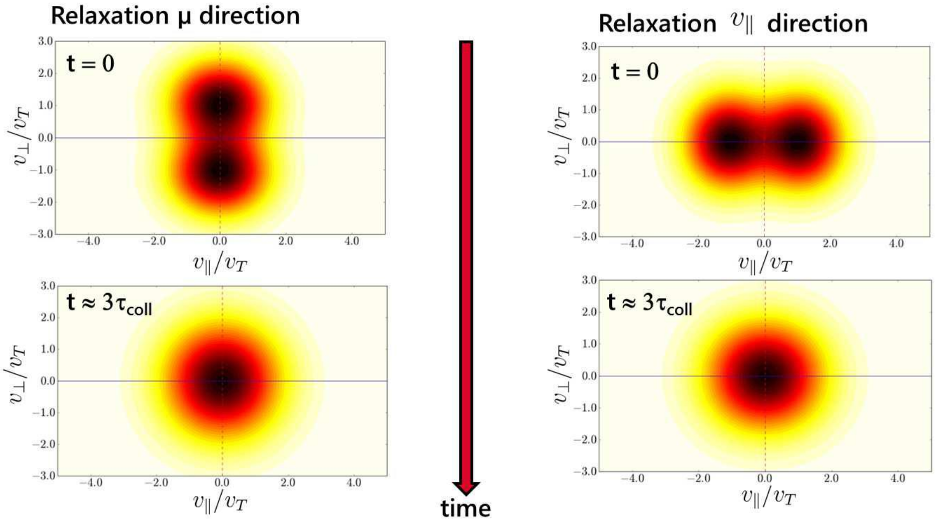

To investigate the dynamical relaxation to the Maxwellian, a case with $T_\| \neq T_\perp$ and $\frac{T_\| - T_\perp}{T_a} \ll 1$ is launched

$$F_a = N_a\left(\frac{m_a}{2\pi T_{\|a}}\right)^{1/2}\frac{m_a}{2\pi T_{\perp a}}\exp\left(-\frac{m_a v_\|^2}{2T_{\|a}} - \frac{m_a v_\perp^2}{2T_{\perp a}}\right)$$

where $T_a = \frac{T_{\parallel a}+2T_{\perp a}}{3}$. Then at first order in $\frac{T_\parallel - T_\perp}{T_a} \ll 1$

$$f_a = 1 + \frac{T_{\parallel a} - T_{\perp a}}{3T_a}\frac{1}{v_{Ta}^2}\left(v_\parallel^2 - \frac{v_\perp^2}{2}\right)$$

Integrating $\partial_t f_a$, weighted by the energy, over the velocity space leads to :

$$\frac{d\ln\left(T_\parallel - T_\perp\right)}{dt} = \frac{16}{15\sqrt{\pi}}\int_0^\infty dx e^{-x^2} x^6 \left(\nu_v + \frac{3}{2}\nu_d\right)$$

This integral can be computed either with the actual expressions of ν_v and ν_d or their approximate values :

$$\begin{cases} \frac{d\ln\left(T_\parallel - T_\perp\right)}{dt} & = -0.80\nu_{aa} \text{ for actual expressions} \\ \frac{d\ln\left(T_\parallel - T_\perp\right)}{dt} & = -0.78\nu_{aa} \text{ for fitted values} \end{cases}$$

The discrepancy is small, thus justifying the fits represented in Fig.3.2 and Fig.3.3. The prediction for the actual expressions of ν_v and ν_d is used as a theoretical prediction and compared with GYSELA results in Fig.3.5. A mismatch of 15% percent is found. This discrepancy is acceptable as most of physics processes studied with gyrokinetic codes are independent of the isotropisation rate.

Figure 3.5.: Top : Time evolution of the perpendicular $T_\perp$ (red), the parallel temperature $T_\parallel$ (green), and the total temperature $T_{tot} = \frac{2T_\perp + T_\parallel}{3}$ (blue). Bottom : Time evolution of the logarithmic difference of temperatures. The slope of the curve gives the relaxation rate.

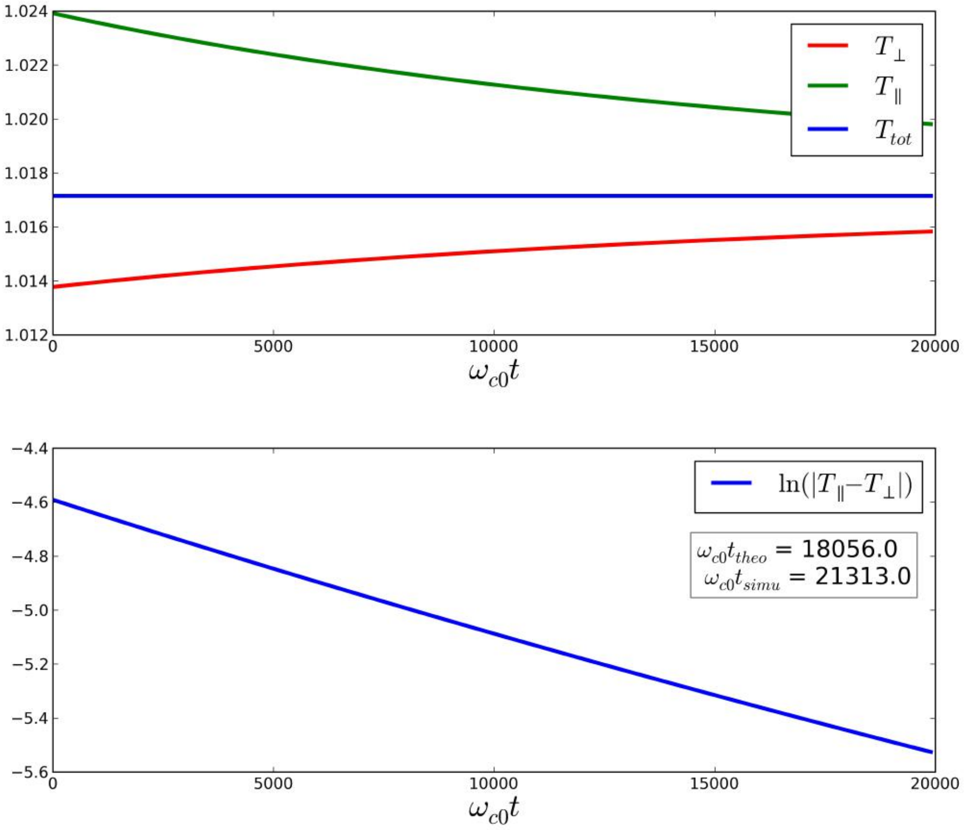

3.5.2. Test with two species

The exchange rates of parallel momentum and energy between two Maxwellians are respectively

$$\begin{aligned} R_{\parallel,Mab} &= -N_a m_a \nu_{ab} \left(V_{\parallel a} - V_{\parallel b} \right) \\ Q_{M,ab} &= -3 \frac{N_a m_a}{m_a + m_b} \nu_{ab} \left(T_a - T_b \right) \end{aligned}$$

It is then easy to show that

$$\begin{aligned}\frac{d\ln\left(V_{\|a}-V_{\|b}\right)}{dt} &= -\left(\nu_{ab}+\nu_{ba}\right)\\ \frac{d\ln\left(T_a-T_b\right)}{dt} &= -2\frac{m_a\nu_{ab}+m_b\nu_{ba}}{m_a+m_b}\end{aligned}$$

These two relations have been checked. The results for the velocities are shown in Fig.3.6 and for temperature in Fig.3.7. The agreement regarding relaxation rates is within one percent. Notice that, in each case, the time evolution is governed by the impurity. This is a direct consequence of the trace impurity limit which is considered here, implying a negligible impact on the main species.

Figure 3.6.: Left : Time evolution of the parallel velocity of the main species $V_{\|,0}$ (red), and of a trace impurity $V_{\|,1}$ (blue). Right : Time evolution of the logarithmic difference of parallel velocities. The slope of the curve gives the momentum exchange rate.

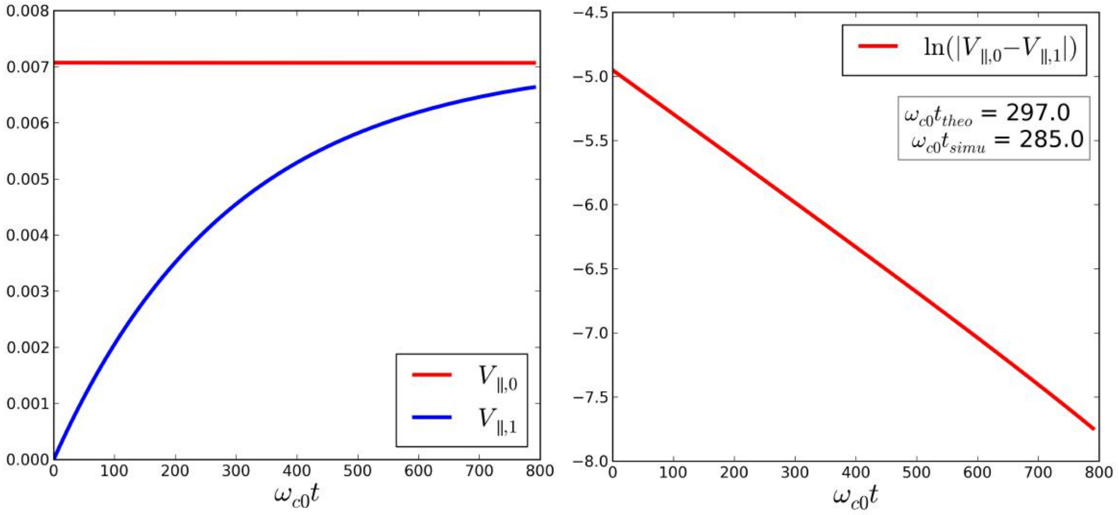

Figure 3.7.: Left : Time evolution of the temperature of the main species T_0 (red), and of a trace impurity T_1 (blue). Right : Time evolution of the logarithmic difference of temperatures. The slope of the curve gives the thermal energy exchange rate.

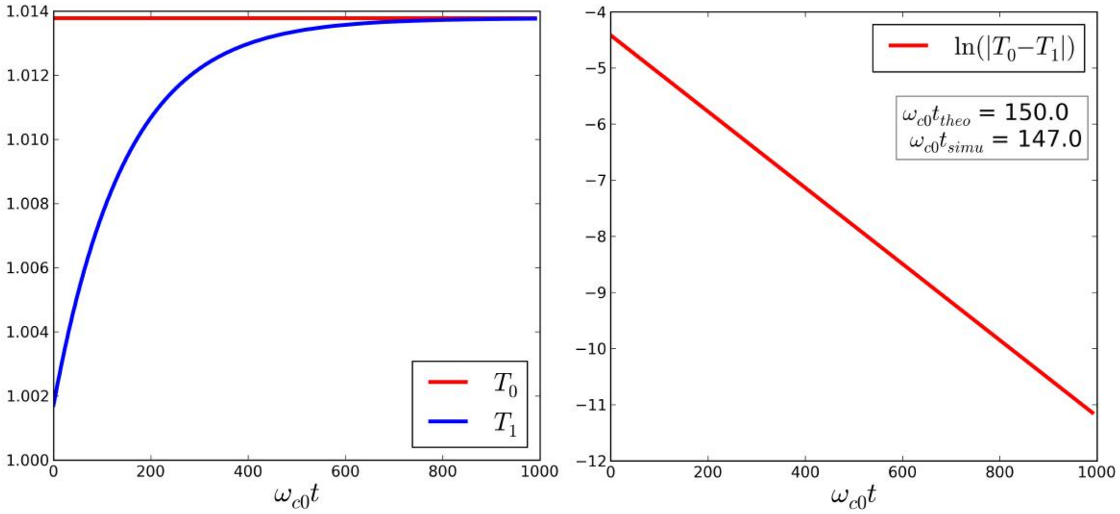

4. Standard neoclassical physics

Contents

3.1. Introduction **55**

3.2. Presentation of the model **56**

3.3. Analytical approximations for an optimized numerical treatment of the collision operator **59**

3.3.1. Separation of the different collision terms 60

3.3.2. Evolution of thermal energy 60

3.3.3. Approximation of the distribution function 61

3.3.4. Treatment of the μ derivatives 64

3.3.5. Evolution equation of the distribution function components 65

3.4. Numerical implementation **70**

3.4.1. Numerical schemes 70

3.4.2. Numerical implementation of conservation properties . . 71

3.4.3. Choice of numerical parameters 72

3.5. Verification of the collision operator **73**

3.5.1. Single species tests 73

3.5.2. Test with two species 76

4.1. Introduction

As mentionned in the part 1.3.4, neoclassical physics is one of the three mechanisms that lead to transport. Physically, it represents the effect of collisions on particle trajectories. In conventional neoclassical theory, it is assumed that the system is axisymmetric and in steady state. In addition, the poloidal asymmetry of the magnetic field plays a key role. This poloidal asymmetry comes from the dependence of the toroidal magnetic field with the major radius $B_\varphi = B_{\varphi,0}\frac{R_0}{R}$. This is why neoclassical theory scales with the $\epsilon = \frac{r}{R_0}$ parameter. Other poloidal asymmetries coming from the plasma are weak but non zero. A generalization of the conventional neoclassical theory by removing one or more of these assumptions is often needed. For instance, the effect of ripple can be tackled by removing the axisymmetric assumption [34]. Concerning the transport of impurities, poloidal asymmetries of the impurity density are often observed experimentally[54]. These poloidal asymmetries are large compared with those predicted by the neoclassical theory and are often associated with the presence of external heating sources like NBI [16] or ICRH [74, 60]. Poloidal asymmetries lead to significant modifications of the neoclassical theory [32, 43, 4]. These effects will be addressed in chapter 6. In the current chapter, we restrict ourselves to the framework of conventional neoclassical theory. The goal is to give some insight into the neoclassical physics while avoiding too heavy calculation. Moreover, this approach allows a verification of the collision operator described in chapter 3.

This chapter starts with a qualitative description of the conventional neoclassical physics allowing the introduction of the three neoclassical regimes. Then some predictions for the single species case are given and compared with GYSELA results. Finally, the neoclassical prediction of impurity flux in the trace limit and neglecting poloidal asymmetries of the impurity is derived. This prediction is compared with GYSELA simulations.

4.2. Physical description of neoclassical theory

Neoclassical physics is the effect of collisions on particle trajectories with finite orbit width. Let us consider an axisymmetric case and assume a steady state situation. It is reminded that in absence of collisions and electromagnetic field evolution, the motion of particles is integrable as mentionned in the section 1.3.3. There are two classes of particles, some are passing and others trapped. When collisions are added, this simple vision is somewhat modified. Indeed, at leading order collisions are equivalent to a diffusion in the velocity space. Therefore, a particle can pass from the trapped to the passing domain (and *vice-versa*) as shown in Fig. 4.1.

Figure 4.1.: Trajectory of a particle (red) in the phase space $\left(\theta, v_{\parallel}\right)$ in presence of collisions. The jumps in the $v_{\parallel}$ direction represent the effect of the diffusion in the velocity due to collisions. Due to this diffusion, a particle can cross the frontier between the trapping and passing domains (green) and change its nature.

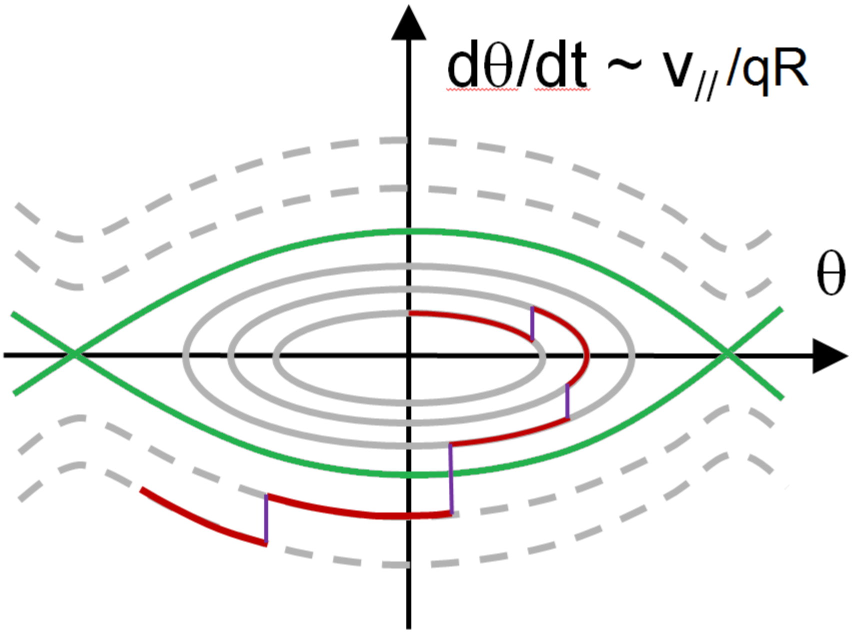

The neoclassical theory predicts a diffusive transport of particles. The neoclassical diffusion coefficient is the sum of two contributions

$$D_{neo} = D_{BP} + D_{PS}$$

- The first one comes from a collisional layer in the phase space near the trapped/passing boundary and is called banana-plateau D_{BP}. As mentionned above, a particle can pass from the trapped to the passing domain due to collisions. The detrapping frequency due to collisions is given by $\nu_{detrap} = \frac{\nu}{\epsilon}$. Trapped particles explore a much larger region than passing ones in the radial direction: their distance with respect to their reference magnetic surface reaches δ_b, which is of the order of $\delta_b \approx 10\rho_c$ for typical plasma parameters. δ_b is the characteristic radial step of trapped particles per collision in the low collisionality regime (banana). As the trapped fraction of particles is given by $f_t \simeq \sqrt{\epsilon}$, the diffusion coefficient associated with collisional detrapping is roughly given by $f_t \nu_{detrap} \delta_b^2 \sim \frac{q^2}{\epsilon^{3/2}} \nu \rho^2$. This expression is valid only if $\nu_{detrap} \leq \omega_b$. Indeed if $\omega_b \leq \nu_{detrap}$, trapped particles do not have the time to experience a full 'banana' orbit before being untrapped by collisions. Therefore the banana-plateau diffusion saturates when $\omega_b \sim \nu_{detrap}$ and is even a decreasing function of the collision frequency for large collisionalities $1 \ll \nu_\star$ where the collisionality has been introduced $\nu_\star = \frac{\nu_{detrap}}{\omega_b}$. Finally, the banana-plateau diffusion takes the form $D_{BP} \sim \frac{q^2}{\epsilon^{3/2}}\nu\rho^2\frac{1}{(1+C_1\nu_\star)\left(1+C_2\epsilon^{3/2}\nu_\star\right)}$ with $C_1, C_2 \sim 1$. This expression allows one to retrieve the two usual limit expressions: for low collisionality $\nu_\star \leq 1$, the diffusion coefficient takes the form $D_{BP} \sim \frac{q^2}{\epsilon^{3/2}}\nu\rho^2$. For intermediate collisionality $1 \leq \nu_\star \leq \epsilon^{-3/2}$, the diffusion coefficient takes the form $D_{BP} \sim \frac{q^2}{\epsilon^{3/2}}\frac{\nu}{\nu_\star}\rho^2 \sim \frac{v_T}{R_0}q\rho^2$.

- The second contribution to the neoclassical transport is associated to passing particles and called Pfirsch-Schlüter D_{PS}. The reasoning for the Pfirsch-Schlüter is the following : the radial diffusion is due to the curvature drift v_D. Therefore, due to collisions there are jumps in the radial direction over a typical length $\Delta r \sim v_D \Delta t \sim \frac{\rho v_T}{R_0}\Delta t$. It is clear from the Fig.4.2 that if the drift is upward, a radial jump on the top of the tokamak leads to an outward flux whereas a radial jump on the bottom of the tokamak leads to an inward flux. Therefore the typical time Δt corresponds to the time for a particle to pass from the top to the bottom. As the parallel motion is interrupted by collisions, it is also a diffusive process with a diffusion coefficient $D_\parallel \sim \frac{v_T^2}{\nu}$. Therefore, the time for a particle to pass from the top to the bottom is given by $\Delta t \sim \frac{(qR_0)^2}{D_\parallel} \sim \nu\left(\frac{qR_0}{v_T}\right)^2$. Finally, the Pfirsch-Schlüter diffusion coefficient is given by $D_{PS} \sim \frac{(\Delta r)^2}{\Delta t} \sim \nu\left(q\rho\right)^2$.

Figure 4.2.: Pfisrch-Schlüter diffusion. On the top, collisions lead to an outward flux. On the bottom collisions lead to an inward flux.

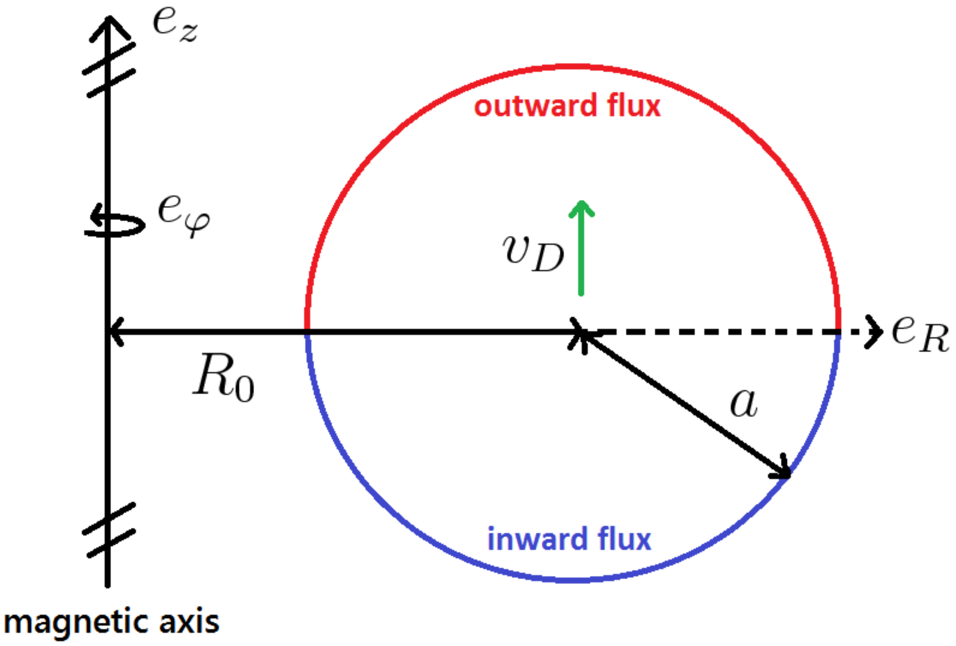

The neoclassical diffusion can be compared with the classical prediction coming from the effect of collisions on the gyromotion and simply given by $D_{cl} = \nu\rho^2$. The comparison is shown in Fig.4.3. This curve allows one to distinguish the definiton of the three colisionality regimes: The banana regime for low collisionalities ($\nu_\star \leq 1$), the plateau regime for intermediate collisionalities ($1 \leq \nu_\star \leq \epsilon^{-3/2}$) and finally the Pfirsch-Schlüter regime for large collisionlities ($\epsilon^{-3/2} \leq \nu_\star$).

In the next sections, the results coming from GYSELA simulations in the abscence of turbulence are compared with neoclassical predictions. These tests are performed for the verification of the collision operator described in chapter 3.

Figure 4.3.: Comparison between the classical prediction (blue), the banana-pateau contribution (red) and the Pfirsch-Schlüter contribution (green)

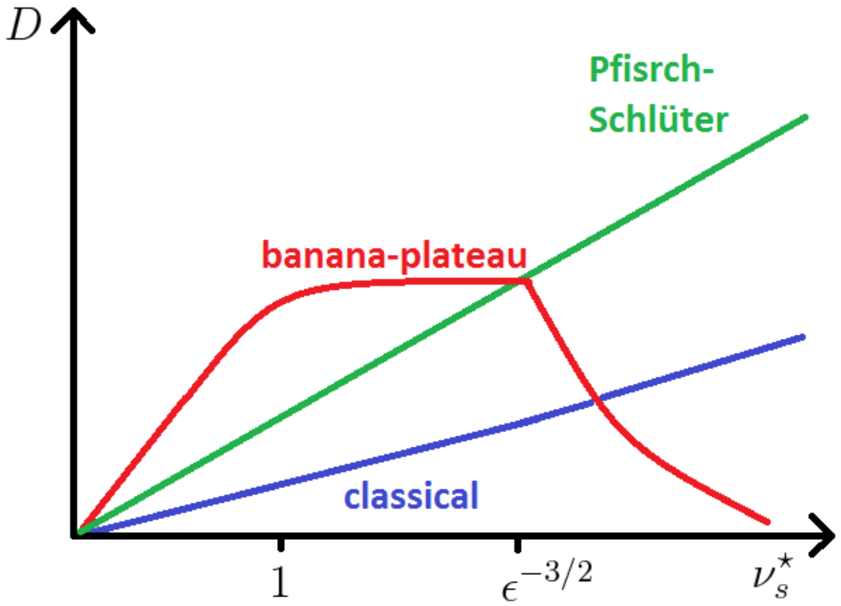

4.3. Neoclassical test of the collision operator : single species case

Satisfying the intrinsic properties of the collision operator, as reported in the section 3.5, is mandatory but relatively easy. A more challenging test is provided by neoclassical theory. For the single species case, the poloidal rotation and heat diffusion coefficient can be compared with theoretical predictions in a pure axisymmetric case, i.e. not allowing any helical instability. These tests allow one to assess different parts of the collision operator depending on the collisionality regime and are useful as their results are sensitive to the details of the collision operator. Before starting, one should notice that neoclassical physics is by nature local. Therefore, for an effective verification of the code, one should ensure for each neoclassical simulation a scale separation between the gradients lengths of the background quantities and the banana width : $\delta_b \ll L_N, L_T$ where L_N and L_T are respectively, the gradient lengths of density and temperature.

4.3.1. Neoclassical diffusion and poloidal rotation

The neoclassical theory is tested by filtering out non axisymmetric ($n \neq 0$, where n is the toroidal mode number) components of the electrical potential. This filtering prevents the onset of turbulence. Four simulations are performed with a scan in $\nu_\star$ going from 10^{-2} to 10. The phase space grid used for these simulations is $\left(r, \theta, \varphi, v_\parallel, \mu\right) = (256, 256, 32, 128, 64)$. The dimension of the tokamak that is simulated is fixed by $\rho_\star = \frac{\rho_i}{a} = \frac{1}{150}$. The results from GYSELA are taken at mid-radius where the inverse aspect ratio $\epsilon = 0.15$ and the safety factor is $q =$1.6. The local gradients are given by $\frac{R_0}{L_T} \simeq 6$ and $\frac{R_0}{L_n} \simeq 0$ where R_0 is the major radius. The collisional time step depends on $\nu_\star$ and the numerical time step is adapted consistently to keep the same temporal resolution of collisions. In the single species neoclassical theory, two quantities are of utmost importance : the poloidal rotation and heat diffusivity. These two quantities are compared with neoclassical predictions.

In neoclassical theory, the poloidal velocity is tied to the thermal gradient via the relation $v_\theta = k_{neo}\left(\nu_\star, \epsilon\right) \frac{\nabla T}{eB}$. Theoretical predictions of k_{neo} are accurate in the asymptotic banana and Pfirsch-Schlüter regimes and approximate in the plateau regime. The sign of the poloidal velocity depends on the collisionality regime : rotation in the ion diamagnetic direction ($k_{neo} > 0$) is expected in the banana regime and the opposite ($k_{neo} < 0$) in the Pfirsch-Schlüter regime. The transition is expected to take place in the plateau regime. A model inspired by Hirshman and Sigmar is given by [61] and predicts k_{neo} in all collisionality regimes including corrections due to finite aspect ratio ϵ. This theoretical prediction is used to benchmark GYSELA's operator. The results are shown in Fig.4.4. The shape of the curve is the same and the inversion of sign takes place in the plateau regime as expected by theory. The agreement is better for the banana regime where the theoretical prediction is more accurate.

Another important quantity predicted by neoclassical theory is the thermal diffusion coefficient χ_{neo}. Even if neoclassical transport is subdominant as compared to the turbulent one for the main species, it can be important for heavy impurities like tungsten and for the main species close to transport barriers where turbulent transport is reduced. To check their validity, GYSELA results are compared with the Chang-Hinton prediction [17] valid in all collisionality regimes . The results are shown in Fig.4.5. Again a satisfactory agreement with analytical prediction is found.

Figure 4.4.: $k_{neo} = eB\frac{v_\theta}{\nabla T}$ versus $\nu_\star$ predicted by theory (dashed line) compared with GYSELA results (red dots)

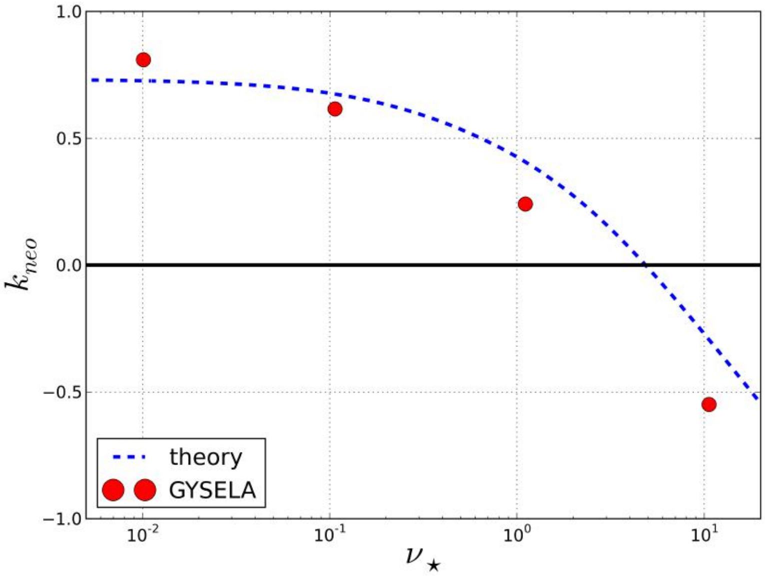

Figure 4.5.: $\chi_{neo} = -\frac{Q}{N\nabla T}$ versus $\nu_\star$ predicted by theory (dashed line) compared with GYSELA results (red dots)

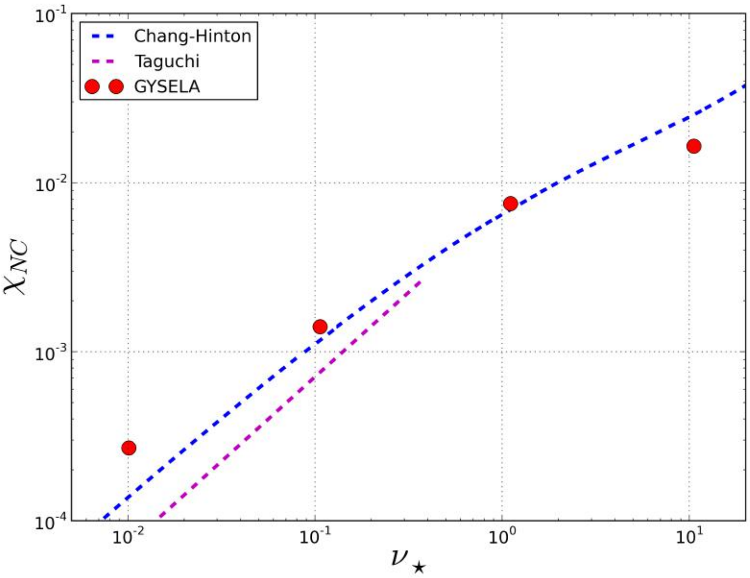

4.3.2. Zonal flow damping

Zonal flows are known to control the level of turbulence by energy transfer from low to high wavenumbers [22]. The only linear damping mechanism for these flows comes from collisional friction. It is then critical to get the correct damping rate of zonal flows to predict the right level of turbulence.

Collisionless plasmas are known to exhibit linearly undamped axisymmetric potential ϕ_{00} although the amplitude of this mode may evolve due to plasma polarization [77]. There is therefore a residual axisymmetric potential ϕ_{00} in the collisionless limit. The level of this residual flow is given by

$$\frac{\phi_{00}(t\rightarrow\infty)}{\phi_{00}(t=0)}=\frac{1}{\alpha}\text{ in the collisionless limit} \qquad (4.3.1)$$

where $\alpha=1+1.6\frac{q^2}{\sqrt{\epsilon}}$. Hinton and Rosenbluth [45] have predicted the collisional damping of this residual flow.

$$\begin{aligned}\frac{\phi_{00}(t')}{\phi_{00}(t'=0)} &= \text{exp}\left(\frac{\beta^2}{\alpha^2}t'\right)\text{erfc}\left(\frac{\beta}{\alpha}\sqrt{t'}\right)\\ &+ \text{erf}\left(\nu_0 t'\right)\alpha\frac{B_\theta^2}{B^2}\left[\begin{array}{c}1.8\left(\nu_0 t'\right)^{5/9}\text{exp}\left(-\left(3\nu_0 t'\right)^{2/3}\right)\\ +1+\frac{1.4}{\epsilon}\text{exp}\left(-\nu_d t'\right)\end{array}\right] \qquad (4.3.2)\end{aligned}$$

with $\beta=\frac{3\pi q^2\bar{\nu}^{1/2}}{\epsilon\Lambda^{3/2}}$, $\Lambda=\lambda\ln\left(16\left(\frac{\epsilon}{\bar{\nu}t}\right)^{1/2}\right)$ with $\lambda\simeq 1$ and some frequencies associated with collisions are defined as $\bar{\nu}=0.61\nu_{ii}$, $\nu_0=1.9\nu_{ii}$, $\nu_d=\frac{\nu_{ii}}{0.64\sqrt{\epsilon}}$. Note that the initial time in Eq.4.3.2 $(t'=0)$ corresponds to the case where all GAM oscillations have been Landau damped and therefore corresponds to the limit $(t\rightarrow\infty)$ of Eq.4.3.1. Details on GAM oscillation and damping can be found in the literature [91, 79]. The first term of Eq.4.3.2 corresponds to the fast collisional smoothing of the distribution function in the trapping boundary layer. The last term is the contribution from high-energy ions which have small collision frequencies and thus dominate the long time behaviour. An extra term erf$\left(\nu_0 t\right)$ has been added in front of the last term of the right hand side to ensure the relation also holds for the initial time.

The collisional damping of the residual can be tested by first launching a collisionless simulation, waiting for GAM decay and then adding collisions. The discretization of the simulation is $\left(r,\theta,\varphi,v_\parallel,\mu\right)=(127,64,8,255,64)$. Flat profiles of density and temperature have been chosen to avoid the radial dependence of the collision frequencies. For the same reason, the profile of the safety factor $q=1.4$ is flat. The other parameters of the simulation are $\rho_\star=\frac{1}{160}$, $\epsilon=0.1$ at mid radius. A good agreement is found between predicted and computed ϕ_{00} decay once collisions are activated as can be seen in Fig.4.6. To have a better match, the value of λ has been adjusted ($\lambda = 1.04$). Note that in the comparison between theory and simulation, GAMs are not fully damped in the simulation. This is the reason of the oscillations observed in Fig.4.6.

The previous bunch of tests provides a successful verification of the intraspecies collisions. In the next section, the conventional neoclassical predictions regarding the transport of heavy impurity is derived analytically and then compared with GYSELA results. These tests allow a verification of the interspecies collisions.

Figure 4.6.: Time evolution of the normalized ϕ_{00} coming from the code GYSELA (red) compared with the theoretical prediction (blue).

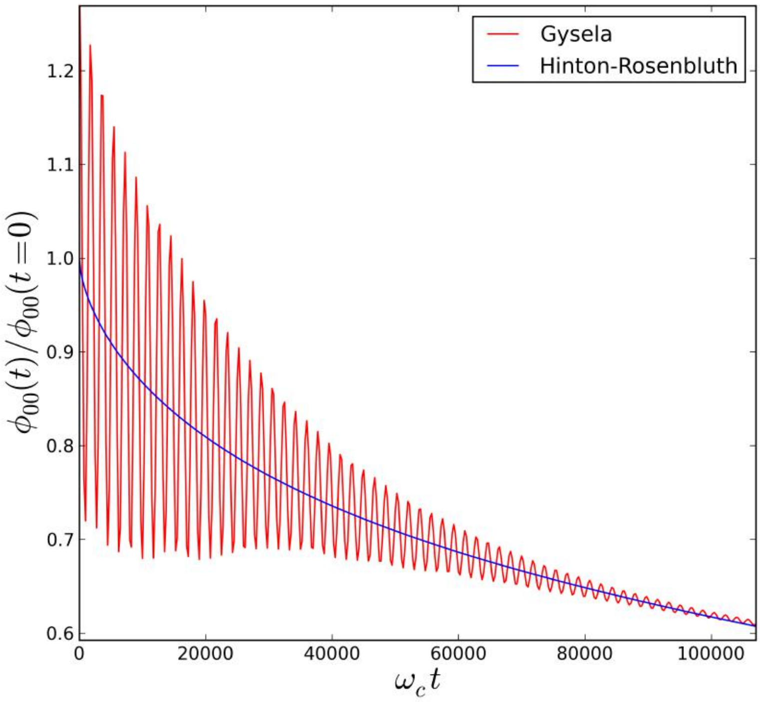

4.4. Neoclassical test of the collision operator : trace impurity

As mentionned in the section 1.4, heavy impurities are not fully ionized even in the core of a tokamak. Therefore, they lead to an important radiative power loss even at low concentration. Neoclassical transport is expected to be dominant for heavy impurities. Furthermore, the divertor of ITER will be in tungsten. In this context, it is natural to test the neoclassical transport of a trace ($\alpha = \frac{N_z Z_z^2}{N_i Z_i^2} \ll 1$) heavy impurity like tungsten. As a starting point, the conventional neoclassical prediction of a trace impurity in the Pfirsch-Schlüter regime is derived. It is then compared with the results of simulations performed with the code GYSELA.

4.4.1. Neoclassical prediction

A derivation of the theoretical prediction for trace impurity transport in the Pfirsch-Schlüter regime can be found in [47]. The main steps for this derivation are the following: first the particle flux is linked to the collisional exchange of momentum via the toroidal momentum conservation. Second, the parallel flows of particle and heat are linked to the gradients. Finally, the parallel flows are linked to the perpendicular ones using conservation of particles and energy respectively. This procedure allows one to write explicitely the dependance of the impurity particle flux with respect to the gradients.

4.4.1.1. Link between neoclassical impurity flux and collisional exchange of momentum

The starting point is to link the radial flux of particles to the collisional friction force. The easiest way to do it is to use the toroidal momentum conservation equation for each species s [78, 2, 52]

$$\partial_t L_{\varphi,s} = Ze\left(\Gamma_s^{\psi} - \Gamma_{E,s}^{\psi}\right) - \partial_\psi \Pi_{\varphi,s}^{\psi} + \left\langle \frac{I}{B} R_{\parallel,s} \right\rangle_{\psi} \tag{4.4.1}$$

with the toroidal momentum $L_{\varphi,s}$, the particle flux Γ_s^{ψ}, the turbulent flux $\Gamma_{E,s}^{\psi}$ and the Reynolds stress $\Pi_{\varphi,s}^{\psi}$ respectively defined as

$$\begin{aligned} L_{\varphi,s} &= m_s \int d\tau u_\varphi F_s \\ \Gamma_s^{\psi} &= \int d\tau F_s v^{\psi} = \left\langle \mathbf{\Gamma}_{\perp,s} \cdot \nabla\psi \right\rangle_{\psi} \\ \Gamma_{E,s}^{\psi} &= \int d\tau F_s \partial_\varphi \bar{\phi} \\ \Pi_{\varphi,s}^{\psi} &= m_s \left\langle \int d^3\boldsymbol{v} u_\varphi v^{\psi} F_s \right\rangle \end{aligned}$$

Where $u_\varphi = \frac{I}{B} v_\parallel$, $v^{\psi} = (\boldsymbol{v}_{E\times B} + \boldsymbol{v}_{D,s}) \cdot \nabla\psi$ and $\bar{\phi}$ is the gyro-averaged electric potential. Here $d\tau = d^3\boldsymbol{v}\frac{d\theta d\varphi}{B\cdot\nabla\theta}$ is the phase space volume element in between two magnetic surfaces ψ and $\psi{+}d\psi$ and $\langle ... \rangle_{\psi}$ indicates the flux surface average. $R_{\parallel,s}$ is the total collisional drag force applied on the species s $R_{\parallel,s} = \sum_{s'} R_{\parallel,ss'}$. Neoclassical theory is done assuming a steady state and no toroidal dependence. Furthermore, the Reynolds stress $\Pi_{\varphi,s}^{\psi}$ is often neglected. Therefore, the relationship Eq.(4.4.1) allows one to express the neoclassical impurity flux coming from the collisional exchange of parallel momentum between species as

$$\Gamma^{\psi}_{s,neo} = -\frac{1}{Ze}\left\langle \frac{I}{B} R_{\parallel,s} \right\rangle \tag{4.4.2}$$

The collisional exchange of parallel momentum is linked to the parallel velocity $V_{\parallel s}$ and the parallel heat flux $q_{\parallel s}$ via the equation [27]

$$R_{\parallel ab} = -N_a m_a \nu_{ab}\left[V_{\parallel a} - V_{\parallel b} - \frac{3}{5}\frac{q_{\parallel a}}{n_a T_a}\left(\frac{1}{1+x_{ab}^2}\right) + \frac{3}{5}\frac{q_{\parallel b}}{n_b T_b}\left(\frac{1}{1+x_{ba}^2}\right)\right] \tag{4.4.3}$$

4.4.1.2. Structure of perpendicular flows

To compute the parallel quantities required for the solving of Eq.(4.4.3), one needs to express first perpendicular quantities. To do so, the idea is to derive a *vectorial* expressions of particle and heat fluxes. This is not obvious because of the *scalar* form of the gyrokinetic equation, i.e.

$$\partial_t \bar{F} + \frac{1}{B^*_{\parallel}} \nabla_{\mathbf{z}} \cdot \left(\dot{\mathbf{z}} B^*_{\parallel} \bar{F} \right) = C\left(\bar{F}\right) \tag{4.4.4}$$

It must be kept in mind that the actual trajectories of particles differ from those of gyrocenters by a cyclotron motion. We consider the limit of large scale flows, which is well described by the drift kinetic limit $k_{\perp}\rho_s \rightarrow 0$ of the gyrokinetic equation Eq.(4.4.4). At first order in ρ_* the particle velocity is of the form $\mathbf{v} = v_{\parallel}\mathbf{b} + \mathbf{v}_E + \mathbf{v}_D$, where $\mathbf{b} = \frac{\mathbf{B}}{B}$, $\mathbf{v}_E$ is the $E \times B$ drift velocity and $\mathbf{v}_D$ is the sum of curvature and ∇B drift velocities. Taking the first moment of Eq.(4.4.4), one gets $\nabla \cdot \mathbf{\Gamma} = 0$ in steady-state, where $\mathbf{\Gamma} = \Gamma_{\parallel}\mathbf{b} + \mathbf{\Gamma}_{\perp}$. Note however that this is a flux of *guiding centers*. One needs the particle flux. This is done by adding the magnetization flux, whose divergence is zero and does not change the conservative form $\nabla \cdot \mathbf{\Gamma} = 0$. Hence

$$\mathbf{\Gamma}_{\perp} = N\mathbf{V}_E + N\left\langle \mathbf{v}_D \right\rangle - \nabla \times \left[N \left\langle \frac{\mu}{Ze}\mathbf{b} \right\rangle_v \right] \tag{4.4.5}$$

where the bracket is an average over the distribution function.

$$\left\langle \ldots \right\rangle_v = \frac{1}{N}\int d^3\mathbf{v}\bar{F}\ldots$$

The perpendicular flow associated with the curvature drift plus magnetization term is

$$\mathbf{\Gamma}^{D}_{\perp} = \left(P_{\parallel} - P_{\perp}\right)\frac{1}{ZeB}\left(\mathbf{b} \times \boldsymbol{\kappa}\right) + \frac{\mathbf{B}}{ZeB^2} \times \nabla P_{\perp}$$

where

$$P_{\parallel} = \int d^3\mathbf{v}\bar{F}mv_{\parallel}^2$$
$$P_{\perp} = \int d^3\mathbf{v}\bar{F}\mu B$$

This perpendicular flux $\mathbf{\Gamma}_{\perp}^{D}$ can be reexpressed as the divergence of a CGL stress tensor

$$\Pi_{ij} = \int d^3\mathbf{v}\bar{F}mv_iv_j = P_{\parallel}b_ib_j + P_{\perp}\left(\delta_{ij} - b_ib_j\right)$$

by noting that

$$\nabla\cdot\mathbf{\Pi} = \nabla P_{\perp} + \left(P_{\parallel} - P_{\perp}\right)\boldsymbol{\kappa} + \left[(\mathbf{B}\cdot\nabla)\left(\frac{P_{\parallel} - P_{\perp}}{B}\right)\right]\mathbf{b} \qquad (4.4.6)$$

so that

$$\mathbf{\Gamma}_{\perp} = N\mathbf{V}_E + \frac{\mathbf{B}}{ZeB^2}\times\nabla\cdot\mathbf{\Pi} \qquad (4.4.7)$$

A similar calculation can be done for the perpendicular energy flux

$$\mathbf{Q}_{\perp} = \frac{3}{2}NT\mathbf{V}_E + N\left\langle\frac{mv^2}{2}\mathbf{v}_D\right\rangle - \nabla\times\left[N\left\langle\frac{mv^2}{2}\frac{\mu}{e}\mathbf{b}\right\rangle\right] \qquad (4.4.8)$$

Introducing the ”energy flux tensor”

$$\Theta_{ij} = \int d^3\mathbf{v}\bar{F}mv_iv_j\frac{mv^2}{2} = \Theta_{\parallel}b_ib_j + \Theta_{\perp}\left(\delta_{ij} - b_ib_j\right)$$

where

$$\Theta_{\parallel} = \int d^3\mathbf{v}\bar{F}mv_{\parallel}^2\frac{mv^2}{2}$$
$$\Theta_{\perp} = \int d^3\mathbf{v}\bar{F}\mu B\frac{mv^2}{2}$$

one gets

$$\mathbf{Q}_{\perp} = \frac{3}{2}NT\mathbf{V}_E + \frac{\mathbf{B}}{ZeB^2}\times\nabla\cdot\mathbf{\Theta} \qquad (4.4.9)$$

where

$$\nabla\cdot\mathbf{\Theta} = \nabla\Theta_{\perp} + \left(\Theta_{\parallel} - \Theta_{\perp}\right)\boldsymbol{\kappa} + \left[(\mathbf{B}\cdot\nabla)\left(\frac{\Theta_{\parallel} - \Theta_{\perp}}{B}\right)\right]\mathbf{b} \qquad (4.4.10)$$

We now consider a Maxwellian distribution function, the average over the distribution function can be recast as

$$\left\langle ...\right\rangle_v = \int_0^{+\infty} du\exp\left(-u\right)\int_{-\infty}^{+\infty}\frac{d\zeta}{\sqrt{2\pi}}\exp\left(-\frac{\zeta^2}{2}\right)... \qquad (4.4.11)$$

where $\zeta = v_{\|}/v_T$ and $u = \mu B/T$ are normalized parallel velocity and perpendicular energy ($v_T = \sqrt{T/m}$). One recovers that $P_{\|} = P_{\perp} = P$ and $\Theta_{\|} = \Theta_{\perp} = \frac{5}{2}NT^2$ so that the perpendicular flux reads

$$\mathbf{\Gamma}_{\perp} = N\frac{\boldsymbol{B}\times\nabla\psi}{B^2}\Omega \tag{4.4.12}$$

where $\Omega\left(\psi\right) = \frac{\partial\phi}{\partial\psi} + \frac{1}{ZeN}\frac{\partial P}{\partial\psi}$ and

$$\mathbf{q}_{\perp} = \mathbf{Q}_{\perp} - \frac{5}{2}T\mathbf{\Gamma}_{\perp} = \frac{5}{2}P\frac{\mathbf{B}}{ZeB^2}\times\nabla T - P\mathbf{V}_E \tag{4.4.13}$$

The second term $-P\mathbf{V}_E$ in Eq.(4.4.13) is usually neglected in standard neoclassical theory as its contribution to the flux average flux is small. The correction $-P\mathbf{V}_E$ appears because the convective energy flux due to the $E\times B$ drift is $\frac{5}{2}P\mathbf{V}_E$ in the hydrodynamic formulation (it is the enthalpy that is convected, not the energy), whereas in kinetic theory, the energy flux can only be $\frac{3}{2}P\mathbf{V}_E$ since the $E\times B$ drift velocity does not depend on energy. This problem has been here and there for a long time, without a satisfactory answer. If one accepts to neglect this term, the perpendicular heat flux appears to be simply

$$\mathbf{q}_{\perp} = \frac{5}{2}P\frac{\mathbf{B}}{ZeB^2}\times\nabla T \tag{4.4.14}$$

which is the classical expression for the perpendicular diamagnetic heat flux.

4.4.1.3. Structure of parallel flows

Now that the perpendicular flows are known, the idea is to use the conservation equations (particle and energy) to link them to parallel quantities. We begin with the particle flux. We use the fact that $\boldsymbol{B}\times\nabla\psi = I\left(\psi\right)\boldsymbol{B} - B^2R^2\nabla\varphi$ to separate the perpendicular flow of particle Eq.(4.4.12) in a compressible part and an incompressible part $\mathbf{\Gamma}_{\perp} = \mathbf{\Gamma}^c + \mathbf{\Gamma}^i$ with

$$\mathbf{\Gamma}^c = N\frac{I}{B^2}\Omega\boldsymbol{B}$$

$$\mathbf{\Gamma}^i = -N\Omega R^2\nabla\varphi$$

It is easy to show the incompressibility of the total particle flux. Indeed the local conservation of particles reads

$$\frac{\partial N}{\partial t} + \nabla\cdot\mathbf{\Gamma} = 0$$

Using the steady state assumption, one gets the incompressibility condition $\nabla\cdot\mathbf{\Gamma} = 0$ over the total particle flux, which is used to link the compressible part of the perpendicular flux to the parallel flux

$$\nabla\cdot\mathbf{\Gamma}=\nabla\cdot\left[\frac{\left(\Gamma_{\perp}^{c}+\Gamma_{\parallel}\right)\boldsymbol{B}}{B}\right]=B\nabla_{\parallel}\left[\frac{\Gamma_{\perp}^{c}+\Gamma_{\parallel}}{B}\right]=0$$

with $\Gamma_{\perp}^{c}=N\frac{I}{B}\Omega$. Since the system is assumed axisymmetric here, it is equivalent to:

$$\begin{aligned}\Gamma_{\parallel} &= K\left(\psi\right)B-\Gamma_{\perp}^{c}\\ \Leftrightarrow NV_{\parallel} &= K\left(\psi\right)B-N\frac{I}{B}\Omega\end{aligned}$$

with $K\left(\psi\right)$ an unknown function at this stage. And so

$$V_{\parallel}=\frac{K\left(\psi\right)B}{N}-\frac{I}{B}\Omega$$

Then multiplying by the magnetic field and taking the flux surface average, it is possible to compute$K\left(\psi\right)$

$$\frac{K\left(\psi\right)}{N}=\frac{\left\langle BV_{\parallel}\right\rangle_{\psi}}{\left\langle B^{2}\right\rangle_{\psi}}+\frac{I\left(\psi\right)\Omega}{\left\langle B^{2}\right\rangle_{\psi}}$$

Finally one gets the expression of parallel velocity

$$V_{\parallel}=\frac{\left\langle BV_{\parallel}\right\rangle_{\psi}B}{\left\langle B^{2}\right\rangle_{\psi}}-I\Omega\left(\frac{1}{B}-\frac{B}{\left\langle B^{2}\right\rangle_{\psi}}\right)\tag{4.4.15}$$

For the parallel heat flux, a similar derivation is performed. To prove that the heat flux is incompressible, the local energy conservation is required

$$\frac{\partial E}{\partial t}+\nabla\cdot\boldsymbol{Q}=0$$

where E is the total energy $E=E_k+E_p$ and $\boldsymbol{Q}$ is the total flux of energy. Here we neglect the contribution of the electric field. In this case $E\simeq E_k$ and $\boldsymbol{Q}\simeq\boldsymbol{q}+\frac{5}{2}T\mathbf{\Gamma}$. Using the stationarity one gets

$$\nabla\cdot\boldsymbol{q}+\frac{5}{2}\left(T\nabla\cdot\mathbf{\Gamma}+\nabla T\cdot\mathbf{\Gamma}\right)=0$$

Using the incompressibility of the particle flux ($\nabla\cdot\mathbf{\Gamma}=0$) one gets

$$\nabla\cdot\boldsymbol{q}+\frac{5}{2}\nabla T\cdot\mathbf{\Gamma}=0$$

In this section it has been assumed that the temperature is a flux function $T(\psi)$ such that $\nabla T \cdot \mathbf{\Gamma} = \frac{\partial T}{\partial \psi} \nabla \psi \cdot \mathbf{\Gamma}_\perp$. As the perpendicular flux of particle Eq.(4.4.12) is orthogonal to $\nabla\psi$ then $\nabla T \cdot \mathbf{\Gamma} = 0$. Therefore, the heat flux is incompressible $\nabla \cdot \boldsymbol{q} = 0$. Then using exactly the same procedure as for the parallel velocity, one gets

$$q_\parallel = \frac{\left\langle B q_\parallel \right\rangle_\psi B}{\left\langle B^2 \right\rangle_\psi} - \frac{5}{2} \frac{P}{Ze} \frac{\partial T}{\partial \psi} I(\psi) \left(\frac{1}{B} - \frac{B}{\left\langle B^2 \right\rangle_\psi} \right) \tag{4.4.16}$$

4.4.1.4. Impurity flux

Using the previously derived expressions of the parallel quantities Eq.(4.4.15) and Eq.(4.4.16), and the definition of the collisional exchange of momentum Eq.(4.4.3), one can compute the parallel exchange of momentum between species due to collisions

$$\begin{aligned} R_{\parallel zi} &= \nu_{zi} \frac{m_z T_z I}{Z_z e} \left(\frac{1}{B} - \frac{B}{\left\langle B^2 \right\rangle_\psi} \right) N_z \\ &\times \left[\frac{\partial \ln N_z}{\partial \psi} - \frac{Z_z}{Z_i} \frac{\partial \ln N_i}{\partial \psi} - H_{theo} \frac{Z_z}{Z_i} \frac{\partial \ln T}{\partial \psi} \right] \end{aligned} \tag{4.4.17}$$

In this expression, the contribution of the impurity parallel heat flux has been dropped due the mass ratio between impurity and the main species. Identical temperatures have also been assumed for both species. Using the parallel momentum exchange due to collisions Eq.(4.4.17), one can compute the neoclassical particle flux Eq.(4.4.2)

$$\Gamma_{z,neo} = \left\langle \mathbf{\Gamma}_z \cdot \nabla r \right\rangle_\psi = -N_z D_{theo} \left[\frac{\partial_r N_z}{N_z} - \frac{Z_z}{Z_i} \frac{\partial_r N_i}{N_i} - H_{theo} \frac{Z_z}{Z_i} \frac{\partial_r T}{T} \right]$$

with

$$D_{theo} = \nu_{zi} \frac{m_z T_z I^2}{(Z_z e)^2} \left(\left\langle \frac{1}{B^2} \right\rangle_\psi - \frac{1}{\left\langle B^2 \right\rangle_\psi} \right) \left(\frac{dr}{d\psi} \right)^2$$

In circular geometry, one has $\frac{dr}{d\psi} = \frac{q}{r}$ and $I^2 \left(\left\langle \frac{1}{B^2} \right\rangle_\psi - \frac{1}{\left\langle B^2 \right\rangle_\psi} \right) \simeq 2r^2$. Therefore

$$D_{theo} \simeq 2 q^2 \nu_{zi} \rho_z^2$$

This expression is close to the one found in the qualitative approach in the first section.

4.4.2. Comparison with GYSELA results

In fusion plasmas, tungsten is only partially stripped and its ionization state depends on the local temperature. But only a single charge state is allowed in the current version of the GYSELA code. Thus a fixed charge is chosen for the tungsten $Z_W = 40$. The main species is deuterium in the banana regime ($\nu_D^\star = 0.1$ at mid radius). Tungsten is therefore in the Pfirsch-Schlüter regime as $\nu_W^\star \simeq \sqrt{2} Z_W^2 \sqrt{\frac{m_D}{m_W}} \nu_D^\star \simeq 236 \nu_D^\star = 23,6$.

Recovering the expected neoclassical expression of the thermal screening coefficient H_{theo} reveals being a stringent test of both the Vlasov part (the left hand side of the gyrokinetic equation, governing the trajectories) and the collision operator. More precisely, the final value – and sign – of H_{theo} results from a partial compensation between two different contributions: one coming from the parallel velocities of both species (of the order of 1 in the Pfirsch-Schlüter regime), and another one coming from the parallel heat flux of the main ions (of the order of $-\frac{3}{2}$ in the Pfirsch-Schlüter regime).

In this framework, the accurate computation of $q_{\parallel i}$ is a critical issue. As a matter of fact, its neoclassical expression Eq.(4.4.16) results from the incompressibility of the total flux $\nabla \cdot \boldsymbol{q}_i = 0$. The transverse flux $q_{\perp i}$ computed in GYSELA is in perfect agreement with the neoclassical prediction, Eq.(4.4.14). Conversely, the present accuracy of the energy balance is not sufficient to recover the expected expression of $q_{\parallel i}$: while the poloidal shape is properly recovered, the magnitude is not. More precisely, the parallel heat flux coming from GYSELA is approximately half of its theoretical prediction. Note however that this issue *is not* related to the collision operator, although it impacts neoclassical transport. Indeed, it comes from the treatment of the Vlasov part of the gyrokinetic equation. For the time being, the solution to overcome this difficulty is to impose that the parallel heat flux takes the expected value Eq.(4.4.16) in the collision operator. This temporary solution has been used to obtain the results in the rest of this section.

The diffusion coefficient and the screening factor in the Pfirsch-Schlüter regime with trace impurities are given respectively by $D_{theo} = 2q^2\,\rho_i^2 \nu_{iz}/\alpha$ and $H_{theo} \simeq -0.5 + 0.29/\left(0.59 + 1.34 g^{-2}\right)$ with $g = \nu_i^\star \epsilon^{3/2}$ [47]. To test this prediction we assume that the flux computed in GYSELA takes the general form

$$\Gamma_z^{gys} = -N_Z D_{gys} \left[\frac{\partial_r N_z}{N_z} - K_{gys} Z \frac{\partial_r N_i}{N_i} - H_{gys} Z \frac{\partial_r T}{T} \right] \tag{4.4.18}$$

with a modified definition of the impurity flux

$$\Gamma_z^{gys} = \frac{dr}{d\psi} \left[\Gamma_z^\psi - \Gamma_{E,z}^\psi - \frac{1}{Z_z e} \left(\partial_t L_{\varphi,z} + \partial_\psi \Pi_{\varphi,z}^\psi \right) \right]$$

The modification of the definition of the impurity flux is required for an accurate comparison between simulation and theoretical prediction. Indeed in the simulations, the contribution of the other terms is non-vanishing and they need to be taken into account.

Using the ansatz Eq.(4.4.18), one can measure D_{gys}, K_{gys} and H_{gys} and to compare them with their analytical predictions D_{theo}, $K_{theo} = 1$ and H_{theo} . To do so, two simulations are used. The first one with $\nabla T \simeq 0$ is used to compute D_{gys} and K_{gys}. Radial density profiles are chosen to get a radial scan of $\frac{\partial_r N_z}{N_z}(r) - Z\frac{\partial_r N_i}{N_i}(r)$ around zero. It is then possible to plot Γ_z^{gys}/N_z as a function of $-D_{gys}\left[\frac{\partial_r N_z}{N_z} - K_{gys} Z \frac{\partial_r N_i}{N_i}\right]$, with D_{gys} and K_{gys} as free parameters determined via a least square method. This approach uses the global character of GYSELA and the locality of the neoclassical transport. Small gradients of density and temperature are considered to minimize the radial dependence of D_{theo} and H_{theo}, making the analysis simpler. For the same reason, a flat profile of the safety factor is chosen ($q = 2$). The other parameters of the simulation are $\rho_\star = \frac{1}{150}$, $\epsilon = 0.15$ at mid radius as in the previous part. The result of this simulation is given in Fig.4.7. The good fit gives confidence in the dependence of the flux of tungsten on the density gradients of both species. The discrepancy with the theoretical prediction for K_{gys} is of few percents and the one on the diffusion coefficient D_{gys} is below 15%.

Figure 4.7.: Normalized particle flux of impurities versus density gradients. The solid line corresponds to GYSELA results and the dotted line to its linear fit.

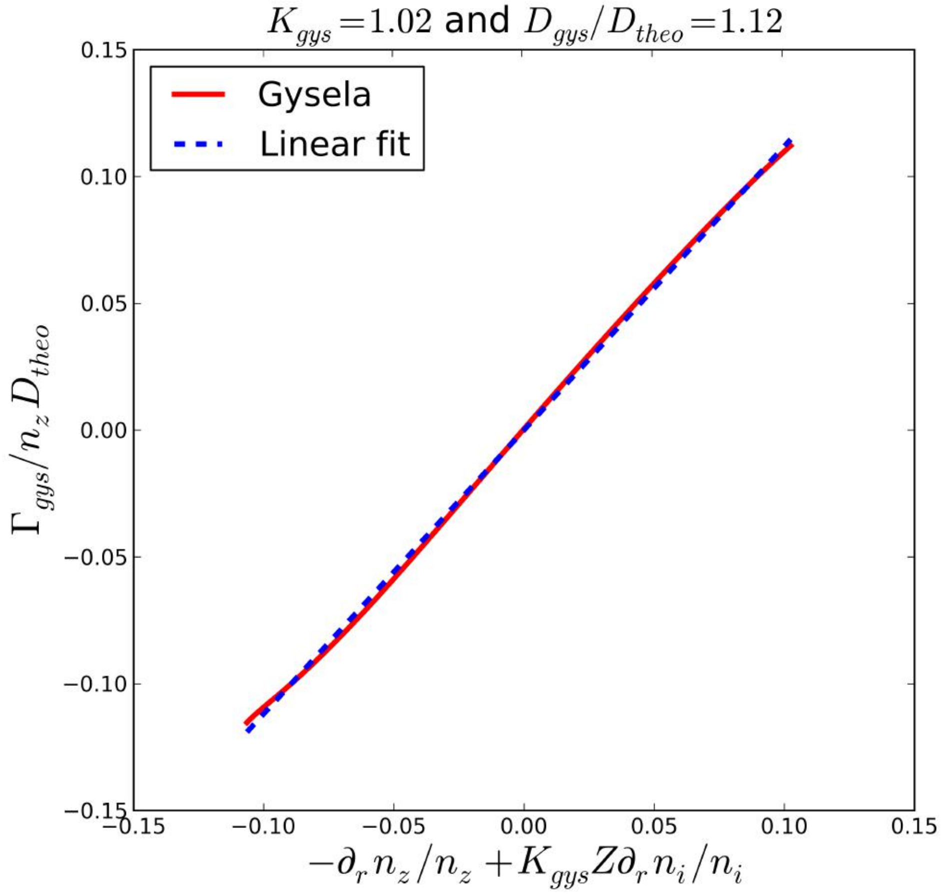

The second step consists in a simulation with $\frac{\nabla N_z}{N_z} - Z\frac{\nabla N_i}{N_i} = 0$. In this case the flux is expected to be directly proportional to the temperature gradient $\Gamma_z = N_Z D_{gys} H_{gys} Z \frac{\nabla T}{T}$ since the previous simulation has shown that $K_{gys} \simeq 1$. Using also the fact that the diffusion coefficient is close to the theoretical prediction, we can replace D_{gys} by D_{theo} in the previous expression and then directly measure H_{gys} using a method similar to the one presented previously. The result is given in Fig.4.8. Again a discrepancy of few percent is found between the results from the code and the theoretical prediction.

Figure 4.8.: Normalized particle flux of impurities versus temperature gradient. The solid line corresponds to GYSELA results and the dotted line to its linear fit.

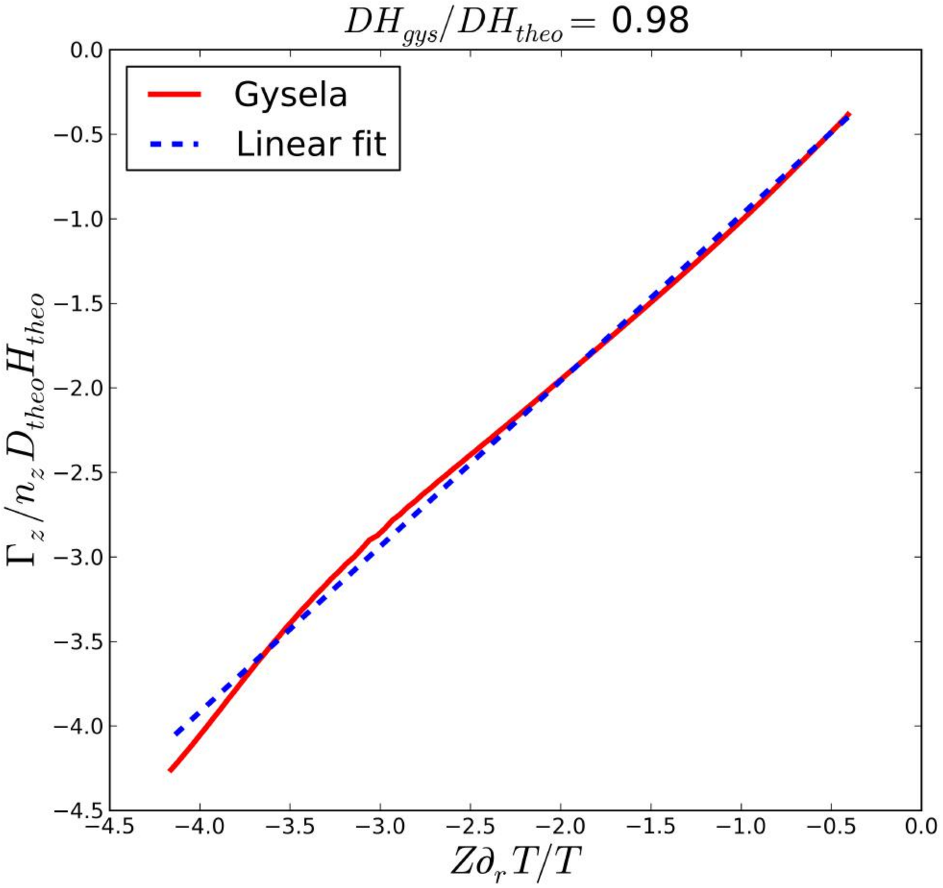

Summary of the chapter

In conclusion, the tests performed in this chapter have shown that GYSELA, with its new collision operator presented in the chapter 3, is able to reproduce successfully the results coming from the conventional neoclassical theory derived in absence of turbulence and external sources. This is an important result in the perspective of impurity transport studies as neoclassical transport is expected to be the main contributor to heavy impurity transport.

5. Turbulent prediction of impurity flux

Contents

4.1. Introduction **80**

4.2. Physical description of neoclassical theory **80**

4.3. Neoclassical test of the collision operator : single species case **84**

- 4.3.1. Neoclassical diffusion and poloidal rotation 84
- 4.3.2. Zonal flow damping 87

4.4. Neoclassical test of the collision operator : trace impurity **88**

- 4.4.1. Neoclassical prediction 89
- 4.4.2. Comparison with GYSELA results 95

Turbulence is one of the three mechanisms of particle transport in tokamak. It is the dominant one for the main ion species and can also have an impact on impurity transport, especially in the case of light impurities or if the collisionality of the impurity is not too large. Turbulence in plasmas is a very rich topic and an exhaustive presentation of its specificities is beyond the scope of this thesis. Instead, a general view of the turbulence observed in tokamak plasmas is given in the first part of this chapter. The second part is devoted to the turbulent transport of impurities.

5.1. ITG turbulence

5.1.1. Underlying instability

Turbulence in plasmas often comes from an underlying linear instability. This instability is always associated with a deviation from thermodynamic equilibrium, providing the necessary source of free energy. The source of free energy can be due to the existence of radial gradients or come from deviation from the Maxwellian distribution function as in the case of the bump on tail instability.

In the nonlinear simulations performed in the frame of this thesis, the instability that leads to turbulence is due to the temperature gradient of the main ion species. Therefore the resulting turbulence is called ITG (Ion Temperature Gradient) driven turbulence. ITG is akin to the so-called “interchange instability”. Interchange instability is locally unstable (stable) on the low (high) field side of the tokamak. These instabilities are indeed due to the presence of the magnetic drift combined with density and/or temperature gradients. A schematic description of an interchange instability is depicted in Fig.5.1. This figure shows a typical situation found on the low field side of a tokamak. Initial potential fluctuations (red and blue circles) are amplified because of an unbalanced advection (v_E) due to the gradient of pressure. In the case depicted, the gradient of the magnetic field intensity ∇B and the gradient of the pressure are pointing in the same direction. In this case, the unbalanced advection leads to an increase of the fluctuations, and therefore to an instability. Conversely, if the gradients were pointing in opposite directions, the situation would be stable. This is the reason why ITG turbulence like other interchange instabilites exhibits stronger turbulence intensity in the low field side of the tokamak.

Figure 5.1.: Qualitative explanation of an interchange instability. The initial potential fluctuations (blue and red circles) are growing due to an unbalanced v_E advection. Indeed due to the pressure gradient, there are more particles going to the right than in the opposite direction. Combined with the vertical drift due to magnetic curvature, this leads to an instability.

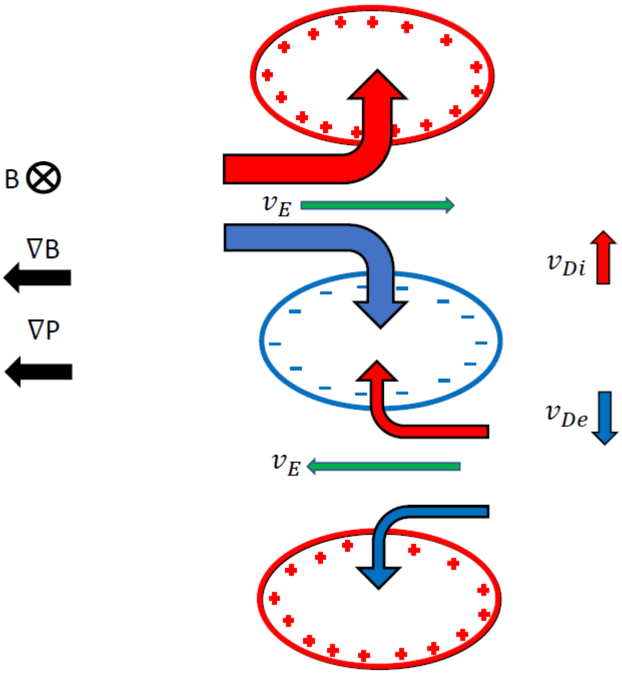

The low field side of the tokamak is always locally unstable to interchange instability, while the high field side is stable. As both areas are magnetically connected, a pending question is whether the overall magnetic field line is stable or not. We know derive the linear stability criterion for ITG turbulence.

5.1.2. Linear stability

5.1.2.1. Equilibrium field, particle trajectories and gyrokinetic equation

The unperturbed part of the magnetic field is written in Clebsch representation,

$$\mathbf{B}_{eq} = \nabla\alpha \times \nabla\psi$$

where $\alpha = \varphi - q(\psi)\theta$, where ψ, φ, and θ are respectively the poloidal flux normalised to -2π, the toroidal and poloidal angles, and $q(\psi)$ is the safety factor. This structure of the field is identical to the one defined in the section 1.3.2 $\mathbf{B}_{eq} = I(\psi)\nabla\varphi + \nabla\varphi \times \nabla\psi$ for a straight field line coordinate θ such that $\mathbf{B}_{eq} \cdot$

$\nabla\varphi/\mathbf{B}_{eq}\cdot\nabla\theta = q(\psi)$. In the special case of a large aspect ratio tokamak with circular concentric magnetic surfaces labeled by their minor radius r, the function ψ is given by $\frac{d\psi}{dr} = \frac{rB_0}{q(r)}$. The inverse aspect ratio $\epsilon = \frac{r}{R_0}$ is considered as a small parameter, and calculations are done at first order in ϵ. The unperturbed equation of motion is integrable, since there exists three invariants of motion, namely the unperturbed Hamiltonian H_{eq}, the magnetic moment μ, and the toroidal canonical momentum $P_\varphi = -e\psi + mRv_\varphi$ where v_φ is the particle toroidal velocity. The gyrocenter distribution function $\bar{F}$ is a function of the variables $(H_{eq}, \mu, P_\varphi, \theta, \varphi)$ (strictly speaking there should also be a label giving the sign of the parallel velocity). The action $\frac{m}{e}\mu$ is conjugated with the gyroangle, while the toroidal canonical momentum is conjugated with the toroidal angle. The last degree of freedom (H_{eq}, θ) can be replaced by a set of action/angle variable, which does not need to be detailed here. The gyrokinetic Vlasov equation reads

$$\frac{\partial \bar{F}}{\partial t} - \left\{\bar{H}, \bar{F}\right\} = 0 \tag{5.1.1}$$

where $\bar{H} = H_{eq} + \bar{h}$ is the total Hamiltonian, and $\{,\}$ denotes the Poisson bracket. This Poisson bracket is fully determined at this stage by the equations of motion expressed in the set of coordinates $(H_{eq}, \mu, P_\varphi, \theta, \varphi)$. It is convenient to write the distribution function as

$$\bar{F}(H_{eq}, \mu, P_\varphi, \theta, \varphi, t) = F_{eq}(\bar{H}, \mu, P_\varphi, t) + \bar{g}(H_{eq}, \mu, P_\varphi, \theta, \varphi, t)$$

where $F_{eq}(H_{eq}, \mu, P_\varphi)$ is the unperturbed distribution function that depends on motion invariants only. Noting that $F_{eq}(\bar{H}, \mu, P_\varphi) \simeq F_{eq}(H_{eq}, \mu, P_\varphi) + \bar{h}\partial_{H_{eq}}F_{eq}$ for small values of the perturbed Hamiltonian, and using $\{\varphi, P_\varphi\} = 1$, $\{\theta, P_\varphi\} = 0$, the following equation over the “resonant”distribution function (i.e. non adiabatic) $\bar{g}$ is derived in the appendix A.

$$\frac{\partial \bar{g}}{\partial t} - \left\{\bar{H}, \bar{g}\right\} = \frac{F_{eq}}{T_{eq}}\left(\frac{\partial}{\partial t} + \Omega^* \frac{\partial}{\partial \varphi}\right)\bar{h} \tag{5.1.2}$$

where $\frac{1}{T_{eq}} = -\frac{\partial}{\partial H_{eq}}\ln F_{eq}$ is the inverse of a “temperature”and $\Omega^* = T_{eq}\frac{\partial \ln F_{eq}}{\partial P_\varphi}$ is the kinetic diamagnetic frequency. Both quantities depend on the motion invariants only. T_{eq} is the usual local temperature when F_{eq} is a Maxwellian. Accordingly, the kinetic diamagnetic frequency can be reexpressed using the approximation $P_\varphi \simeq -e\psi$:

$$\Omega^* = -\frac{q}{r}\frac{T_{eq}}{eB_0}\left[\frac{\partial \ln N_{eq}}{\partial r} + \left(\frac{H_{eq}}{T_{eq}} - \frac{3}{2}\right)\frac{\partial \ln T_{eq}}{\partial r} + \frac{\left(v_\parallel - V_{\parallel,eq}\right)}{v_T^2}\frac{\partial V_{\parallel,eq}}{\partial r}\right]$$

There and in the following, F_{eq} is considered to be a Maxwellian. The function $\bar{g}$ is then expressed as a function of the non canonical set of gyrocenter coordinates $\left(r, \theta, \varphi, v_{\|}\right)$. The corresponding Poisson bracket in the gyrokinetic Vlasov equation on $\bar{g}$ reads

$$\{F, G\} = \frac{\mathbf{B}^*}{mB_{||}^*} \cdot \left(\nabla F \frac{\partial G}{\partial v_{\|}} - \frac{\partial F}{\partial v_{\|}} \nabla G\right) - \frac{\mathbf{b}_{eq}}{eB_{||}^*} \cdot \nabla F \times \nabla G \tag{5.1.3}$$

where m is the mass, e the charge, $\mathbf{b}_{eq} = \frac{\mathbf{B}_{eq}}{B_{eq}}$ the unit vector along the magnetic field, $\mathbf{B}^* = \mathbf{B}_{eq} + \frac{mv_{\|}}{e} \nabla \times \mathbf{b}_{eq}$ and $B_{||}^* = \mathbf{b}_{eq} \cdot \mathbf{B}^*$ is the Jacobian of the gyrocenter transformation. The Poisson bracket Eq.(5.1.3) fully determines the equations of motion. In the electrostatic limit, these are

$$\frac{d\mathbf{x}}{dt} = -\{H_{eq}, \mathbf{x}\} = \mathbf{v}_D + \mathbf{v}_E + v_{\|}\mathbf{b}_{eq}$$

$$m\frac{dv_{\|}}{dt} = -\left\{H_{eq}, mv_{\|}\right\} = -\mathbf{b}_{eq} \cdot \nabla\left(\mu B_{eq} + e\mathcal{J}\phi\right) + mv_{\|}\boldsymbol{\kappa} \cdot \left(\mathbf{v}_D + \mathbf{v}_E\right)$$

where

$$\mathbf{v}_D = \frac{1}{e}\frac{\mathbf{b}_{eq}}{B_{||}^*} \times \left(\mu \nabla B_{eq} + mv_{\|}^2 \boldsymbol{\kappa}\right)$$

is the magnetic drift velocity ($\boldsymbol{\kappa} = (\mathbf{b}_{eq} \cdot \nabla)\mathbf{b}_{eq}$ is the field curvature) and

$$\mathbf{v}_E = \frac{\mathbf{b}_{eq}}{eB_{||}^*} \times \nabla \bar{h}$$

the $E \times B$ drift velocity ($\bar{h} = e\mathcal{J}\phi$ is the perturbed Hamiltonian, ϕ is the perturbed electric potential and $\mathcal{J}$ the gyroaverage operator). The volume element in the velocity space reads $d^3\mathbf{v} = 2\pi\frac{1}{m}B_{||}^* d\mu dv_{\|}$.

At this stage, no approximation was done apart from the ones based on the standard collisionless gyrokinetic ordering. ITG is coming from the passing particles. Therefore we now focus on the role of passing particles, i.e. neglect particle trapping. For highly passing particles, this is equivalent to ignore the mirror force and the parallel electric force in the parallel equation of motion (weak non linear term). Given this framework, the compressional term in the parallel equation of motion can be ignored as well because it is of the same order of magnitude as the terms neglected. The parallel velocity then appears to be a motion invariant, as expected for highly passing particles. The gyrokinetic Vlasov equation can then be reformulated as follows:

$$\frac{\partial \bar{g}}{\partial t} - \left\{ \bar{H}, \bar{g} \right\} = \frac{\partial \bar{g}}{\partial t} + v_\parallel \nabla_\parallel \bar{g} + \mathbf{v}_E \cdot \nabla \bar{g} + \mathbf{v}_D \cdot \nabla \bar{g}$$
$$= \frac{F_{eq}}{T_{eq}} \left(\frac{\partial}{\partial t} + \Omega^* \frac{\partial}{\partial \varphi} \right) \bar{h} \tag{5.1.4}$$

5.1.2.2. Linearization

The electric potential is split in an axisymmetric component $\langle \phi \rangle_\varphi (\psi, \theta)$ and a helical perturbation $\tilde{\phi} (\psi, \theta, \varphi)$, i.e. $\phi = \langle \phi \rangle_\varphi + \tilde{\phi}$. We place ourselves in the rotating referential for which the flux surface averaged electric field is zero. Therefore the term $\mathbf{v}_E \cdot \nabla \bar{g}$ is strictly non linear and neglected for the linear analysis. In the following we are interested in the helical part, which is the one which can be unstable. The ballooning representation is used [19, 76, 87], i.e.

$$\tilde{\phi}(\psi, \theta, \varphi, t) = \sum_{\mathbf{k}\omega} \phi_{n\omega}(\theta_k, \theta + 2p\pi) \exp \left\{ in \left[\varphi - q(\psi) \left(\theta - \theta_k + 2p\pi \right) \right] - i\omega t \right\} \tag{5.1.5}$$

where $\mathbf{k} = (n, \theta_k, p)$. The integer p spans the interval $]-\infty, +\infty[$. However for a ballooned turbulence, it is sufficient to keep the component $p = 0$ only. In this case, a useful reformulation of Eq.(5.1.5) in the set of field aligned coordinates is

$$\tilde{\phi}(\psi, \alpha, \theta, t) = \sum_{\mathbf{k}\omega} \phi_{\mathbf{k}\omega} \exp \left\{ i \left[n\theta_k q(\psi) + n\alpha - \omega t \right] \right\} \tag{5.1.6}$$

where we recall that $\alpha = \varphi - q(\psi) \theta$. Considering large toroidal numbers $n \gg 1$ and after a bit of algebra detailed in the appendix B , it can be shown that Eq.(5.1.4) can be written

$$\Omega_t \frac{\partial \bar{g}_{\mathbf{k}\omega}}{\partial \theta} - i \left(\omega - \omega_D \right) \bar{g}_{\mathbf{k}\omega} = -i \left(\omega - \omega_\star \right) h_{\mathbf{k}\omega} \frac{F_{eq}}{T_{eq}} \tag{5.1.7}$$

where the transit frequency is defined as $\Omega_t = \frac{v_\parallel}{qR_0}$. ω_D stands for a frequency associated to the field curvature

$$\omega_D = k_\theta v_D \left[\cos\theta + s \left(\theta - \theta_k \right) \sin\theta \right]$$

where $v_D = \| \boldsymbol{v}_D \|$ and finally, a modified diamagnetic frequency is defined as

$$\omega_\star = n\Omega^* = \frac{k_\theta T_{eq}}{eB_0} \left[\frac{\partial \ln N_{eq}}{\partial r} + \left(\frac{H_{eq}}{T_{eq}} - \frac{3}{2} \right) \frac{\partial \ln T_{eq}}{\partial r} + \frac{\left(v_\parallel - V_{\parallel,eq} \right)}{v_T^2} \frac{\partial V_{\parallel,eq}}{\partial r} \right] \tag{5.1.8}$$

Also, the poloidal wavevector is defined as $k_\theta = -\frac{nq}{r}$ and the magnetic shear is $s=\frac{r}{q}\frac{dq}{dr}$. Eq.(5.1.7) is a first order linear differential equation. The solution of this equation is an integral form

$$\bar{g}_{\mathbf{k}\omega}=-i\frac{\omega-\omega_\star}{\Omega_t}\frac{F_{eq}}{T_{eq}}\int_{\theta_{min}}^{\theta}d\theta'\exp\left\{i\left[\Lambda_{\mathbf{k}\omega}\left(\theta\right)-\Lambda_{\mathbf{k}\omega}\left(\theta'\right)\right]\right\}h_{\mathbf{k}\omega}\left(\theta'\right)$$

with $\frac{\partial\Lambda_{\mathbf{k}\omega}}{\partial\theta}=\frac{\omega-\omega_D}{\Omega_t}$. The causality imposes the choice $\theta_{min}=-\text{sign}\ (\Omega_t)\times\infty$. This expression can be written differently by using the Heaviside function H:

$$\bar{g}_{\mathbf{k}\omega}=\frac{\omega-\omega_\star}{\omega}\frac{F_{eq}}{T_{eq}}\int_{-\infty}^{\infty}d\theta' G\left(\theta,\theta'\right)h_{\mathbf{k}\omega}\left(\theta'\right)\qquad(5.1.9)$$

with

$$G\left(\theta,\theta'\right)=-i\frac{\omega}{\Omega_t}\exp\left\{i\left[\Lambda_{\mathbf{k}\omega}\left(\theta\right)-\Lambda_{\mathbf{k}\omega}\left(\theta'\right)\right]\right\}H\left[\left(\theta-\theta'\right)\text{sign}(\Omega_t)\right]$$

The next step consists in using the Poisson equation to link the ”resonant” distribution function g with the potential ϕ. This equation reads

$$\int d^3v\mathcal{J}\bar{g}=\frac{N_{eq}}{T_{eq}}\left(1+\tau\right)e\phi\qquad(5.1.10)$$

where $\tau=\frac{T_i}{T_e}$. The dispersion relation then reads

$$\int d^3v\mathcal{J}\left[\frac{\omega-\omega_\star}{\omega}\frac{F_{eq}}{T_{eq}}\int_{-\infty}^{\infty}d\theta' G\left(\theta,\theta'\right)\mathcal{J}\phi_{\mathbf{k}\omega}\left(\theta'\right)\right]=\frac{N_{eq}}{T_{eq}}\left(1+\tau\right)\phi_{\mathbf{k}\omega}$$

This expression is equivalent to the one derived by Romanelli (Eq.(5) of [75]). This formula is pretty general but difficult to exploit directly due to its integro-differential form. Different limits have been derived analytically, allowing for simpler expressions but with restrained validity domains.

ITG is an instability with a threshold value [62]. This threshold is of utmost importance for confinement. Indeed, above the threshold the turbulent flux is rapidly increasing thus leading to a profile relaxation. In practice, profiles are close to the threshold value. This is called “profile stiffness” [33].

An extensive study of the linear stability criteria with a gyrokinetic code [57] allows one to derive a linear threshold criteria in the infinite aspect ratio limit $\epsilon\rightarrow 0$

$$\frac{R}{L_{T,c}^{l}}=\max\left\{\left(1+\tau\right)\left(1.33+1.91\frac{s}{q}\right),0.8\frac{R}{L_N}\right\}\qquad(5.1.11)$$

Fig.5.2 illustrates Eq.(5.1.11) in the case $s=q$. Above the curve, ITG is unstable and below it is stable. From Eq.(5.1.11) it is clear that τ and $\frac{s}{q}$ have a stabilizing effect for ITG, as well as large values of $\frac{R}{L_N}$.

Figure 5.2.: Linear threshold for the ITG instability in the case $s = q$

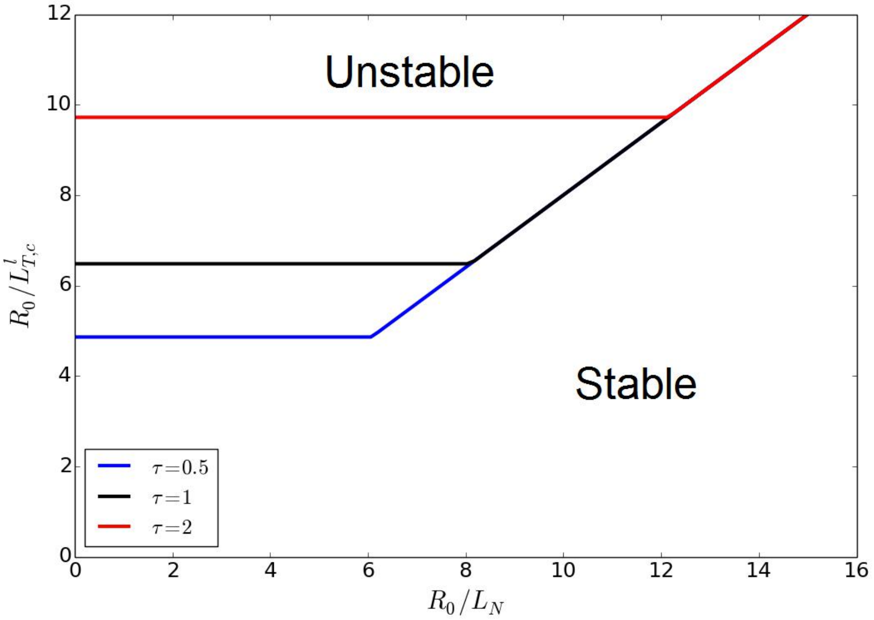

5.1.3. Turbulence saturation processes

In the previous section, a linear stability analysis of ITG mode has been derived. This approach gives a threshold temperature gradient for the ITG turbulence. It is known that in the non-linear regime, the effective threshold is larger. This characteristics, sometimes called "Dimits shift" in reference to the pionnering work done by A. M. Dimits et al. [25], is often attributed to the non-linear generation of zonal flows by turbulence. Part of the free energy extracted from the instability is then transferred by non-linear coupling to the large scale zonal flow. Zonal flows back react on turbulence by transferring energy from low wavelengths to high wavelengths via a diffusion process in k-space [22]. These processes reduce the effective source of energy available for turbulence growth. Ultimately, a zonal flow saturates at a level governed either by collisional damping [45, 27] and/or the non linear destabilization of the zonal mode via different possible mechanisms [22] (Kelvin-Helmholtz instability, other tertiary mode instability, hyper diffusion). This mechanism of turbulence saturation is depicted in Fig.5.3. It is an efficient saturation mechanism because zonal flows are not Landau damped [77], therefore they can saturate at a relatively large level. A new and more general approach of the turbulent generation of large scale structures including zonal flows is derived in the chapter 7.

Note that other saturation mechanisms for turbulence can be at play. For instance, mode-mode coupling transfer energy to small scales structures which are eventually damped (for instance by collisions). Background profiles can also relax thus leading to a decrease of the linear drive for turbulence. Non-linear wave-particle interaction can also transfer energy to another species (i.e. electrons in the case of ITG).

Figure 5.3.: Mechanism for turbulence generation and saturation by zonal flows

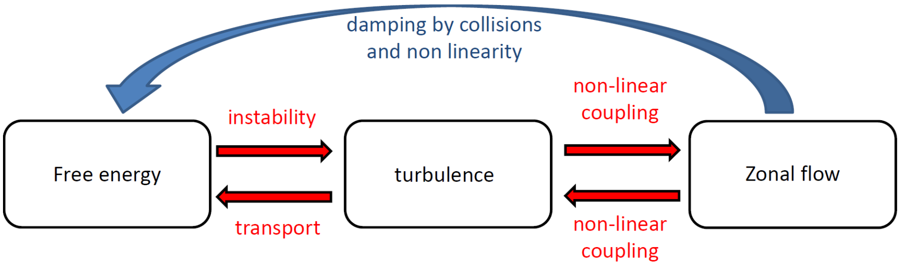

5.2. Theoretical prediction of impurity transport related with turbulence

In the previous section, the generation and saturation of ITG turbulence has been presented. This turbulence can generate an impurity particle flux. The turbulent impurity flux takes the general form

$$\Gamma_{z,turb} = \langle \boldsymbol{\Gamma}_{z,turb} \cdot \nabla r \rangle = \left\langle \int d^3v f_z \left(\boldsymbol{v}_E^{n\neq 0} \cdot \nabla r \right) \right\rangle_{\psi,t}$$

where $f_z = F_z - F_{eq,z}$ is the perturbed distribution function of the impurity and $\langle \cdot \rangle_{\psi,t}$ refers to both flux surface and time average. Note that only modes $n \neq 0$ are considered here. Indeed, although axisymmetric modes ($n = 0$) can be generated by turbulence via non linear coupling (cf. chapter 7), they are linearly stable. Therefore, restricting the definition of the turbulent flux to the modes linearly unstable, one discards the contribution of $n = 0$ modes in $\Gamma_{z,turb}$. Using the fact that $\boldsymbol{v}_E \cdot \nabla r \sim -\frac{\partial_\theta \phi}{B}$ and taking the Fourier transform, one obtains

$$\Gamma_{z,turb} = \sum_{\boldsymbol{k}\omega} \int f_{z,\boldsymbol{k}\omega} \left(-ik_\theta \frac{\phi_{\boldsymbol{k}\omega}}{B} \right)^\star d^3v \tag{5.2.1}$$

The linear response of the distribution function is given by (proof can be find in the appendix C)

$$f_{z,\boldsymbol{k}\omega} = -\left[1 - \frac{\omega - \omega_\star}{\omega - \omega_d - k_\parallel v_\parallel} \mathcal{J} \right] eZ\phi_{\boldsymbol{k}\omega} \frac{F_{z,eq}}{T_{z,eq}} \tag{5.2.2}$$

where $k_\parallel$ is the wavevector associated to the parallel direction. Combining Eq.(5.2.1) and (5.2.2), one gets

$$\Gamma_{z,turb} = -\sum_{\boldsymbol{k}\omega}\int \frac{F_{z,eq}}{T_{z,eq}}\left(-ik_\theta\frac{\phi_{\boldsymbol{k}\omega}}{B}\right)^\star\left[1-\mathcal{J}\frac{\omega-\omega_\star}{\omega-\omega_d-k_\parallel v_\parallel}\mathcal{J}\right]eZ\phi_{\boldsymbol{k}\omega}d^3v \qquad (5.2.3)$$

The non resonant part (term proportional to $\Re\left(1-\mathcal{J}\frac{\omega-\omega_\star}{\omega-\omega_d-k_\parallel v_\parallel}\mathcal{J}\right)$) is exactly zero as $\sum_{\boldsymbol{k},\omega}k_\theta\left|\phi_{\boldsymbol{k},\omega}\right|^2=0$ and can be discarded. Eq.(5.2.3) is the flux of particles. In GYSELA, the computed flux corresponds to the flux of gyrocenters. It is given by

$$\bar{\Gamma}_{z,turb} = \left\langle\int d^3v\bar{F}_z\left(\bar{\boldsymbol{v}}_E^{n\neq0}\cdot\nabla r\right)\right\rangle_{\psi,t}$$

Both definitions differ by a polarization term. By a similar procedure as for the particule flux, the gyrocenter flux can be shown to take the form:

$$\begin{aligned}
\bar{\Gamma}_{z,turb} &= \sum_{\boldsymbol{k}\omega}\int\Im\left(\frac{\omega-\omega_\star}{\omega-\omega_d-k_\parallel v_\parallel}\right)\left(-ik_\theta\frac{\mathcal{J}\phi_{\boldsymbol{k}\omega}}{B}\right)^\star eZ\mathcal{J}\phi_{\boldsymbol{k}\omega}\frac{F_{z,eq}}{T_{z,eq}}d^3v\\
&= \sum_{\boldsymbol{k}\omega}\int\Im\left(\frac{\omega-\omega_\star}{\omega-\omega_d-k_\parallel v_\parallel}\right)\frac{ieZB}{k_\theta T_{z,eq}}\left(-ik_\theta\frac{\mathcal{J}\phi_{\boldsymbol{k}\omega}}{B}\right)\left(-ik_\theta\frac{\mathcal{J}\phi_{\boldsymbol{k}\omega}}{B}\right)^\star F_{z,eq}d^3v\\
&= \sum_{\boldsymbol{k}\omega}\int\Im\left(\frac{\omega-\omega_\star}{\omega-\omega_d-k_\parallel v_\parallel}\right)\frac{ieZB}{k_\theta T_{z,eq}}\left|\bar{v}_{E,\boldsymbol{k}\omega}\right|^2F_{z,eq}d^3v
\end{aligned}$$

where $\left|\bar{v}_{E,\boldsymbol{k},\omega}\right|^2=\left|k_\theta\frac{\mathcal{J}\phi_{\boldsymbol{k},\omega}}{B}\right|^2$. Using the Sokhotski–Plemelj theorem, the imaginary part can be replaced by $\Im\left(\frac{\omega-\omega_\star}{\omega-\omega_d-k_\parallel v_\parallel}\right)=-i\pi\left(\omega-\omega_\star\right)\delta\left(\omega-\omega_d-k_\parallel v_\parallel\right)$. Therefore the turbulent flux can be reexpressed as

$$\bar{\Gamma}_{z,turb} = \pi\sum_{\boldsymbol{k}\omega}\int\left(\omega-\omega_\star\right)\frac{eZB}{k_\theta T_{z,eq}}\delta\left(\omega-\omega_d-k_\parallel v_\parallel\right)\left|\bar{v}_{E,\boldsymbol{k},\omega}\right|^2F_{z,eq}d^3v$$

Using the expression of the diamagnetic frequency Eq.(5.1.8), one gets

$$\begin{aligned}
\bar{\Gamma}_{z,turb} = {}& -\pi Z\sum_{\boldsymbol{k}\omega}\int\delta\left(\omega-\omega_d-k_\parallel v_\parallel\right)\left|\bar{v}_{E,\boldsymbol{k},\omega}\right|^2F_{z,eq}d^3v\\
&\times\left[\frac{\partial\ln N_{z,eq}}{\partial r}+\left(\frac{H_{eq}}{T_{z,eq}}-\frac{3}{2}\right)\frac{\partial\ln T_{z,eq}}{\partial r}+\frac{\left(v_\parallel-V_{\parallel z,eq}\right)}{v_T^2}\frac{\partial V_{\parallel z,eq}}{\partial r}-\frac{eB}{k_\theta T_{z,eq}}\omega\right]
\end{aligned} \qquad (5.2.4)$$

The velocity integral is intricate due to the resonance condition. But it is clear from Eq.(5.2.4) that the flux of impurity takes the general form

$$\bar{\Gamma}_{z,turb} = D_N N_{z,eq}\left[\frac{\partial \ln N_{z,eq}}{\partial r} + C_T \frac{\partial \ln T_{z,eq}}{\partial r} + C_V \frac{\partial V_{\parallel z,eq}}{\partial r} + V_p\right] \tag{5.2.5}$$

with

$$\begin{aligned}
D_N &= -\frac{\pi Z}{N_{z,eq}} \sum_{\boldsymbol{k}\omega} \int \delta\left(\omega - \omega_d - k_\parallel v_\parallel\right) \left|\bar{v}_{E,\boldsymbol{k},\omega}\right|^2 F_{z,eq} d^3v \\
D_N N_{z,eq} C_T &= -\pi Z \sum_{\boldsymbol{k}\omega} \int \left(\frac{H_{eq}}{T_{z,eq}} - \frac{3}{2}\right) \delta\left(\omega - \omega_d - k_\parallel v_\parallel\right) \left|\bar{v}_{E,\boldsymbol{k},\omega}\right|^2 F_{z,eq} d^3v \\
D_N N_{z,eq} C_V &= -\pi Z \sum_{\boldsymbol{k}\omega} \int \frac{\left(v_\parallel - V_{\parallel z,eq}\right)}{v_T^2} \delta\left(\omega - \omega_d - k_\parallel v_\parallel\right) \left|\bar{v}_{E,\boldsymbol{k},\omega}\right|^2 F_{z,eq} d^3v \\
D_N N_{z,eq} V_p &= \pi Z \sum_{\boldsymbol{k}\omega} \int \frac{eB}{k_\theta T_{z,eq}} \omega \delta\left(\omega - \omega_d - k_\parallel v_\parallel\right) \left|\bar{v}_{E,\boldsymbol{k},\omega}\right|^2 F_{z,eq} d^3v
\end{aligned}$$

The terms D_N, C_T, C_V and V_p represent respectively diffusion, thermo-diffusion, roto-diffusion and pure convection. The values of these coefficients can be found for instance in [5] where they were derived in the plasma rotating frame. The latter approach makes explicit the specific contributions of the centrifugal force and of the Coriolis force.

Some qualitative conclusions can be drawn from Eq.(5.2.5). First of all, the turbulent impurity flux scales like the turbulence intensity squared $\bar{\Gamma}_{z,turb} \propto \left|\bar{v}_{E,\boldsymbol{k},\omega}\right|^2$. This result is intuitive: more turbulent fluctuations lead to a larger turbulent flux. Thermo-diffusion and roto-diffusion are expected to change sign depending on the turbulence nature of the underlying instability. Both terms are expected to give an outward flux for ITG turbulence [14]. The sign of the pure convection is not as clear and depends on the specific situation.

6. Neoclassical impurity flux in presence of poloidal asymmetries

Contents

5.1. ITG turbulence 100
  5.1.1. Underlying instability 100
  5.1.2. Linear stability 101
  5.1.3. Turbulence saturation processes 106
5.2. Theoretical prediction of impurity transport related with turbulence 107

6.1. Experimental evidence of poloidal asymmetries of impurity

Poloidal asymmetry of the impurity distribution is often observed experimentally. An example coming from a JET discharge [58] is shown in the Fig.6.1. In this figure, the radiated power shows a large poloidal asymmetry in the center. This asymmetry is associated with a density asymmetry of the impurity. Poloidal asymmetries are often associated with external heating systems. A way to appreciate how heating systems can generate poloidal asymmetries of the impurity density is to consider the following formula [10, 16]

$$\begin{aligned}\frac{N_z(\psi,\theta)}{N_z^\star(\psi)} &= \frac{T_{\perp,z}(\psi,\theta)}{T_{\perp,z}^\star(\psi)} \\ &\quad \times \exp\left\{-\frac{eZ\left[\phi(\psi,\theta)-\phi^\star(\psi)\right]}{T_{\parallel,z}(\psi)} + \frac{m_z\Omega_z^2}{2T_{\parallel,z}(\psi)}\left[R^2(\psi,\theta)-R^{\star 2}(\psi)\right]\right\}\end{aligned} \tag{6.1.1}$$

where the quantities with a star are taken at the outer mid-plane $f^\star(\psi) = f(\psi,\theta=0)$. In this formula, a rigid body like rotation is assumed for the impurity Ω_z. In Eq.(6.1.1), the poloidal asymmetry of the perpendicular temperature is associated with anisotropy.

$$\frac{T_{\perp,z}(\psi,\theta)}{T_{\perp,z}^\star(\psi)} = \left[\frac{T_{\perp,z}^\star(\psi)}{T_{\parallel,z}(\psi)} + \left(1-\frac{T_{\perp,z}^\star(\psi)}{T_{\parallel,z}(\psi)}\right)\frac{B^\star(\psi)}{B(\psi,\theta)}\right] \tag{6.1.2}$$

Eq.(6.1.1) clearly shows that toroidal rotation can generate density asymmetry. This is in particular the case when Neutral Beam Injection (NBI) is used for current generation [6]. The combination of Eq.(6.1.1) and Eq.(6.1.2) indicates that anisotropic heating like the one provided by Ion Cyclotron Resonance Heating (ICRH) can produce an asymmetric density distribution [60, 74].

Figure 6.1.: Poloidal reconstruction of radiative power loss in a JET discharge [58]. This radiative power is attributed to impurity.

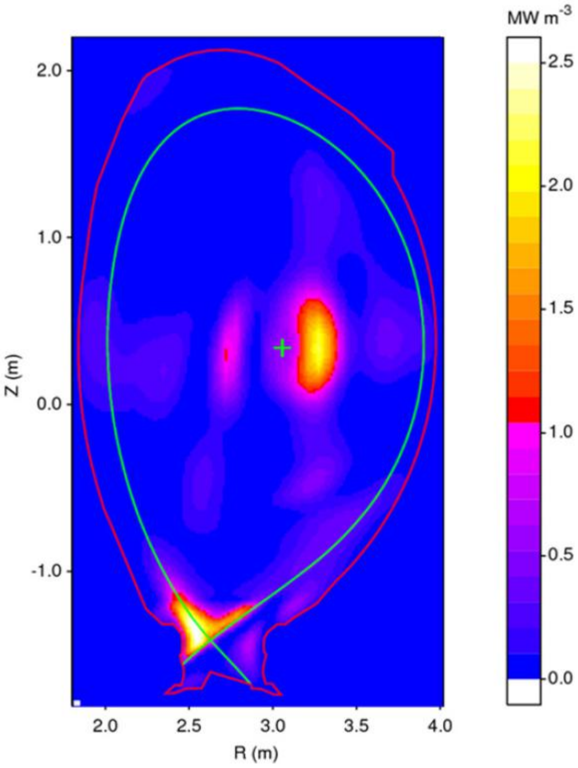

6.2. Neoclassical impurity flux in presence of large poloidal asymmetries and pressure anisotropy

In current tokamaks, heavy impurities like tungsten are in the Pfirsch-Schlüter regime. But on larger devices, like ITER, heavy impurities should be in the plateau regime due to higher temperatures. The banana-plateau contribution of the impurity flux is expected to be linked to the pressure anisotropy. Moreover, the poloidal asymmetry of the impurity density is known to modify significantly (up to an order of magnitude) neoclassical flux of impurity in the Pfirsch-Schlüter regime [4]. It is therefore natural to take into account both pressure anisotropy and poloidal asymmetries of the impurity for the computation of the neoclassical flux of impurities.

The computation of the neoclassical impurity flux in this framework is done in three steps. First, the perpendicular flow is expressed. An unknown function $K_z(\psi, \theta)$, related to the impurity poloidal velocity, is then determined using the incompressibility of the flow and parallel force balance. It leads to the expression of the impurity flux.

6.2.1. Structure of the impurity flow in presence of poloidal asymmetries

We come back to the computation performed in section 4.4.1. For the main ion species, it is assumed that there are no changes. In other words, poloidal asymmetries and anisotropy of the ion species are still at their neoclassical level which is small. On the other hand, large poloidal asymmetries and anisotropy are now allowed for the impurity.

We now come back to the general expression of the impurity flux derived in the drift kinetic limit (i.e. neglecting finite Larmor radius effects) in section 4.4.1.

$$\mathbf{\Gamma}_z = \Gamma_{\|z}\mathbf{b}_{eq} + N_z\frac{\mathbf{B}}{B^2}\times\nabla\phi + \frac{\mathbf{B}}{ZeB^2}\times\nabla\cdot\mathbf{\Pi}_z \tag{6.2.1}$$

where the CGL tensor $\mathbf{\Pi}_z$ reads

$$\mathbf{\Pi}_z = P_{\perp z}\mathbf{I} + \Pi_{\|z}\mathbf{b}_{eq}\mathbf{b}_{eq}$$

and $\Pi_{\|z} = P_{\|z} - P_{\perp z}$. It has been shown (Eq.(4.4.6)) that the divergence of the CGL tensor reads

$$\nabla\cdot\mathbf{\Pi}_z = \nabla P_{\perp z} + \Pi_{\|z}\boldsymbol{\kappa} + \left[(\mathbf{B}\cdot\nabla)\left(\frac{\Pi_{\|z}}{B}\right)\right]\mathbf{b}_{eq}$$

Where $\boldsymbol{\kappa} = -\mathbf{b}_{eq}\times(\nabla\times\mathbf{b}_{eq})$ is the field curvature. Noting that $\nabla\phi = \frac{\partial\phi}{\partial\psi}\nabla\psi + \frac{\partial\phi}{\partial\theta}\nabla\theta$ and $\nabla P_{\perp z} = \frac{\partial P_{\perp z}}{\partial\psi}\nabla\psi + \frac{\partial P_{\perp z}}{\partial\theta}\nabla\theta$, and using the identity

$$\frac{\mathbf{B}}{B^2}\times\nabla\psi = I\frac{\mathbf{B}}{B^2} - R^2\nabla\varphi$$

one can express the impurity flux as follow

$$\mathbf{\Gamma}_z = K_z\mathbf{B} - N_z\Omega_zR^2\nabla\varphi + \frac{\Pi_{\|z}}{ZeB}\left(\mathbf{b}_{eq}\times\boldsymbol{\kappa}\right) + \left(N_z\frac{\partial\phi}{\partial\theta} + \frac{1}{Ze}\frac{\partial P_{\perp z}}{\partial\theta}\right)\frac{\mathbf{B}}{B^2}\times\nabla\theta$$

All quantities depend on (ψ,θ) and the following definitions have been introduced

$$\Omega_z = \frac{\partial\phi}{\partial\psi} + \frac{1}{N_zZe}\frac{\partial P_{\perp z}}{\partial\psi}$$

$$K_z = \frac{\Gamma_{\|z}}{B} + \frac{I}{B^2}N_z\Omega_z$$

6.2.2. Determination of the poloidal variation of K_z

The poloidal variation of $K_z(\psi,\theta)$ is constrained by the incompressibility of the flow $\nabla\cdot\mathbf{\Gamma}_z = 0$, which reads

$$(\mathbf{B}\cdot\nabla)\,K_z + \nabla\cdot\tilde{\mathbf{\Gamma}}_z = 0 \tag{6.2.2}$$

where

$$\tilde{\mathbf{\Gamma}}_z = \frac{\Pi_{\parallel z}}{ZeB}\left(\mathbf{b}_{eq}\times\boldsymbol{\kappa}\right) + \left(N_z\frac{\partial\phi}{\partial\theta} + \frac{1}{Ze}\frac{\partial P_{\perp z}}{\partial\theta}\right)\frac{\mathbf{B}}{B^2}\times\nabla\theta$$

The expression of the divergence of a vector $\boldsymbol{V}$ that does not depend on φ is

$$\frac{\nabla\cdot\boldsymbol{V}}{\mathbf{B}\cdot\nabla\theta} = \frac{\partial}{\partial\psi}\left(\frac{\boldsymbol{V}\cdot\nabla\psi}{\mathbf{B}\cdot\nabla\theta}\right) + \frac{\partial}{\partial\theta}\left(\frac{\boldsymbol{V}\cdot\nabla\theta}{\mathbf{B}\cdot\nabla\theta}\right)$$

Using the following relations

$$\begin{aligned}
(\mathbf{b}_{eq}\times\boldsymbol{\kappa})\cdot\nabla\psi &= I\mathbf{B}\cdot\nabla\theta\frac{\partial}{\partial\theta}\left(\frac{1}{B}\right)\\
(\mathbf{b}_{eq}\times\boldsymbol{\kappa})\cdot\nabla\theta &= -I\mathbf{B}\cdot\nabla\theta\frac{\partial}{\partial\psi}\left(\frac{1}{B}\right)\\
(\mathbf{B}\times\nabla\theta)\cdot\nabla\psi &= -I\mathbf{B}\cdot\nabla\theta
\end{aligned}$$

one then obtains

$$\frac{\nabla\cdot\tilde{\mathbf{\Gamma}}_z}{\mathbf{B}\cdot\nabla\theta} = \frac{\partial}{\partial\theta}\left[\frac{1}{B}\frac{\partial}{\partial\psi}\left(\frac{I\Pi_{\parallel z}}{ZeB}\right)\right] - \frac{\partial}{\partial\psi}\left\{\frac{I}{ZeB^2}\left[N_zZe\frac{\partial\phi}{\partial\theta} + \frac{\partial P_{\perp z}}{\partial\theta} + B\frac{\partial}{\partial\theta}\left(\frac{\Pi_{\parallel z}}{B}\right)\right]\right\} \tag{6.2.3}$$

At this stage, one can note that in the absence of poloidal asymmetries $(\partial_\theta = 0)$ and pressure anisotropy $\left(\Pi_{\parallel z} = 0\right)$, $\nabla\cdot\tilde{\mathbf{\Gamma}}_z = 0$. Therefore K_z depends on ψ only as in the case developed in section 4.4.1. For low Mach number, the parallel force balance reads

$$\mathbf{B}\cdot\nabla\theta\left[N_zZe\frac{\partial\phi}{\partial\theta} + \frac{\partial P_{\perp z}}{\partial\theta} + B\frac{\partial}{\partial\theta}\left(\frac{\Pi_{\parallel z}}{B}\right)\right] = BR_{\parallel zi} \tag{6.2.4}$$

Then putting together Eq.(6.2.2), (6.2.3) and (6.2.4) an equation for K_z can be derived

$$\frac{\partial}{\partial\theta}\left[K_z + \frac{1}{B}\frac{\partial}{\partial\psi}\left(\frac{I\Pi_{\parallel z}}{ZeB}\right)\right] = \frac{\partial}{\partial\psi}\left[\frac{IR_{\parallel zi}}{ZeB\,(\mathbf{B}\cdot\nabla\theta)}\right] \tag{6.2.5}$$

We note here that an integration on θ of Eq.(6.2.5) leads to $\frac{\partial\Gamma^{\psi}_{z,neo}}{\partial\psi} = 0$, where the neoclassical impurity flux is given by Eq.(4.4.2) $\Gamma^{\psi}_{z,neo} = -\frac{I}{Ze}\left\langle\frac{R_{\parallel zi}}{B}\right\rangle_\psi$. This condition can seem surprising at first sight. But on second thoughts, this condition is natural. Indeed, in the approach considered, there is no source of particles, no turbulence and we consider a steady state solution. The neoclassical flux of impurity is therefore equal to a constant. To alleviate this conceptual paradox, one should keep in mind that we neglect time derivatives in the neoclassical theory because they typically scale as the inverse of the confinement time which is much larger than any other typical time of the problem. But rigorously, time derivatives are not equal to zero. Having this fact in mind, we continue our analysis.

Unfortunately, the analytical solution of Eq.(6.2.5) is not trivial as $R_{\parallel zi}$ is an implicit function of K_z. To continue the analytical derivation, we neglect the rhs of Eq.(6.2.5). This is the equivalent of neglecting locally the collisional contribution in the parallel force balance Eq.(6.2.4). It can be shown that this approximation is valid if $Z\sqrt{\epsilon}\nu_{\star,i}q \ll 1$. This approximation is therefore valid for light impurities or if the collisionality of the main ion species is low enough. Note that even though the collision friction is neglected locally in the parallel force balance Eq.(6.2.4), it has to be kept in its flux surface average version, for the expression of the neoclassical flux. It is quite remarkable that no solubility problem arises when the friction force is neglected locally in Eq.(6.2.4). The function K_z then reads $K_z(\psi,\theta) = K_{z0}(\psi) + K_{z1}(\psi,\theta)$, where

$$K_{z0} = \langle K_z \rangle_\psi$$

$$K_{z1} = -\frac{1}{B}\frac{\partial}{\partial\psi}\left(\frac{I\Pi_{\parallel z}}{ZeB}\right) + \left\langle \frac{1}{B}\frac{\partial}{\partial\psi}\left(\frac{I\Pi_{\parallel z}}{ZeB}\right)\right\rangle_\psi \tag{6.2.6}$$

Here, the bracket denotes the flux surface average :

$$\langle f \rangle_\psi = \frac{\oint \frac{d\theta d\varphi}{\mathbf{B}\cdot\nabla\theta} f}{\oint \frac{d\theta d\varphi}{\mathbf{B}\cdot\nabla\theta}}$$

6.2.3. Neoclassical flux

If the main ion is in the banana regime, it can be shown that the friction force reads (proof is in appendix D)

$$R_{\parallel zi} = m_z \nu_{zi}\left\{-N_Z \frac{T_i}{eB}\frac{I}{L_\psi} + B\left(N_z u - K_z\right)\right\} \tag{6.2.7}$$

where $\frac{1}{L_\psi} = \frac{1}{L_{\psi,i}} + \frac{1}{L_{\psi,z}}$ with $\frac{1}{L_{\psi,i}} = \frac{\partial \ln P_i}{\partial\psi} - \frac{3}{2}\frac{\partial \ln T_i}{\partial\psi}$ and $\frac{1}{L_{\psi,z}} = -\frac{1}{T_i Z N_z}\frac{\partial P_{\perp z}}{\partial\psi}$. $L_{\psi,i}$ is a flux function whereas $L_{\psi,z}$ is a function of ψ and θ. In Eq.(6.2.7) u is a flux function given by

$$u = \left(k_{neo} - \frac{3}{2}\right) \frac{I}{e \left\langle B^2 \right\rangle_\psi} \frac{\partial T_i}{\partial \psi} \tag{6.2.8}$$

This quantity is closely link to the poloidal rotation of the main ion species as can be seen in its expression. If the main ion is in the banana regime, impurities in the trace limit $\frac{N_z Z^2}{N_i} \ll 1$ and large aspect ratio are considered $\epsilon \ll 1$, then $k_{neo} \simeq 1.17$ and u takes the limit given in the literature [32] $u \simeq -0.33 \frac{I}{e\langle B^2\rangle} \frac{\partial T_i}{\partial \psi}$. This value is used in the following. Note that ν_{zi} is also a flux function. Using Eq.(6.2.4), while keeping the friction force leads to the solubility constraint

$$\left\langle \frac{B R_{\parallel zi}}{N_z} \right\rangle_\psi = \left\langle \frac{\mathbf{B} \cdot \nabla \theta}{N_z} \left[\frac{\partial P_{\perp z}}{\partial \theta} + B \frac{\partial}{\partial \theta} \left(\frac{\Pi_{\parallel z}}{B} \right) \right] \right\rangle_\psi \tag{6.2.9}$$

Combining Eq.(6.2.6), Eq.(6.2.7) and Eq.(6.2.9), one finds

$$\begin{aligned} K_{z0} = & -\frac{T_i I}{e} \left\langle \frac{1}{L_\psi} \right\rangle_\psi \left\langle \frac{B^2}{N_Z} \right\rangle_\psi^{-1} + u \left\langle B^2 \right\rangle_\psi \left\langle \frac{B^2}{N_z} \right\rangle_\psi^{-1} \\ & + \left\langle \frac{B}{N_z} \frac{\partial}{\partial \psi} \left(\frac{I \Pi_{\parallel z}}{ZeB} \right) \right\rangle_\psi \left\langle \frac{B^2}{N_z} \right\rangle_\psi^{-1} - \left\langle \frac{1}{B} \frac{\partial}{\partial \psi} \left(\frac{I \Pi_{\parallel z}}{ZeB} \right) \right\rangle_\psi \\ & - \frac{1}{m_z \nu_{zi}} \left\langle \frac{\mathbf{B} \cdot \nabla \theta}{N_z} \left[\frac{\partial P_{\perp z}}{\partial \theta} + B \frac{\partial}{\partial \theta} \left(\frac{\Pi_{\parallel z}}{B} \right) \right] \right\rangle_\psi \left\langle \frac{B^2}{N_z} \right\rangle_\psi^{-1} \end{aligned} \tag{6.2.10}$$

These expression of K_{z0} can then be plugged into the friction force to calculate the impurity radial flux $\Gamma^\psi_{z,neo}$, i.e.

$$\Gamma^\psi_{z,neo} = \Gamma^\psi_{z,BP} + \Gamma^\psi_{z,PS} \tag{6.2.11}$$

$$\Gamma^\psi_{z,BP} = -\frac{I}{Ze} \frac{1}{\left\langle \frac{B^2}{N_z} \right\rangle_\psi} \left\langle \frac{\mathbf{B} \cdot \nabla \theta}{N_z} \left[\frac{\partial P_{\perp z}}{\partial \theta} + B \frac{\partial}{\partial \theta} \left(\frac{\Pi_{\parallel z}}{B} \right) \right] \right\rangle_\psi \tag{6.2.12}$$

$$\begin{aligned}\Gamma^{\psi}_{z,PS} \quad = \quad & \frac{I}{Ze} m_z \nu_{zi} \left\{ \frac{T_i}{e} \frac{I}{L_{\psi,i}} \left(\left\langle \frac{N_z}{B^2} \right\rangle_{\psi} - \frac{1}{\left\langle \frac{B^2}{N_z} \right\rangle_{\psi}} \right) - u \left(\langle N_z \rangle_{\psi} - \frac{\langle B^2 \rangle_{\psi}}{\left\langle \frac{B^2}{N_z} \right\rangle_{\psi}} \right) \right. \\ & + \frac{T_i I}{e} \left(\left\langle \frac{N_z}{B^2 L_{\psi,z}} \right\rangle_{\psi} - \left\langle \frac{1}{L_{\psi,z}} \right\rangle_{\psi} \frac{1}{\left\langle \frac{B^2}{N_z} \right\rangle_{\psi}} \right) \\ & \left. - \left\langle \frac{1}{B} \frac{\partial}{\partial \psi} \left(\frac{I \Pi_{\| z}}{ZeB} \right) \right\rangle_{\psi} + \frac{\left\langle \frac{B}{N_z} \frac{\partial}{\partial \psi} \left(\frac{I \Pi_{\| z}}{ZeB} \right) \right\rangle_{\psi}}{\left\langle \frac{B^2}{N_z} \right\rangle_{\psi}} \right\} \end{aligned} \tag{6.2.13}$$

Eq.(6.2.12) can be seen as a modification of the banana-plateau flux. Note that it is independent of the interspecies collisionality and will therefore dominate for low collisionality regimes.

The first and second terms of Eq.(6.2.13) are identical to Eq.(10) of [4] for which only poloidal density asymmetries are considered. The third term corresponds to a simple diffusion which is often neglected but can become important when impurity peaking is strong. The last two terms are entirely controlled by K_{z1}, and represent a modification of the friction force due to the impurity pressure anisotropy.

6.3. Comparison with results from gyrokinetic simulations

The goal of this section is to assess the relative importance of the various contributions in the neoclassical prediction derived in the previous section Eq.(6.2.11) using the results of simulations performed with the GYSELA code.

6.3.1. Choice of the simulation parameters

Different simulations have been performed with the GYSELA code to test the theoretical prediction previously derived. Two parameters have been played with: the nature of the impurity (He versus W) and the collisionality of the main ion at mid-radius. Helium is considered as fully ionized $Z = 2$, whereas a fixed charge state ($Z = 40$) is taken for tungsten cases. For these simulations, the main ion species is deuterium and the impurity is in the trace limit $\left(\frac{N_z Z^2}{N_i} \sim 10^{-3}\right)$. The electron response is adiabatic. The size of the machine simulated is fixed by the dimensionless parameter $\rho_{\star,i} = \frac{\rho_i}{a} = \frac{1}{190}$ where ρ_i is the Larmor radius of a thermal ion at mid-radius. GYSELA uses a simplified geometry with circular concentric magnetic surfaces characterized by an inverse aspect ratio $\frac{R_0}{a} = 4.4$ and a safety factor profile $q\left(r\right) = 1.5 + 1.3 \exp\left[2.5 \log\left(\frac{r}{a}\right)\right]$. The two ion species are initiated with identical density and temperature profiles $\frac{d\ln n_s(r)}{dr} = -2.2 \cosh^{-2}\left(\frac{\rho-0.5}{0.04}\right)$ and $\frac{d\ln T_s(r)}{dr} = -6 \cosh^{-2}\left(\frac{\rho-0.5}{0.04}\right)$. To approach a statistical steady state, an isotropic source of energy is added [38]. Its amplitude depends only on the radius. Finally, the outer boundary condition is ensured via a penalization technique [24]. More precisely, a krook term with a radial dependence is applied on the distribution function. It allows to extract the energy coming from the heat flux without injecting/removing particles.

The phase-space grid is well resolved. In the case of helium impurity, the numerical resolution is $\left(N_r, N_\theta, N_\varphi, N_{v_\parallel}, N_\mu\right) = (256, 512, 32, 127, 64)$, whereas for tungsten the resolution is higher $\left(N_r, N_\theta, N_\varphi, N_{v_\parallel}, N_\mu\right) = (512, 1024, 32, 127, 64)$. This difference of resolution comes from the dependence of the Larmor radius of the impurity $\rho_z = \frac{1}{Z}\sqrt{\frac{m_z}{m_i}}\rho_i$ (assuming $T_i = T_z$). In both cases, the time step is $\Delta t\omega_{ci} = 16$ and is chosen to resolve accurately both turbulent and collisional time scales. Because of this high resolution and the presence of two species, the numerical cost of this simulation is very large. In order to reduce this cost, the following strategy has been used: in a first stage, the code is run without impurity until statistical steady-state with a resolution of $\left(N_r, N_\theta, N_\varphi, N_{v_\parallel}, N_\mu\right) = (256, 512, 32, 127, 64)$ which is enough for the main ion species. If the impurity that is studied is tungsten, a second step is performed, with a resolution increased in view of the later impurity introduction $\left(N_r, N_\theta, N_\varphi, N_{v_\parallel}, N_\mu\right) = (512, 1024, 32, 127, 64)$. This step, performed without impurities, is done to allow for some reorganization of the system when numerical resolution is increased. Eventhough this reorganization is rather short, it is numerically cheaper to perform it in absence of impurities. Finally, the impurity is added when statistical steady-state is reached without impurities. Despite this strategy, the convergence of a simulation with impurity toward a statistical steady-state still requires several millions of CPU hours.

The various scanned parameters are given in Tab.6.1. The result of the three performed simulations has been used to derive the theoretical prediction presented in section 6.2. But it has been rapidly realized that the numerical cost of a converged simulation would severely limit the number of cases that could be studied. In particular, the cases with the lower collisionalities were really far from convergence. It has therefore been decided to focus on a single well resolved simulation for a quantitative comparison between theory and simulation. Considering the problem of convergence, the choice of a “large” collisionality has been made: $\nu_i^\star\left(\frac{r}{a} = 0.5\right) = 10^{-1}$. Tungsten has been chosen for this well resolved simulation for two reasons: Firstly, the understanding of tungsten transport is important in current tokamak discharges, in particular for the tokamak WEST which should run with full tungsten divertor and walls. Secondly, tungsten has been chosen to have a collisionality profile of the impurity close to the

Table 6.1.: Parameters scanned

simulation	$\nu_i^\star\left(\frac{r}{a}=0.5\right)$	impurity
A	10^{-2}	He
B	10^{-2}	W
C	10^{-1}	W

plateau/Pfirsch-Schlüter transition in order to compare the simulation and theoretical predictions of the banana/plateau and the Pfirsch-Schlüter fluxes with a single simulation. The collisionality of tungsten in the considered simulation is given in the Fig.6.2. The impurity is in the Pfirsch-Schlüter regime in all the simulation domain but in the region ranging between $0.15 \leq \frac{r}{a} \leq 0.4$ where it is close to the plateau regime.

Despite the choice to focus on a single simulation, this simulation is not in the quasi steady-state and departure from stationarity is expected to play a role in particular in the parallel force balance Eq.(6.2.4). As the model derived in the previous section is strictly valid only for steady-state, a perfect match between the neoclassical flux given by the code and the theoretical prediction is not expected. Nevertheless, it turns out that the flux predicted by the model presented in section 6.2.3 gives the right order of magnitude for the impurity flux coming from GYSELA as will be discussed hereafter. Note that the cost of this single simulation is approximately 3 millions of CPU hours. This cost did not allow a large scan of parameters.

Figure 6.2.: Radial variation of collisionality of the impurity (blue). The limit between plateau and Pfirsch-Schlüter regime is represented by the black line

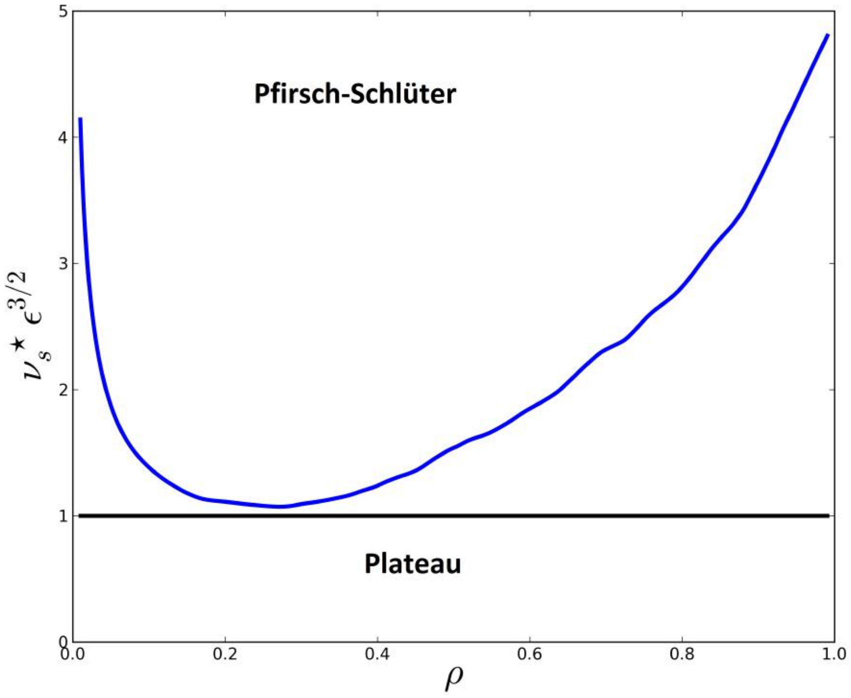

6.3.2. Definitions of fluxes

The flux of particles coming from GYSELA does not make any difference between neoclassical and turbulent fluxes as both are treated self-consistently within the code. This observation raises the question of how to separate the two contributions *a posteriori*. For this purpose, the definitions proposed by Esteve et al. [31] are used:

$$\langle \Gamma_s^{neo} \cdot \nabla\psi \rangle_\psi = \left\langle \int d^3v \bar{f}_s \left(\boldsymbol{v}_{D,s} + \bar{\boldsymbol{v}}_E^{n=0} \right) \cdot \nabla\psi \right\rangle_\psi \tag{6.3.1}$$

$$\left\langle \Gamma_s^{turb} \cdot \nabla\psi \right\rangle_\psi = \left\langle \int d^3v \bar{f}_s \bar{\boldsymbol{v}}_E^{n\neq0} \cdot \nabla\psi \right\rangle_\psi \tag{6.3.2}$$

where $\bar{\boldsymbol{v}}_E^{n=0} = \langle \bar{\boldsymbol{v}}_E \rangle_\varphi$ and $\bar{\boldsymbol{v}}_E^{n\neq0} = \bar{\boldsymbol{v}}_E - \bar{\boldsymbol{v}}_E^{n=0}$. The definition of these fluxes is not unique and some authors call “turbulent” the flux associated with the $E \times B$ drift and “neoclassical” the flux associated with the magnetic field drift. These fluxes are defined as

$$\left\langle \Gamma_s^D \cdot \nabla\psi \right\rangle_\psi = \left\langle \int d^3v \bar{f}_s \boldsymbol{v}_{D,s} \cdot \nabla\psi \right\rangle_\psi \tag{6.3.3}$$

$$\left\langle \Gamma_s^E \cdot \nabla\psi \right\rangle_\psi = \left\langle \int d^3v \bar{f}_s \bar{\boldsymbol{v}}_E \cdot \nabla\psi \right\rangle_\psi \tag{6.3.4}$$

Fig.6.3 depicts the different fluxes for the impurity in the simulation presented in the previous section. There is a clear difference between the definitions of the turbulent and neoclassical fluxes (solid lines) and the definitions sometimes found in the literature (dotted lines). This observation tells us that the axisymmetric modes of the electric potential actively contribute to the impurity flux. Note also that turbulent and neoclassical fluxes are of the same order of magnitude, although sometimes of different signs. The overall transport of tungsten is mainly inward in this simulation.

For a fair comparison with the theoretical prediction of the neoclassical flux derived in the section 6.2, it is mandatory to use the definition given in this thesis Eq.(6.3.1). This comparison is discussed in section 6.3.4.

Figure 6.3.: Radial variation of the impurity fluxes. These fluxes are time averaged on approximately $3000\omega_{ci}$.

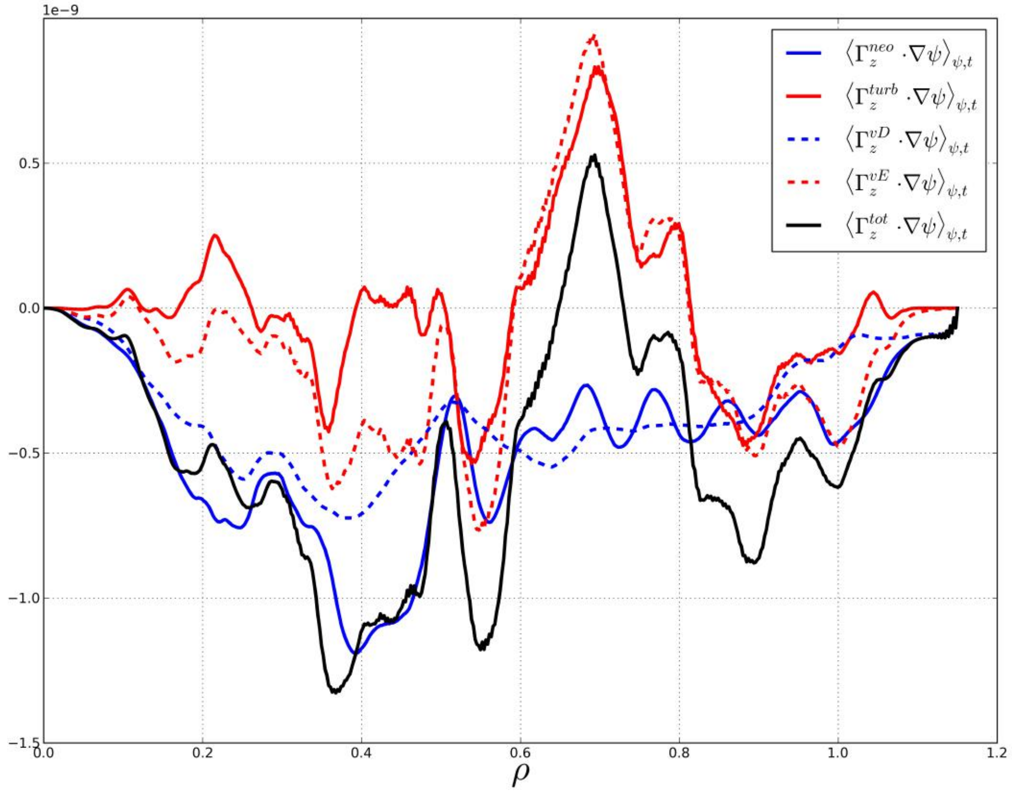

6.3.3. Poloidal asymmetries and anisotropy

In the considered GYSELA simulation, the poloidal asymmetries are generated by turbulence. The poloidal asymmetry of the tungsten density Fig.6.4 is of the order of 30% and can be expressed in the form [4]

$$N_z = \langle N_z \rangle (\psi) \left[1 + \delta (\psi) \cos\theta + \Delta (\psi) \sin\theta\right]$$

The knowledge of $\delta(\psi)$ and $\Delta(\psi)$ then allows one to compute the impact of density asymmetries on the first and third terms of $(6.2.11)$, which correspond to terms already present in the literature [4]. Indeed, one can show that these terms take the following simple expressions [4]:

$$\left\langle \frac{N_z}{B^2} \right\rangle_\psi - \frac{1}{\left\langle \frac{B^2}{N_Z} \right\rangle_\psi} = \frac{\langle N_z \rangle_\psi}{\langle B^2 \rangle_\psi} \left[2\epsilon\left(\epsilon + \delta\right) + \frac{\delta^2 + \Delta^2}{2}\right] \tag{6.3.5}$$

$$\langle N_z \rangle_\psi - \frac{\langle B^2 \rangle_\psi}{\left\langle \frac{B^2}{N_z} \right\rangle_\psi} = \langle N_z \rangle_\psi \left[\epsilon\delta + \frac{\delta^2 + \Delta^2}{2}\right] \tag{6.3.6}$$

In these expressions, the contribution of density poloidal asymmetry is contained only in the δ and Δ terms. Fig.6.5 shows the radial shape of Eq.$(6.3.5)$ and Eq.$(6.3.6)$ for the GYSELA simulation. It readily appears that both expressions remain close to their value at $\delta = \Delta = 0$, i.e. in the absence of any poloidal asymmetry. More precisely, the relative impact of the poloidal asymmetry of density compared with the one of the magnetic field is moderate in the deep core and weak in the outer part of the simulation.

Fig.6.6 shows that the poloidal asymmetries of both parallel and perpendicular pressure are significant in the inner part of the simulation where the banana/plateau contribution is expected to be important $(0.15 \leq \frac{r}{a} \leq 0.4)$.

Figure 6.4.: Left: poloidal asymmetry of the impurity density. Right: reconstruction of the poloidal asymmetry with $\delta\left(\psi\right)$ and $\Delta\left(\psi\right)$

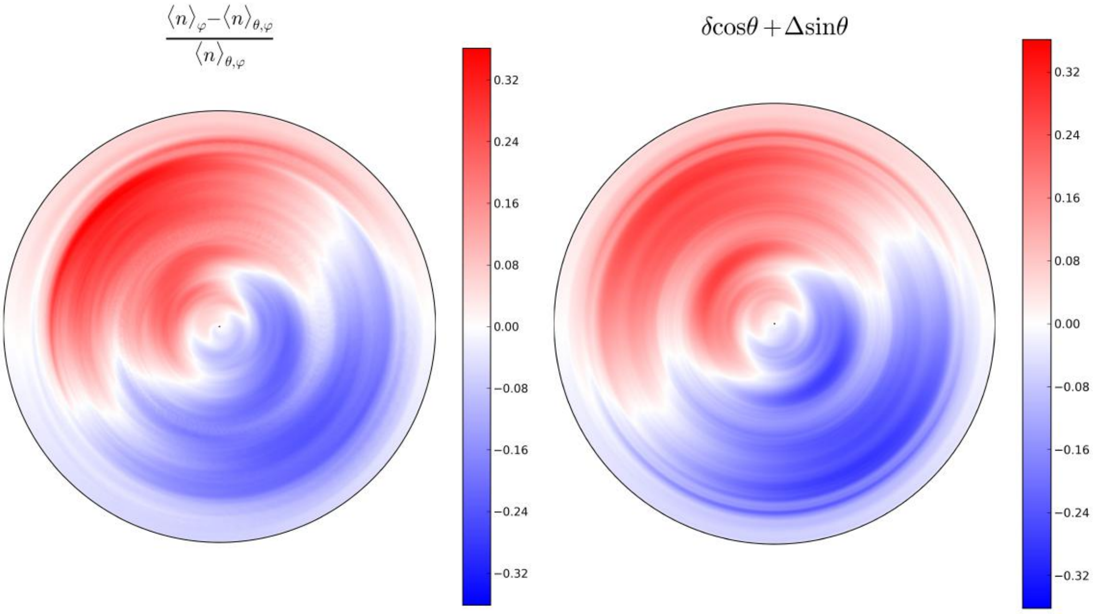

Figure 6.5.: Radial shape of Eq.(6.3.5) in red and Eq.(6.3.6) in green. The blue curve represents the radial shape of Eq.(6.3.5) in the absence of poloidal asymmetry of the impurity density, i.e. for $\delta = \Delta = 0$.

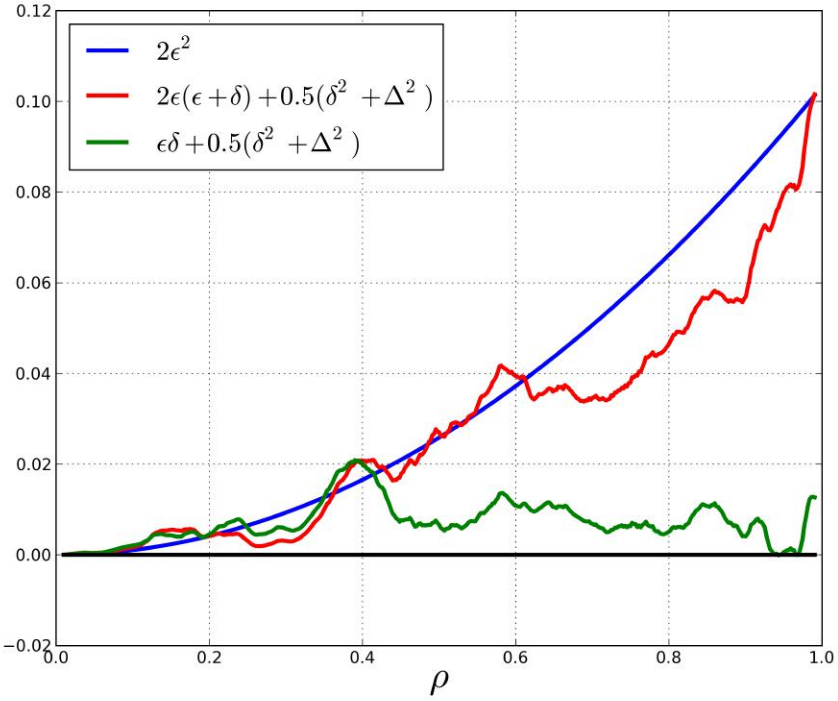

Figure 6.6.: Left: parallel pressure. Middle: perpendicular pressure. Right: CGL tensor divided by the magnetic field.

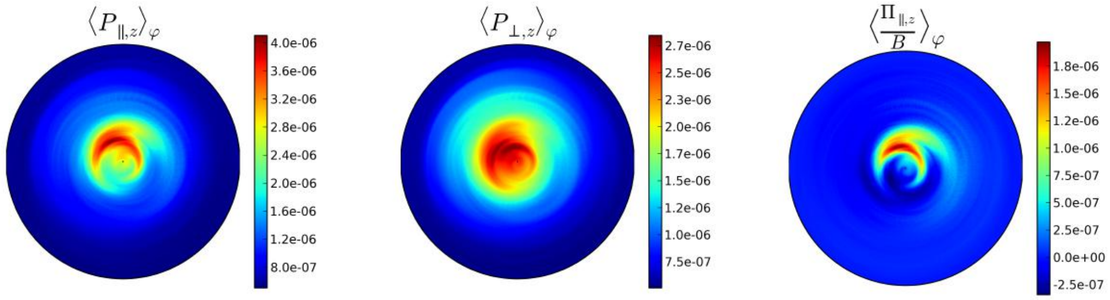

6.3.4. Comparison between GYSELA results and theoretical predictions

An important point for the comparison between the theoretical prediction and the results of the GYSELA code is the value of the screening factor. From the theoretical point of view, the Pfirsch-Schlüter component of the screening factor should be $H^{PS}_{theo} = -\frac{1}{2}$. This can be seen in the derivation performed in section 4.4.1. Alternatively, this value is contained in the expression of $\frac{1}{L_{\psi,i}} = \frac{\partial \ln P_i}{\partial \psi} - \frac{3}{2}\frac{\partial \ln T_i}{\partial \psi} = \frac{\partial \ln N_i}{\partial \psi} - \frac{1}{2}\frac{\partial \ln T_i}{\partial \psi}$. In this expression, there is a factor $+1$ coming from the difference of velocities ($\frac{\partial \ln P_i}{\partial \psi}$) and a factor $-\frac{3}{2}$ coming from the parallel heat flux ($-\frac{3}{2}\frac{\partial \ln T_i}{\partial \psi}$). It has already been mentioned in section 4.4.2 that the value of the parallel heat flux coming from GYSELA is not in agreement with the theoretical prediction Eq.(4.4.16). More precisely, the poloidal shape is in fair agreement with the theoretical prediction but the amplitude is approximately half the one predicted. For the neoclassical benchmark presented in section 4.4.2, this problem has been circumvented by imposing the parallel heat flux to take its theoretical value. With this trick a fair agreement has been found between the pure neoclassical case performed with GYSELA and the standard neoclassical prediction. In the simulation presented in this chapter, this trick was not used to avoid any artificial modification of the results of GYSELA. In the simulation used in this chapter, the parallel heat flux is still about one half of its theoretical prediction Eq.(4.4.16). The effect of this disagreement is to reduce drastically the thermal screening factor of the Pfirsch-Schlüter component $H^{PS}_{GYS} \simeq 0$.

The origin of the disagreement between the predicted parallel heat flux and the one observed in the code is still unclear. A remaining bug in the advection part of the code appears unlikely given the numerous tests and benchmarks already successfully performed [38], although it cannot be ruled out completly. Alternatively, the discrepancy could be due to some shortcomings of the theoretical prediction. Interstingly, we mention here that a benchmark of the gyrokinetic code GT5D against the standard neoclassical prediction in presence of impurity, in the same spirit as the one performed in section 4.4.2, seems to give a screening factor in the Pfirsch-Schlüter regime close to zero $H^{PS}_{GT5D} \simeq 0$, in line with GYSELA's results. The relative agreement between GYSELA and GT5D which are two independent codes points in the direction of a limitation of the thermal screening prediction. This observation could results from the necessity to take more moments in the development made in section 3.3.3. Indeed, it has been recently realized that the Pfirsch-Schlüter screening factor can be modified by the third moment of the distribution function in the development (j=2 in Eq.(3.3.3)) [50, 69]. If the third moments is retained, the Pfirsch-Schlüter screening factor is predicted to be close to zero. This explanation is still under investigation to explain the observations made by both codes. In the rest of this section, two distinct predictions are then used for the Pfirsch-Schlüter contribution of the flux Eq.(6.2.13). The first one, labeled with $H = -0.5$, is the one coming from the theory, i.e. with $\frac{1}{L_{\psi,i}} = \frac{\partial \ln P_i}{\partial \psi} - \frac{3}{2}\frac{\partial \ln T_i}{\partial \psi} = \frac{\partial \ln N_i}{\partial \psi} - \frac{1}{2}\frac{\partial \ln T_i}{\partial \psi}$. The second, labeled $H = 0$, is the same prediction but using a different definition of the ion gradient contribution $\frac{1}{L_{\psi,i}} = \frac{\partial \ln P_i}{\partial \psi} - \frac{\partial \ln T_i}{\partial \psi} = \frac{\partial \ln N_i}{\partial \psi}$. This distinction makes a huge difference in the outer part of the simulation, as discussed in the following.

Fig.6.7 shows the radial dependence of the banana/plateau contribution Eq.(6.2.12) (green curve) and the Pfirsch-Schlüter contribution Eq.(6.2.13) with the two definitions for $L_{\psi,i}$. The Pfirsch-Schlüter prediction with $H = -\frac{1}{2}$ is depicted in red and the one wit $H = 0$ is depicted in blue. From this figure, it is clear that the banana/plateau contribution is large where the impurity is close to the plateau regime ($0.15 \leq \frac{r}{a} \leq 0.4$) as expected . For the Pfirsch-Schlüter component, there is a large impact of the screening factor, especially in the outer part of the simulation.

The final test consists in comparing the neoclassical flux coming from GYSELA with the neoclassical prediction Eq.(6.2.11). The definition of the neoclassical flux is given in Eq.(6.3.1).The comparison between the GYSELA results (black curve) and the theoretical prediction (red and blue curves) is depicted on Fig.6.8. The right order of magnitude is recovered with a vanishing thermal screening $H = 0$ (blue curve) as expected from the previous discussion.

Figure 6.7.: Components of the neoclassical flux. The banana/plateau contribution Eq.(6.2.12) is represented in green. The Pfirsch-Schlüter contribution Eq.(6.2.13) with $H = -\frac{1}{2}$ and $H = 0$ are depicted respectively by the red and the blue curves. The various profiles, including their possible asymmetries, are taken from the GYSELA simulation.

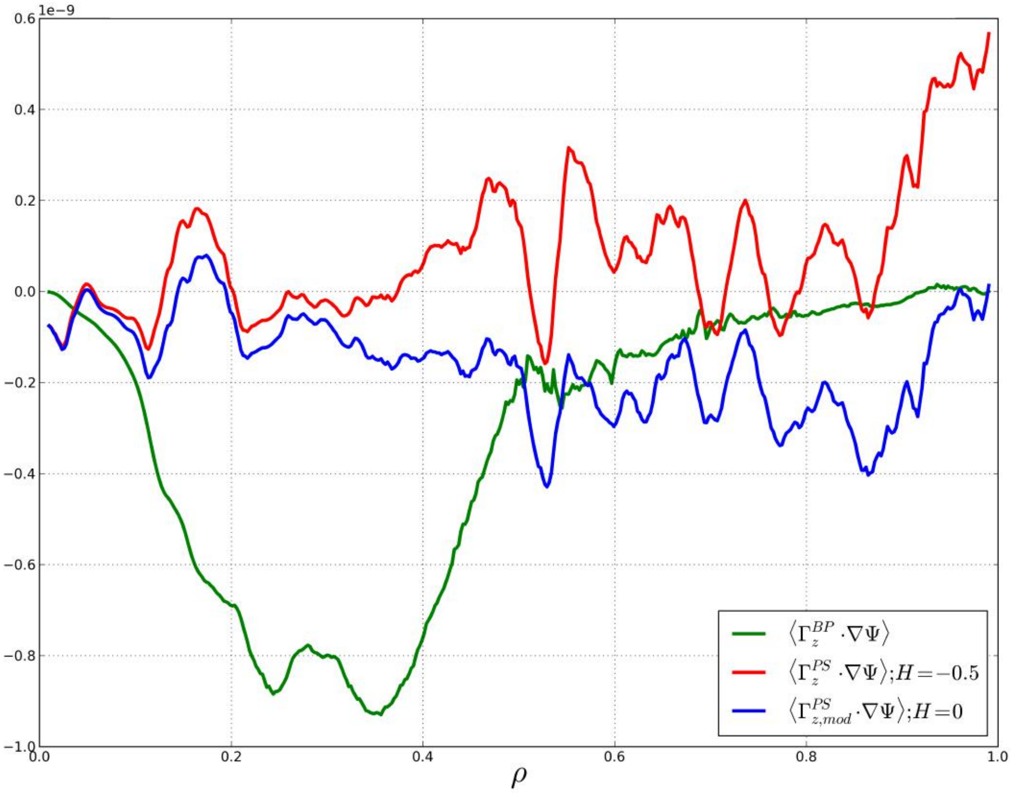

Figure 6.8.: Radial comparison of the theoretical predictions of the neoclassical radial impurity flux ($H = -\frac{1}{2}$ in red, $H = 0$ in blue) with the neoclassical flux coming from the GYSELA code (black).

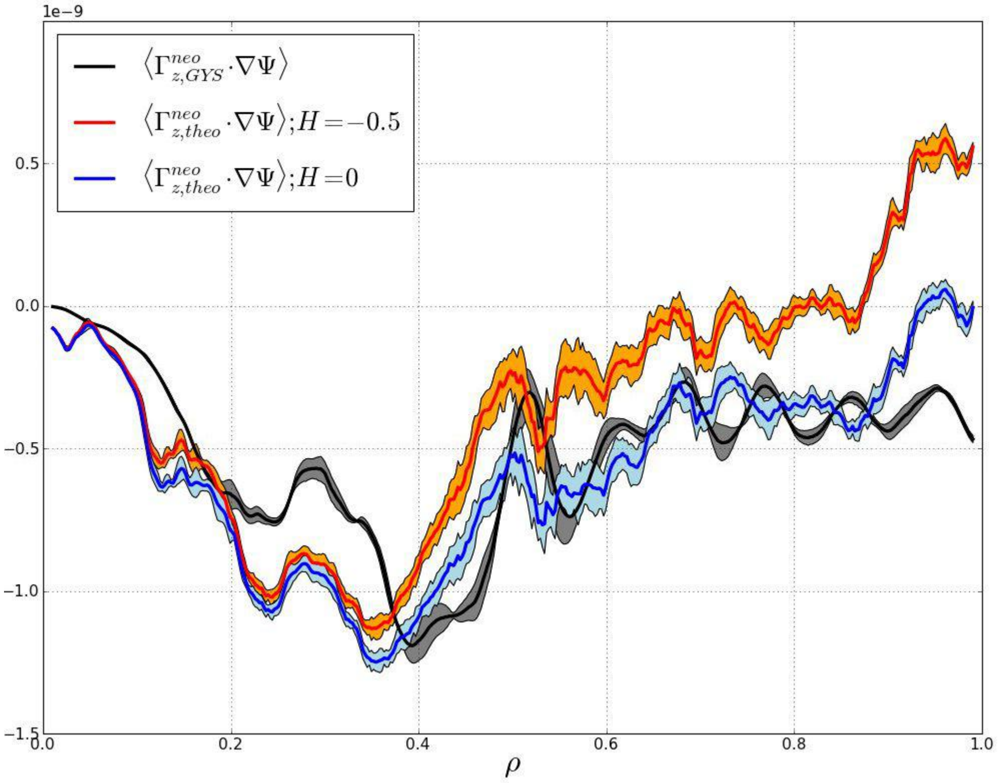

6.4. Discussion on the theoretical model

There is a rather good agreement between the theoretical prediction and the neoclassical flux coming from GYSELA provided a vanishing thermal screening factor $H \simeq 0$ is assumed. This point has already been discussed in the previous section. In this section, other limitations of the theoretical model developed in section 6.2 are discussed. The goal of this discussion is to clarify the limitations of the current theoretical prediction in view of future developments.

A first limitation of the model is to assume subsonic flows even for the impurity. Supersonic flows of impurity are indeed often observed in tokamaks, especially when NBI is applied. Note that in the GYSELA simulation used to test the model, the maximum Mach number is $\sim 40\%$ as shown in Fig.6.9. As the corrections are proportional to the square of the Mach number (see for instance the dependence in Ω_z^2 of Eq.(6.1.1)), the approximation of subsonic flows is acceptable in this particular case. To take into account the corrections due to supersonic flows, the full gyrokinetic equation should be used in the derivation instead of its drift kinetic limit. It would also introduce the gyroviscous stress tensor which is due to FLR effects. In the same spirit, the model should take into account the Reynolds stress contribution to the stress tensor $\mathbf{\Pi}_z$. Indeed, due to presence of turbulence there is a non negligible force (divergence of the Reynolds stress) that should be taken into account in the parallel force balance. This is a difficult task but it would probably lead to a modification of the neoclassical flux.

Figure 6.9.: Mach number of the impurity

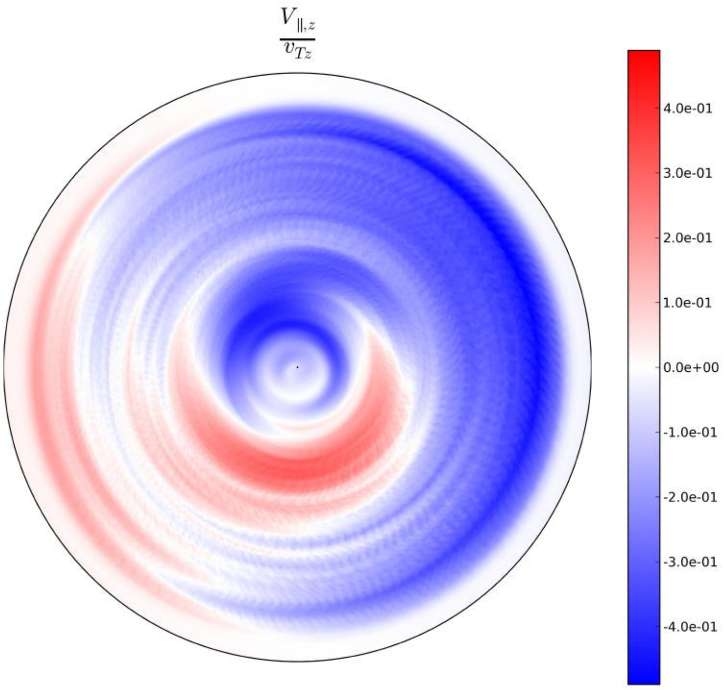

Another limitation of the model concerns the main ion species. More precisely, the derivation of Eq.(6.2.8) is done assuming that the main ion species is rotating poloidally at the speed prescribed by neoclassical theory (cf derivation of u in appendix D). This hypothesis can easily breaks down due to the presence of turbulence [23]. This is the case in the GYSELA simulation presented in the previous section.

Finally, it is mentioned that the rhs of Eq.(6.2.5) has been neglected. This approximation could modify the theoretical prediction, especially in the Pfirsch-Schlüter regime. But it is probably a small effect.

Summary of the chapter

In this chapter, a theoretical prediction of the neoclassical impurity flux in presence of large anisotropy and poloidal asymmetries has been derived. This prediction has been compared with the neoclassical flux coming from a simulation performed with the code GYSELA in presence of turbulence. In this simulation large anisotropy and poloidal asymmetries are generated by the turbulence. A good agreement is found between the theoretical prediction and the flux coming from the code GYSELA if a vanishing thermal screening factor is taken for the theoretical prediction.

7. A mechanism of turbulent generation of poloidal asymmetries

Contents

6.1. Experimental evidence of poloidal asymmetries of impurity . . . 111

6.2. Neoclassical impurity flux in presence of large poloidal asymmetries and pressure anisotropy . . . 112

- 6.2.1. Structure of the impurity flow in presence of poloidal asymmetries . . . 113
- 6.2.2. Determination of the poloidal variation of K_z . . . 114
- 6.2.3. Neoclassical flux . . . 115

6.3. Comparison with results from gyrokinetic simulations 117

- 6.3.1. Choice of the simulation parameters . . . 117
- 6.3.2. Definitions of fluxes . . . 120
- 6.3.3. Poloidal asymmetries and anisotropy . . . 122
- 6.3.4. Comparison between GYSELA results and theoretical predictions . . . 124

6.4. Discussion on the theoretical model . . . 127

A large part of the results of this chapter can be found in the article [26]. This chapter clarifies how turbulence can generate low frequency structures of the electric potential with poloidal asymmetries. These structures in turn impact the poloidal repartition of impurities which finally modifies the neoclassical flux as shown in the previous chapter.

The chapter is organised as follows. First, it is shown numerically that poloidal asymmetry of the electric potential generates poloidal asymmetry of the impurity. Secondly, a general introduction on the problem of turbulent generation of poloidal asymmetries of the electric potential in a tokamak is given. It allows one to clarify the relationship between several large scale structures of the electric potential which are often studied separately. The method used to calculate poloidal asymmetries of the electric potential is then described in section 7.3. The link between the turbulence drive term and the turbulent Reynolds stress is established in section 7.4. Finally, the main properties of poloidal convective cells are given in section 7.5.

7.1. Evidence of impurity poloidal asymmetries generated by poloidal asymmetries of the electric potential

In the previous chapter, a turbulent simulation performed with the code GYSELA has been presented. In this simulation, strong poloidal asymmetries of the impurity quantities are present. These poloidal asymmetries are not generated by external sources as the only source used is an isotropic source of energy which depends only on the radius. Moreover, neoclassical theory predicts weak poloidal asymmetries. In the simulation, poloidal asymmetries are therefore generated by turbulence. One way for turbulence to generate poloidal asymmetries of the impurity fluid moments (density, temperature..) is to generate an electric potential with poloidal asymmetries. Indeed, it has been shown in the previous chapter that there is a link between those poloidal asymmetries Eq.(6.1.1)[10, 16]

$$\begin{aligned}\frac{N_z(\psi,\theta)}{N_z^\star(\psi)} &= \frac{T_{\perp,z}(\psi,\theta)}{T_{\perp,z}^\star(\psi)}\\ &\times\exp\left\{-\frac{eZ\left[\phi(\psi,\theta)-\phi^\star(\psi)\right]}{T_{\parallel,z}(\psi)}+\frac{m_z\Omega_z^2}{2T_{\parallel,z}(\psi)}\left[R^2(\psi,\theta)-R^{\star 2}(\psi)\right]\right\}\end{aligned}$$

From Eq.(6.1.1), it is clear that even weak poloidal asymmetries of the electric field can lead to significant poloidal asymmetries for heavy impurities due to their large charge Z. Fig.7.1 shows that in the considered simulation, the poloidal asymmetry of the electric potential is of order of $\frac{e(\phi_{n=0}-\phi_{m=0,n=0})}{T}\sim 1\%$ where m

and n are respectively the poloidal and toroidal mode numbers. As a reminder, the amplitude of the density asymmetry for the impurity is of the order of 30%. As the charge of the impuriy is $Z = 40$, the right order of magnitude of poloidal asymmetry of the impurity density is retrieved with this simple argument. This was already observed in a previous study with the code GYSELA [31].

To quantify the relationship between electric potential and impurity poloidal asymmetries, a numerical test has been performed. The same simulation as the one presented in chapter 6 has been performed except that a numerical filter allowing to remove all axisymmetric modes of the potential with poloidal asymmetries $(m \neq 0, n = 0)$ has been applied at each time step. Fig.7.2 depicts the poloidal asymmetry of the impurity density in both cases using the following definitions $N_z = \langle N_z \rangle (\psi) \left[1 + \delta(\psi) \cos\theta + \Delta(\psi) \sin\theta\right]$. From this figure, it is clear that the poloidal asymmetry of the electric field has an impact on the poloidal asymmetry of the impurity density. In the following of this chapter a clarification of the mechanism of turbulent generation of axisymmetric modes ($n = 0$) of the electric potential is given. One should note that there are still poloidal asymmetries of the impurity density when the axisymmetric part of the electric field exhibits no poloidal asymmetry. This is due to non linear coupling between modes (m_1, n) and $(m_2, -n)$ where $m_1 + m_2 \neq 0$ and $n \neq 0$. This point is clarified in the section 7.5.4.

Figure 7.1.: Amplitude of the non zonal electric potentital in the GYSELA simulation

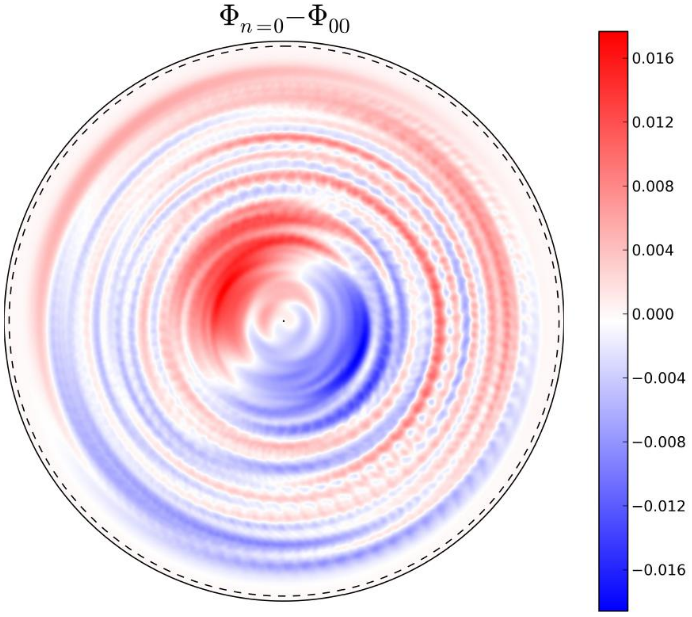

Figure 7.2.: Comparison of density poloidal asymmetry with (solid line) or without (dotted line) poloidal asymmetry of electric potential. A time average on several turbulence correlation time has been performed.

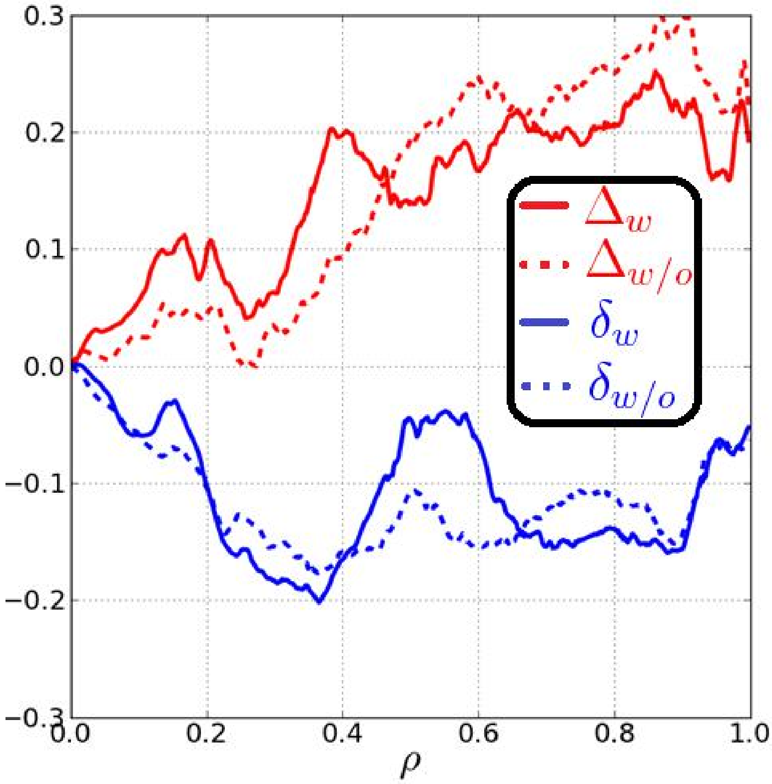

7.2. Context for the generation of axisymmetric modes of the electric potential

Poloidal asymmetries of the $E \times B$ plasma flow are usually neglected in neoclassical transport. Indeed the predicted level of asymmetry is quite small in conventional neoclassical theory, so that its effect is considered as negligible [46, 44]. Toroidal momentum transport is however an exception, since it appears to be sensitive to poloidal asymmetries, even at the neoclassical level [89]. This picture changes somewhat if poloidal variations of the electric potential are generated by turbulence. Steady or slowly varying structures may then boost neoclassical fluxes. These structures are know called ”poloidal convective cells”, since once isolated from axisymmetric flows (mean and zonal flows), and turbulence vortices (helical patterns), poloidal asymmetries of the electric potential are usually characterized by closed streamlines with typically a few lobes in the poloidal plane of a tokamak, and no variation in the toroidal direction. In other words, poloidal convective cells are modes with a toroidal wave number $n = 0$

and poloidal wave numbers $m \neq 0$ (usually $m = 1$ prevails). In this classification , zonal flows are $n = 0, m = 0$ modes, while turbulent vortices are characterized by $n \neq 0$, $m \neq 0$. Convective cells have a long history in the context of drift waves, sometimes related to different objects [70, 18, 71, 51, 66]. The word ”poloidal” is used here to make their definition more precise. One should note that recent experimental measurements have evidenced asymmetries of the plasma poloidal flow which may be related to steady convective cells [82, 83]. One important point related to both observations and theory is the difference between asymmetries of the electric potential and the flow. The $E \times B$ drift velocity is $\mathbf{v}_E = \frac{\mathbf{B}\times\nabla\phi}{B^2}$, where $\mathbf{B}$ is the unperturbed magnetic field and ϕ the electric potential. Any fully symmetric potential, i.e. that depends on the radial coordinate only, already produces flow poloidal asymmetries because the magnetic field depends on the poloidal angle. One cause is that the magnetic field strength decreases as the major radius in a tokamak. Other sources of asymmetries come into play for shaped geometries. It turns out that this effect could only partially explain flow asymmetries on the Tore Supra tokamak. Poloidal asymmetries of the electric potential were invoked to explain the observation [82, 83]. In the following, a large aspect ratio, circular equilibrium limit is considered. In this case poloidal asymmetries in potential imply poloidal asymmetries in poloidal flow.

One obvious mechanism for the effect of convective cells on neoclassical transport is the modification of the distribution function by the asymmetric potential, that correlates with its associated $E \times B$ electric drift velocity, and/or with the magnetic drift velocity to produce additional fluxes to the standard neoclassical value. One has however to be careful when using this argument, since the flux driven by the $E \times B$ drift velocity contains a contribution due to the response of the distribution function to the magnetic drift that tends to counter-balance this effect [42, 84]. Also poloidal variations of the electric potential induce asymmetries of the density of an impurity, which in turn enhance its neoclassical flux [4]. This effect is expected to be particularly large for heavy impurities in core plasmas, since a Boltzmann type response is proportional to the charge number. It was proposed as an explanation for synergies between turbulent and neoclassical fluxes of impurities observed with the GYSELA code [31]. Another reason for investigating poloidal flow asymmetries is their potential role in turbulence self-organisation, via vortex shearing. The understanding of turbulence self-organization has been an active area of research in the past decades. It is well known that zonal flows are instrumental in these processes. Indeed they are generated by turbulence via the Reynolds stress, and in turn self-regulate turbulence by transferring energy from large scales to small scales [22]. The intensity of Zonal Flows is quite large compared with other helical turbulent structures, because they are not Landau damped [77, 80]. Another player in turbulence self-regulation is the Geodesic Acoustic Mode (GAM) [88] , which is the sum of two axisymmetric components of the potential: a zonal plus an up-down asymmetric component, i.e. a combination of $n = 0$, $m = 0$ and $n = 0$, $m = \pm 1$ modes. The whole GAM structure oscillates at a frequency that scales with the acoustic frequency, and is driven by perpendicular flow compression, proportional to the geodesic curvature (hence the name GAM [88, 41]). These modes are also driven by turbulence via mode coupling, and can back-react on the turbulence background [20]. GAMs have been shown however to be less effective than zonal flows in this retro-action process, due to their high frequency [39]. Moreover they are Landau damped in contrast with Zonal Flows. Therefore one open issue is whether low frequency poloidal flow asymmetries can have an impact on turbulence in a way similar to Zonal Flows, as proposed in [85]. Let us note that some recent turbulence simulations seem to indicate that this effect is weak, while the synergy with neoclassical fluxes appears to be prominent in most transport channels, except momentum transport [8].

Quite curiously a predictive analytical calculation of the dynamics and amplitude of poloidal convective cells is not available in the literature. A previous attempt exists [36], which was originally intended to explain the anti-correlation between fluxes of momentum driven by $E \times B$ and magnetic drifts seen in several gyrokinetic simulations. However this calculation does not account for the coexistence of convective cells with zonal flows and GAMs, an important expected property of a comprehensive theory. A model that enables a simultaneous estimate of Zonal Flows, GAMs and convective cells is proposed. A complete theory of convective cells generation is out of scope here, as it requires to keep the whole dynamics of trapped and passing particles and the inclusion of collisions, to recover the correct dynamics of zonal flows at low frequency [77, 45]. Instead a simpler model that keeps only passing particles, and neglects the effect of trapped particles is used. The Vlasov gyrokinetic equation can then be solved for $n = 0, m = 0, \pm 1$ modes, assuming non linear terms are given. The latter corresponds to the turbulence drive, and can be shown to be related to the turbulent Reynolds stress. The calculation is done at low Mach number and in absence of RF heating sources. So asymmetries found here differ from those related to the centrifugal force or RF effects [16, 74], though these effects could be addressed in the present approach. This method allows one to recover exactly the GAMs dispersion relation, and to compute poloidal convective cells in an intermediate range of frequencies that goes down to the trapping frequency. Two mechanisms of generation are identified: the generation of cells due to compressional effect of zonal flows, and the poloidal asymmetry of the Reynolds stress due to turbulence ballooning. The first one is dominant in the range of frequency of the order of the curvature frequency, while the latter appears to be prominent at very low frequency. One interesting finding is that the asymmetry of poloidal convective cells is in-out at low frequencies, and up-down at intermediate and high frequencies (GAMs).

7.3. Evolution of a toroidally symmetric mode

For the simple geometry of concentric circular magnetic surfaces considered here, flow asymmetries are due to asymmetries of the electric potential, i.e. with a toroidal wavenumber $N = 0$, and poloidal wavenumbers $|M| \geq 1$. The electric potential is first split in an axisymmetric component $\langle\phi\rangle_\varphi(\psi,\theta)$ and a helical perturbation $\tilde{\phi}(\psi,\theta,\varphi)$, i.e. $\phi = \langle\phi\rangle_\varphi + \tilde{\phi}$. The axisymmetric part is written as a Fourier series

$$\langle\phi\rangle_\varphi(\psi,\theta) = \sum_{M\Omega} \phi_{M\Omega}(\psi)\exp\left\{i\left(M\theta - \Omega t\right)\right\}$$

As in the chapter 5, a ballooning representation is used for the non axisymmetric part Eq.(5.1.6):

$$\tilde{\phi}(\psi,\alpha,\theta,t) = \sum_{\mathbf{k}\omega} \phi_{\mathbf{k}\omega}(\theta)\exp\left\{i\left[n\theta_k q(\psi) + n\alpha - \omega t\right]\right\}$$

Different notations are used for the frequencies Ω and poloidal wave numbers M of the axisymmetric potential on the one hand, and the toroidal wave numbers and frequencies n,ω of the helical perturbations. We omit to specify the null toroidal wave number $N = 0$ of axisymmetric perturbations, which are made distinct from helical fluctuations by these different notations (i.e. capital vs lower case letters). Taking the Fourier transform in radial position and assuming $\frac{M}{r} \ll K_r$, one can compute the linear solution of the Vlasov equation Eq.(5.1.4) for the axisymmetric perturbations

$$-i\left(\Omega - M\Omega_t\right)\bar{g}_{M\Omega} + \Omega_D\left(\bar{g}_{M+1,\Omega} - \bar{g}_{M-1,\Omega}\right) = -i\Omega\frac{F_{eq}}{T_{eq}}\bar{h}_{M\Omega} - \left[\tilde{\bar{v}}_E\cdot\nabla\tilde{\bar{g}}\right]_{M\Omega} \tag{7.3.1}$$

where $\Omega_D = \frac{K_r\rho_i v_T}{4R_0}\left(2\frac{v_\parallel^2}{v_T^2} + \frac{v_\perp^2}{v_T^2}\right)$ and $\Omega_t = \frac{v_\parallel}{q(r)R_0}$. Note that the direct basis $(e_r, e_\theta, e_\varphi)$ has been chosen. The non linear term $\left[\langle\bar{\mathbf{v}}_E\rangle_\varphi\cdot\nabla\langle\bar{g}\rangle_\varphi\right]_{M\Omega} \simeq 0$ is neglected, since 1st order terms only are kept. However this term may play a role in the dynamics, and could actually provide a saturation mechanism that does not have a counter-part for zonal flows. In principle, poloidal asymmetries are associated with modes with $N = 0$ and $|M| \geq 1$... However it appears that the ratio of the M poloidal harmonic of the electric potential to its $M = 0$ value goes like $(K_r\rho_i)^M$, as already well known for GAMs [80]. Hence the analysis is restricted to low values of $k_r\rho_i$ in order to keep only 3 modes $M = 0$ and $M = 1$, and $M = -1$. The relation Eq.(7.3.1) can then be written

$$\left\{\bar{g}\right\} = -i\Omega G^{-1}\frac{F_{eq}}{T_{eq}}\left\{\bar{h}\right\} - G^{-1}\left\{\left[\tilde{\bar{v}}_E\cdot\nabla\tilde{\bar{g}}\right]\right\} \tag{7.3.2}$$

where

$$\{\bar{g}\} = \begin{pmatrix} \bar{g}_{-1,\Omega} \\ \bar{g}_{0,\Omega} \\ \bar{g}_{1,\Omega} \end{pmatrix}$$

$$\left\{\bar{h}\right\} = \begin{pmatrix} \bar{h}_{-1,\Omega} \\ \bar{h}_{0,\Omega} \\ \bar{h}_{1,\Omega} \end{pmatrix}$$

$$\left\{\left[\tilde{\bar{v}}_E \cdot \nabla\tilde{\bar{g}}\right]\right\} = \begin{pmatrix} \left[\tilde{\bar{v}}_E \cdot \nabla\tilde{\bar{g}}\right]_{-1,\Omega} \\ \left[\tilde{\bar{v}}_E \cdot \nabla\tilde{\bar{g}}\right]_{0,\Omega} \\ \left[\tilde{\bar{v}}_E \cdot \nabla\tilde{\bar{g}}\right]_{1,\Omega} \end{pmatrix}$$

and

$$G = \begin{pmatrix} -i\Omega_+ & \Omega_D & 0 \\ -\Omega_D & -i\Omega & \Omega_D \\ 0 & -\Omega_D & i\Omega_- \end{pmatrix}$$

where $\Omega_\pm = \Omega_t \pm \Omega$. The determinant of the G matrix is det G=-$i\Omega\left(\Omega_+\Omega_- + 2\Omega_D^2\right)$. A useful quantity is the transpose of its comatrix, given by

$$\text{com } G^t = \begin{pmatrix} \Omega_-\Omega + \Omega_D^2 & -i\Omega_D\Omega_- & \Omega_D^2 \\ i\Omega_D\Omega_- & \Omega_+\Omega_- & i\Omega_D\Omega_+ \\ \Omega_D^2 & -i\Omega_D\Omega_+ & -\Omega_+\Omega + \Omega_D^2 \end{pmatrix}$$

Assuming adiabatic electrons and keeping a single hydrogenoid (charge number $Z = 1$) ion species, the quasi-neutrality equation reads

$$\frac{N_{eq}}{T_{eq}}\left[1 + \left(1 - \delta\left(M\right)\right)\tau\right]\{h\} = \int \mathcal{J}\{\bar{g}\}\, d^3v \tag{7.3.3}$$

where $\tau = \frac{T_i}{T_e}$ is the ratio of ion to electron temperatures, and $\mathcal{J}$ is the gyroaverage operator. Combining the quasi-neutrality condition Eq.(7.3.3) with the equation on $\{\bar{g}\}$ Eq.(7.3.2), and assuming the gyroaverage operator commutes with all quantities at all frequencies, one gets

$$\begin{aligned} &\frac{N_{eq}}{T_{eq}}\left[1 + \left(1 - \delta\left(M\right)\right)\tau\right]\{h\} + i\Omega \int G^{-1}\frac{F_{eq}}{T_{eq}}\mathcal{J}^2\{h\}\, d^3v \\ &= -\int G^{-1}\mathcal{J}\left\{\left[\tilde{\bar{v}}_E \cdot \nabla\tilde{\bar{g}}\right]\right\} d^3v \end{aligned} \tag{7.3.4}$$

Eq.(7.3.4) is the formal solution that gives the amplitude of the poloidal convective cells. It can be expressed as $\mathcal{E} \cdot \{h\} = \{S\}$. Defining $\langle\cdot\rangle_v = \int \cdot \frac{F_{eq}}{N_{eq}} d^3v$ and using the fact that $\langle g \rangle_v = 0$ whatever g odd with respect to $v_\parallel$, one can show that

$$\mathcal{E} = \frac{N_{eq}}{T_{eq}} \begin{pmatrix} \mathcal{E}_a & -i\mathcal{E}_c & \mathcal{E}_d \\ i\mathcal{E}_c & \mathcal{E}_b & -i\mathcal{E}_c \\ \mathcal{E}_d & i\mathcal{E}_c & \mathcal{E}_a \end{pmatrix}$$

where

$$\begin{aligned} \mathcal{E}_a &= 1 + \tau + L_0(\Omega) - L_2(\Omega) \\ \mathcal{E}_b &= \left\langle 1 - \mathcal{J}^2 \right\rangle_v + 2L_2(\Omega) \\ \mathcal{E}_c &= L_1(\Omega) \\ \mathcal{E}_d &= -L_2(\Omega) \end{aligned} \tag{7.3.5}$$

where

$$L_j(\Omega) = \left\langle \frac{\Omega^{2-j}\Omega_D^j}{\Omega_+\Omega_- + 2\Omega_D^2} \mathcal{J}^2 \right\rangle_v \tag{7.3.6}$$

Assuming that $\mathcal{J}\left[\tilde{\tilde{v}}_E \cdot \nabla\tilde{\tilde{g}}\right]_{M,\Omega}$ is an even function of $v_\parallel$, it can be shown that

$$\{S\} = \frac{1}{\Omega} \begin{pmatrix} S_{1,0} + i\left(S_{0,-1} - S_{2,-1} - S_{2,1}\right) \\ -iS' - S_{1,-1} + S_{1,1} + 2iS_{2,0} \\ -S_{1,0} + i\left(S_{0,1} - S_{2,-1} - S_{2,1}\right) \end{pmatrix}$$

where

$$S_{j,M} = \int \frac{\Omega^{2-j}\Omega_D^j}{\left(\Omega_+\Omega_- + 2\Omega_D^2\right)} \mathcal{J}\left[\tilde{\tilde{v}}_E \cdot \nabla\tilde{\tilde{g}}\right]_{M,\Omega} d^3v$$

and

$$S' = \int \mathcal{J}\left[\tilde{\tilde{v}}_E \cdot \nabla\tilde{\tilde{g}}\right]_{0,\Omega} d^3v$$

Two typical frequencies $\Omega_{th} = \frac{v_T}{q(r)R_0}$, $\Omega_{Dth} = \frac{K_r\rho_i v_T}{R_0} = qK_r\rho_i\Omega_{th}$, and two dimensionless parameters $\tilde{K} = K_r\rho_i$ and $\tilde{\Omega} = \frac{\Omega}{\Omega_{th}}$ have been introduced. It is reminded that the hypothesis $\tilde{K} \ll 1$ is used, consistently with the low number of poloidal harmonics that are kept $M = 0, 1, -1$. In this limit, one has $\langle 1 - \mathcal{J}^2 \rangle_v = \tilde{K}^2$.

7.3.1. GAMs

In this section, large frequencies are considered $\tilde{\Omega} = O(1)$. In this case, noting that $\mathcal{J} = 1 + O\left(\tilde{K}^2\right)$, and the fact that whatever the function f even with respect to $v_\parallel$

$$\left\langle \frac{f}{\Omega_+\Omega-} \right\rangle_v = \frac{1}{2\Omega}\left(\left\langle \frac{f}{\Omega_-} \right\rangle_v - \left\langle \frac{f}{\Omega_+} \right\rangle_v \right) = \frac{1}{\Omega}\left\langle \frac{f}{\Omega-} \right\rangle_v \tag{7.3.7}$$

one can show that the coefficients $L_j\left(\Omega\right)$ Eq.(7.3.6) become at leading order

$$\begin{aligned}
L_0\left(\Omega\right) &= \frac{\tilde{\Omega}}{\sqrt{2}}\zeta\left(\frac{\tilde{\Omega}}{\sqrt{2}}\right)\\
L_1\left(\Omega\right) &= \frac{q\tilde{K}}{2\sqrt{2}}\left[\sqrt{2}\tilde{\Omega}+\left(1+\tilde{\Omega}^2\right)\zeta\left(\frac{\tilde{\Omega}}{\sqrt{2}}\right)\right]\\
L_2\left(\Omega\right) &= \frac{q^2\tilde{K}^2}{4}\left[3+\tilde{\Omega}^2+\frac{\sqrt{2}}{\tilde{\Omega}}\left(\frac{\tilde{\Omega}^4}{2}+\tilde{\Omega}^2+1\right)\zeta\left(\frac{\tilde{\Omega}}{\sqrt{2}}\right)\right] \qquad (7.3.8)
\end{aligned}$$

where $\zeta\left(z\right)=\frac{1}{\sqrt{\pi}}\int_{-\infty}^{\infty}\frac{e^{-x^2}}{x-z}dx$ is the plasma dispersion function. The simplification Eq.(7.3.7) implies also $S_{j,M}=\int\frac{\Omega^{1-j}\Omega_D^j}{\Omega_-}\mathcal{J}\left[\tilde{\bar{v}}_E\cdot\nabla\tilde{\bar{g}}\right]_{M,\Omega}d^3v$ at leading order. The following quantities are defined

$$\begin{aligned}
X_0 &= \frac{N_{eq}}{T_{eq}}\left[1+\tau+L_0\left(\Omega\right)\right]\\
X_1 &= \frac{N_{eq}}{T_{eq}}L_1\left(\Omega\right)\\
X_2 &= \frac{N_{eq}}{T_{eq}}\left[\tilde{K}^2+2L_2\left(\Omega\right)\right] \qquad (7.3.9)
\end{aligned}$$

where the functions $L_j\left(\Omega\right)$ are given by Eq.(7.3.8) when $\tilde{\Omega}=O(1)$. At this stage, one should remark that notations have been chosen such that $X_j=O\left(\tilde{K}^j\right)$ and $S_{j,M}=O\left(\tilde{K}^j\right)$. These properties greatly simplify the computation. With these notations, the determinant of $\mathcal{E}$ is given by

$$\det\mathcal{E}=X_0\left[X_0X_2-2X_1^2\right]+O\left(\tilde{K}^4\right) \qquad (7.3.10)$$

One should notice that the relation $\det\mathcal{E}=0$ gives the kinetic GAM dispersion relation. Indeed, replacing the coefficients X_i Eq.(7.3.9) in the expression Eq.(7.3.10) leads to

$$\begin{aligned}
&\zeta\left(\frac{\tilde{\Omega}}{\sqrt{2}}\right)\left\{\frac{\tilde{\Omega}}{\sqrt{2}}+\frac{q^2}{\sqrt{2}}\left[\frac{\tau}{2}\tilde{\Omega}^3+\left(\frac{3}{2}+\tau\right)\tilde{\Omega}+\frac{1+\tau}{\tilde{\Omega}}\right]\right\}\\
&+1+\tau+\frac{\tau}{2}q^2\tilde{\Omega}^2+\frac{3}{2}q^2\left(1+\tau\right)+\frac{q^2}{4}\zeta^2\left(\frac{\tilde{\Omega}}{\sqrt{2}}\right)=0
\end{aligned}$$

which is the fully kinetic dispersion relation of GAMs [90, 92, 80]. Assuming that the order of $\mathcal{J}\left[\tilde{\tilde{v}}_E \cdot \nabla \tilde{\tilde{g}}\right]_{M,\Omega}$ is independent of M, it appears that

$$\begin{aligned} i\Omega h_{-1,\Omega}\text{det}\mathcal{E} = &\ iX_0X_1S' + X_0X_1\left(S_{1,-1} - S_{1,1}\right) \\ &+ \left(X_1^2 - X_0X_2\right)S_{0,-1} + X_1^2 S_{0,1} + O\left(\tilde{K}^3\right) \end{aligned}$$

$$\begin{aligned} i\Omega h_{1,\Omega}\text{det}\mathcal{E} = &- iX_0X_1S' + X_0X_1\left(S_{1,1} - S_{1,-1}\right) \\ &+ \left(X_1^2 - X_0X_2\right)S_{0,1} + X_1^2 S_{0,-1} + O\left(\tilde{K}^3\right) \end{aligned}$$

$$i\Omega h_{0,\Omega}\text{det}\mathcal{E} = X_0^2 S' + iX_0^2\left(S_{1,1} - S_{1,-1}\right) + iX_0X_1\left(S_{1,-1} - S_{1,1}\right) + O\left(\tilde{K}^2\right)$$

At leading order, one has $h_{-1,\Omega} = -h_{1,\Omega}$. Hence the mode poloidal dependence is $\sin\theta$ (up-down asymmetry), as expected for GAMs. It is shown in section 7.4 that S' is linked to the turbulent Reynolds stress tensor. This calculation shows that for the GAM limit, the side bands $M = \pm 1$ are mainly fed via the toroidal coupling with the mode $M = 0$. This result is new and non trivial, as one could have also expected a direct feeding via a source of the form $\mathcal{J}\left[\tilde{\tilde{v}}_E \cdot \nabla \tilde{\tilde{g}}\right]_{1,\Omega}$ to be competitive.

7.3.2. Poloidal convective cells

Lower frequencies are now considered $\tilde{\Omega} \ll \tilde{K} \ll 1$. The analysis is restricted to the first order terms in $\tilde{\Omega}$. Using the property

$$\left\langle \frac{f}{\Omega_t^2 + 2\Omega_D^2} \right\rangle_v = -\frac{i}{\sqrt{2}} \left\langle \frac{f}{\Omega_D\left(\Omega_t - i\sqrt{2}\Omega_D\right)} \right\rangle_v \tag{7.3.11}$$

for any even function $f(v_\parallel)$, it turns out that at leading order the functions L_j Eq.(7.3.6) become

$$\begin{aligned} L_0\left(\Omega\right) &= -\sqrt{\pi}\frac{\tilde{\Omega}^2}{q\tilde{K}} \ln\left(i\frac{\tilde{\Omega}}{q\tilde{K}}\right) \\ L_1\left(\Omega\right) &= \frac{\sqrt{\pi}}{2}\tilde{\Omega} \\ L_2\left(\Omega\right) &= \frac{\sqrt{\pi}}{4}q\tilde{K} \end{aligned} \tag{7.3.12}$$

The simplification Eq.(7.3.11) leads to the redefinition of the source term:

$$\begin{aligned} S_{j,M} &= -\frac{i}{\sqrt{2}}\int \frac{\Omega^{2-j}\Omega_D^{j-1}}{\Omega_t - i\sqrt{2}\Omega_D}\mathcal{J}\left[\tilde{\tilde{v}}_E \cdot \nabla\tilde{\tilde{g}}\right]_{M,\Omega} d^3v \\ &= O\left(\tilde{K}^{j-1}\right) \times O\left(\tilde{\Omega}^{2-j}\right) \end{aligned}$$

Using this ordering, the potential at leading order is given by

$$\begin{aligned} i\Omega h_{-1,\Omega} &= \frac{T_{eq}}{N_{eq}}\ \tfrac{1}{(1+\tau)q\tilde{K}}\left(i\tilde{\Omega}S' + q\tilde{K}\left(S_{2,-1} + S_{2,1}\right)\right) \\ i\Omega h_{1,\Omega} &= \frac{T_{eq}}{N_{eq}}\ \tfrac{1}{(1+\tau)q\tilde{K}}\left(-i\tilde{\Omega}S' + q\tilde{K}\left(S_{2,-1} + S_{2,1}\right)\right) \\ i\Omega h_{0,\Omega} &= \frac{T_{eq}}{N_{eq}}\frac{2S'}{\sqrt{\pi}q\tilde{K}} \end{aligned}$$

Two limit cases are found. In the intermediate frequency regime $\tilde{K}^2 \ll \tilde{\Omega} \ll \tilde{K}$, one gets

$$-h_{-1,\Omega} = h_{1,\Omega} = -\frac{T_{eq}}{N_{eq}}\frac{S'}{(1+\tau)\,q\tilde{K}\Omega_{th}}$$

This corresponds to a $\sin(\theta)$ poloidal structure (up-down asymmetry). It appears that the main drive comes from the source S' that is a $N = 0, M = 0$ component of the source. It is shown in the next section that it is related to the flux surface average of the turbulent Reynolds stress , i.e. the same source as zonal flows. The underlying mechanism is flow compressibility, that results in a pumping of $N = 0, M = \pm 1$ modes by $N = 0, M = 0$ zonal flows - i.e. a sideband effect.

The second limit corresponds to quasi-stationary structures, i.e. very low frequencies $\tilde{\Omega} \ll \tilde{K}^2$, for which at leading order

$$h_{-1,\Omega} = h_{1,\Omega} = \frac{T_{eq}}{N_{eq}}\frac{\left(S_{2,-1} + S_{2,1}\right)}{i\Omega\left(1+\tau\right)}$$

It corresponds to a $\cos(\theta)$ poloidal variation (in-out asymmetry). The source terms $S_{2,\pm 1}$ corresponds to $M = \pm 1$ components of the turbulent source. Hence the drive rather comes from turbulence ballooning, which induces in turn a ballooning of the turbulence source, i.e. non zero poloidal harmonics of the turbulent drive.

7.4. Link between source terms and turbulent Reynolds stress tensor

It turns out that the leading term is often proportional to the source term S'. In this part a connection is established between this quantity and the Reynolds stress tensor. In other words a kinetic version of the Taylor identity [67] is demonstrated. The first step, detailed in appendix E consists in demonstrating that the turbulent source $\mathcal{J}\left[\bar{\mathbf{v}}_E \cdot \nabla \bar{g}\right]_{M\Omega}$ can be written as a flux, $\mathcal{J}\left[\bar{\mathbf{v}}_E \cdot \nabla \bar{g}\right]_{M\Omega} = \frac{\partial \Gamma_\Pi}{\partial \psi}$, where the flux Γ_Π is a flux of vorticity

$$\Gamma_\Pi = \int_0^T \frac{dt}{T} \int_0^{2\pi} \frac{d\theta}{2\pi} e^{-iM\theta + i\Omega t} \int_0^{2\pi} \frac{d\alpha}{2\pi} \mathcal{J}\left(\bar{\mathcal{E}}_\alpha \bar{f}\right)$$

and $\bar{\mathcal{E}}_\alpha = \frac{\partial(\mathcal{J}\phi)}{\partial \alpha}$ is the α component of the gyroaverage electric field. Therefore

$$S' = \frac{\partial}{\partial \psi}\left[\int_0^T \frac{dt}{T} e^{i\Omega t} \int_0^{2\pi} \frac{d\theta}{2\pi} \sigma\right] \tag{7.4.1}$$

where $\sigma = \int \frac{d\alpha}{2\pi} \int d^3 v \mathcal{J}\left(\bar{\mathcal{E}}_\alpha \bar{f}\right)$ and the time T should be longer than the time scale of convective cells, i.e. typically longer than a turbulence auto-correlation time. One is left with the computation of σ. From now on, the calculation is restricted to the large wavelength limit $k_\perp \rho_i < 1$. Using $\mathcal{J} \simeq 1 + \frac{m\mu}{2e^2 B_{eq}} \nabla_\perp^2$, one finds

$$\mathcal{J}\left(\bar{\mathcal{E}}_\alpha \bar{f}\right) = \mathcal{E}_\alpha \mathcal{J} \bar{f} + \frac{m\mu}{e^2 B_{eq}} \bar{f} \nabla_\perp^2 \mathcal{E}_\alpha + \frac{m\mu}{e^2 B_{eq}} \nabla_\perp \mathcal{E}_\alpha \cdot \nabla_\perp \bar{f}$$

It is convenient to calculate the contribution of $\mathcal{J}\bar{f}$ by using the Poisson equation that writes

$$\frac{N_{eq} e^2}{T_{e,eq}}\left(\phi - \langle\phi\rangle_\psi\right) - \nabla \cdot \left(\frac{N_{eq} m}{B_{eq}^2} \nabla_\perp \phi\right) = e \int \mathrm{d}^3 \mathbf{v} \mathcal{J} \bar{f}$$

Then

$$\begin{aligned}\int d^3 v \mathcal{J}\left(\bar{\mathcal{E}}_\alpha \bar{f}\right) = \mathcal{E}_\alpha \frac{N_{eq} e}{T_{e,eq}}\left(\phi - \langle\phi\rangle_\psi\right) \\ - \mathcal{E}_\alpha \nabla \cdot \left(\frac{N_{eq} m}{e B_{eq}^2} \nabla_\perp \phi\right) \\ + \frac{m}{e^2 B_{eq}^2} \nabla \cdot \left(\bar{P}_\perp \nabla_\perp \mathcal{E}_\alpha\right)\end{aligned}$$

where $\bar{P}_\perp = \int d^3 v \mu B_{eq} \bar{f}$. The next step consists in integrating with respect to α. The terms proportional to $\left(\phi - \langle\phi\rangle_\psi\right)$ is obviously not contributing. The terms

$\frac{N_{eq}m}{eB_{eq}^2}$ are varying at large scales and so their derivatives can be neglected. Then

$$\sigma = \frac{N_{eq}m}{eB_{eq}^2}\int_0^{2\pi}\frac{d\alpha}{2\pi}\left[\ \tfrac{1}{eN_{eq}}\nabla\cdot\left(\bar{P}_\perp\nabla_\perp\mathcal{E}_\alpha\right)\ -\mathcal{E}_\alpha\nabla\cdot\left(\nabla_\perp\phi\right)\right]$$

Using integration by part and the fact that $\mathcal{E}_\alpha\nabla\cdot(\nabla_\perp\phi) = \nabla\cdot(\mathcal{E}_\alpha\nabla_\perp\phi) - \frac{1}{2}\partial_\alpha\left|\nabla_\perp\phi\right|^2$. One can show that

$$\sigma = -\frac{N_{eq}m}{eB_{eq}^2}\int_0^{2\pi}\frac{d\alpha}{2\pi}\nabla\cdot\left[\left(\mathcal{E}_\alpha + \frac{\mathcal{P}_\alpha}{eN_{eq}}\right)\nabla_\perp\phi\right]$$

where $\mathcal{P}_\alpha = \frac{\partial\bar{P}_\perp}{\partial\alpha}$. The definition of the divergence in ballooning coordinates is

$$\nabla\cdot\mathbf{U} = \frac{1}{\sqrt{g}}\frac{\partial}{\partial\psi}\left(\sqrt{g}\mathbf{U}\cdot\nabla\psi\right) + \frac{1}{\sqrt{g}}\frac{\partial}{\partial\alpha}\left(\sqrt{g}\mathbf{U}\cdot\nabla\alpha\right)$$

where $\sqrt{g} = \frac{1}{\mathbf{B}_{eq}\cdot\nabla\theta}$ is the Jacobian. The ψ dependence of g can be neglected. One then finds

$$\sigma = -\frac{\partial}{\partial\psi}\left[\frac{N_{eq}m}{eB_{eq}^2}\int\frac{d\alpha}{2\pi}\ \left(\mathcal{E}_\alpha + \tfrac{\mathcal{P}_\alpha}{eN_{eq}}\right)\left(\mathcal{E}_\psi\left|\nabla\psi\right|^2 + \mathcal{E}_\alpha\nabla\psi\cdot\nabla\alpha\right)\ \right]$$

where $\mathcal{E}_\psi = \frac{\partial\phi}{\partial\Psi}$. Note that $\nabla\psi\cdot\nabla\alpha = -q\nabla\psi\cdot\nabla\theta - \frac{\partial q}{\partial\psi}\theta\left|\nabla\psi\right|^2$. Moreover one has the following properties in ballooning representation

$$\begin{aligned}\phi &= \sum_{\mathbf{k}}\phi_{\mathbf{k}}(\theta,t)\exp\left\{i\left[n\theta_k q(\psi) + n\alpha\right]\right\}\\ \mathcal{E}_\psi &= \sum_{\mathbf{k}} in\frac{\partial q}{\partial\psi}\theta_k\phi_{\mathbf{k}}(\theta,t)\exp\left\{i\left[n\theta_k q(\psi) + n\alpha\right]\right\}\\ \mathcal{E}_\alpha &= \sum_{\mathbf{k}} in\phi_{\mathbf{k}}(\theta,t)\exp\left\{i\left[n\theta_k q(\psi) + n\alpha\right]\right\}\end{aligned}$$

where it is reminded that $n\phi_{\mathbf{k}} \gg \frac{\partial\phi_{\mathbf{k}}}{\partial\theta}$. Similar relations can be derived for the perpendicular pressure. Using also the limit $\Omega \lll \omega$, one gets

$$\sigma = \frac{\partial}{\partial\psi}\left[\frac{N_{eq}m}{eB_{eq}^2}\sum_{\mathbf{k}}\ n^2\left(\phi_{\mathbf{k}} + \tfrac{\bar{P}_{\perp,\mathbf{k}}}{N_{eq}e}\right)\phi_{\mathbf{k}}^\star\ \left(\frac{\partial q}{\partial\psi}\left(\theta - \theta_k\right)\left|\nabla\psi\right|^2 + q\nabla\psi\cdot\nabla\theta\right)\right]$$

If we moreover assume the distribution function is mainly advected by the turbulent $E\times B$ drift velocity, then $\bar{f}_{\mathbf{k},\omega} = -\frac{F_{eq}}{T_{eq}}\frac{n\Omega_\star}{\omega}h_{\mathbf{k},\omega}$, and one has

$$\sigma = \frac{\partial}{\partial\psi}\left[\frac{N_{eq}m}{eB_{eq}^2}\sum_{\mathbf{k}}\ n^2\left(1 - \tfrac{n\Omega_\star}{\omega}\right)\left|\phi_{\mathbf{k}}\right|^2\ \left(\frac{\partial q}{\partial\psi}\left(\theta - \theta_k\right)\left|\nabla\psi\right|^2 + q\nabla\psi\cdot\nabla\theta\right)\right]$$

It then appears that σ is close to $-\frac{\partial}{\partial r}\left(\frac{\partial\psi}{\partial r}\frac{N_{eq}m}{eB_{eq}}\Pi_{RS}\right)$, where $\Pi_{RS}=\langle v_{Er}\left(v_{E\theta}+V_\theta^*\right)\rangle$ is the turbulent Reynolds stress tensor, with FLR effects. It is a function of radius r, poloidal angle θ, and time t. Using Eq.(7.4.1), source S' is then shown to be related to the $M=0$ component of the stress tensor

$$S'=-\frac{N_{eq}eB_{eq}}{T_{eq}}\rho_i^2\frac{\partial^2}{\partial r^2}\Pi_{RS,0}\left(r,\Omega\right)$$

where ρ_i is the thermal ion gyroradius. Radial variations of $\frac{\partial\psi}{\partial r}$ and all equilibrium quantities have been ignored compared to variations of the turbulence intensity to get this estimate. Other source components $S_{i,M}$ are more difficult to estimate accurately, but can be shown to scale as the Reynolds stress tensor.

7.5. Discussion

7.5.1. Phase and amplitude of poloidal convective cells

The results obtained for poloidal convective cells are now examined. In the intermediate frequency regime $\Omega\le\Omega_D$, the level of the $M=1$ mode is given by

$$\frac{\phi_{1,\Omega}}{B_{eq}}=-\frac{\phi_{-1,\Omega}}{B_{eq}}=-K_r\rho_i\frac{\Pi_{RS,0}(\Omega)}{\left(1+\tau\right)\frac{v_T}{R_0}}$$

This corresponds to an up-down asymmetric potential, i.e. $\sin\theta$ structure. This level is finite. For $\Omega\sim\Omega_D$, the level of zonal flow is given by $\phi_{0,\Omega}\sim\frac{\Pi_{RS}}{v_T/R_0}$. Hence the level of poloidal convective cell is smaller than a typical saturated zonal flow by a factor $K_r\rho_i$. The main drive mechanism is in this case the perpendicular compressibility of the flow.

The low frequency regime $\Omega\le\Omega_D K\rho_i$ is more intriguing. Admitting that the source term $(S_{2,-1}+S_{2,1})$ is of the order of S' times a factor f_{bal} representative of the level of turbulence ballooning, one gets the estimate

$$\frac{\phi_{1,\Omega}}{B_{eq}}=\frac{\phi_{-1,\Omega}}{B_{eq}}=-iK_r^2\rho_i^2f_{bal}\frac{\Pi_{RS,0}(\Omega)}{\left(1+\tau\right)\Omega}$$

No convergence is found for $\Omega\to0$ unless the Reynolds stress frequency spectrum vanishes at low frequency, which is unlikely. The same behavior occurs for zonal flows. This indicates a lack of dissipative processes, probably due to a break-down of the theory in absence of particle trapping. Note however that the ratio $\frac{\phi_{1,\Omega}}{\phi_{0,\Omega}}$ is regular and of the order of $K_r\rho_i$. The poloidal asymmetry is of the form $\cos\theta$, i.e. in-out, and the drive appears to be the asymmetry of the turbulent stress tensor due to turbulence ballooning.

7.5.2. Numerical solution

We assume that the source terms are separable in energy, Ω and M , i.e. we prescribe the following form

$$\left\{\left[\tilde{\tilde{v}}_E \cdot \nabla \tilde{\tilde{g}}\right]\right\} = F_{eq} s_M \mathcal{S}(\tilde{\Omega})$$

where $s_{-M} = s_M$ is real, and the frequency spectrum $\mathcal{S}(\tilde{\Omega})$ is chosen as a Lorentzian

$$\mathcal{S}(\tilde{\Omega}) = \frac{1}{\pi} \frac{\Delta\tilde{\Omega}}{\Omega^2 + \Delta\tilde{\Omega}^2}$$

All matrix $\mathcal{E}_{MM'}$ and source elements S_M can then be expressed as combinations of the functions $L_j(\Omega)$. The latter can be calculated numerically using a collocation method (see appendix F)[12, 29]. Inverting numerically the matrix $\mathcal{E}$ then provides the values of $h = \mathcal{E}^{-1} \cdot S$. In the following, parameters are safety factor $q = 1.5$, normalised radial wavenumber $K_r\rho_i = 0.1$, ion to electron temperature ratio $\tau_i = 1$, amplitude of source term $s_0 = -1$, sideband ratios $s_1/s_0 = s_{-1}/s_0 = 0.5$, and frequency width of the source $\Delta\tilde{\Omega} = 0.1$.

Fig.7.3 shows the frequency spectra of $\Omega h_{0,\Omega}$ and $\Omega h_{1,\Omega}$. A GAM signature appears clearly at high frequency, while zonal flows and poloidal convective cells appear at low frequencies. Hence the level of the $m = 1$ component of the electric potential is smaller than the $m = 0$ component by a factor $K_r\rho_i$, in agreement with estimate $\left|\frac{\Omega h_{1,\Omega}}{\Omega h_{0,\Omega}}\right| \sim K_r\rho_i$. Fig.7.4 and Fig.7.5 show respectively the ratio $\frac{h_{1,\Omega}}{h_{-1,\Omega}}$ and the phase of $\frac{h_{1,\Omega}}{h_{0,\Omega}}$. It appears that the ratio $\frac{h_{1,\Omega}}{h_{-1,\Omega}}$ is about -1 in the GAM range, while the angle of $\frac{h_{1,\Omega}}{h_{0,\Omega}}$ is $90°$ (up-down asymmetry). At lower frequency $\frac{\Omega q R_0}{v_T} \sim K_r\rho_i$, the ratio $\frac{h_{1,\Omega}}{h_{-1,\Omega}}$ is again close to -1, i.e. up-down asymmetry, but with a polarity closer to $-90°$, i.e. opposite to GAMs. The very low frequency limit $\frac{\Omega q R_0}{v_T} \leq (K_r\rho_i)^2$ is more difficult to assess. The collocation method imposes to choose a frequency mesh with the same mesh size as the velocity variable. Low frequency then means a highly resolved velocity space, and therefore a large computation time. The difficulty is circumvented by increasing the value of $K_r\rho_i$ up to 0.25. It can then be checked in Fig.7.6 that the ratio $\frac{h_{1,\Omega}}{h_{-1,\Omega}}$ is close to 1 at vanishing frequency, in agreement with a mostly in-out asymmetrical poloidal convective cells. In summary, GAMs and convective cells in the intermediate frequency range are up-down asymmetrical, while low frequency cells are in-out asymmetrical. It also stressed that the polarity of a poloidal convective cell is rarely as clean cut as a GAM, i.e. it varies continuously with the frequency.

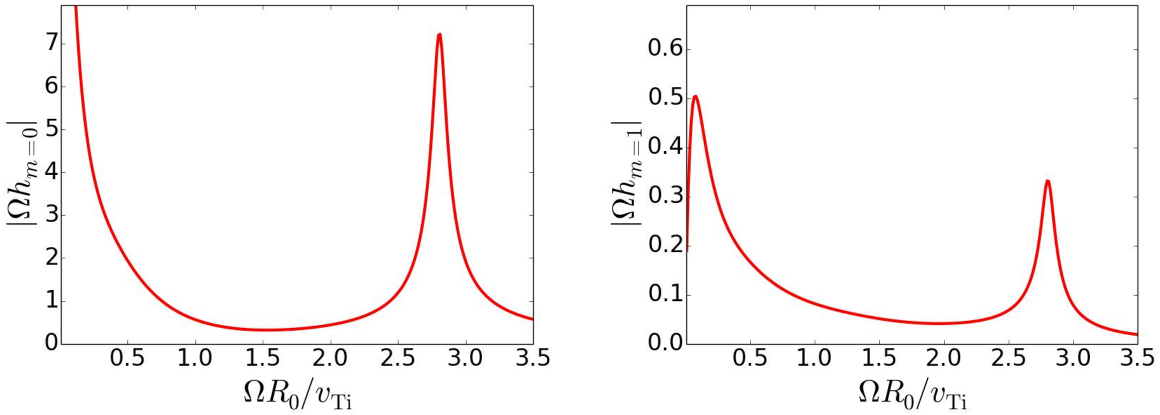

Figure 7.3.: *Absolute value of* $\Omega h_{0,\Omega}$ *and* $\Omega h_{1,\Omega}$

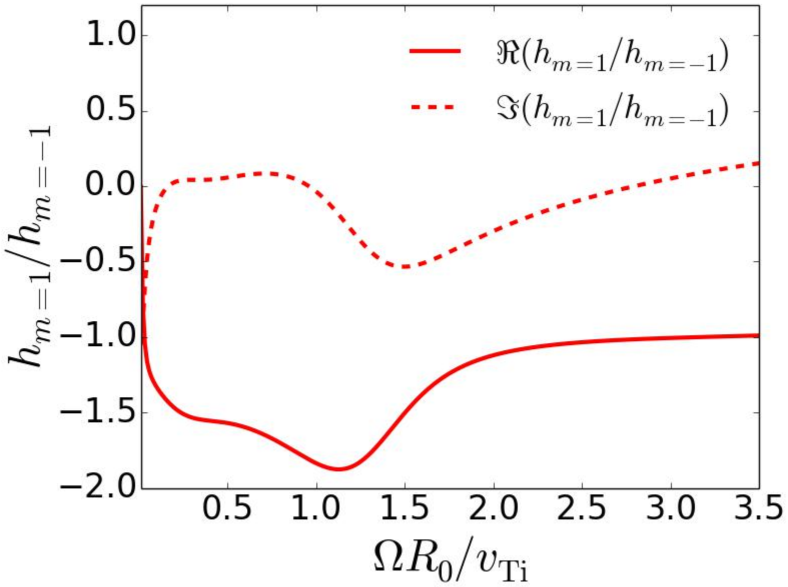

Figure 7.4.: *Real and imaginary parts of the ratio* $\frac{h_{1,\Omega}}{h_{-1,\Omega}}$ *vs* Ω

7.5.3. Limits of the model

The model does not account for trapped particles. This is visible by considering the limit $\Omega_D \lessapprox \Omega$ and looking at the dynamics of the mode $M = 0$. In this case, at leading order in $\tilde{K} = K_r\rho_i$, one gets

$$i\Omega h_{0,\Omega}\mathrm{det}\mathcal{E} = X_0^2 S'$$

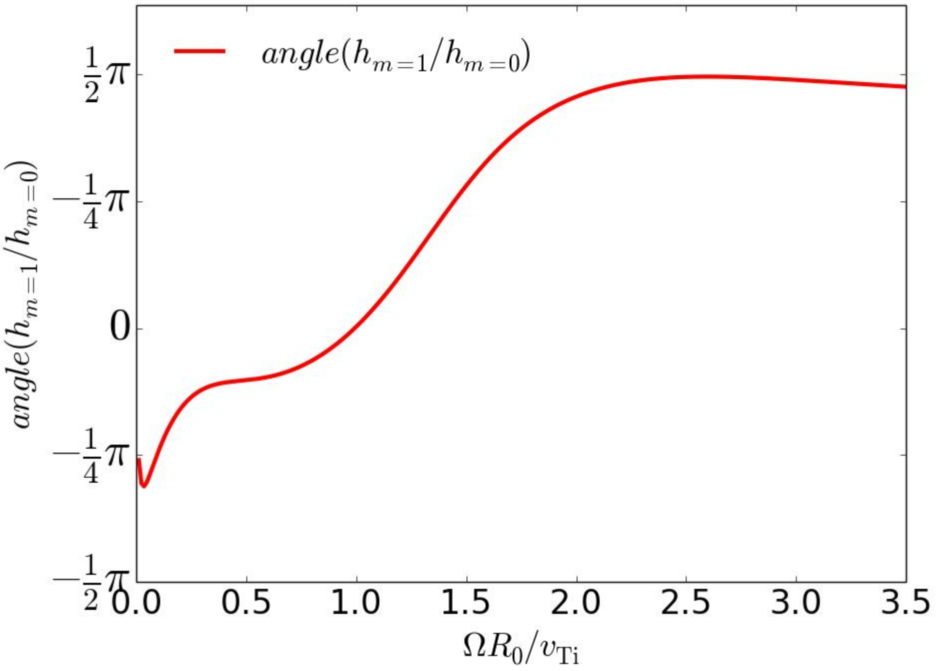

Figure 7.5.: *Phase of* $\frac{h_{1,\Omega}}{h_{0,\Omega}}$

where

$$\det\mathcal{E} \simeq \left(\frac{N_{eq}}{T_{eq}}\right)^3 (1+\tau)^2 \tilde{K}^2 \left[1+\frac{q^2}{2}\left(1+\frac{\pi}{2(1+\tau)}+i\frac{\sqrt{2\pi}}{\tilde{\Omega}}\right)\right]$$

Since the source S' is equal to $\tilde{K}^2\frac{N_{eq}eB_{eq}}{T_{eq}}\Pi_{RS,0}(\Omega)$, where $\Pi_{RS}(t)$ is the $M=0$, component of the turbulent Reynolds stress at scale K, one finds the following equation for the zonal flow

$$\left[1+\frac{q^2}{2}\left(1+\frac{\pi}{2(1+\tau)}\right)\right]\frac{\partial}{\partial t}\left(\frac{\phi_0}{B_{eq}}\right) = -\Pi_{RS,0}(t) - \sqrt{\frac{\pi}{2}}\frac{qv_T}{R_0}\frac{\phi_0}{B_{eq}}$$

The right hand side of the equation is the expected value with a neoclassical damping in plateau regime. The factor in front of the time derivative corresponds to the renormalisation of inertia due to the passing particles. It differs from the fluid classical value $1+2q^2$ [49] since the prefactor of q^2 is of the order of 1, i.e. twice smaller. If the trapped particles were taken into account, this factor should be $1+1.6\frac{q^2}{\sqrt{\epsilon}}$ [77], where $\epsilon=\frac{r}{R_0}$.

Trapping is important when the frequency Ω is of the order of the bounce frequency $\frac{v_T}{qR_0}\sqrt{\epsilon}$. The present modelis valid for $\Omega\sim\Omega_D$ only if $K_r\rho_i > \frac{\sqrt{\epsilon}}{q}$. This

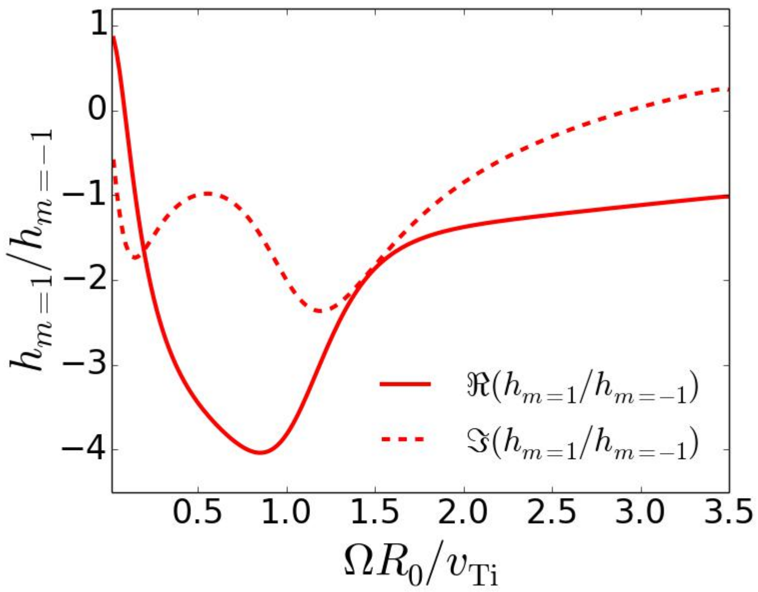

Figure 7.6.: *Real and imaginary parts of the ratio* $\frac{h_{1,\Omega}}{h_{-1,\Omega}}$ *vs* Ω *for* $K_r\rho_i = 0.25$

obviously excludes large scale flows, and requires small values of the inverse aspect ratio. The very low frequency regime $\Omega \sim \Omega_D K_r \rho_i$ seems even more difficult to reach since is requires $K_r^2\rho_i^2 > \frac{\sqrt{\epsilon}}{q}$, which would only occur for highly corrugated flows in the radial direction. We also recall that the non linear term $\left[\langle \overline{\mathbf{v}}_E\rangle_\varphi \cdot \nabla \langle \bar{g}\rangle_\varphi\right]_{M\Omega} \simeq 0$, which represents the advection by the convective cell of the associated distribution function, was ignored in this analysis, though it may play some role in the dynamics. Recent numerical simulations actually suggest that its amplitude is comparable to the Reynolds stress tensor S' in some cases [8].

7.5.4. Poloidal asymmetry of the distribution function

Most of this chapter is dedicated to the turbulent generation of axisymmetric modes ($n = 0$) of the electric potential. But the numerical test presented in section 7.1 has shown that even in the abscence of poloidal asymmetry of the electric field, the distribution function can displays large poloidal asymmetries (density in the case shown in section 7.1). An explanation of this observation is contained in Eq.(7.3.2)

$$\{\bar{g}\} = -i\Omega G^{-1}\frac{F_{eq}}{T_{eq}}\left\{\bar{h}\right\} - G^{-1}\left\{\left[\tilde{\bar{v}}_E \cdot \nabla\tilde{\bar{g}}\right]\right\}$$

Indeed, if one considers a special case without poloidal asymmetry for the axisymmetric part of the potential $\bar{h}_{-1,\Omega} = \bar{h}_{1,\Omega} = 0$, the axisymmetric part of the distribution function can still dispays poloidal asymmetries $\bar{g}_{-1,\Omega}, \bar{g}_{1,\Omega} \neq 0$. This is due to the perpendicular compressibility of the flow (off diagonal terms of G^{-1} proportionnal to Ω_D) and the ballooning of the turbulence ($\left[\tilde{\bar{v}}_E \cdot \nabla \tilde{\bar{g}}\right]_{-1,\Omega}, \left[\tilde{\bar{v}}_E \cdot \nabla \tilde{\bar{g}}\right]_{1,\Omega} \neq 0$).

Summary of the chapter

In this chapter, the turbulent generation of poloidal asymmetry for heavy impurities has been clarified. Two mechanisms have been identified. On the one hand, perpendicular compressibility of the flow allows the excitation of $M = \pm 1$ modes by the $M = 0$ mode. This mechanism is dominant for large frequencies. On the other hand, the ballooning of the turbulence directly produces a poloidal asymmetry of the source term for the axisymmetric modes of the potential and distribution function. This mechanism seems to be dominant for lower frequencies.

Conclusion

In fusion plasmas, impurities refer to any species different from deuterium and tritium, the fusion nuclei. Reactor plasmas will have both intrinsic – the helium ashes (alpha particles) – and extrinsic impurities, the latter coming from the plasma-wall interactions or being voluntarily injected (medium Z impurities in this case) so as to radiate the power at the plasma periphery. Understanding impurity transport is of utmost importance as core accumulation has a deleterious effects on plasma performance, by diluting the deuterium-tritium fuel and by radiating energy. In worst cases, the latter can lead to disruptions, i.e. the sudden loss of plasma confinement. There are three mechanisms of impurity transport. One is associated with turbulence, the second is coming from neoclassical (i.e. collisions) physics and the last one is due to MHD activity. This thesis focuses on the two firsts mechanisms and on their possible synergies. For this study, both mechanisms must be treated on an equal footing. Therefore a gyrokinetic approach has been adopted and the gyrokinetic code GYSELA has been chosen for the numerical calculation.

A new linearized collision operator valid for arbitrary species (mass, charge) and arbitrary concentration (trace or non-trace) has been developed and implemented in the GYSELA code. This collision operator possesses the most relevant properties which should be fulfilled by any full-f linearized operator within the gyrokinetic framework [1], in marked difference with the previous GYSELA version on two aspects. Firstly, it takes into account derivatives with respect to the adiabatic invariant μ , which is crucial for the isotropisation role of collisions in the velocity space. To do so, a projection of the distribution function on Laguerre polynomials in the μ direction allows treating the derivatives with respect to μ analytically. Finite differences are used for the parallel velocity derivatives. Secondly, a distinction has been made between the modulus diffusion rate ν_v and the deflection frequency ν_d . This distinction is especially crucial for treating accurately the collisions of electrons on ions and the case of non-trace impurities. The conservation properties (number of particles, momentum and energy) have been tested successfully. The relaxation toward the isotropic Maxwellian and the exchange rates of momentum and energy between species are also in good agreement with theoretical prediction.

---

[1] The present operator still proceeds from 2 simplifications, which are regarded as less important: (i) it does not account for the classical diffusion coefficient, which emerges when accounting for the gyroaverage of the distribution function, and (ii) the Jacobian coming from the gyrokinetic transform is neglected (technically speaking, $B_{\parallel}^*$ is replaced by B).

Neoclassical physics has been tested with the new collision operator. In the single species case, diffusion and poloidal rotation have been tested successfully in all collisionality regimes. Moreover, zonal flow collisional damping is in good agreement with theoretical prediction. This is a crucial point for the turbulence saturation, since these large-scale turbulence-driven poloidal flows are known to efficiently contribute to the saturation of ion-scale turbulence. Concerning the impurity transport, the standard neoclassical prediction (assuming weak poloidal asymmetries of the impurity fluid moments and of the electric potential) of diffusion, pinch velocity and thermal screening has been retrieved.

Poloidal asymmetry of the impurity density is often observed experimentally. This asymmetry is known to modify significantly the neoclassical prediction of impurity flux: the diffusion coefficient can vary by orders of magnitudes, while the pinch velocity can even reverse sign. Impurity density asymmetries boost only the Pfirsch-Schlüter contribution of the neoclassical flux. This regime is relevant for heavy impurities in current tokamaks. But heavy impurities should be closer to the banana/plateau regime in larger machines like ITER. The banana/plateau contribution is associated with pressure anisotropy. Therefore, a generalized approach of neoclassical impurity transport allowing for large pressure anisotropy and poloidal asymmetries of the impurity quantities has been developed. The main conclusion is that the banana/plateau flux of impurities can also be strongly impacted by the combined presence of pressure anisotropy and poloidal asymmetries. Large pressure anisotropy and poloidal asymmetries can be externally controlled by means of anisotropic heating sources (e.g. Ion Cyclotron Resonance Heating) and torque injection (e.g. Neutral Beam Injection) in the view of impurity control and/or self-generated by turbulence. The simulations reported in this PhD thesis, performed with GYSELA have confirmed that turbulence can produce pressure anisotropy and poloidal asymmetries by turbulence. Neoclassical theory has been modified to account for large pressure anisotropy and poloidal asymmetries. This analytical model agrees well with simulation results.

In this framework, so as to help reaching quantitative predictions regarding impurity transport, but also to provide a tentative explanation to some reported experimental evidence of asymmetric flows, the turbulent generation of poloidal asymmetries has been clarified by means of an original derivation which encompasses – and extends to the low frequency regime – the physics of the Geodesic Acoustic Modes. Two mechanisms have been identified for the generation of so-called convective cells, which correspond to axisymmetric modes (i.e. independent of the toroidal coordinate, characterized by a vanishing toroidal wave number $n = 0$) of the electric potential with large poloidal wave length (in practice mainly $m = \pm 1$ modes, with m the poloidal wave number). The first mechanism comes from the fact that turbulence is ballooned. That means that the Reynolds stress is larger where the turbulence intensity is maximum, i.e. on the low field side. In this case, the mode displays an in-out asymmetry. The second mechanism is associated with the compressibility of the flow. The mode then displays an up-down asymmetry.

In summary, it has been established that the standard neoclassical theory must be modified for heavy impurities in situations where turbulence drives pressure anisotropy and poloidal asymmetries. A new model has been derived, that allows a better understanding of the synergies between neoclassical and turbulent impurity transport observed with the code GYSELA. This study has demonstrated the necessity to take into account different parameters for a quantitative prediction of impurity transport in large devices like ITER. Firstly, the banana/plateau component of the neoclassical flux and its modification by large anisotropy and poloidal asymmetries is required. Secondly, it is necessary to account for the effect of turbulent generated poloidal asymmetry on neoclassical transport. This point is even more critical in large devices for which external sources should have a smaller impact than in current devices.

This study opens the way to various possible continuations. Firstly, a parametric scan could be done near the reference case presented in this thesis. The most critical parameters for a quantitative prediction on larger devices are the collisionality $\nu_\star$ and the normalized Larmor radius $\rho_\star$. Secondly, external sources could be added to demonstrate the predictive capability of the code GYSELA by comparing with experimental results. Once this capability proven, the study of the competition between externally and turbulent driven poloidal asymmetry would be necessary to evaluate the capability to control impurity transport by external sources on large devices. Finally, the inclusion of kinetic electrons (trapped electrons can now be treated kinetically in GYSELA), would also be highly desirable, keeping in mind the limitations imposed by the large numerical resources required by such multi-species flux-driven simulations. Indeed, this could change the nature of the turbulence by allowing more instabilities.

Appendix

A. Derivation of the Vlasov with $\bar{g}$

The goal of this appendix is to derive Eq.(5.1.2) starting from Eq.(5.1.1)

$$\frac{\partial \bar{F}}{\partial t} - \left\{\bar{H}, \bar{F}\right\} = 0$$

Using the relationship $\bar{F}(H_{eq}, \mu, P_\varphi, \theta, \varphi, t) = F_{eq}(\bar{H}, \mu, P_\varphi, t) + \bar{g}(H_{eq}, \mu, P_\varphi, \theta, \varphi, t)$, one gets

$$\frac{\partial \bar{g}}{\partial t} - \left\{\bar{H}, \bar{g}\right\} = -\frac{\partial}{\partial t} F_{eq}(\bar{H}, \mu, P_\varphi, t) + \left\{\bar{H}, F_{eq}(\bar{H}, \mu, P_\varphi, t)\right\}$$

For the time derivative on the rhs, we use the relationship $F_{eq}(\bar{H}, \mu, P_\varphi) \simeq F_{eq}(H_{eq}, \mu, P_\varphi) + \bar{h}\partial_{H_{eq}} F_{eq}(H_{eq}, \mu, P_\varphi)$ where $\bar{H} = H_{eq} + \bar{h}$. Adding the fact that $\frac{\partial}{\partial t} F_{eq}(H_{eq}, \mu, P_\varphi, t)$, one gets

$$\frac{\partial}{\partial t} F_{eq}(\bar{H}, \mu, P_\varphi, t) = \partial_{H_{eq}} F_{eq}(H_{eq}, \mu, P_\varphi) \frac{\partial \bar{h}}{\partial t}$$

To treat the Poisson bracket on the rhs, one uses the fact F_{eq} is a function of the invariants $F_{eq} = \sum_k J_k \frac{\partial F_{eq}}{\partial J_k}$ where J_k are the actions of the movement. As $\{H_{eq}, J_k\} = 0$ whatever k, one gets

$$\left\{\bar{H}, F_{eq}(\bar{H}, \mu, P_\varphi, t)\right\} = \sum_k \frac{\partial F_{eq}}{\partial J_k} \left\{\bar{h}, J_k\right\}$$

The only non vanishing Poisson bracket is $\left\{\bar{h}, P_\varphi\right\}$. As $\{\psi, P_\varphi\} = 0$, $\{\theta, P_\varphi\} = 0$ and $\{\varphi, P_\varphi\} = 1$ then $\left\{\bar{h}, P_\varphi\right\} = \frac{\partial \bar{h}}{\partial \varphi}$. Therefore

$$\frac{\partial \bar{g}}{\partial t} - \left\{\bar{H}, \bar{g}\right\} = F_{eq} \left(-\frac{\partial \ln F_{eq}}{\partial H_{eq}} \frac{\partial}{\partial t} \bar{h} + \frac{\partial \ln F_{eq}}{\partial P_\varphi} \frac{\partial \bar{h}}{\partial \varphi} \right)$$

Defining the inverse of a "temperature" $\frac{1}{T_{eq}} = -\frac{\partial}{\partial H_{eq}} \ln F_{eq}$ and the kinetic geomagnetic frequency $\Omega^* = T_{eq} \frac{\partial \ln F_{eq}}{\partial P_\varphi}$, one finally gets Eq.(5.1.1)

$$\frac{\partial \bar{g}}{\partial t} - \left\{\bar{H}, \bar{g}\right\} = \frac{F_{eq}}{T_{eq}} \left(\frac{\partial}{\partial t} + \Omega^* \frac{\partial}{\partial \varphi} \right) \bar{h}$$

B. Vlasov equation of the resonant part of the distribution in ballooning representation

The goal of this appendix is to derive Eq.(5.1.7) starting from Eq.(5.1.4):

$$\frac{\partial \bar{g}}{\partial t} + v_\parallel \nabla_\parallel \bar{g} + \mathbf{v}_E \cdot \nabla \bar{g} + \mathbf{v}_D \cdot \nabla \bar{g} = \frac{F_{eq}}{T_{eq}} \left(\frac{\partial}{\partial t} + \Omega^* \frac{\partial}{\partial \varphi} \right) \bar{h}$$

and using the ballooning representation Eq.(5.1.6):

$$\tilde{\phi}(\psi, \alpha, \theta, t) = \sum_{\mathbf{k}\omega} \phi_{\mathbf{k}\omega} \exp\left\{ i \left[n\theta_k q(\psi) + n\alpha - \omega t \right] \right\}$$

The parallel derivative present in Eq.(5.1.4) can be written

$$\begin{aligned} v_\parallel \nabla_\parallel \bar{g} &= \frac{v_\parallel}{R_0} \left(\partial_\varphi + \frac{1}{q} \partial_\theta \right) \bar{g} \\ &= \frac{v_\parallel}{R_0} \sum_{\mathbf{k}\omega} \left[in \left(1 - \frac{q}{q} \right) \bar{g}_{\boldsymbol{k}\omega} + \frac{1}{q} \partial_\theta \bar{g}_{\boldsymbol{k}\omega} \right] \exp\left\{ i \left[n\theta_k q(\psi) + n\alpha - \omega t \right] \right\} \\ &= \Omega_t \sum_{\mathbf{k}\omega} \partial_\theta \bar{g}_{\boldsymbol{k}\omega} \exp\left\{ i \left[n\theta_k q(\psi) + n\alpha - \omega t \right] \right\} \qquad \text{(B.1)} \end{aligned}$$

where $\Omega_t = \frac{v_\parallel}{qR_0}$. The term with the magnetic drift becomes

$$\begin{aligned} \mathbf{v}_D \cdot \nabla \bar{g} &= v_D \left(\sin\theta \partial_r + \frac{\cos\theta}{r} \partial_\theta \right) \bar{g} \\ &= -v_D \sum_{\mathbf{k}\omega} in \frac{q}{r} \left[\cos\theta + (\theta - \theta_k) \sin\theta \frac{r}{q} \partial_r q(\psi) \right] \bar{g}_{\boldsymbol{k}\omega} \exp\left\{ i \left[n\theta_k q(\psi) + n\alpha - \omega t \right] \right\} \end{aligned}$$

The derivatives of $\bar{g}_{\boldsymbol{k}\omega}$ have been neglected $\partial_r \bar{g}_{\boldsymbol{k}\omega} \ll n \left(\theta_k - \theta \right) \partial_r q(\psi) \bar{g}_{\boldsymbol{k}\omega}$ and $\partial_\theta \bar{g}_{\boldsymbol{k}\omega} \ll nq \bar{g}_{\boldsymbol{k}\omega}$ because large toroidal wavenumbers are considered. Using the relationships $s = \frac{r}{q} \partial_r q(\psi)$ and $k_\theta = -\frac{nq}{r}$, one get

$$\mathbf{v}_D \cdot \nabla \bar{g} = i \sum_{\mathbf{k}\omega} \omega_D \bar{g}_{\boldsymbol{k}\omega} \exp\left\{ i \left[n\theta_k q(\psi) + n\alpha - \omega t \right] \right\} \qquad \text{(B.2)}$$

where

$$\omega_D = k_\theta v_D \left[\cos\theta + s \left(\theta - \theta_k \right) \sin\theta \right]$$

Using Eq.(B.1) and Eq.(B.2), then Eq.(5.1.7) is naturally coming from Eq.(5.1.4):

$$\Omega_t \frac{\partial \bar{g}_{\mathbf{k}\omega}}{\partial \theta} - i\left(\omega - \omega_D\right) \bar{g}_{\mathbf{k}\omega} = -i\left(\omega - \omega_\star\right) h_{\mathbf{k}\omega} \frac{F_{eq}}{T_{eq}}$$

C. Linear response of the distribution function

The goal of this appendix is to derive the linear response of the distribution function Eq.(5.2.2). The first step is to link the perturbed distribution function of particles to the resonant distribution function of gyrocenters Eq(2.1.3)

$$F_z\left(\boldsymbol{x}, \boldsymbol{v}, t\right) = -\frac{Ze}{T_{z,eq}\left(\boldsymbol{x}\right)} F_{z,eq}\left(\boldsymbol{x}, \boldsymbol{v}\right) \left[\phi\left(\boldsymbol{x}, t\right) - \bar{\phi}\left(\boldsymbol{x}_G, t\right)\right] + \bar{F}_z\left(\boldsymbol{x}_G, \boldsymbol{v}_G, t\right)$$

This relation combined with the definition of $\bar{g}$: $\bar{F}(H_{eq}, \mu, P_\varphi, \theta, \varphi, t) = F_{eq}(\bar{H}, \mu, P_\varphi, t) + \bar{g}(H_{eq}, \mu, P_\varphi, \theta, \varphi, t)$ and the development of the distribution function $F_{eq}(\bar{H}, \mu, P_\varphi) \simeq F_{eq}(H_{eq}, \mu, P_\varphi) + Ze\mathcal{J}\phi\partial_{H_{eq}} F_{eq}(H_{eq}, \mu, P_\varphi)$ where $\bar{H} = H_{eq} + \bar{h}$ gives

$$f_z = -eZ\frac{F_{z,eq}}{T_{z,eq}}\phi + \bar{g}_z$$

The second step of the computation is to use the linear response of the resonant part of the gyro center distribution function $\bar{g}_z$ that is directly coming from Eq.(5.1.7)

$$\bar{g}_{z,\boldsymbol{k}\omega} = \frac{\omega - \omega_\star}{\omega - \omega_d - k_\parallel v_\parallel} \mathcal{J} eZ\phi_{\boldsymbol{k}\omega}\frac{F_{z,eq}}{T_{z,eq}}$$

where the term $\Omega_t \frac{\partial \bar{g}_{\mathbf{k}\omega}}{\partial \theta}$ has been replaced by $ik_\parallel v_\parallel \bar{g}_{\mathbf{k}\omega}$ for the simplicity of the notation. Rigorously, the notation $k_\parallel v_\parallel$ has to be understood has an operator. Putting all together, one gets Eq.(5.2.2)

$$f_{z,\boldsymbol{k}\omega} = -\left[1 - \frac{\omega - \omega_\star}{\omega - \omega_d - k_\parallel v_\parallel}\mathcal{J}\right] eZ\phi_{\boldsymbol{k}\omega}\frac{F_{z,eq}}{T_{z,eq}}$$

D. Derivation of the collisional parallel momentum exchange for trace and heavy impurities

The goal of this appendix is to derive Eq.(6.2.7) and Eq.(6.2.8). We begin our derivation by taking the expression of the collisional exchange of momentum Eq.(4.4.17) in the case of a trace $\left(\frac{N_z Z^2}{N_i} \ll 1\right)$ heavy impurity $\left(\frac{m_z}{m_i} \gg 1\right)$

$$R_{\parallel zi} = -N_z m_z \nu_{zi}\left[V_{\parallel z} - V_{\parallel z} + \frac{3}{5}\frac{q_{\parallel i}}{N_i T_i}\right] \tag{D.1}$$

Moreover, the parallel velocity of any species can be expressed in the form

$$V_{\parallel s}=\frac{K_s}{N_s}B-\frac{I\Omega_s}{B} \tag{D.2}$$

with $\Omega_s=\frac{\partial\phi}{\partial\psi}+\frac{1}{N_zeZ}\frac{\partial P_{\perp s}}{\partial\psi}$ for any species s. In the same spirit, the parallel heat flux of the main ion takes the form

$$\frac{q_{\parallel i}}{N_iT_i}=L_iB-\frac{5}{2}\frac{I}{eB}\frac{\partial T_i}{\partial\psi} \tag{D.3}$$

where L_i is a flux function. Substituting Eq.(D.2) and Eq.(D.3) in Eq.(D.1), one gets directly Eq.(6.2.7)

$$R_{\parallel zi}=m_z\nu_{zi}\left\{-N_Z\frac{T_i}{eB}\frac{I}{L_\psi}+B\left(N_zu-K_z\right)\right\}$$

at the condition to define $\frac{1}{L_\psi}=\frac{1}{L_{\psi,i}}+\frac{1}{L_{\psi,z}}$ with $\frac{1}{L_{\psi,i}}=\frac{\partial\ln P_i}{\partial\psi}-\frac{3}{2}\frac{\partial\ln T_i}{\partial\psi}$ and $\frac{1}{L_{\psi,z}}=-\frac{1}{T_iZN_z}\frac{\partial P_{\perp z}}{\partial\psi}$ and

$$u=\frac{K_i}{N_i}-\frac{3}{5}L_i$$

The second step of this appendix is to prove the expression of u Eq.(6.2.8). The first step is to compute $\frac{K_i}{N_i}$, to do so we use the vector expression of the ion velocity

$$\boldsymbol{V}_i=\frac{K_i}{N_i}\boldsymbol{B}-\Omega_iR^2\nabla\varphi \tag{D.4}$$

The poloidal velocity of the main ion is kown in the neoclassical theory $v_\theta=k_{neo}\left(\nu_\star,\epsilon\right)\frac{\nabla T}{eB}$. The poloidal projection of Eq.(D.4) then leads to

$$\frac{K_i}{N_i}=k_{neo}\frac{I}{e\left\langle B^2\right\rangle_\psi}\frac{\partial T_i}{\partial\psi}$$

L_i can be computed directly with Eq.(4.4.16)

$$L_i=\frac{\left\langle B\frac{q_{\parallel i}}{N_iT_i}\right\rangle_\psi}{\left\langle B^2\right\rangle_\psi}-\frac{5}{2}\frac{I}{e\left\langle B^2\right\rangle_\psi}\frac{\partial T_i}{\partial\psi}$$

It has been showned [47] that $\left\langle B\frac{q_{\parallel i}}{N_iT_i}\right\rangle_\psi\sim\sqrt{\epsilon}L_i$. Then at lowest order in ϵ, Eq.(6.2.8) is retrieved

$$u=\left(k_{neo}-\frac{3}{2}\right)\frac{I}{e\left\langle B^2\right\rangle_\psi}\frac{\partial T_i}{\partial\psi}$$

E. Flux of vorticity

We calculate in this appendix, the turbulent drive of poloidal convective cells $\mathcal{J}\left[\bar{\mathbf{v}}_E\cdot\nabla\bar{g}\right]_{M\Omega}$. This source term can be recast as

$$\mathcal{J}\left[\bar{\mathbf{v}}_E\cdot\nabla\bar{g}\right]_{M\Omega}=\mathcal{J}\left[\frac{\mathbf{B}_{eq}}{B_{eq}^2}\cdot\left(\nabla\left(\mathcal{J}\phi\right)\times\nabla\bar{g}\right)\right]_{M\Omega}$$

The gradient of any field can be written as $\nabla\phi=\frac{\partial\phi}{\partial\theta}\nabla\theta+\frac{\partial\phi}{\partial\psi}\nabla\psi+\frac{\partial\phi}{\partial\alpha}\nabla\alpha$. Let us note that

$$\frac{\partial\phi}{\partial\theta}\left|\nabla\theta\right|\ll\frac{\partial\phi}{\partial\psi}\left|\nabla\psi\right|,\frac{\partial\phi}{\partial\alpha}\left|\nabla\alpha\right|$$

in the frame of the ballooning representation, i.e. the gradient of fluctuations along the field lines is much smaller than the transverse gradients. This also implies that transverse gradients of fluctuations are larger than gradients of metric elements or of any equilibrium quantity. Another consequence is that the gyroaverage operator $\mathcal{J}$ commutes with quantities that depend on θ only. This implies that

$$\nabla\left(\mathcal{J}\phi\right)\times\nabla\bar{g}=\left(\frac{\partial\left(\mathcal{J}\phi\right)}{\partial\alpha}\frac{\partial\bar{g}}{\partial\psi}-\frac{\partial\left(\mathcal{J}\phi\right)}{\partial\psi}\frac{\partial\bar{g}}{\partial\alpha}\right)\mathbf{B}_{eq}$$

Using integration by part on the α integral, it is possible to show that

$$\left[\bar{\mathbf{v}}_E\cdot\nabla\bar{g}\right]_{M\Omega}=\int_0^T\frac{dt}{T}e^{i\Omega t}\int\frac{d\theta}{2\pi}e^{-iM\theta}\int\frac{d\alpha}{2\pi}\frac{\partial}{\partial\Psi}\left(\bar{\mathcal{E}}_\alpha\bar{g}\right)$$

where $\bar{\mathcal{E}}_\alpha=\frac{\partial(\mathcal{J}\phi)}{\partial\alpha}$. Using the large wavelength limit $k_\perp\rho_i\ll1$ the gyroaverage can be expressed simply $\mathcal{J}\simeq1+\frac{m\mu}{2e^2B_{eq}}$. The perpendicular laplacian is in fact close to the complete laplacian $\nabla_\perp^2$ for small parallel gradients. Moreover, the general definition of the laplacian for the set of coordinates $x^i=(\psi,\alpha,\theta)$ is

$$\nabla_\perp^2\phi=\frac{1}{\sqrt{g}}\frac{\partial}{\partial x^i}\left(\sqrt{g}\nabla x^i\cdot\nabla x^j\frac{\partial\phi}{\partial x^j}\right)$$

where $\sqrt{g}=\frac{1}{\mathbf{B}_{eq}\nabla\theta}$ is the Jacobian. With the ordering given before, and a quasi-circular equilibrium $\nabla\alpha\cdot\nabla\psi\simeq0$, one gets the following approximation

$$\nabla_\perp^2\phi\simeq\frac{1}{\sqrt{g}}\frac{\partial}{\psi}\left(\sqrt{g}\left|\nabla\psi\right|^2\frac{\partial\phi}{\partial\psi}\right)+\left|\nabla\alpha\right|^2\frac{\partial^2\phi}{\partial\alpha^2}$$

where the metric elements $\left|\nabla\psi\right|^2$, and $\left|\nabla\alpha\right|^2$ do not depend on α . It can then be shown that $\mathcal{J}\left[\bar{\mathbf{v}}_E\cdot\nabla\bar{g}\right]_{M\Omega}=\frac{\partial\Gamma_\Pi}{\partial\psi}$

$$\Gamma_\Pi=\int_0^T\frac{dt}{T}\int\frac{d\theta}{2\pi}e^{-iM\theta+i\Omega t}\int\frac{d\alpha}{2\pi}\mathcal{J}\left(\bar{\mathcal{E}}_\alpha\bar{g}\right)$$

We note that $\bar{g}$ can be replaced safely by $\bar{f}$ since the adiabatic response does not contribute to the flux as $\int \frac{d\alpha}{2\pi}\bar{\mathcal{E}}_\alpha\left(\mathcal{J}\phi\right) = 0$.

F. Treatment of the resonant functions $L_j\left(\Omega\right)$ and numerical solution

The Bessel functions are expanded at lowest order in K^2. It then appears that the matrix $\mathcal{E}$ and the source $\{S\}$ can be expressed as

$$\begin{aligned}
\mathcal{E}_a &= \left(1+\tau\right)\left\langle 1\right\rangle_v + L_0 - L_2\\
\mathcal{E}_b &= K^2 + 2L_2\\
\mathcal{E}_c &= L_1\\
\mathcal{E}_d &= -L_2
\end{aligned} \tag{F.1}$$

and

$$\begin{aligned}
-i\Omega\left\{S\right\}_{M=-1} &= \left(-iL_1 + L_0 - 2L_2\right)\mathcal{S}(\Omega)s_{-1}\\
-i\Omega\left\{S\right\}_{M=0} &= \left(-1 + 2L_2\right)\mathcal{S}(\Omega)s_0\\
-i\Omega\left\{S\right\}_{M=1} &= \left(iL_1 + L_0 - 2L_2\right)\mathcal{S}(\Omega)s_1
\end{aligned} \tag{F.2}$$

where

$$L_j\left(\Omega\right) = \left\langle \frac{\Omega^{2-j}\Omega_D^j}{\Omega_+\Omega_- + 2\Omega_D^2}\right\rangle$$

and the prefactor $\frac{N_{eq}}{T_{eq}}$ has been removed in all kinetic integrals. The potential $\{h\}$ is given by the relation $\{h\} = \mathcal{E}^{-1}\{S\}$.

The dimensionless functions $L_j\left(\Omega\right)$ can be expressed in normalized form as

$$L_j\left(\tilde{\Omega}\right) = \left(\frac{\tilde{\Omega}}{q}\right)^{2-j}\int_0^{+\infty} due^{-u}\int_{-\infty}^{+\infty}\frac{d\zeta}{\sqrt{\pi}}e^{-\zeta^2}\frac{\bar{\Omega}_D^j}{R} \tag{F.3}$$

where $u = \frac{1}{2}\frac{v_\perp{}^2}{v_T^2}$, $\zeta = \frac{1}{\sqrt{2}}\frac{v_\parallel}{v_T}$, $R = \frac{2}{q^2}\zeta^2 + 2\bar{\Omega}_D^2 - \left(\frac{\tilde{\Omega}}{q}\right)^2$, and $\bar{\Omega}_D = \frac{\tilde{K}}{2}\left(u + 2\zeta^2\right)$. These are resonant integrals, which must be continued analytically to ensure a proper inverse Laplace transport (Landau prescription). This is most easily done by introducing an elliptical change of variables

$$\begin{aligned}
\zeta(\rho,\theta) &= \frac{q}{\sqrt{2}}\tilde{K}\rho\sin\theta\\
u(\rho,\theta) &= \sqrt{2}\rho\cos\theta - \tilde{K}^2q^2\rho^2\sin^2\theta
\end{aligned}$$

The quantities of interest (magnetic drift frequency, resonance, and energy) have still simple expressions in this set of variables

$$\begin{aligned}
&R(\rho,\theta) = \tilde{K}^2\rho^2 - \left(\tfrac{\tilde{\Omega}}{q}\right)^2 \\
&\bar{\Omega}_D(\rho,\theta) = \tfrac{\tilde{K}}{\sqrt{2}}\rho\cos\theta \\
&E(\rho,\theta) = u + \zeta^2 = \sqrt{2}\rho\cos\theta - \tfrac{1}{2}\tilde{K}^2 q^2\rho^2\sin^2\theta
\end{aligned}$$

The Jacobian of the change of this variables is $J = q\tilde{K}\rho$. The resonant integrals Eq.(F.3) can then be recast in the following convenient form

$$L_j\left(\varpi\right) = \frac{q\tilde{K}}{\sqrt{\pi}}\varpi^{2-j}\int_0^{+\infty} d\rho\frac{2\rho}{\rho^2-\varpi^2}\int_0^{\theta_0(\rho)} d\theta e^{-E}\bar{\Omega}_D^j$$

where the angle $\theta_0(\rho)$ is such that $\cos\theta_0 = -a + \sqrt{1+a^2}$, $a = \frac{1}{\sqrt{2}\tilde{K}^2q^2\rho}$, $\bar{\Omega}_D = \frac{1}{\sqrt{2}}\rho\cos\theta$, and $\varpi = \frac{\tilde{\Omega}}{q\tilde{K}}$. The cut-off $\theta \leq \theta_0$ ensures that the perpendicular energy u is always positive. For positive and real values of $\tilde{K}$, the Laplace contour prescription in Ω translates to the same one on the normalized variable ϖ. Hence the integrals to be calculated are of the form

$$L_j(\varpi) = \varpi^{2-j}\int_0^{+\infty} d\rho\frac{2\rho G_j(\rho)}{\rho^2-\varpi^2}$$

where the functions

$$G_j(\rho) = \frac{q\tilde{K}}{\sqrt{\pi}}\int_0^{\theta_0(\rho)} d\theta e^{-E}\bar{\Omega}_D^j$$

are smooth in ρ. This formulation allows an easy implementation of the Landau prescription by using the identity

$$\frac{2\rho}{\rho^2-\varpi^2} = \frac{1}{\rho-\varpi} + \frac{1}{\rho+\varpi}$$

Restricting the analysis to $\Re(\Omega) > 0$, one find the rule

$$L_j(\varpi) = \begin{cases}
\varpi^{2-j}\int_0^{+\infty} d\rho\frac{2\rho G_j(\rho)}{\rho^2-\varpi^2} & \Im(\varpi) > 0 \\
\varpi^{2-j}P.P.\int_0^{+\infty} d\rho\frac{2\rho G_j(\rho)}{\rho^2-\varpi^2} + i\pi\varpi^{2-j}G_j(\varpi) & \Im(\varpi) = 0 \\
\varpi^{2-j}\int_0^{+\infty} d\rho\frac{2\rho G_j(\rho)}{\rho^2-\varpi^2} + 2i\pi\varpi^{2-j}G_j(\varpi) & \Im(\varpi) < 0
\end{cases}$$

The principal part that appears in the function L_0 exhibits a logarithmic singularity near $\varpi = 0$ that is regularized by the ϖ^2 prefactor . The functions L_1 and L_2 are regular near $\varpi = 0$. The functions L_j can be computed in the domain $\Re(\tilde{\Omega}) < 0$ by using the properties $L_j(-\tilde{\Omega}) = \left[L_j(\tilde{\Omega})\right]^*$ for positive $\tilde{K}$. All these integrals are calculated numerically by using a collocation integration method [12, 29].

The asymptotic forms Eq.(7.3.8) are recovered when $\tilde{\Omega} \geq 1$ with an excellent accuracy.

Bibliography

[1] I. G. Abel, M. Barnes, S. C. Cowley, W. Dorland, and A. A. Schekochihin. Linearized model fokker-planck collision operators for gyrokinetic simulations. i. theory. *Physics of Plasmas*, 15(12):122509, 2008. doi: 10.1063/1.3046067. URL http://dx.doi.org/10.1063/1.3046067.

[2] J. Abiteboul, X. Garbet, V. Grandgirard, S. J. Allfrey, Ph. Ghendrih, G. Latu, Y. Sarazin, and A. Strugarek. Conservation equations and calculation of mean flows in gyrokinetics. *Physics of Plasmas*, 18(8):082503, 2011. doi: 10.1063/1.3620407. URL https://doi.org/10.1063/1.3620407.

[3] Jae-H Ahn, X Garbet, H Lutjens, and R Guirlet. Dynamics of heavy impurities in non-linear mhd simulations of sawtoothing tokamak plasmas. *Plasma Physics and Controlled Fusion*, 58(12):125009, 2016. URL http://stacks.iop.org/0741-3335/58/i=12/a=125009.

[4] C Angioni and P Helander. Neoclassical transport of heavy impurities with poloidally asymmetric density distribution in tokamaks. *Plasma Physics and Controlled Fusion*, 56(12):124001, 2014. URL http://stacks.iop.org/0741-3335/56/i=12/a=124001.

[5] C. Angioni, F. J. Casson, C. Veth, and A. G. Peeters. Analytic formulae for centrifugal effects on turbulent transport of trace impurities in tokamak plasmas. *Physics of Plasmas*, 19(12):122311, 2012. doi: 10.1063/1.4773051. URL https://doi.org/10.1063/1.4773051.

[6] C. Angioni, F. J. Casson, P. Mantica, T. Pütterich, M. Valisa, E. A. Belli, R. Bilato, C. Giroud, and P. Helander. The impact of poloidal asymmetries on tungsten transport in the core of jet h-mode plasmas. *Physics of Plasmas*, 22(5):055902, 2015. doi: 10.1063/1.4919036. URL https://aip.scitation.org/doi/abs/10.1063/1.4919036.

[7] C. Angioni, M. Sertoli, R. Bilato, V. Bobkov, A. Loarte, R. Ochoukov, T. Odstrcil, T. Pütterich, J. Stober, and The ASDEX Upgrade Team. A comparison of the impact of central ecrh and central icrh on the tungsten behaviour in asdex upgrade h-mode plasmas. *Nuclear Fusion*, 57(5):056015, 2017. URL http://stacks.iop.org/0029-5515/57/i=5/a=056015.

[8] Y. Asahi, V. Grandgirard, Y. Sarazin, P. Donnel, X. Garbet, Y. Idomura, G. Dif-Pradalier, and G. Latu. Synergy of turbulent and neoclassical transport through poloidal convective cells. *To be submitted in Plasma Physics and Controlled Fusion*, 2018.

[9] M. Barnes, I. G. Abel, W. Dorland, D. R. Ernst, G. W. Hammett, P. Ricci, B. N. Rogers, A. A. Schekochihin, and T. Tatsuno. Linearized model fokker-planck collision operators for gyrokinetic simulations. ii. numerical implementation and tests. *Physics of Plasmas*, 16(7):072107, 2009. doi: 10.1063/1.3155085. URL `http://dx.doi.org/10.1063/1.3155085`.

[10] R. Bilato, O. Maj, and C. Angioni. Modelling the influence of temperature anisotropies on poloidal asymmetries of density in the core of rotating plasmas. *Nuclear Fusion*, 54(7):072003, 2014. URL `http://stacks.iop.org/0029-5515/54/i=7/a=072003`.

[11] N. Bonanomi, P. Mantica, C. Giroud, C. Angioni, P. Manas, S. Menmuir, and JET Contributors. Light impurity transport in jet ilw l-mode plasmas. *Nuclear Fusion*, 58(3):036009, 2018. URL `http://stacks.iop.org/0029-5515/58/i=3/a=036009`.

[12] M. Brambilla and R. Bilato. Advances in numerical simulations of ion cyclotron heating of non-maxwellian plasmas. *Nuclear Fusion*, 49(8):085004, 2009. URL `http://stacks.iop.org/0029-5515/49/i=8/a=085004`.

[13] Alain J. Brizard. A guiding-center fokker-planck collision operator for nonuniform magnetic fields. *Physics of Plasmas*, 11(9):4429–4438, 2004. doi: 10.1063/1.1780532. URL `https://doi.org/10.1063/1.1780532`.

[14] Y. Camenen, A. G. Peeters, C. Angioni, F. J. Casson, W. A. Hornsby, A. P. Snodin, and D. Strintzi. Impact of the background toroidal rotation on particle and heat turbulent transport in tokamak plasmas. *Physics of Plasmas*, 16(1):012503, 2009. doi: 10.1063/1.3057356. URL `https://doi.org/10.1063/1.3057356`.

[15] J. Candy and R.E. Waltz. An eulerian gyrokinetic-maxwell solver. *Journal of Computational Physics*, 186(2):545 – 581, 2003. ISSN 0021-9991. doi: https://doi.org/10.1016/S0021-9991(03)00079-2. URL `http://www.sciencedirect.com/science/article/pii/S0021999103000792`.

[16] F J Casson, C Angioni, E A Belli, R Bilato, P Mantica, T Odstrcil, T Pütterich, M Valisa, L Garzotti, C Giroud, J Hobirk, C F Maggi, J Mlynar, and M L Reinke. Theoretical description of heavy impurity transport and its application to the modelling of tungsten in jet and asdex upgrade. *Plasma Physics and Controlled Fusion*, 57(1):014031, 2015. URL `http://stacks.iop.org/0741-3335/57/i=1/a=014031`.

[17] C. S. Chang and F. L. Hinton. Effect of impurity particles on the finite aspect ratio neoclassical ion thermal conductivity in a tokamak. *The Physics of Fluids*, 29(10):3314–3316, 1986. doi: 10.1063/1.865847. URL `http://aip.scitation.org/doi/abs/10.1063/1.865847`.

[18] C.Z. Cheng and H. Okuda. Theory and numerical simulations on collisionless drift instabilities in three dimensions. *Nuclear Fusion*, 18(5):587, 1978. URL `http://stacks.iop.org/0029-5515/18/i=5/a=001`.

[19] J. W. Connor, J. B. Taylor, and H. R. Wilson. Shear damping of drift waves in toroidal plasmas. *Phys. Rev. Lett.*, 70:1803–1805, Mar 1993. doi: 10.1103/PhysRevLett.70.1803. URL `https://link.aps.org/doi/10.1103/PhysRevLett.70.1803`.

[20] G. D. Conway, C. Angioni, F. Ryter, P. Sauter, and J. Vicente. Mean and oscillating plasma flows and turbulence interactions across the $l-h$ confinement transition. *Phys. Rev. Lett.*, 106:065001, Feb 2011. doi: 10.1103/PhysRevLett.106.065001. URL `https://link.aps.org/doi/10.1103/PhysRevLett.106.065001`.

[21] J. Crank and P. Nicolson. A practical method for numerical evaluation of solutions of partial differential equations of the heat-conduction type. *Advances in Computational Mathematics*, 6(1):207–226, Dec 1996. ISSN 1572-9044. doi: 10.1007/BF02127704. URL `https://doi.org/10.1007/BF02127704`.

[22] P H Diamond, S-I Itoh, K Itoh, and T S Hahm. Zonal flows in plasmas - a review. *Plasma Physics and Controlled Fusion*, 47(5):R35, 2005. URL `http://stacks.iop.org/0741-3335/47/i=5/a=R01`.

[23] G. Dif-Pradalier, V. Grandgirard, Y. Sarazin, X. Garbet, and Ph. Ghendrih. Interplay between gyrokinetic turbulence, flows, and collisions: Perspectives on transport and poloidal rotation. *Phys. Rev. Lett.*, 103:065002, Aug 2009. doi: 10.1103/PhysRevLett.103.065002. URL `https://link.aps.org/doi/10.1103/PhysRevLett.103.065002`.

[24] G. Dif-Pradalier, G. Hornung, X. Garbet, Ph. Ghendrih, V. Grandgirard, G. Latu, and Y. Sarazin. The exb staircase of magnetised plasmas. *Nuclear Fusion*, 57(6):066026, 2017. URL `http://stacks.iop.org/0029-5515/57/i=6/a=066026`.

[25] A. M. Dimits, G. Bateman, M. A. Beer, B. I. Cohen, W. Dorland, G. W. Hammett, C. Kim, J. E. Kinsey, M. Kotschenreuther, A. H. Kritz, L. L. Lao, J. Mandrekas, W. M. Nevins, S. E. Parker, A. J. Redd, D. E. Shumaker, R. Sydora,

and J. Weiland. Comparisons and physics basis of tokamak transport models and turbulence simulations. *Physics of Plasmas*, 7(3):969–983, 2000. doi: 10.1063/1.873896. URL https://doi.org/10.1063/1.873896.

[26] P. Donnel, X. Garbet, Y. Sarazin, Y. Asahi, F. Wilczynski, E. Caschera, G. Dif-Pradalier, P. Ghendrih, and C. Gillot. Turbulent generation of poloidal asymmetries of the electric potential in a tokamak. *Plasma Physics and Controlled Fusion*, 2018. URL http://iopscience.iop.org/10.1088/1361-6587/aae4fe.

[27] P. Donnel, X. Garbet, Y. Sarazin, V. Grandgirard, Y. Asahi, N. Bouzat, E. Caschera, G. Dif-Pradalier, C. Ehrlacher, P. Ghendrih, C. Gillot, G. Latu, and C. Passeron. A multi-species collisional operator for full-f global gyrokinetics codes: Numerical aspects and verification with the gysela code. *Computer Physics Communications*, 2018. ISSN 0010-4655. doi: https://doi.org/10.1016/j.cpc.2018.08.008. URL http://www.sciencedirect.com/science/article/pii/S0010465518303035.

[28] W. Dorland, F. Jenko, M. Kotschenreuther, and B. N. Rogers. Electron temperature gradient turbulence. *Phys. Rev. Lett.*, 85:5579–5582, Dec 2000. doi: 10.1103/PhysRevLett.85.5579. URL https://link.aps.org/doi/10.1103/PhysRevLett.85.5579.

[29] R. Dumont. Private communication.

[30] D. Estève, X. Garbet, Y. Sarazin, V. Grandgirard, T. Cartier-Michaud, G. Dif-Pradalier, P. Ghendrih, G. Latu, and C. Norscini. A multi-species collisional operator for full-f gyrokinetics. *Physics of Plasmas*, 22(12):122506, 2015. doi: 10.1063/1.4937373. URL http://dx.doi.org/10.1063/1.4937373.

[31] D. Estève, Y. Sarazin, X. Garbet, V. Grandgirard, S. Breton, P. Donnel, Y. Asahi, C. Bourdelle, G. Dif-Pradalier, C. Ehrlacher, C. Emeriau, Ph. Ghendrih, C. Gillot, G. Latu, and C. Passeron. Self-consistent gyrokinetic modeling of neoclassical and turbulent impurity transport. *Nuclear Fusion*, 58(3):036013, 2018. URL http://stacks.iop.org/0029-5515/58/i=3/a=036013.

[32] T Fülöp and P Helander. Nonlinear neoclassical transport in a rotating impure plasma with large gradients. 6:3066–3075, 08 1999.

[33] X Garbet, P Mantica, F Ryter, G Cordey, F Imbeaux, C Sozzi, A Manini, E Asp, V Parail, R Wolf, and the JET EFDA Contributors. Profile stiffness and global confinement. *Plasma Physics and Controlled Fusion*, 46 (9):1351, 2004. URL http://stacks.iop.org/0741-3335/46/i=9/a=002.

[34] X. Garbet, J. Abiteboul, E. Trier, Ö. Gürcan, Y. Sarazin, A. Smolyakov, S. Allfrey, C. Bourdelle, C. Fenzi, V. Grandgirard, P. Ghendrih, and P. Hennequin. Entropy production rate in tokamaks with nonaxisymmetric magnetic fields. *Physics of Plasmas*, 17(7):072505, 2010. doi: 10.1063/1.3454365. URL https://doi.org/10.1063/1.3454365.

[35] X. Garbet, Y. Idomura, L. Villard, and T.H. Watanabe. Gyrokinetic simulations of turbulent transport. *Nuclear Fusion*, 50(4):043002, 2010. URL http://stacks.iop.org/0029-5515/50/i=4/a=043002.

[36] X Garbet, Y Asahi, P Donnel, C Ehrlacher, G Dif-Pradalier, P Ghendrih, V Grandgirard, and Y Sarazin. Impact of poloidal convective cells on momentum flux in tokamaks. *New Journal of Physics*, 19(1):015011, 2017. URL http://stacks.iop.org/1367-2630/19/i=1/a=015011.

[37] T. Görler, X. Lapillonne, S. Brunner, T. Dannert, F. Jenko, F. Merz, and D. Told. The global version of the gyrokinetic turbulence code gene. *Journal of Computational Physics 230, 7053*, 2011.

[38] V. Grandgirard, J. Abiteboul, J. Bigot, T. Cartier-Michaud, N. Crouseilles, G. Dif-Pradalier, Ch. Ehrlacher, D. Estève, X. Garbet, Ph. Ghendrih, G. Latu, M. Mehrenberger, C. Norscini, Ch. Passeron, F. Rozar, Y. Sarazin, E. Sonnendrucker, A. Strugarek, and D. Zarzoso. A 5d gyrokinetic full-f global semi-lagrangian code for flux-driven ion turbulence simulations. *Computer Physics Communications*, 207:35 – 68, 2016. ISSN 0010-4655. doi: https://doi.org/10.1016/j.cpc.2016.05.007. URL http://www.sciencedirect.com/science/article/pii/S0010465516301230.

[39] T. S. Hahm, M. A. Beer, Z. Lin, G. W. Hammett, W. W. Lee, and W. M. Tang. Shearing rate of time-dependent exb flow. *Physics of Plasmas*, 6(3): 922–926, 1999. doi: 10.1063/1.873331. URL https://doi.org/10.1063/1.873331.

[40] T. S. Hahm, Lu Wang, and J. Madsen. Fully electromagnetic nonlinear gyrokinetic equations for tokamak edge turbulence. *Physics of Plasmas*, 16(2):022305, 2009. doi: 10.1063/1.3073671. URL https://doi.org/10.1063/1.3073671.

[41] K. Hallatschek and D. Biskamp. Transport control by coherent zonal flows in the core/edge transitional regime. *Phys. Rev. Lett.*, 86:1223–1226, Feb 2001. doi: 10.1103/PhysRevLett.86.1223. URL https://link.aps.org/doi/10.1103/PhysRevLett.86.1223.

[42] P Helander. Comments on 'neoclassical heat flux due to poloidal electric field in arbitrary collisionality regime'. *Plasma Physics and Controlled Fu-*

sion, 37(1):57, 1995. URL http://stacks.iop.org/0741-3335/37/i=1/a=005.

[43] P. Helander. Bifurcated neoclassical particle transport. *Physics of Plasmas*, 5(11):3999–4004, 1998. doi: 10.1063/1.873121. URL https://doi.org/10.1063/1.873121.

[44] F. L. Hinton and R. D. Hazeltine. Theory of plasma transport in toroidal confinement systems. *Rev. Mod. Phys.*, 48:239–308, Apr 1976. doi: 10.1103/RevModPhys.48.239. URL https://link.aps.org/doi/10.1103/RevModPhys.48.239.

[45] F L Hinton and M N Rosenbluth. Dynamics of axisymmetric exb and poloidal flows in tokamaks. *Plasma Physics and Controlled Fusion*, 41(3A):A653, 1999. URL http://stacks.iop.org/0741-3335/41/i=3A/a=059.

[46] F. L. Hinton and Marshall N. Rosenbluth. Transport properties of a toroidal plasma at low-to-intermediate collision frequencies. *The Physics of Fluids*, 16(6):836–854, 1973. doi: 10.1063/1.1694436. URL https://aip.scitation.org/doi/abs/10.1063/1.1694436.

[47] S Hirshman and D.J. Sigmar. Neoclassical transport of impurities in tokamak plasmas. 21:1079, 01 1981.

[48] S. P. Hirshman and D. J. Sigmar. Approximate fokker-planck collision operator for transport theory applications. *The Physics of Fluids*, 19(10):1532–1540, 1976. doi: 10.1063/1.861356. URL http://aip.scitation.org/doi/abs/10.1063/1.861356.

[49] S.P. Hirshman. The ambipolarity paradox in toroidal diffusion, revisited. *Nuclear Fusion*, 18(7):917, 1978. URL http://stacks.iop.org/0029-5515/18/i=7/a=004.

[50] M. Honda. Impact of higher-order flows in the moment equations on pfirsch-schlüter friction coefficients. *Physics of Plasmas*, 21(9):092508, 2014. doi: 10.1063/1.4895795. URL https://doi.org/10.1063/1.4895795.

[51] W. Horton. Drift waves and transport. *Rev. Mod. Phys.*, 71:735–778, Apr 1999. doi: 10.1103/RevModPhys.71.735. URL https://link.aps.org/doi/10.1103/RevModPhys.71.735.

[52] Yasuhiro Idomura. Accuracy of momentum transport calculations in full- f gyrokinetic simulations. *Computational Science & Discovery*, 5(1):014018, 2012. URL http://stacks.iop.org/1749-4699/5/i=1/a=014018.

[53] Yasuhiro Idomura, Masato Ida, Takuma Kano, Nobuyuki Aiba, and Shinji Tokuda. Conservative global gyrokinetic toroidal full-f five-dimensional vlasov simulation. *Computer Physics Communications*, 179(6):391 – 403, 2008. ISSN 0010-4655. doi: https://doi.org/10.1016/j.cpc.2008.04.005. URL http://www.sciencedirect.com/science/article/pii/S0010465508001409.

[54] L C Ingesson, H Chen, P Helander, and M J Mantsinen. Comparison of basis functions in soft x-ray tomography and observation of poloidal asymmetries in impurity density. *Plasma Physics and Controlled Fusion*, 42(2):161, 2000. URL http://stacks.iop.org/0741-3335/42/i=2/a=308.

[55] ITER. Tritium breeding. URL https://www.iter.org/mach/tritiumbreeding.

[56] F. Jenko, W. Dorland, M. Kotschenreuther, and B. N. Rogers. Electron temperature gradient driven turbulence. *Physics of Plasmas*, 7(5):1904–1910, 2000. doi: 10.1063/1.874014. URL https://doi.org/10.1063/1.874014.

[57] F. Jenko, W. Dorland, and G. W. Hammett. Critical gradient formula for toroidal electron temperature gradient modes. *Physics of Plasmas*, 8(9):4096–4104, 2001. doi: 10.1063/1.1391261. URL https://doi.org/10.1063/1.1391261.

[58] E. Joffrin, M. Baruzzo, M. Beurskens, C. Bourdelle, S. Brezinsek, J. Bucalossi, P. Buratti, G. Calabro, C.D. Challis, M. Clever, J. Coenen, E. Delabie, R. Dux, P. Lomas, E. de la Luna, P. de Vries, J. Flanagan, L. Frassinetti, D. Frigione, C. Giroud, M. Groth, N. Hawkes, J. Hobirk, M. Lehnen, G. Maddison, J. Mailloux, C.F. Maggi, G. Matthews, M. Mayoral, A. Meigs, R. Neu, I. Nunes, T. Puetterich, F. Rimini, M. Sertoli, B. Sieglin, A.C.C. Sips, G. van Rooij, I. Voitsekhovitch, and JET-EFDA Contributors. First scenario development with the jet new iter-like wall. *Nuclear Fusion*, 54(1):013011, 2014. URL http://stacks.iop.org/0029-5515/54/i=1/a=013011.

[59] S. Jolliet, A. Bottino, P. Angelino, R. Hatzky, T.M. Tran, B.F. Mcmillan, O. Sauter, K. Appert, Y. Idomura, and L. Villard. A global collisionless pic code in magnetic coordinates. *Computer Physics Communications*, 177(5):409 – 425, 2007. ISSN 0010-4655. doi: https://doi.org/10.1016/j.cpc.2007.04.006. URL http://www.sciencedirect.com/science/article/pii/S0010465507002251.

[60] Ye O Kazakov, T Fülöp, I Pusztai, and T Johnson. Effect of plasma shaping and resonance location on minority ion temperature anisotropy in tokamak plasmas heated with icrh. *Journal of Physics: Conference Series*, 401

(1):012011, 2012. URL http://stacks.iop.org/1742-6596/401/i=1/a=012011.

[61] Y. B. Kim, P. H. Diamond, and R. J. Groebner. Neoclassical poloidal and toroidal rotation in tokamaks. *Physics of Fluids B: Plasma Physics*, 3(8): 2050–2060, 1991. doi: 10.1063/1.859671. URL http://dx.doi.org/10.1063/1.859671.

[62] M. Kotschenreuther, W. Dorland, M. A. Beer, and G. W. Hammett. Quantitative predictions of tokamak energy confinement from firs principles simulations with kinetic effects. *Physics of Plasmas*, 2(6):2381–2389, 1995. doi: 10.1063/1.871261. URL https://doi.org/10.1063/1.871261.

[63] Guillaume Latu. Contribution to high-performance simulation and highly scalable numerical schemes. Technical report, CEA, 2018.

[64] Z. Lin, T. S. Hahm, W. W. Lee, W. M. Tang, and R. B. White. Turbulent transport reduction by zonal flows: Massively parallel simulations. *Science*, 281 (5384):1835–1837, 1998. ISSN 0036-8075. doi: 10.1126/science.281.5384.1835. URL http://science.sciencemag.org/content/281/5384/1835.

[65] P. Manas, Y. Camenen, S. Benkadda, W. A. Hornsby, and A. G. Peeters. Enhanced stabilisation of trapped electron modes by collisional energy scattering in tokamaks. *Physics of Plasmas*, 22(6):062302, 2015. doi: 10.1063/1.4922754. URL https://doi.org/10.1063/1.4922754.

[66] C. J. McDevitt and P. H. Diamond. Low-q resonances, transport barriers, and secondary electrostatic convective cells. *Physics of Plasmas*, 14(11): 112306, 2007. doi: 10.1063/1.2806327. URL https://doi.org/10.1063/1.2806327.

[67] M. McIntyre. On global-scale atmospheirc circulations. *"Perspective in fluid dynamics" Cambridge university press*, 2000.

[68] D. R. Nicholson. Introduction to plasma theory. 1983. doi: 10.1017/S0263034600000677.

[69] K. Obrejan. Private communication.

[70] Hideo Okuda and John M. Dawson. Theory and numerical simulation on plasma diffusion across a magnetic field. *The Physics of Fluids*, 16(3):408–426, 1973. doi: 10.1063/1.1694356. URL https://aip.scitation.org/doi/abs/10.1063/1.1694356.

[71] H L Pecseli, J J Rasmussen, H Sugai, and K Thomsen. Evolution of externally excited convective cells in plasmas. *Plasma Physics and Controlled*

Fusion, 26(8):1021, 1984. URL http://stacks.iop.org/0741-3335/26/i=8/a=007.

[72] A. G. Peeters and D. Strintzi. The effect of a uniform radial electric field on the toroidal ion temperature gradient mode. *Physics of Plasmas*, 11 (8):3748–3751, 2004. doi: 10.1063/1.1762876. URL https://doi.org/10.1063/1.1762876.

[73] M. Psimopoulos. Plasma kinetic theory i. *Astrophysics and Space Science*, 256(1):77–84, Mar 1997. ISSN 1572-946X. doi: 10.1023/A:1001104112246. URL https://doi.org/10.1023/A:1001104112246.

[74] M L Reinke, I H Hutchinson, J E Rice, N T Howard, A Bader, S Wukitch, Y Lin, D C Pace, A Hubbard, J W Hughes, and Y Podpaly. Poloidal variation of high- z impurity density due to hydrogen minority ion cyclotron resonance heating on alcator c-mod. *Plasma Physics and Controlled Fusion*, 54(4):045004, 2012. URL http://stacks.iop.org/0741-3335/54/i=4/a=045004.

[75] F. Romanelli. Ion temperature-gradient-driven modes and anomalous ion transport in tokamaks. *Physics of Fluids B: Plasma Physics*, 1(5):1018–1025, 1989. doi: 10.1063/1.859023. URL https://doi.org/10.1063/1.859023.

[76] F. Romanelli and F. Zonca. The radial structure of the ion temperature gradient driven mode. *Physics of Fluids B: Plasma Physics*, 5(11):4081–4089, 1993. doi: 10.1063/1.860576. URL https://doi.org/10.1063/1.860576.

[77] M. N. Rosenbluth and F. L. Hinton. Poloidal flow driven by ion-temperature-gradient turbulence in tokamaks. *Phys. Rev. Lett.*, 80:724–727, Jan 1998. doi: 10.1103/PhysRevLett.80.724. URL https://link.aps.org/doi/10.1103/PhysRevLett.80.724.

[78] B. Scott and J. Smirnov. Energetic consistency and momentum conservation in the gyrokinetic description of tokamak plasmas. *Physics of Plasmas*, 17(11):112302, 2010. doi: 10.1063/1.3507920. URL https://doi.org/10.1063/1.3507920.

[79] H. Sugama, T.-H. Watanabe, and M. Nunami. Linearized model collision operators for multiple ion species plasmas and gyrokinetic entropy balance equations. *Physics of Plasmas*, 16(11):112503, 2009. doi: 10.1063/1.3257907. URL http://dx.doi.org/10.1063/1.3257907.

[80] T.-H. Sugama, H.and Watanabe. Collisionless damping of geodesic acoustic modes. *Journal of Plasma Physics*, 72(6):825 to 828, 2006. doi: 10.1017/S0022377806004958.

[81] T.Vernay, S. Brunner, L. Villard, B. Mcmillan, O. Sauter, S. Jolliet, T. Tran, and A. Bottino. Global collisional gyrokinetic simulations of itg microturbulence starting from a neoclassical equilibrium. 260:012021, 12 2012.

[82] L. Vermare, P. Hennequin, O. D. Gurcan, X. Garbet, C. Honore, F. Clairet, J. C. Giacalone, P. Morel, and A. Storelli. Poloidal asymmetries of flows in the tore supra tokamak. *Physics of Plasmas*, 25(2):020704, 2018. doi: 10.1063/1.5022122. URL https://doi.org/10.1063/1.5022122.

[83] L. Vermare, P. Hennequin, O. D. Gurcan, C. Honore, P. Morel, A. Storelli, F. Clairet, P. Donnel, X. Garbet, R. Giacalone, J. C.and Sabot, and the Tore Supra Team. Poloidal asymmetry and dynamics of perpendicular flow in tore supra plasmas. *Proceedings of the 45th EPS conference on plasma physics*, 2018.

[84] T. Vernay, S.Brunner, L. Villard, B. McMillan, S. Jolliet, T. Tran, A. Bottino, and J. Graves. Neoclassical equilibria as starting point for global gyrokinetic microturbulence simulations. *Physics of Plasmas*, 17(12):122301, 2010. doi: 10.1063/1.3519513. URL https://doi.org/10.1063/1.3519513.

[85] Z. X. Wang, J. Q. Li, J. Q. Dong, and Y. Kishimoto. Generic mechanism of microturbulence suppression by vortex flows. *Phys. Rev. Lett.*, 103:015004, Jul 2009. doi: 10.1103/PhysRevLett.103.015004. URL https://link.aps.org/doi/10.1103/PhysRevLett.103.015004.

[86] T.-H. Watanabe and H. Sugama. Velocity space structures of distribution function in toroidal ion temperature gradient turbulence. *Nuclear Fusion*, 46 (1):24, 2006. URL http://stacks.iop.org/0029-5515/46/i=1/a=003.

[87] W.Connor, R.J. Hastie, and J.B. Taylor. High mode number stability of an axisymmetric toroidal plasma. *Proceedings of the Royal Society of London A: Mathematical, Physical and Engineering Sciences*, 365(1720): 1–17, 1979. ISSN 0080-4630. doi: 10.1098/rspa.1979.0001. URL http://rspa.royalsocietypublishing.org/content/365/1720/1.

[88] Niels Winsor, John L. Johnson, and John M. Dawson. Geodesic acoustic waves in hydromagnetic systems. *The Physics of Fluids*, 11(11):2448–2450, 1968. doi: 10.1063/1.1691835. URL https://aip.scitation.org/doi/abs/10.1063/1.1691835.

[89] S. K. Wong and V. S. Chan. Self-consistent poloidal electric field and neoclassical angular momentum flux. *Physics of Plasmas*, 16(12):122507, 2009. doi: 10.1063/1.3278597. URL https://doi.org/10.1063/1.3278597.

[90] D. Zarzoso, X. Garbet, Y. Sarazin, R. Dumont, and V. Grandgirard. Fully kinetic description of the linear excitation and nonlinear saturation of fast-ion-driven geodesic acoustic mode instability. *Physics of Plasmas*, 19(2):

022102, 2012. doi: 10.1063/1.3680633. URL https://doi.org/10.1063/1.3680633.

[91] F. Zonca and L. Chen. Radial structures and nonlinear excitation of geodesic acoustic modes. *EPL (Europhysics Letters)*, 83(3):35001, 2008. URL http://stacks.iop.org/0295-5075/83/i=3/a=35001.

[92] Fulvio Zonca, Liu Chen, and Robert A Santoro. Kinetic theory of low-frequency alfven modes in tokamaks. *Plasma Physics and Controlled Fusion*, 38(11):2011, 1996. URL http://stacks.iop.org/0741-3335/38/i=11/a=011.